



MONASH University

***A STUDY ON WAKE VORTEX ALLEVIATION OF A WING WITH A
REVERSE DELTA TYPE ADD-ON DEVICE USING PARTICLE IMAGE
VELOCIMETRY (PIV)***

AFAQ ALTAF

B.Eng (Aerospace), MSc (Mechanical Engineering)

A thesis submitted for the degree of *Doctor of Philosophy* at
Monash University in 2015

Department of Mechanical Engineering
SCHOOL OF ENGINEERING
MONASH UNIVERSITY

Copyright Notice

© Afaq Altaf (2015). Except as provided in the Copyright Act 1968, this thesis may not be reproduced in any form without the written permission of the author.

I certify that I have made all reasonable efforts to secure copyright permissions for third-party content included in this thesis and have not knowingly added copyright content to my work without the owner's permission.

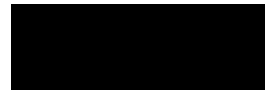
Abstract

The hazardous consequences of a following aircraft encountering the wake turbulence of a large lead aircraft has been well documented and current practice of mandatory separation is less than ideal. The motivation of this project is to develop improved passive add-on devices that are both practical and efficient in alleviating this problem. Particle Image Velocimetry was used in a closed loop low speed wind tunnel to investigate the vortex structures of a half-span wing model with a slender reverse delta type add-on device in the landing configuration. The experimental setup is repeated for various angles of attack and roll angles, and different dimensions of the reverse delta type add-on device. This work investigates the characteristics of the resultant vortices produced by the reverse delta type add-on device, and the wingtip/flap-tip of the half-span wing model by analyzing the flow field in downstream planes perpendicular to the free stream direction. The vortex characteristics dependence on angle of attack and roll, at mean chord based Reynolds number is also analyzed. The peak tangential velocity, peak vorticity and the circulation magnitude of the resultant vortices produced downstream of the half-span wing model are explored. The results are analyzed thoroughly in order to determine if there is any significant decay in the resultant vortex structures. It was found that the reverse delta type add-on device reduces significantly the tangential velocity, vorticity and circulation magnitude by up to 82.9%, 92.6% and 42.8%, respectively and increases the resultant vortex core radius by a factor of 6.57. As it is desirable that add-on devices have a minimal impact on the overall wing, a six component force balance was used to obtain the aerodynamic performance of the half-span wing model. It was found that the reverse delta type add-on device causes a maximum lift reduction of 4.9% and a maximum drag increment of 15.2%.

Declaration

I hereby declare that this thesis contains no material which has been accepted for the award of any other degree or diploma at any university or equivalent institution and that, to the best of my knowledge and belief, this thesis contains no material previously published or written by another person, except where due reference is made in the text of the thesis.

Signature

A solid black rectangular box used to redact the signature.

Date

08/12/2015

This thesis is dedicated to my parents

Prof. Dr. Mohd Altaf Hussain Ahangar and Mrs. Mahjabeena Altaf



My wife

Mrs. Samreen Manzoor

Acknowledgements

The amount of work that has gone into this thesis could not have been possible without the guidance, support and encouragement of many.

First and foremost, I would like to express my sincere gratitude towards my supervisor, Dr. Tan Boon Thong, for providing continuous support and guidance throughout the research work spanning four years. Your encouragement and invaluable advice has helped in my growth as a researcher.

I would also like to express my gratitude to my co-supervisor, Prof. Dr. Ashraf Ali Omar, for endlessly supporting me despite the physical distance and for his constructive feedback and suggestions to improve the quality of my work.

I would like to thank Prof. Dr. Waqar Asrar for encouraging me during times of crisis and for providing constant guidance in experimental aerodynamics.

I would like to thank Mr. Haziq Nasir for simulating the flow over the research model.

I would like to thank the technical staff at the automotive laboratory of IIUM for helping me throughout my research work. I would personally like to thank Mohd Norhafiz Bin Adnan, Firdaus Hakeem Bin Ma'arof and Azliza Binti Embong. Wind tunnel testing and PIV experimental setups would not have been possible without their generous help.

I would like to thank my parents, Prof. Dr. Mohd Altaf Hussain Ahangar and Mrs. Mahajabeena Altaf, whose support has been never-ending and unconditional, for giving me the much needed motivation to complete this journey.

I would like to thank my wife, Mrs. Samreen Manzoor, for being by my side during challenging times and helping me sail through them. Without her love, support and motivation, completion of this thesis would not have been possible.

Finally, I would like to thank my family members for all the love and support they showered on me. I am thankful to them for providing me with invaluable advice.

Table of Contents

Copyright Notice.....	ii
Abstract.....	iii
Declaration.....	iv
Acknowledgements.....	vi
List of Figures.....	ix
List of Tables.....	xiv
Nomenclature.....	xv
List of Abbreviations.....	xviii
CHAPTER ONE	
INTRODUCTION.....	1
1.1 WAKE VORTEX ENCOUNTERS.....	1
1.2 WAKE FORMATION AND DECAY.....	5
1.3 WAKE VORTEX FORMULATION.....	6
1.4 PROBLEM STATEMENT.....	8
1.5 RESEARCH PHILOSOPHY.....	8
1.6 RESEARCH OBJECTIVES.....	8
1.7 SCOPE OF RESEARCH.....	9
1.8 SIGNIFICANCE OF THE STUDY.....	10
1.9 THESIS ORGANIZATION.....	11
CHAPTER TWO	
LITERATURE REVIEW.....	12
2.1 INTRODUCTION.....	12
2.2 WAKE VORTEX HAZARDS.....	12
2.3 WAKE VORTEX SOLUTIONS.....	15
2.3.1 DETECTION AND AVOIDANCE.....	16
2.3.2 WAKE VORTEX ALLEVIATION.....	20
2.3.2.1 Passive Wake Vortex Alleviation.....	21
2.3.2.2 Active Wake Vortex Alleviation.....	29
2.4. SUMMARY.....	32
CHAPTER THREE	
EXPERIMENTAL APPARATUS AND METHODOLOGY.....	33
3.1 INTRODUCTION.....	33
3.2 EXPERIMENTAL APPARATUS.....	33
3.2.1 The Wind Tunnel.....	33
3.2.2 The Half-Span Wing Model.....	36
3.2.3 The Reverse Delta Type Add-on Devices.....	37
3.2.4 The complete model.....	39
3.3 RESEARCH METHODOLOGY.....	42
3.4 EXPERIMENTAL PROCEDURE.....	45
3.5 PIV UNCERTAINTY ANALYSIS.....	49
3.5.1 STATISTICAL UNCERTAINTY.....	50
3.5.2 UNCERTAINTY IN THE WING ANGLE OF ATTACK.....	50
3.5.3 UNCERTAINTY IN DISPLACEMENT.....	51
3.5.4 TOTAL UNCERTAINTY.....	52
3.6 SUMMARY.....	52

CHAPTER FOUR	
THREE DIMENSIONAL FLOW BOUNDARY CORRECTIONS	53
4.1 INTRODUCTION.....	53
4.2 BUOYANCY	53
4.3 SOLID BLOCKAGE.....	54
4.4 WAKE BLOCKAGE	56
4.5 STREAMLINE CURVATURE	56
4.6 DATA CORRECTIONS	58
4.7 SUMMARY	60
CHAPTER FIVE	
RESULTS AND DISCUSSIONS	61
5.1 INTRODUCTION.....	61
5.2 CASE 1	62
5.2.1 Velocity Vectors and Vorticity Contours.....	63
5.2.2 Tangential Velocity	77
5.2.3 Circulation.....	78
5.2.4 Aerodynamic Performance	82
5.3 CASE 2	85
5.3.1 Velocity Vectors and Vorticity Contours.....	86
5.3.2 Tangential Velocity	97
5.3.3 Circulation.....	98
5.3.4 Aerodynamic Performance	100
5.4 CASE 3	102
5.4.1 Velocity Vectors and Vorticity Contours.....	103
5.4.2 Tangential Velocity	114
5.4.3 Aerodynamic Performance	115
5.5 CASE 4	117
5.5.1 Velocity Vectors and Vorticity Contours (wingtip location)	118
5.5.2 Velocity Vectors and Vorticity Contours (flap-tip location)	129
5.5.3 Aerodynamic Performance	140
5.6 CASE 5	142
5.6.1 Velocity Vectors and Vorticity	144
5.7 Lift and Drag Penalties of Wake Vortex Alleviation Methods	156
5.8 SUMMARY	158
CHAPTER SIX	
CONCLUSIONS AND RECOMMENDATIONS	160
6.1 CONCLUSIONS.....	160
6.2 RECOMMENDATIONS FOR FURTHER STUDIES	163
6.3 SUMMARY	164
References.....	166
Publications.....	173

List of Figures

<u>Figure No:</u>	<u>Page No:</u>
Figure 1.1: Types of aircraft wake vortex encounters	3
Figure 1.2: International Civil Aviation Organization's (ICAO's) Weight Class Dependent Separation Criteria	4
Figure 1.3: Stages of wake vortex lifespan	6
Figure 2.1: Wake turbulence accidents per aircraft category	13
Figure 2.2: Wake turbulence accidents per flight phase	13
Figure 2.3: Altitude of wake turbulence events in U.S.	14
Figure 2.4: Degree of upset due to wake turbulence events in U.S.	14
Figure 2.5: Types of motion induced by wake turbulence in U.S.	15
Figure 2.6: The Green Wake Project Concept	18
Figure 2.7: Wing add-on devices tested in C-Wake and AWIATOR projects	26
Figure 2.8: Schematic of RHDW experimental setup	27
Figure 3.1: Parametric view of the IIUM wind tunnel	34
Figure 3.2: Schematic diagram of IIUM closed-loop low-speed wind tunnel	34
Figure 3.3: IIUM wind tunnel components	35
Figure 3.4: Schematic Diagram of the IIUM six component force balance	35
Figure 3.5: Schematic diagram of the half-span wing model	36
Figure 3.6: Half-span wing model in the wind tunnel	37
Figure 3.7: Schematic of the reverse delta type add-on devices	38
Figure 3.8: Image of the reverse delta type add-on devices	38
Figure 3.9: Plot of geometric size of reverse delta type add-on device versus Lift and drag coefficient	39
Figure 3.10: Schematic diagram showing the angle of attack and roll angle variation of the reverse delta type add-on device	39
Figure 3.11: Image showing the movable mounting used for angle of attack And roll angle variation of the reverse delta type add-on device	40

Figure 3.12: Schematic diagram of the half-span wing model with a reverse delta type add-on device attached	41
Figure 3.13: Image of the half-span wing model with a reverse delta type add-on device attached	41
Figure 3.14: Principle layout of a PIV system	43
Figure 3.15: Schematic diagram of the experimental setup	46
Figure 3.16: Image of the experimental setup in the wind tunnel	47
Figure 3.17: Schematic diagram of the downstream measurement planes	48
Figure 3.18: PIV image map of the wingtip vortex at $\alpha=7^\circ$ at $x/(b/2)=0.548$	49
Figure 4.1: Body shape factor versus thickness ratio for a number of bodies	55
Figure 4.2: Ratio of tunnel test section shape versus (model span/tunnel width) for a number of tunnel types	55
Figure 4.3: Boundary correction factor (δ) for a wing with uniform loading in a closed rectangular tunnel	57
Figure 4.4: Downwash correction factor (τ_2) for open and closed jets	58
Figure 5.1: Schematic of the half-span wing model with a large reverse delta type add-on device attached (Case 1)	62
Figure 5.2: Streamlines showing the merging of the wingtip vortex, flap-tip vortex and reverse delta type add-on device vortices downstream (Case 1)	62
Figure 5.3: Interaction of co-rotating cylindrical vortices	65
Figure 5.4: Velocity Vectors, Tangential Velocity Magnitude and Vorticity Contours at $x/(b/2)=0.021$ for Case 1	70
Figure 5.5: Velocity Vectors, Tangential Velocity Magnitude and Vorticity Contours at $x/(b/2)=0.548$ for Case 1	72
Figure 5.6: Velocity Vectors, Tangential Velocity Magnitude and Vorticity Contours at $x/(b/2)=1.075$ for Case 1	74
Figure 5.7: Velocity Vectors, Tangential Velocity Magnitude and Vorticity Contours at $x/(b/2)=2.387$ for Case 1	76
Figure 5.8: Non-dimensional tangential velocity distributions of HLC, HLC with S-rdw and HLC with L-rdw for Case 1	77
Figure 5.9: Vortex strength $\Gamma/V_\infty(b/2)$ versus radius $r/(b/2)$ of wingtip vortex of	

HLC, HLC with S-rdw and HLC with L-rdw for Case 1	80
Figure 5.10: Column chart of peak tangential velocity magnitude of all investigated configurations at four downstream planes for Case 1	81
Figure 5.11: Column chart of vorticity magnitude of all investigated configurations at four downstream planes for Case 1	82
Figure 5.12: Aerodynamic performance of the Plain Wing, HLC, HLC with S-rdw and HLC with L-rdw (Case 1)	83
Figure 5.13: Schematic of the half-span wing model with a large reverse delta type add-on device attached (Case 2)	85
Figure 5.14: Streamlines showing the merging of the wingtip vortex, flap-tip vortex and reverse delta type add-on device vortices downstream (Case 2)	85
Figure 5.15: Velocity Vectors, Tangential Velocity Magnitude and Vorticity Contours at $x/(b/2)=0.021$ for Case 2	90
Figure 5.16: Velocity Vectors, Tangential Velocity Magnitude and Vorticity Contours at $x/(b/2)=0.548$ for Case 2	92
Figure 5.17: Velocity Vectors, Tangential Velocity Magnitude and Vorticity Contours at $x/(b/2)=1.075$ for Case 2	94
Figure 5.18: Velocity Vectors, Tangential Velocity Magnitude and Vorticity Contours at $x/(b/2)=2.387$ for Case 2	96
Figure 5.19: Non-dimensional tangential velocity distributions of HLC, HLC with S-rdw and HLC with L-rdw for Case 2	97
Figure 5.20: Vortex strength $\Gamma/V_\infty(b/2)$ versus radius $r/(b/2)$ of wingtip vortex of HLC, HLC with S-rdw and HLC with L-rdw for Case 2	100
Figure 5.21: Aerodynamic performance of the Plain Wing, HLC, HLC with S-rdw and HLC with L-rdw (Case 2)	101
Figure 5.22: Schematic of the half-span wing model with a large reverse delta type add-on device attached (Case 3)	102
Figure 5.23: Streamlines showing the merging of the flap-tip vortex and the reverse delta type add-on device vortices (Case 3)	102
Figure 5.24: Velocity Vectors, Tangential Velocity Magnitude and Vorticity Contours at $x/(b/2)=0.021$ for Case 3	107
Figure 5.25: Velocity Vectors, Tangential Velocity Magnitude and Vorticity Contours at $x/(b/2)=0.548$ for Case 3	109

Figure 5.26: Velocity Vectors, Tangential Velocity Magnitude and Vorticity Contours at $x/(b/2)=1.075$ for Case 3	111
Figure 5.27: Velocity Vectors, Tangential Velocity Magnitude and Vorticity Contours at $x/(b/2)=2.387$ for Case 3	113
Figure 5.28: Non-dimensional tangential velocity distributions of HLC, HLC with S-rdw and HLC with L-rdw for Case 3	114
Figure 5.29: Aerodynamic performance of the Plain Wing, HLC, HLC with S-rdw and HLC with L-rdw (Case 3)	115
Figure 5.30: Schematic of the half-span wing model with a large reverse delta type add-on device attached (Case 4)	117
Figure 5.31: Streamlines showing the merging of the flap-tip vortex and the reverse delta type add-on device vortices (Case 4)	118
Figure 5.32: Velocity Vectors, Tangential Velocity Magnitude and Vorticity Contours at $x/(b/2)=0.021$ for Case 4 (wingtip location)	122
Figure 5.33: Velocity Vectors, Tangential Velocity Magnitude and Vorticity Contours at $x/(b/2)=0.548$ for Case 4 (wingtip location)	124
Figure 5.34: Velocity Vectors, Tangential Velocity Magnitude and Vorticity Contours at $x/(b/2)=1.075$ for Case 4 (wingtip location)	126
Figure 5.35: Velocity Vectors, Tangential Velocity Magnitude and Vorticity Contours at $x/(b/2)=2.387$ for Case 4 (wingtip location)	128
Figure 5.36: Velocity Vectors, Tangential Velocity Magnitude and Vorticity Contours at $x/(b/2)=0.021$ for Case 4 (flap-tip location)	133
Figure 5.37: Velocity Vectors, Tangential Velocity Magnitude and Vorticity Contours at $x/(b/2)=0.548$ for Case 4 (flap-tip location)	135
Figure 5.38: Velocity Vectors, Tangential Velocity Magnitude and Vorticity Contours at $x/(b/2)=1.075$ for Case 4 (flap-tip location)	137
Figure 5.39: Velocity Vectors, Tangential Velocity Magnitude and Vorticity Contours at $x/(b/2)=2.387$ for Case 4 (flap-tip location)	139
Figure 5.40: Aerodynamic performance of the Plain Wing, HLC, HLC with S-rdw and HLC with L-rdw (Case 4)	140
Figure 5.41: Schematic of the half-span wing model with a large reverse delta type add-on device attached (Case 5)	142
Figure 5.42: Column chart of peak tangential velocity magnitude of all investigated configurations at four downstream planes for Case 5	143

Figure 5.43: Column chart of vorticity magnitude of all investigated configurations at four downstream planes for Case 5	144
Figure 5.44: Velocity Vectors, Tangential Velocity Magnitude and Vorticity Contours at $x/(b/2)=0.021$ for Case 5	149
Figure 5.45: Velocity Vectors, Tangential Velocity Magnitude and Vorticity Contours at $x/(b/2)=0.548$ for Case 5	151
Figure 5.46: Velocity Vectors, Tangential Velocity Magnitude and Vorticity Contours at $x/(b/2)=1.075$ for Case 5	153
Figure 5.47: Velocity Vectors, Tangential Velocity Magnitude and Vorticity Contours at $x/(b/2)=2.387$ for Case 5	155

List of Tables

<u>Table No:</u>	<u>Page No:</u>
Table 2.1: Current spacing between aircraft in nautical miles (nm)	19
Table 4.1: Corrected values of aerodynamic coefficients	60
Table 4.2: Percentage change in the corrected and uncorrected values	60
Table 5.1: Overall findings of Case 1	84
Table 5.2: Overall findings of Case 2	101
Table 5.3: Overall findings of Case 3	116
Table 5.4: Overall findings of Case 4 (wingtip)	120
Table 5.5: Overall findings of Case 4 (flap-tip)	131
Table 5.6: Overall findings of Case 4	141
Table 5.7: Overall findings of Case 5	146
Table 5.8: Findings of all cases studied	146
Table 5.9: Comparison of lift and drag penalties with other wake vortex alleviation techniques	156

Nomenclature

ϕ_{rdw}	Roll angle of reverse delta wing (deg)
δ	Boundary correction factor
λ	Ratio of tunnel height to tunnel width
σ	Variance
τ_1	Factor depending on tunnel test section shape and the model span to tunnel width ratio
τ_2	Downwash correction factor
ε_{sb}	Solid blockage
ε_t	Total blockage
ε_{wb}	Wake blockage
ΔC_{Di}	Induced drag increment due to the boundaries
$\Delta CL,$	Additive correction to the lift coefficient
$\Delta C_{m,sc}$	Additive correction to the moment coefficient
$\Delta \alpha_i$	Induced angle due to the boundaries
$\Delta \alpha_{sc}$	Streamline curvature effect on angle of attack
a	Wing lift curve slope
B	Test section width (m)
b	Wing span (m)
c	Chord length (m)
C	Tunnel Test section area (m ²)
C_D	Drag Coefficient
C_{Du}	Uncorrected drag coefficient
C_L	Lift coefficient
C_{Lu}	Uncorrected lift coefficient

C_m	Moment coefficient
C_{mu}	Uncorrected moment coefficient
H	Test section height (m)
k	Number of points (m)
K	Ratio of wing span to tunnel width
K_1	Body shape factor
L/D	Lift to drag ratio
l_t	Tail length (m)
N	Number of measurement samples
q	Dynamic pressure (pa)
q_u	Uncorrected dynamic pressure (pa)
r	Radius (m)
r_c	Core radius (m)
Re_c	Reynolds number based on mean chord length
Re_u	Uncorrected Reynolds number based on mean chord length
S	Wing area (m ²)
t	Thickness (m)
V	Free stream Velocity (m/s)
V_∞	Free stream velocity (m/s)
V_i	Mean velocity (m/s)
V_u	Uncorrected free stream velocity (m/s)
V_θ	Tangential velocity (m/s)
x	Stream-wise coordinate (m)
x/c	Ratio of stream-wise coordinate and chord length
y	Span-wise coordinate (m)

z	Transverse coordinate (m)
α	Angle of attack of main wing (deg)
α_{rdw}	Angle of attack of reverse delta type add-on device (deg)
α_u	Uncorrected angle of attack of main wing (deg)
Γ	Circulation (m^2/s)
ΔD_B	Buoyancy Correction

List of Abbreviations

AVOSS	Aircraft Vortex Spacing System
AWIATOR	Aircraft Wing with Advanced Technology OpeRation
CCD	Charge Coupled Device
CFD	Computational Fluid Dynamics
CW	Continuous Wave
DFS	Differential Flap Setting
DNS	Direct Numerical Simulation
DSS	Differential Spoiler Setting
et al.	(<i>et alia</i>), and others
FAA	Federal Aviation Administration
FLAME	Future Laser Atmospheric Measurement Equipment
HDW	Half Delta Wing
HLC	High Lift Configuration
ICAO	International Civil Aviation Organization
IFR	Instrument Flight Rules
IIUM	International Islamic University Malaysia
ISO	International Organization for Standardization
LES	Large Eddy Simulation
LIDAR	Laser Doppler Radar
L-rdw	Large Reverse Delta Wing
MFLAME	Multifunction Future Laser Atmospheric Measurement Equipment
NACA	National Advisory Committee for Aeronautics
NASA	National Aeronautics and Space Administration
Nd:YAG	Neodymium Yttrium Aluminium Garnet

PIV	Particle Image Velocimetry
RANS	Reynolds-Averaged Navier-Stokes
RHDW	Reverse Half Delta Wing
S-rdw	Small Reverse Delta Wing
UV LIDAR	Ultra Violet Laser Doppler Radar
VFR	Visual Flight Rules

CHAPTER ONE

INTRODUCTION

1.1 WAKE VORTEX ENCOUNTERS

Due to the continuous air traffic growth, current separation rules are becoming highly inadequate to cope with future air traffic needs. This is motivating the study of wake vortices with the objective of reducing the current spacing between aircrafts while maintaining the same level of safety. Understanding of wake vortex behaviour would lead to the development of constructive measures of control. The study and control of swirling vortex flows is vital towards developing ways to suppress wingtip and flap-tip vortices generated by commercial aircraft and result in their rapid decay which leads to a reduction in the hazard posed to trailing aircraft (Coustols et al., 2006).

Wake vortices generated by all aircraft are an unavoidable consequence of the creation of lift. Wake vortices are generated by high pressure air from the lower surface of the wing flowing around the wingtip/flap-tip into the low pressure air above the wing. The result is a pair of vortices that originate from the wingtips/flap-tips in opposite directions, creating an area of turbulence behind the aircraft. Aircrafts with multiple flaps and cutouts (gaps) between the flaps, initially produce multiple vortices, which quickly combine into one vortex for each wing (Veillette, 2002).

The intensity of the wake vortices generated by a specific aircraft is determined by factors such as the aircraft's weight, speed, configuration (amount of flaps and slats extension), wingspan, angle of attack and the atmospheric conditions in which the aircraft is being flown (Veillette, 2002). Wake vortices can persist as long as three minutes, depending on various factors, including wind conditions (FAA, 2002). Trailing vortices from wingtips

have been observed to persist for many kilometres (Andrews, 1970). Wake vortex encounters pose a severe hazard to trailing aircraft, especially when the trailing aircraft are smaller in size (McGowen, 1968). Flying in close proximity to the airport runway, where take-off and landing occur, increase the level of hazard because the wake vortex circulation is at a maximum (Arndt et al., 1991). Wake vortex and turbulence generated by large aircraft is strong and can be unsafe to trailing aircraft. Depending on the aircraft's position and orientation with respect to the wake, it can experience sudden upwash or downwash, uncontrollable rolls and sudden loss of altitude (Ortega et. al., 2002), see Figure 1.1. Wake turbulence has resulted in fatal accidents at low altitudes during landing approaches because of insufficient time and altitude for pilots to recover full control of their aircraft after being severely affected by the strong vortices (Veillette, 2002). The possibility to recuperate from hazardous forms of wake turbulence depends on altitude, manoeuvrability and power of the aircraft. A trailing plane travelling at a speed of 60 m/s, flying axially into the tip vortex generated by a Boeing 757, experiences huge changes in incident flow angle which can both stall the wing and generate large rolling moments that are beyond the control of the aircraft ailerons (Page et al., 1991).

On December 17, 2013; A Boeing 737-800 (Malaysian Airlines, Flight Number MH170), flying in from Jakarta, experienced severe turbulence while preparing to land at the Kuala Lumpur International Airport (KLIA), due to an air vortex caused by an earlier landing by an Airbus 380 super jumbo. The vortex caused the Boeing 737-800 to pitch down and to the sides during its descent (The Star Newspaper, 18 December 2013). This particular incident highlights the severity of the vortices created by larger aircraft. To avoid trailing aircraft experiencing strong swirling vortical flow, the spacing between aircrafts within the take-off and landing corridors at busy airports is maintained according to the International Civil Aviation Organization's (ICAO's) Weight Class Dependent Separation Criteria, see

figure 1.2. This in-turn increase the time intervals between consecutive landings and take-offs (Babie and Nelson, 2004).

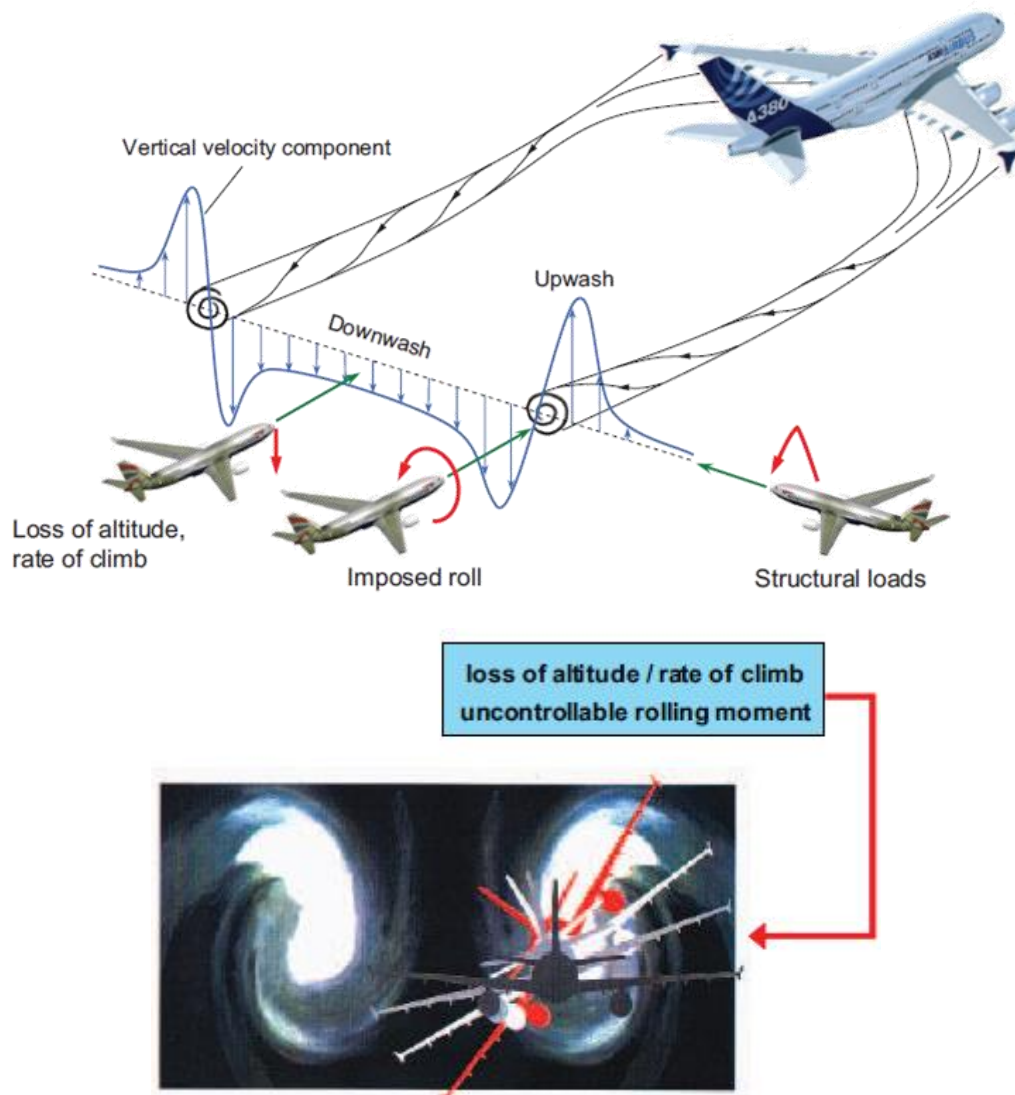


Figure 1.1: Types of aircraft wake vortex encounters [Roeland, 2007].

Babie and Nelson (2004) state that air traffic control authorities have approved a set of operational regulations that have provided commercial aviation with a safe solution to the problem of aircraft wake vortex encounters. The regulations include aircraft segregation by size, controlling flight paths during take-off and landing, and keeping a fixed separation between aircrafts based on the size of the lead aircraft. Due to an uncertainty in knowing the location of the vortices relative to the flight path, the separation distances between aircrafts

are selected based on an overly conservative basis. These measures limit the traffic volume at major airports since a lesser number of aircrafts can be handled daily than could be handled if an effective solution to wake vortex encounters becomes available.

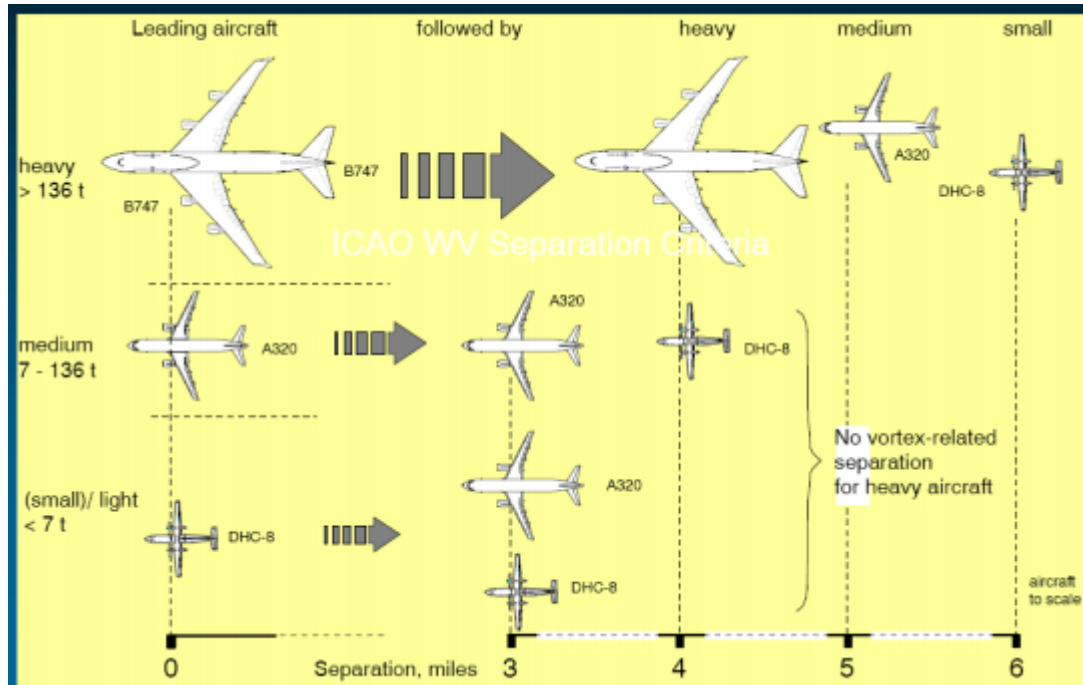


Figure 1.2: International Civil Aviation Organization's (ICAO's) Weight Class Dependent Separation Criteria [Elsenaar, 2006].

The minimum distance required between two aircraft at approach and landing is mostly a function of visibility conditions and the relative sizes of the lead and trailing aircraft involved. For good visibility conditions, when visual flight rules (VFR) are in use, the separation between aircraft is the responsibility of the pilot of the trailing aircraft. For poor visibility, when instrument flight rules (IFR) are in use, the separation between the aircraft is the responsibility of the air traffic controller who must adhere to Federal Aviation Administration (FAA) rules. The separations are based on the maximum take-off weights of the lead and trailing aircraft and must be followed when the airport functions under IFR.

Spalart (1998) gives a detailed account of arguments that have been made in respect to why the present spacing rules work. The “predictable decay” argument states that the spacing rules permit sufficient time for the vortices to individually diffuse such that if a wake vortex

encounter happens, the effect on the trailing aircraft would be slight. The “stochastic collapse” argument states that spacing is large enough to almost guarantee that some instability will terminate the vortices before the trailing aircraft approaches the wake vortices shed by the lead aircraft. However, no spacing rules were ever clearly derived from either argument.

1.2 WAKE FORMATION AND DECAY

Considering the downstream development of the wake, the vortex wake can be classified into four regions in terms of the ratio of x/b , where x is horizontal distance downstream measured from the wingtip and b is wing span of the aircraft (see Figure 1.3), as stated by Breitsamter (2011):

- i. The near field, $x/b \leq 0.5$, is characterized by the development of highly concentrated vortices, shed at all surface discontinuities (eg. Flap-tips, spoiler-tips, wingtips, etc.).
- ii. The extended near field, $0.5 < x/b \leq 10$, is where the wake vortex roll-up process occurs and the merging of dominant vortices occurs, leading progressively to two counter-rotating vortices. The roll-up process is the formation of a highly concentrated vortex which slowly increases in size and strength. The roll-up process of vortices is of great interest as this process determines the characteristic parameters of the vortices and, as a consequence, the flow in the wake of the aircraft.
- iii. The mid and far field, $10 < x/b \leq 100$, is where the wake vortex descends in the atmosphere and linear instabilities appear.
- iv. The dispersion region, $x/b > \sim 100$, is where instabilities have fully developed leading to a strong interaction between the two counter-rotating vortices resulting in their collapse.

Note that the above given values are for quiet air. For other weather conditions with turbulence or shear, these values can be considerably less.

Near field studies are mostly conducted in a wind tunnel test section. Wind tunnel studies focus on vortex formation and roll-up process. In the present study, the near field and extended near field measurements are carried out using Particle Image Velocimetry (PIV).

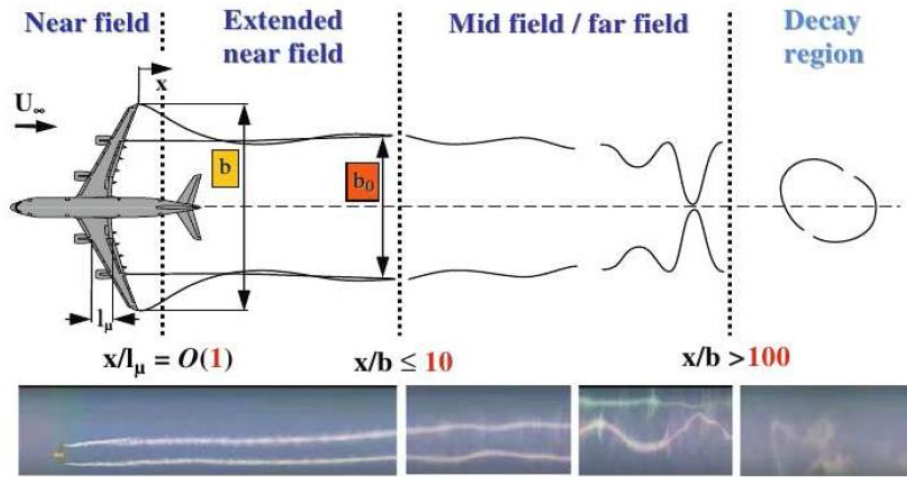


Figure 1.3: Stages of wake vortex lifespan [Breitsamter, 2011].

1.3 WAKE VORTEX FORMULATION

For level flight

$$L = C_L \left(\frac{\rho_\infty}{2} \right) U_\infty^2 \left(\frac{b^2}{\Lambda} \right) = mg \quad (1.1)$$

where Λ is the aspect ratio.

Applying the Kutta-Joukowski theorem, the root circulation Γ_0 is given as:

$$dL = \rho_\infty U_\infty \Gamma(y) dy, \text{ with } L = \rho_\infty U_\infty \Gamma_0 b_0$$

where b_0 is the lateral distance between the vorticity centroids of the two rolled-up counter-rotating vortices.

Circulation strength, Γ_0 , is proportional to the total lift and inversely proportional to the airspeed V_∞ and the lateral spacing b_0 between the vorticity centroids:

$$\Gamma_0 = \frac{L}{\rho_\infty U_\infty b_0} = \frac{C_L U_\infty b}{2\Lambda s} \quad (1.2)$$

The span-wise load factor is defined as, $s = \frac{b_0}{b}$.

For elliptical circulation distribution, the span-wise load factor is given by: $s = \frac{\pi}{4}$.

The corresponding root circulation is then given by:

$$\Gamma_0 = \frac{2C_L U_\infty b}{\pi\Lambda} \quad (1.3)$$

In the absence of vertical wind, the vortices will sink due to mutual induction. Using the Biot-Savart law, the induced velocity w_0 on the vorticity centroids results in:

$$w_0 = \frac{\Gamma_0}{2\pi b_0} = \frac{C_L U_\infty b}{4\pi\Lambda s^2} \quad (1.4)$$

For elliptical distribution, the induced velocity w_0 is given by:

$$w_0 = \frac{4C_L U_\infty}{\pi^3\Lambda} \quad (1.5)$$

The time interval at which the vortex pair moves downwards by a distance equal to the vortex spacing b_0 is given by:

$$t_0 = \frac{b_0}{w_0} = \frac{2\pi(sb)^2}{\Gamma_0} = \frac{4\pi\Lambda s^3 b}{C_L U_\infty} \quad (1.6)$$

For elliptical distribution, the time interval is given by:

$$t_0 = \frac{\pi^4}{16} \frac{\Lambda b}{C_L U_\infty} \quad (1.7)$$

The above equations show the importance of the wing span loading parameter ‘ s ’ on key parameters such as the initial circulation strength (inversely proportional to s), initial vortex sink speed (inversely proportional to s^2) and the characteristic time scale for vortex decay (proportional to s^3).

1.4 PROBLEM STATEMENT

Aircraft wake vortex flow is turbulent swirling flow that is formed behind an aircraft as it passes through air. The problem faced by the aviation industry is how to alleviate the wake vortex generated by aircrafts so as to avoid trailing aircraft to be immersed in turbulent vortical flows which can cause a high degree of instability and loss of control. In order to avoid wake vortex encounters, ICAO has prescribed a minimum separation criterion between two aircraft during the approach, landing and take-off corridors. The current spacing rules in place are based on worst case scenarios and allow far more separation distance between aircraft than is really needed to avoid accidents. However, the financial repercussions of these separation requirements are staggering (Matalanis & Eaton, 2007).

1.5 RESEARCH PHILOSOPHY

Although many proposed ideas of wake vortex alleviation have been developed and in some cases put in to practise, there are still deficiencies that result in either insufficient wake vortex alleviation, too high a performance penalty or both. The next chapter will review this in detail. This study explores characteristics of the vortices generated downstream of a half-span wing model with a reverse delta type add-on device. The findings from this study will determine if the reverse delta type add-on device has the capability to significantly alleviate wake vortices and the associated performance penalty.

1.6 RESEARCH OBJECTIVES

The research objectives are to:

1. Design a reverse delta type add-on device that would help in significant wake vortex alleviation.

2. Show that the reverse delta type add-on device has minimal detrimental effect on the wing performance by measuring and comparing lift and drag performance data.
3. Quantify the wake vortex alleviation in the near field and extended near field by measuring flow fields downstream of the wing section using Particle Image Velocimetry (PIV).

1.7 SCOPE OF RESEARCH

This thesis is part of a wider effort of alleviating wake vortex by using an add-on device. The purpose of this research is to develop a feasible solution to wake vortex encounters that will enable a reduction in separation distance between two aircraft during approach, landing and take-off without compromising safety.

The scope of research is summarized as follows:

1. Half-span wing model equipped with a slat (maximum deflection 15°), a flap (maximum deflection 20°) and two sets of reverse delta type add-on devices are used as vortex generators. The vortices are generated at discontinuities along the half-span wing model.
2. Particle Image Velocimetry (PIV), a minimally intrusive measurement technique, is used to obtain instantaneous velocity measurements.
3. Near and extended near field measurements are carried out in a low speed closed loop wind tunnel to study the influence of the reverse delta type add-on device on wake vortex alleviation at high lift configuration.
4. Vortex structures of the half-span wing model with a reverse delta type add-on device are quantitatively compared with high lift configuration in terms of vortex roll-up, peak tangential velocity, peak vorticity and circulation strength. The effect

of the interactions of the add-on device vortices and the wingtip/flap-tip vortex are also stated.

5. A six component force balance is used to obtain the aerodynamic performance of the half-span wing model with/without a reverse delta type add-on device to quantify the performance penalty resulting from such an add on device.

This thesis will provide a benchmark for further studies of add-on devices. If a reverse delta type add-on device enables sufficient wake vortex alleviation to take place or hastens wake vortex decay, it could help reduce/minimize the dangers posed by wake vortex encounters and it would yield substantial benefits to the aviation industry by reducing the separation distance between aircraft during take-off and landing phases.

1.8 SIGNIFICANCE OF THE STUDY

Adding more runways to airports is not a practical solution as most large airports are close to major metropolitan areas where expansion would be difficult and expensive. If one major airport suffers delays due to runway expansion, it could send ripples through the entire world causing major delays for many other airports. Expansion would be necessary at several major airports in order to cater to the ever increasing volume of air traffic. Also, stern noise regulations are in place at many airports. This makes expansion of airports situated near residential areas difficult as large chunks of residential areas will have to be cleared to allow for airport expansions and also minimize the effects of noise pollution.

Thus, a better approach to manage wake vortex hazard would be to find ways of increasing the aircraft handling capacity at airports by reducing the required separation between aircraft. This study focuses on using a reverse delta type add-on device to alter the roll-up process of the wake vortices generated behind a half-span wing and also to increase the resultant vortex core dimension significantly to hasten vortex dissipation.

1.9 THESIS ORGANIZATION

To fully understand the main purpose of this research, the thesis has been divided into eight chapters.

Chapter one provides an introduction of the wake vortex encounters, wake formation and decay, and the wake vortex formulation. It also includes the problem statement, research philosophy, research objectives, research methodology and scope of research.

Chapter two provides a review of the available literature concerning different strategies of reducing wake vortex encounters.

Chapter three discusses in detail the experimental apparatus and experimental procedure. An elaborate theoretical background and working principle of PIV is provided along with an in-depth PIV uncertainty analysis.

Chapter four discusses in detail the three dimensional flow boundary corrections and the necessity to perform such corrections.

Chapter five contains PIV results which have been thoroughly analyzed to yield the tangential velocity distributions and circulation distributions. Also included are the six component force balance results. Detailed discussions of the results are provided to better understand the impact of a reverse delta type add-on device on wake vortex alleviation.

Chapter six contains relevant conclusions which summarize the overall statements made in the thesis. It also provides recommendations for further studies.

CHAPTER TWO

LITERATURE REVIEW

2.1 INTRODUCTION

Many attempts to solve the problem of wake vortex encounters have been made in the past. A large amount of research has been conducted, a variety of techniques have been explored, and plentiful fundamental knowledge about wake vortex has been gained (Coustols et. al., 2006; Breitsamter, 2011; Matalanis & Eaton, 2007). Although some techniques have shown potential, no solution has emerged that overcomes wake vortex problems in practice and enables the required aircraft spacing distances near airports to be reduced without compromising safety.

Before discussing solutions to wake vortex problems, it is vital to discuss the hazards of wake vortex on trailing aircraft.

This chapter will highlight the hazards of wake vortex on trailing aircraft and major research work carried out as a means of finding permanent and practical solution to the wake vortex problem.

2.2 WAKE VORTEX HAZARDS

U.S. wake turbulence accidents statistical data (1983-2002) indicates that most accidents involve small aircrafts during their approach and landing phase (Veillette, 2002). Figure 2.1 shows the wake turbulence accidents per aircraft category and Figure 2.2 shows the wake turbulence accidents per flight phase.

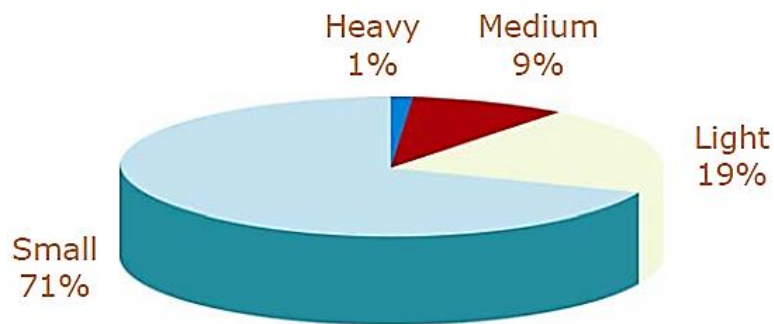


Figure 2.1: Wake turbulence accidents per aircraft category [Veillette, 2002].

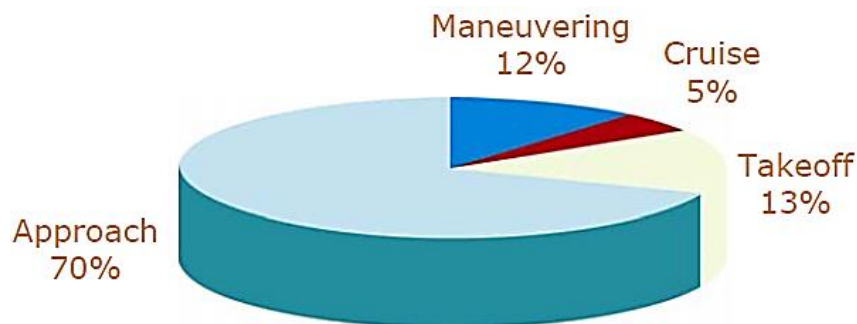


Figure 2.2: Wake turbulence accidents per flight phase [Veillette, 2002].

The *Maneuvering* category in Figure 2.2 includes anything that cannot occur in the other categories listed (i.e. Take-off, Cruise and Approach).

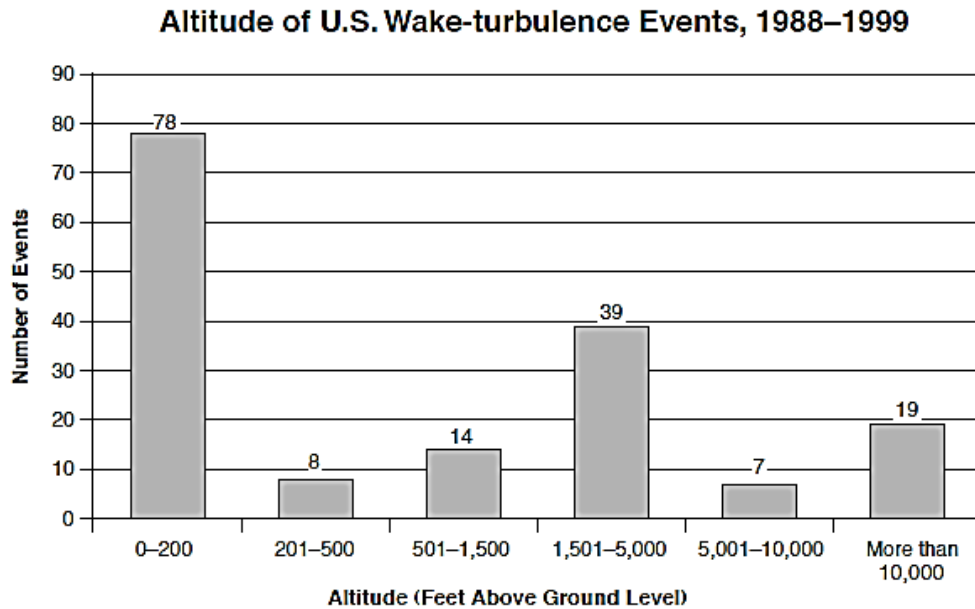
Studies and statistical data (Veillette, 2002) on wake turbulence indicates that:

- More than half of wake turbulence accidents occur during approach and landing.
- Most wake turbulence accidents occur at very low altitudes (less than 200 feet above the runway threshold), see Figure 2.3.
- 90% of wake turbulence accidents involve aircraft that weigh less than 13,600 kg (30,000 lb).
- In 99% of the reported events, the effects of wake turbulence are abrupt and occur without any warning.

Many of the wake turbulence events reported had severe effects on trailing aircraft.

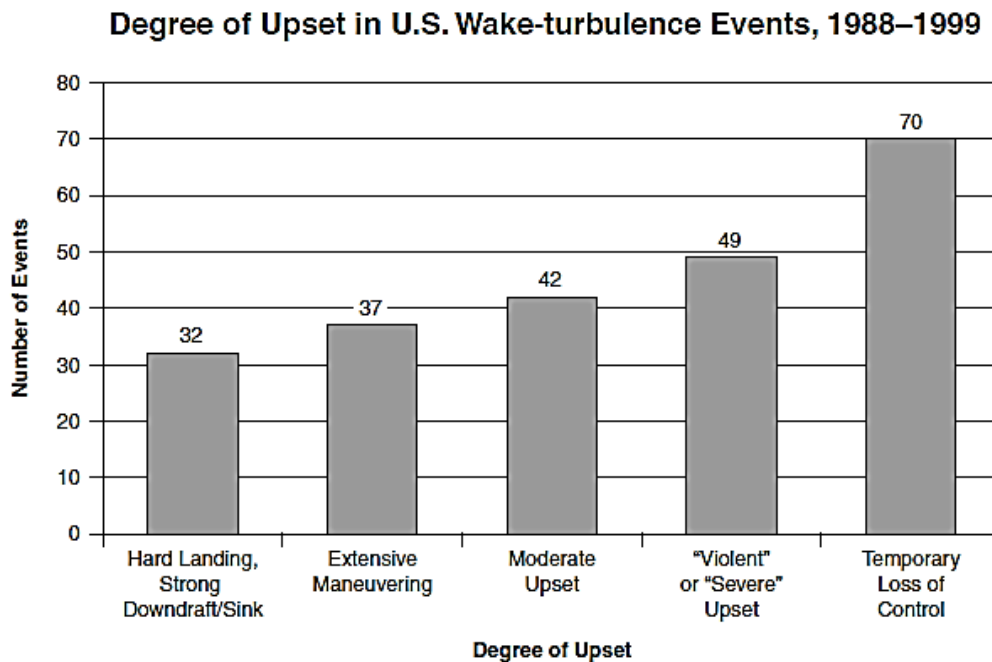
Figure 2.4 summarizes the degree of upset due to wake turbulence (as reported by aircraft pilots).

Reports on 16 events (approximately 10% of all events) said that pilots had refused to accept a take-off clearance because of wake turbulence, and reports on 9 events (approximately 5% of all events) said that pilots rejected a take-off because of the risk of a wake turbulence event occurring.



Source: Patrick R. Veillette, Ph.D., from U.S. National Aeronautics and Space Administration Aviation Safety Reporting System data on 165 events

Figure 2.3: Altitude of wake turbulence events in U.S. [Veillette, 2002].

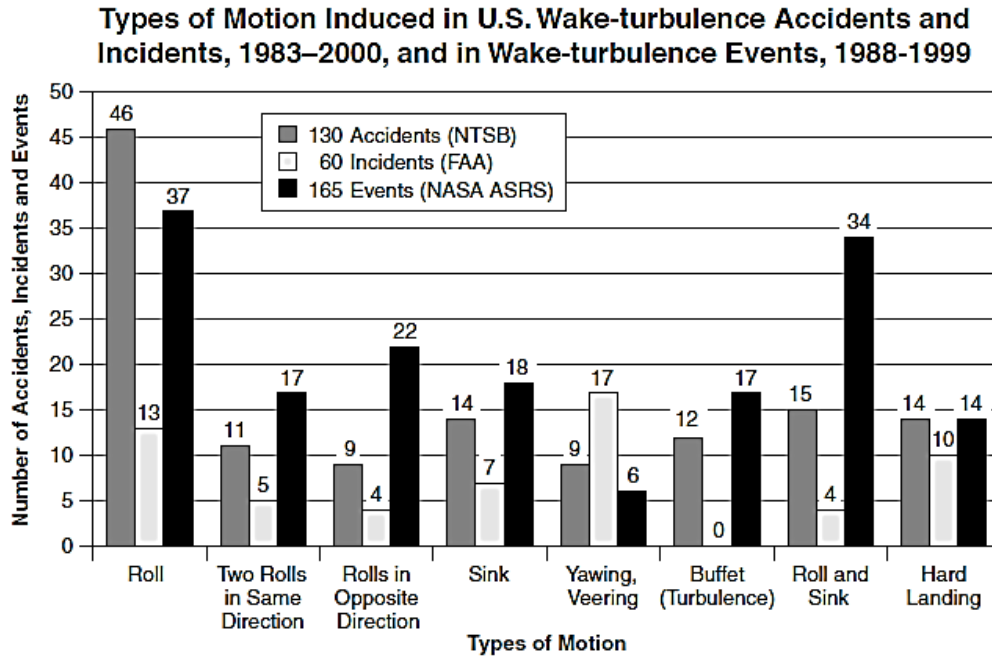


Note: Some of the 165 events were recorded in more than one category.

Source: Patrick R. Veillette, Ph.D., from U.S. National Aeronautics and Space Administration Aviation Safety Reporting System data on 165 events

Figure 2.4: Degree of upset due to wake turbulence events in U.S. [Veillette, 2002].

When a trailing aircraft is upset from its flight path by wake turbulence from a lead aircraft, the trailing aircraft responds by various types of motions. Figure 2.5 summarizes the types of motions induced by wake turbulence in the U.S.



Source: Patrick R. Veillette, Ph.D., from U.S. National Transportation Safety Board (NTSB) data on 130 accidents, U.S. Federal Aviation Administration (FAA) data on 60 incidents and U.S. National Aeronautics and Space Administration (NASA) Aviation Safety Reporting System (ASRS) data on 165 events

Figure 2.5: Types of motion induced by wake turbulence in U.S. [Veillette, 2002].

2.3 WAKE VORTEX SOLUTIONS

Different research projects and integrated research programs were and are conducted for the aviation industry in relation to the wake vortex problem. They are concerned with the following topics

1. Wake vortex detection and avoidance, and
2. Wake vortex alleviation.

Detection and avoidance is a technique used to determine the severity of the vortices generated downstream of a lead aircraft and to determine the flow path of vortices so that trailing aircraft may avoid the vortex paths and hence, reduce the likelihood of a wake vortex encounter.

Wake vortex alleviation attempts to reduce the circulation intensity of the wake vortex and thus the effects of wake vortex. This is achieved by modifying wings so that the vortex core dimension increases and this hastens wake vortex decay.

2.3.1 DETECTION AND AVOIDANCE

The basic idea behind detection and avoidance technique is to determine the flow path of the wake vortices during aircraft approach, landing and take-off. Detection and avoidance technique also helps in determining if the wake vortices shed by a lead aircraft pose any danger to the trailing aircraft. The necessary aircraft separation between the lead and trailing aircraft can then be determined and implemented.

Laser Doppler Radar (LIDAR) was among the first techniques studied for making velocity measurements in large airspaces. Theory and an early application of this technique are discussed by Huffaker et al. (1970). A continuous wave (CW) laser was used and measurement ranges greater than 500 metres were achieved. However, a measurement range of 500 metres is not enough for an aircraft in the approach or landing phase to avoid the wake turbulence ahead.

Thomson and Meng (1976) performed simulations to further study the LIDAR technique to figure out if it could be practically implemented at an airport. Later, Hannon and Thomson (1994) experimented with pulsed LIDAR rather than CW. It was found that the pulse time limits the accuracy in velocity measurements but greater ranges ($> 2\text{km}$) could be achieved.

Harris et al. (2002) successfully measured the wakes of several large aircraft by using a pulsed LIDAR system oriented axially.

Another technique used as a detection and avoidance strategy is Radar Acoustic Detection. Rubin et al. (2000) verified that a Radar Acoustic sounding system could be used

to precisely identify and measure wake vortices of several commercial aircraft of diverse sizes. The results were in agreement with CW LIDAR measurements.

Ample research work has been conducted on developing a vortex detection system that can be used to safely reduce aircraft spacing by enabling aircrafts not to cross the paths of vortices. From FLAME (Future Laser Atmospheric Measurement Equipment) and MFLAME (Multifunction Future Laser Atmospheric Measurement Equipment) investigations, it is clear that pilots and aircraft manufacturers believe that it is necessary to possess an on-board detection system to guarantee the required safety level by remote detection of possible residual wake vortex on the entire approach path (Babie and Nelson, 2004; Hinton et al., 1999; Robinson, 1996; Schwarz, 2010).

From FLAME and other studies, significant economic and environmental impact of shorter approach separation distances is expected by increasing aircraft movements of 10% to 15% at major airports. This will lead to an increase in airport revenue, potential fuel saving and reduce pressure to build new runways and new airports. MFLAME equipment was installed at the extremity of a runway on Toulouse airport so as to enable measurements in a configuration very similar to an on-board detection from a follower aircraft. The airborne-like detection was successful in measuring the strength of the residual wake generated by landing aircraft on a runway at Toulouse airport. FLAME and MFLAME technology is currently used in USA for airborne-like detection of residual wake (Combe et. al., 2000).

Green Wake Project (Schwarz, 2010), Figure 2.6, uses UV LIDAR (Ultra Violet Laser Doppler Radar) for wake vortex detection. UV LIDAR detects wake vortices and wind shear in a timely manner. It anticipates and mitigates the effect of wake vortices and wind shear on the aircraft and occupants. Green Wake Project targets increased crew and passenger safety in dense airspace and higher airport capacity via reduced air traffic separation.

Attempts have been made for developing a single system for dynamically determining aircraft separation distances by integrating wake detection systems, real-time weather conditions, and vortex decay and transport predictions. The Aircraft Vortex Spacing System (AVOSS) developed by National Aeronautics and Space Administration (NASA) is continually developing to incorporate new developments that occur in each contributing discipline. AVOSS has conducted field trials at Dallas/Fort Worth airport. A thorough description of AVOSS is given in Hinton (1996).

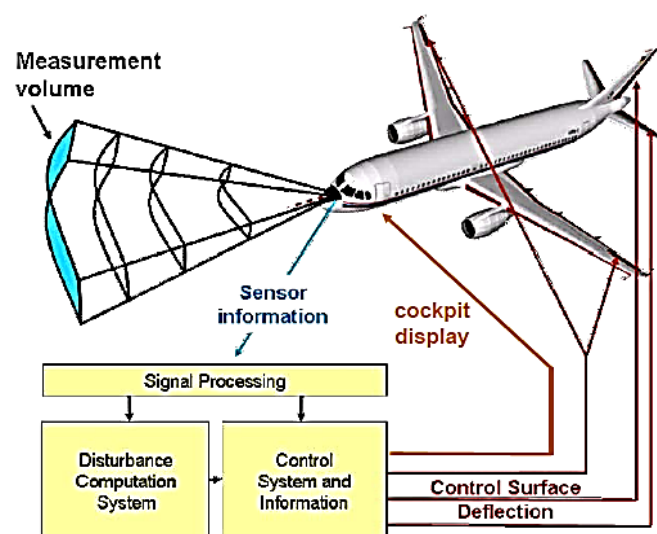


Figure 2.6: The Green Wake Project Concept [Schwarz, 2010].

Measurements and modelling of wake vortices indicate that the Federal Aviation Administration's (FAA) present aircraft separation rules are often based on an overly conservative basis (Shaw and Cole, 2002). The actual separation required between aircraft can be reduced if the wake of a lead aircraft is too weak to pose any danger to the trailing aircraft. Thus, allowing more aircraft to land and take-off from a single runway.

The aim of detection and avoidance strategies is to survey the airspace during approach near the airport to determine whether it is safe for another aircraft to take-off or land. The necessary spacing is determined for each aircraft which enters or leaves the airspace by scanning the airspace for wake turbulence. No time is wasted in waiting for wakes to settle that are not there or are too weak to be of threat. The main difficulty associated with these

strategies is the constant measurement of a large airspace quickly and with good accuracy. Detection and avoidance measurement techniques have been researched and developed since the day wake vortex hazard became known.

However, detection and avoidance strategies that have been researched and developed are costly, and not yet reliable enough to be implemented. A major disadvantage of detection and avoidance strategies is that on a calm day they are of no help in preventing delays at airports when wake vortices tend to loiter around chaotically in the airspace.

Table 2.1 displays the current spacing between aircraft. The spacing is given in nautical miles for IFR conditions on a single runway. Shorter aircraft spacing used under VFR condition suggests that the spacing required by IFR standards is overly conservative. Current IFR separation standards require spacing of 3 to 6 nautical miles between leading and following aircraft, depending on their respective weight classes. These standards are driven by the need to avoid dangers associated with wake vortices trailing each aircraft and could otherwise be reduced to spacing of 2.5 nautical miles or less (Butler, 1993).

Table 2.1
Current spacing between aircraft in nautical miles (nm).

Lead Aircraft	Follower Aircraft		
	Small	Large	Heavy
Small	3	3	3
Large	4	3	3
Heavy	6	5	4

Several detection and avoidance techniques have been used to conduct field trials in the recent past, such as LIDAR, AVOSS, FLAME, MFLAME and Green Wake Project, but none of them have been in continuous operational use due to high operational costs and reliability

issues (Breitsamter, 2011). So far, none of the detection and avoidance techniques has been effective in reducing the aircraft spacing rules. Aircraft spacing rules will most likely change only when detection and avoidance techniques could be made more reliable and completely effective on calm days.

2.3.2 WAKE VORTEX ALLEVIATION

Wake vortex alleviation deals with reducing the effects of wake vortex by reducing the circulation intensity or increasing the vortex core dimensions through wing modification (using winglets or wing fences) so that wake vortex decay is hastened. Since it is impossible to inhibit aircraft wake vortices, ways of alleviating, destroying or at least minimizing their intensity in the shortest time/distance have to be considered. There are two main strategies that can be pursued for wake vortex alleviation.

1. One is to act at the source, in the near-field, by either promoting small scale instabilities or by introducing new turbulence in the vortex core. This would increase the diffusion or turbulent dissipation in the core and lead to a larger and less intense core that diffuses more rapidly.
2. Second is to create in the far-field a multiple-vortex system to promote long-wave instabilities and to trigger perturbations to obtain a premature wake collapse.

Wind tunnel investigations mostly concentrate on the near field due to the test section size limitations. The near field studies are characterized by the vortex formation and roll-up process. From the seventies to present, numerous works have documented the velocity and vorticity fields for various configurations of transport aircraft (Croom, 1976 & 1979; Coustols, 2006; Breitsamter, 2011).

Far field is defined as the region where the trailing vortices persist for a long distance downstream and no significant decrease in the vortex strength is noticed.

Wake vortex alleviation strategies fall into two categories, namely, passive and active wake vortex alleviation strategies. Passive strategies are defined as ones that require no external drive of any kind, and active strategies are ones that do.

2.3.2.1 Passive Wake Vortex Alleviation

Passive wake vortex alleviation strategies depend on modifying the vortex wake in a steady fashion with no external input. Passive techniques are researched wherein the goal is to use a passive device that would modify the vortex rollup process so that the resultant wake is too weak to pose any hazard to trailing aircraft or excite some instability in the vortex that will lead to rapid diffusion of vorticity.

Some vortex modification concepts make use of multiple vortex pair systems (Fabre et. al., 2002; Durston et. al., 2005; Savas, 2005). The addition of a strong vortex pair counter-rotating to the basic tip vortices can lead to more diffused vortices whose strength is the sum of the co-rotating and counter-rotating vortices.

The most promising concepts of passive wake vortex alleviation involve modification of the wing by means of winglets or wing fences attached to the suction surface of the wing. These wing devices either create countersign vorticity that subsequently diminishes the intensity of the rolled up vortex or cause the vortex core dimension to be increased, which also hastens vortex dissipation (Rossow, 1991).

Rossow (1978) conducted wind tunnel tests and attempted to determine an ideal placement and orientation for a fin design. It was found that vertical fins mounted on the upper surface of a wing could lower the wake-induced rolling moments on an encountering wing by a factor of 3 or more. The most promising fin configuration found for the Boeing 747 model is a fin positioned 48% outboard from the centreline to the wingtip with a height

equal to 0.014 wingspans, a chord equal to 0.085 wingspans, and at 18 degree angle of attack. This fin configuration caused a 10% increase in drag but no lift penalty.

Schell et al. (2000), Ozger et al. (2001), Heyes and Smith (2005), and Scholl et al. (2006) performed experiments with various fin designs on research plan-forms as well as realistic aircraft wing shapes. The fin mounted on the upper surface of the wing was used as a means to create small scale instabilities into the aircraft wake. It was shown that more diffused wakes could be achieved.

In Schell et al. (2000), wind tunnel tests of a fin mounted at different positions on a wing are examined. They state that influence of the fin on lift is not significant. The wing fin has very little change on the core radius of the wingtip vortex, whereas the maximum tangential velocity of the wingtip vortex decreases by up to 15%. The outboard flap vortex is much more influenced by the wing fin, which leads to a strong increase of the core radius by more than 100% and to a decrease of the maximum tangential velocity by about 50%. This happens because the wing fin is closer to the outboard flap vortex.

In Ozger et al. (2001), wind tunnel tests of a fin at different angles of incidence mounted at the outboard flap edge region of a wing are examined. The wing fin gives rise to 7% lift penalty. For fin incidence angle 20 degree, the fin causes an increase of 200% in the flap vortex core radius and 40% decrease in the maximum tangential velocity of the flap vortex.

In Heyes and Smith (2005), experiments were conducted on various vortex generator geometries in a small low speed wind tunnel using Particle Image Velocimetry (PIV). The best geometry was deemed triangular since generators of this shape produced substantial vortex enlargement with relatively low lift penalty.

In Scholl et al. (2006), experiments were conducted in a water tunnel using Stereo PIV (SPIV). The wing is equipped with a fin on the suction side. Different flap and fin settings are

employed, and the effects on roll-up and meandering of the vortices are observed. It is found that the influence of fins on induced rolling moment is minimal. However, the fins increase the meandering amplitude of the wake vortices, which decreases the actual hazard to following aircraft through dynamic effects.

Corsiglia et al. (1971) used a small vertical panel, termed a vortex dissipater, mounted on the wing upper surface near the wing tip to inject instability in the wake of the aircraft. The vortex dissipater caused modification of the vortex. Using hot wire anemometry, they indicated that a relatively small wing tip vortex dissipater was capable of increasing the vortex core dimension of the dissipated vortex and reducing the maximum rotational velocity in the dissipated vortex by a factor of three. Flight tests with the vortex dissipater indicated that the rolling acceleration and the degree of roll control required was less in the modified vortex than the unmodified vortex.

Lezius (1975) studied the effect of a triangular leading edge extension at the wingtip. Flow visualizations performed in a water tow tank showed that the modified wingtip produced a more diffused wake than the clean wing, but no quantitative measurements were made.

Patterson (1975) tested with splines mounted directly downstream of the wingtip such that the instability created by the bluff shape would interfere directly with the tip vortex. The use of splines effectively increased the vortex core size but they also gave rise to a large drag penalty (just under 20%).

Traub et al. (1998) conducted an experimental investigation to determine the effectiveness of a wing-tip device designed to attenuate the trailing vortex of a lifting, flat-plate wing. Results showed 28% reduction in maximum rotary velocity of the trailing vortex, 52.6% reduction in magnitude of maximum vorticity and a significant increase in the vortex core size.

Ortega et al. (2002, 2003), Haverkamp et al. (2003) and Durston et al. (2005) have conducted experiments using passive wake vortex alleviation techniques to promote small scale instabilities into the vortex system to increase diffusion of vorticity and to create larger less intense vortex cores.

Ortega et al. (2002, 2003) performed tow tank experiments using PIV with a rectangular wing equipped with triangular flaps at the tips that extend from the trailing edge. These flaps created a pair of inboard counter-rotating flap vortices with respect to the tip vortices. The strength of the inboard vortices of various flap sizes studied ranged -40% to -70% of the outboard vortex strength. The flapped wing vortices instigated a rapidly growing instability wherein each flap vortex became entangled with its outboard counterpart in a periodic fashion. As the instability grew rapidly, the vorticity was rendered far less coherent. The results indicate that the instability in the wake of the triangular-flapped wings offers a possible mechanism to reduce significantly the wake hazard problem.

Stumpf (2004) investigated the same mechanism as Ortega et al. (2002, 2003) numerically using RANS and LES to model the wake of a real aircraft. Durston et al. (2005) used tail wings, rather than triangular flaps, to produce the same instability with equal success. Haverkamp et al. (2003) also followed the work of Ortega et al. using triangular flaps to passively excite the same vortex instability.

Coustols et al. (2006) have summarized the works of C-wake and AWIATOR projects. A cylinder type device installed under the pylon extension fairing of the outboard nacelle was used to inject periodic disturbances into the flap vortex to develop instabilities into the four vortex system. However, this device could not alter the wake significantly. A half wish bone device was installed between the inboard nacelle and the fuselage on the lower surface of the wing to generate a counter-rotating vortex, with respect to the wingtip vortex, to create

instability into the wake. The half wish bone as a vortex generator was found to be ineffective.

Tests have also been conducted with spoilers of delta type plan-form deployed in the area of the outboard flap vortex to create a zone of highly turbulent flow (Breitsamter, 2011). A significant enlargement of the viscous core by 50–90% occurs accompanied by a reduction in maximum induced velocities of about 50% and in the maximum induced rolling moment of about 30%. It was found that the use of delta type spoilers minimally affects the overall flight performance. A maximum lift reduction of 2.9% was recorded for a double delta spoiler configuration.

Differential Flap Setting (DFS) is a passive technique which focuses on affecting the wake by deploying the inboard and outboard trailing-edge flaps at different angles. Numerous studies focus on DFS as a conceivable mean to lessen the induced rolling moment (Bellastrada and Breitsamter, 2006; Coustols et al., 2003). DFS increases the number of merging processes (due to an increase in the number of near field vortices) throughout the roll-up process causing the enlargement of the main vortex and reduction of peak cross flow velocities. However, Breitsamter (2011) states that “a multiple vortex system with counter-rotating neighbored vortices of appropriate circulation ratio, which persists long enough for developed medium wave instabilities, is hardly achievable by applying DFS.”

Croom (1976, 1977, 1979) studied the effect of spoilers (air brakes) on the suction side of wings on commercial aircraft. Wind tunnel and flight tests showed that significant increase in the vortex core size was achieved.

The technique of differential spoiler setting (DSS) in a scaled half-model aircraft, was tested using Particle Image Velocimetry (Elsayed et al., 2010; Elsayed et al., 2011) and numerically (Ludin et al., 2013) to characterize the generated wake vortices in the near wake field. The experimental results reveal a noticeable shift of wing loading along with the direct

interaction of the spoiler's wake and flap tip vortex. Furthermore, the diameter of the merged vortex had increased by a factor of up to 2.72, relative to the undisturbed flap tip vortex. Similarly, a 44% decrease of the maximum cross-flow velocity was observed for the case of deployed spoilers, relative to undisturbed flap-tip vortex maximum cross flow velocity. It was concluded from the overall results that the DSS technique is capable of alleviating the wake vortex by reducing the maximum induced rolling moment coefficient to nearly one third of the undisturbed flap tip vortex value in the near field. Numerical results were in agreement with the experimental data.

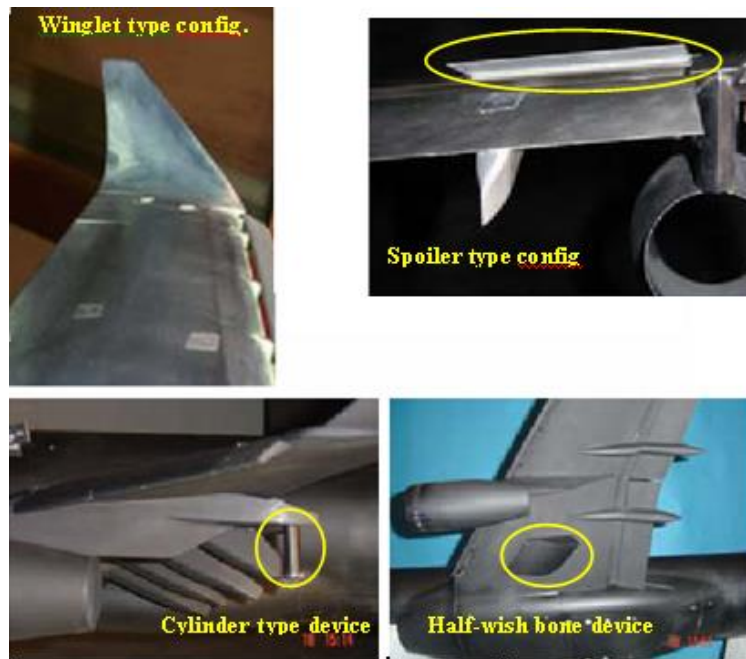


Figure 2.7: Wing add-on devices tested in C-Wake and AWIATOR projects [Coustols et al., 2006].

A tip mounted slender half delta wing (HDW) was used to modify the wingtip vortex generated by a rectangular NACA 0012 wing (Lee and Pereira, 2013). Compared to the baseline wing, the roll-up process of the tip vortex was found to be significantly modified (the HDW vortex was found to undergo an unexpected early breakdown, characterized by a suddenly enlarged and diffused vortex), as a result of the breakdown of the HDW vortex. Addition of the HDW produced an increase in lift coefficient and total drag coefficient.

The use of a reverse half delta wing as a wingtip vortex control device has been studied by Lee and Su, 2012. The strength of the wingtip vortex generated behind a semi-span rectangular NACA 0012 wing, at $Re = 2.45 \times 10^5$, was reduced by the use of a tip-mounted 65° sweep reverse half-delta wing (RHDW) with zero deflection. The RHDW was found to produce a weaker tip vortex with a lower vorticity level compared to the baseline wing. The reason being that since the tip of the RHDW is swept along or downstream of the trailing edges, the wing lies outside the tip's zone of influence, thus, the tip vortices became more diffused and discernible as α was increased. The tip vortex of the RHDW configuration also had a significantly lowered core circulation with a smaller core radius (up to $\alpha \leq 12^\circ$) and a lower peak tangential velocity ($V_{\theta, \text{peak}}$) compared to the baseline wing. 43%, 56.4%, 25.3% and 42% reduction in ζ_{peak} (peak vorticity), Γ_c (core circulation), r_c (core radius), and $V_{\theta, \text{peak}}$ (peak tangential velocity), for instance, at $\alpha = 10^\circ$, respectively, was obtained compared to the baseline wing. The values of Γ_c , r_c , and $V_{\theta, \text{peak}}$ were also found to increase monotonically with increasing α for both baseline wing and RHDW wing. The RHDW was also found to produce a weaker tip vortex with a lower vorticity level compared to the baseline wing. It was further noticed that the weakened tip vortex also produced a smaller lift-induced drag in comparison with the baseline wing at the same lift condition.

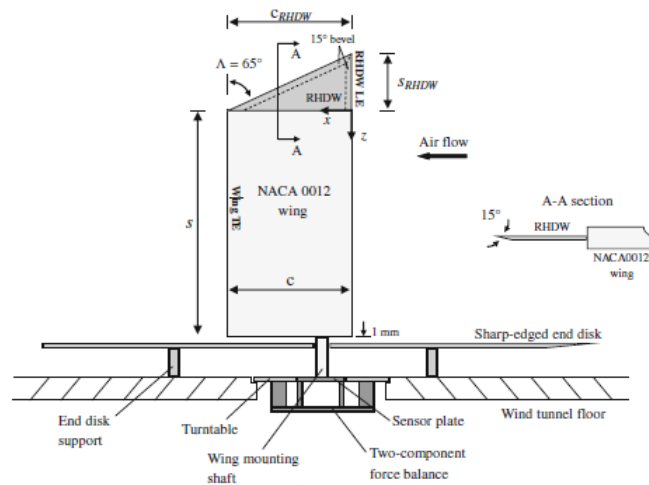


Figure 2.8: Schematic of RHDW experimental setup [Lee and Su, 2012].

In Lee and Su's (2012) work, the reduction in peak vorticity, core circulation, core radius and peak tangential velocity by using a RHDW at the tip of a NACA 0012 wing would have most probably occurred due to the flow separation at the junction of the root of the RHDW and NACA 0012 wing and not entirely due to the usage of a RHDW as an add-on device at the tip of the NACA 0012 wing.

In the present study, using a reverse delta type add-on device on a half-span wing model, the interaction of the add-on device vortices with the wingtip/flap-tip vortex is solely dependent on realistic vortex interactions. A whole reverse delta type add-on device is used in the present study as a half reverse delta type add-on device would not instigate sufficient instability into the vortex system.

Recent investigations have pointed out that reverse delta type add-on devices may have the capability to be used in vortex alleviation (Coustols et. al., 2006; Breitsamter, 2011; Lee and Su, 2012; Altaf, et. al., 2011 & 2015; Ludin et. al., 2015). Reverse delta type add-on device vortices are expected to excite some instability (countersign vorticity) into the wingtip and flap-tip vortices and modify the vortex roll up process. The interaction of the vortices is expected to create a weaker resultant vortex with a reduction in peak vorticity, maximum tangential velocity and core circulation. These are expected to lead to an enlarged (larger vortex cores) and diffused resultant vortex which can enhance wake vortex decay and thus, lead to wake vortex alleviation.

The main advantage of using passive techniques is the simplicity and ease of construction associated with them but they are also associated with significant lift and drag penalties. However, lift and drag penalties can be reduced by having the add-on devices present in the flow only when needed and stowed when not. Also, using add-on devices of an aerodynamic shape rather than being of blunt geometry can reduce the lift and drag penalties associated with them.

2.3.2.2 Active Wake Vortex Alleviation

Active wake vortex alleviation strategies rely upon hastening selected modes of instabilities by some time dependent forcing (e.g. elevator oscillations, oscillating inboard and outboard flaps, oscillating ailerons and rudders) to disturb the wake of an aircraft and excite natural instabilities. These instabilities should then lead to rapid attenuation of the vortex system.

Crow's instability occurs when aircraft vortices interact with disturbances, such as engine contrails, producing visible distortions in the shape of the contrail. Crow's (1970) analysis revealed the existence of an in-viscid, long wavelength sinusoidal instability whose amplitude grows exponentially with time and would likely lead to periodic linking of the two counter-rotating vortex pair to produce a series of vortex rings. Crow's instability is typically excited by atmospheric turbulence.

Chevalier, (1973) performed flight tests to demonstrate how Crow instability can be excited by elevator oscillations. Later, Crow and Bate Jr. (1976) developed a new model for wake lifespan that incorporated the effects of atmospheric turbulence. They concluded that atmospheric turbulence levels would often be unable to excite Crow instability within a short time to change aircraft separation rules. This was later confirmed by Direct Numerical Simulation (DNS) computations of Spalart and Wray (1996).

Crow and Bate (1976) then proposed to excite the Crow instability by periodically oscillating the inboard and outboard flaps on an aircraft such that a significant fraction of the lift moves inboard and outboard while the total lift of the aircraft is held constant.

Bilanin and Widnall (1973) conducted tow tank experiments on a full span NACA 0012 wing equipped with conventional inboard and outboard flaps. They excited the Crow instability by periodical flap oscillations to move a large fraction of the lift inboard and outboard while keeping lift constant to $\pm 2\%$. They showed that this kind of forcing affects

both the strength and core size of the vortices, thus, causing a rapid destruction of the vortex pair.

Barber and Tymczyszyn (1980) conducted flight tests with large commercial aircraft to excite Crow instability by using lateral-control oscillations. Although the spoiler deflections were too large to be practicable during take-off or landing, they demonstrated that the wake can be completely destroyed within three nautical miles of the lead aircraft. The tow tank experiments of Jordan (1983) were in agreement with their work.

Roll oscillations of an aircraft as a means for exciting Crow instability were considered by Rossow (1986). Flight tests with B-747 and L-1011 transport aircraft were carried out. Both aircraft had their landing flaps extended and several spoilers deployed. The B-747 shed a fairly strong vortex near the fuselage and the L-1011 did not. The L-1011 shed a vortex near its wingtip that is stronger relative to the flap vortices than the B-747. These two factors combine to bring about much larger vortex distortions in the B-747's wake than in the L-1011's wake. It was concluded that the time-averaged wake-induced rolling moment was substantially reduced for the B-747 case. However, the main problem with such a strategy is the undesirable impact upon passenger comfort.

Ralf et al. (2007) studied the vortex wake of a rectangular wing with simultaneous oscillations of ailerons and winglet-integrated rudders in a water towing tank. They observed that, depending on the aileron and rudder deflections, a correctly chosen oscillation frequency leads to faster decay of the vortex wake in comparison to the static case. The results demonstrate that a significant reduction of the rolling moment induced on a following wing can be achieved in the near field.

Crouch et al. (2001) performed DNS and tow tank experiments on commercial aircraft four vortex system configurations. They established that Crow instability could be excited with periodic oscillations of the conventional inboard and outboard flaps while holding lift

nearly constant. Results show that the multiple vortex configuration system breaks up the trailing vortices more rapidly than a comparable excitation of the Crow instability on a single pair of vortices. Significant reductions in linking times (the time required for the vortices to pinch on the centerline) were achieved.

Haverkamp et al. (2005) studied the influence of outboard flaps on the wake of a rectangular wing in a towing tank. A four vortex system configuration arises from the outboard flaps extension. The results indicate that the induced rolling moment coefficient is reduced by more than 50% and the effective vortex size is significantly increased.

Heyes and Smith (2004) and Bearman et al. (2006) excited Crow instability in wind tunnel experiments using pulsed span-wise blowing of a jet sheet from the wingtips. The vortex responded to a varying range of pulsing frequencies but as the frequency was increased, the amplitude of the response became smaller. However, this required high blowing rates, and assessment of the aerodynamic effects upon the wing were not performed. Significant drop in lift is expected.

Margaris et al. (2008) experimentally assessed the effect of a cold jet on a single trailing vortex in wind and water tunnels. Reduction in vorticity levels is achieved when the cold jet is located close to the vortex.

The greatest drawback of active wake vortex alleviation strategies is the additional mechanical requirements and fatigue, caused by periodic oscillations, on conventional flaps, rudders and ailerons. One known aircraft crash has occurred due to strong periodic oscillations of the rudder being applied to maneuver the aircraft away from the wake turbulence shed by a lead aircraft that took off minutes before it (American Airlines Flight 587, 2001). The aggressive use of the rudder controls by the co-pilot caused the vertical stabilizer to snap off the plane and caused the plane to plummet into the ground killing all on-board.

2.4. SUMMARY

For the last couple of decades wake vortex encounters have become a growing concern for the aviation industry. Numerous attempts have been made at alleviating vortex wakes but none have provided desirable results.

There is a need to eliminate consequences of wake vortex encounters so that aircraft spacing can be reduced. Detection and avoidance techniques do not offer much relief from wake vortex encounters as they are costly, not very reliable, and are ineffective during calm days. Wake vortex alleviation is a better alternative to avoid hazardous wake vortex encounters. The goal of wake vortex alleviation is to render harmless the residual wake of the aircraft. This can either be done by instigating instabilities into the wake by passive means such as using passive add-on devices or by active means such as aileron, flap and rudder oscillations. The use of aircraft control oscillations is dangerous as an overuse of the control surfaces may cause them to snap off and risk the safety of passengers. Passive wake vortex alleviation techniques are safe but they generate lift and drag penalties. However, it is possible to reduce lift and drag penalties of passive wake vortex alleviation techniques by having the add-on devices present in the flow only when needed and stowed when not, and using add-on devices of an aerodynamic shape rather than of blunt geometry.

CHAPTER THREE

EXPERIMENTAL APPARATUS AND METHODOLOGY

3.1 INTRODUCTION

It is essential that an appropriate apparatus be used for a specific experimental study. For this work, experiments have been conducted in a closed-loop low-speed wind tunnel at 12 m/s. Particle Image Velocimetry (PIV) has been used to obtain instantaneous velocity measurements.

This chapter highlights the experimental apparatus used and explains in detail the experimental procedure. Also, a detailed PIV uncertainty analysis has been conducted.

3.2 EXPERIMENTAL APPARATUS

3.2.1 The Wind Tunnel

The experiment was carried out in the closed-loop low-speed wind tunnel at the International Islamic University Malaysia (IIUM). The wind tunnel test section dimensions are 2.3 m (width), 1.5 m (height) and 6.0 m (length). The main structure of the wind tunnel is made of steel, except in the test section: the walls are made of acrylic glass and aluminum. The test section has very good visual accessibility through transparent removable acrylic glass side panels. The maximum velocity in the test section is 50 m/s. The wind tunnel has a free-stream turbulence intensity of 0.07% in the flow direction, 0.10% in the lateral direction and 0.11% in the vertical direction. The schematic diagram of the wind tunnel is shown in Figure 3.2. The schematic diagram of the IIUM wind tunnel components is shown in Figure 3.3.

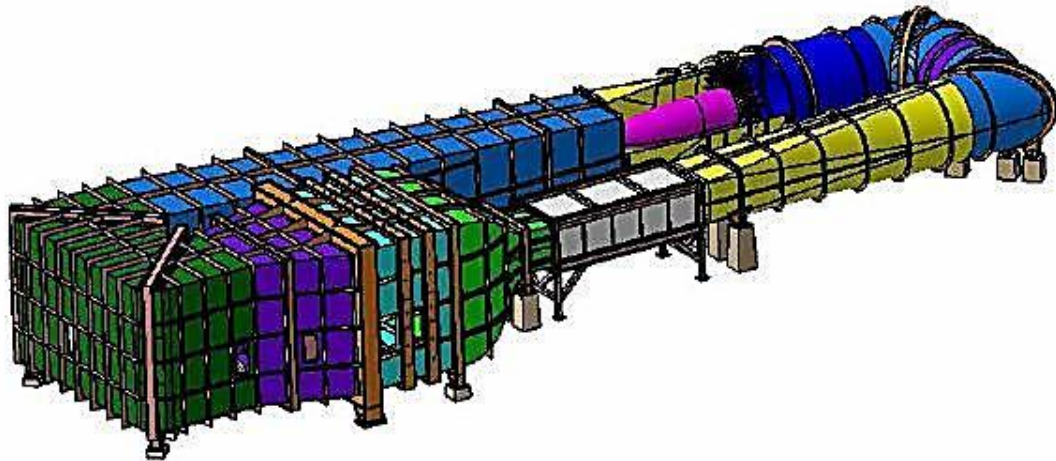


Figure 3.1: Parametric view of the IIUM wind tunnel.

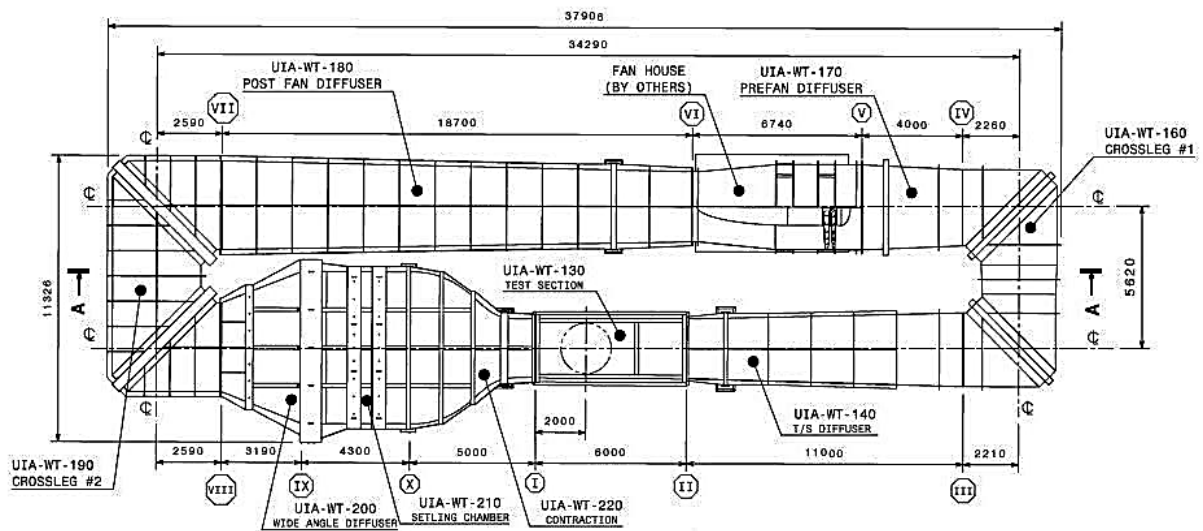


Figure 3.2: Schematic diagram of IIUM closed-loop low-speed wind tunnel.

The settling chamber of the wind tunnel starts from the inlet section of the wide angle diffuser until the inlet section of contraction. The wide angle diffuser functions to slow down the wind flow. The honeycomb is designed to reduce the turbulence level of the flow. Then, the four screens located after the honeycomb are used to increase the uniformity and reduce the turbulence intensity of the flow. The contraction is the last section of the circuit to prepare the flow before entering the test section. The improper design of contraction might generate unwanted separations and propagate them to the test section. The shape of the contraction must be carefully designed to provide the best wind flow structure to the test section.

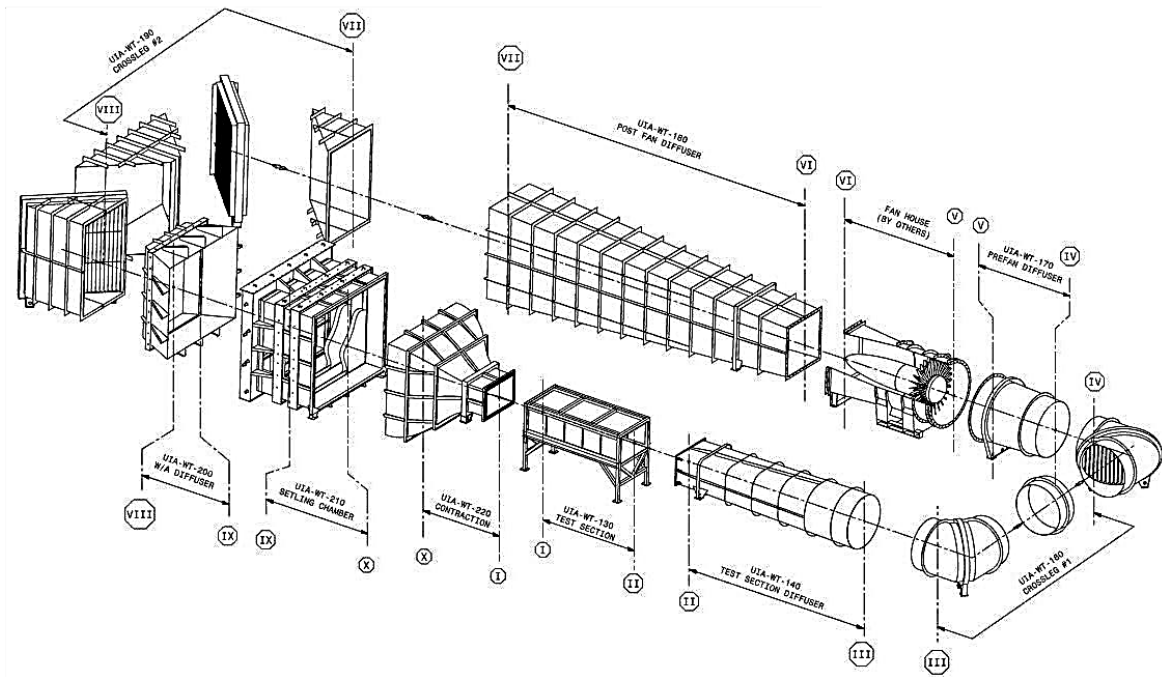


Figure 3.3: IIUM wind tunnel components.

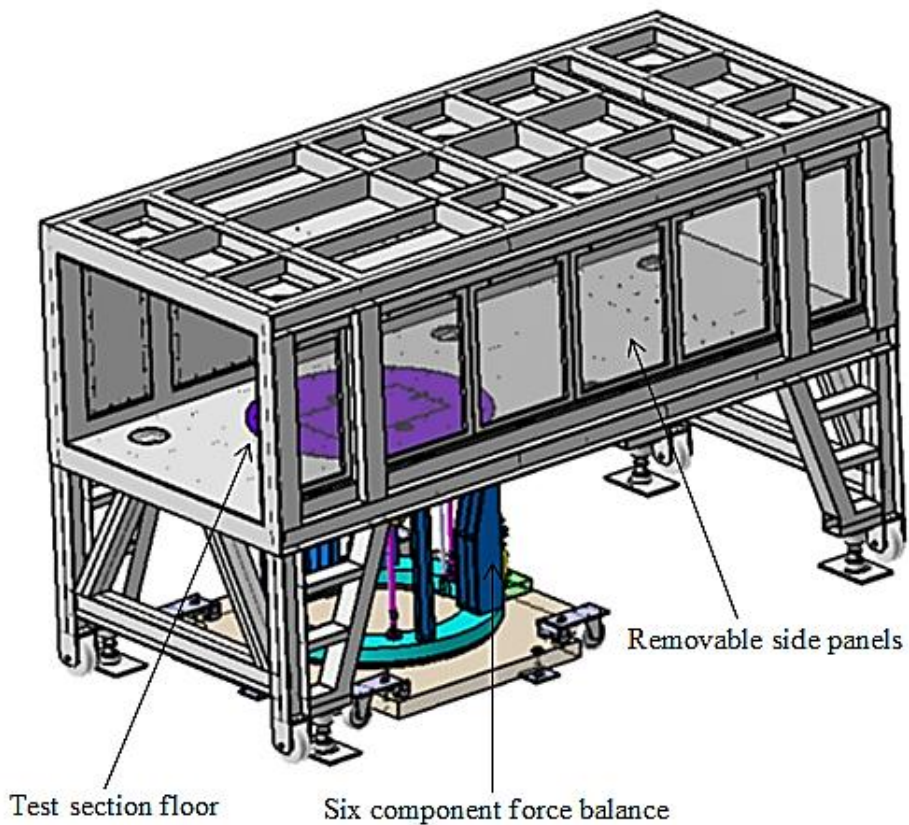


Figure 3.4: Schematic Diagram of the IIUM six component force balance.

The test section is equipped with an external six component force balance which permits the measurement of all aerodynamic loads on a model. It is attached to the test

section floor from below. Schematic diagram of the external six component force balance is shown in Figure 3.4.

3.2.2 The Half-Span Wing Model

The half-span wing model used in this work consists of a wing with a tapered NACA 23012 profile, average chord length $c = 0.371$ m, half-span $(b/2) = 0.93$ m and half wing area $S = 0.321$ m². Figure 3.5 shows the schematic diagram of the half-span wing model and Figure 3.6 shows the half-span wing model in the wind tunnel.

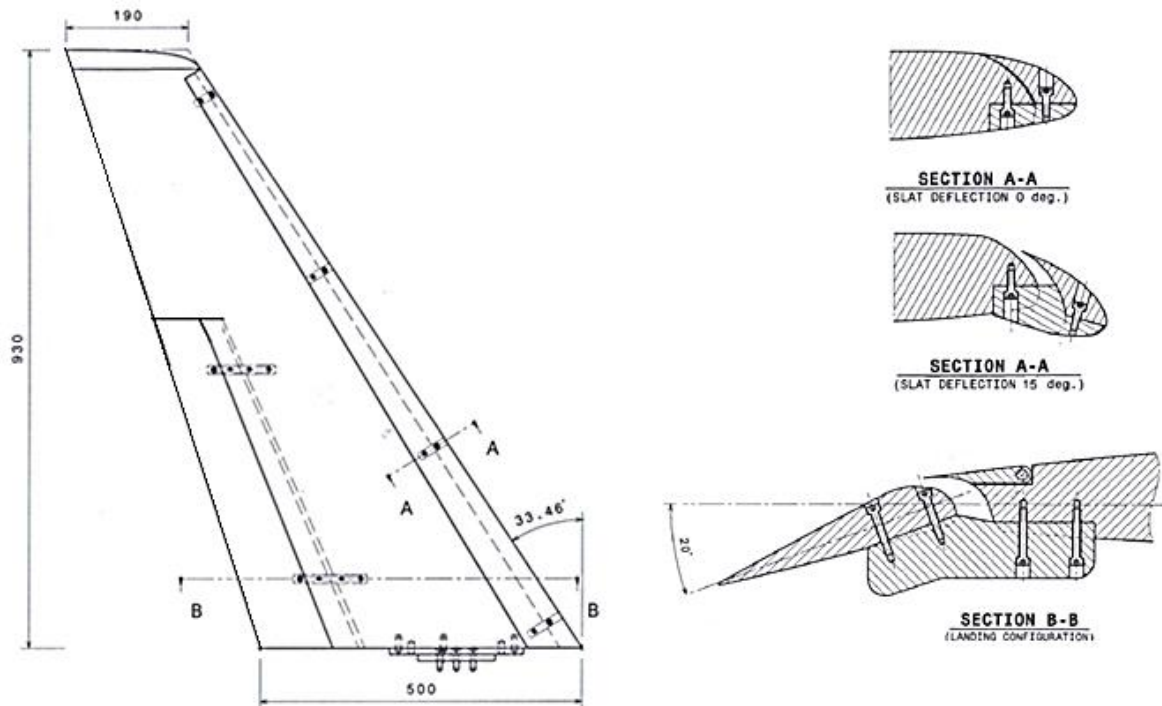


Figure 3.5: Schematic diagram of the half-span wing model.

The half-span wing model was tested at High Lift Configuration (HLC); slat deflection = 15°, flap deflection = 20° and angle of attack = 7°. The angle of attack of the half-span wing model is the angle between its chord and the flow direction. A lift coefficient of $C_L=1.06$ is obtained when the wing is in this configuration and used as the target lift coefficient. All model configurations are tested for this target lift coefficient value.



Figure 3.6: Half-span wing model in the wind tunnel.

3.2.3 The Reverse Delta Type Add-on Devices

The reverse delta type add-on device is to be used only during take-off and landing. For the rest of the flight envelop, the add-on device is to be stowed in the wing. The add-on device is to be stowed in the main wing similar to how flight spoilers are embedded within the main wing of an aircraft and is to be extended and retracted using hydraulic systems similar to how flight spoilers are extended and retracted. In some cases (chapter 5, case 1), the add-on device may protrude out of the main wing body. However, due to its aerodynamic shape, the lift and drag penalties will most likely be negligible when it is stowed in the main wing.

A reverse delta type add-on device is bounded by a leading edge and by a pair of trailing edges extending from the ends of the leading edge towards a trailing apex point. Two sets of reverse delta type add-on devices are used for this work, as shown in Figure 3.7 and

3.8. The small reverse delta type add-on device (S-rdw) [for simplicity; the abbreviation rdw (reverse delta wing) will be used] dimensions are; chord length $c = 160$ mm, span $b = 120$ mm. The large reverse delta type add-on device (L-rdw) dimensions are; chord length $c = 200$ mm, span $b = 150$ mm. Both the reverse delta type add-on devices have a thickness of 3 mm, sweep angle 69.4° and bevel angle of 20° .

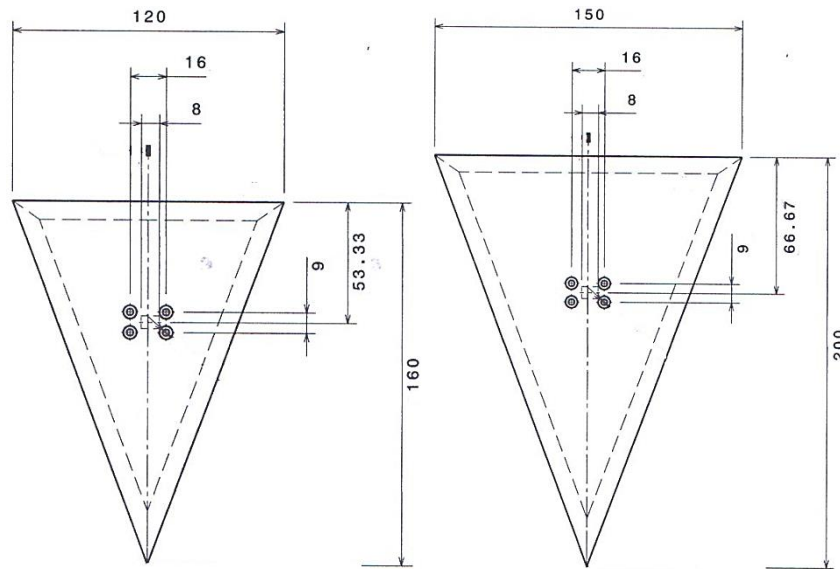


Figure 3.7: Schematic of the reverse delta type add-on devices (from left: small reverse delta type add-on device (S-rdw) and large reverse delta type add-on device (L-rdw)).

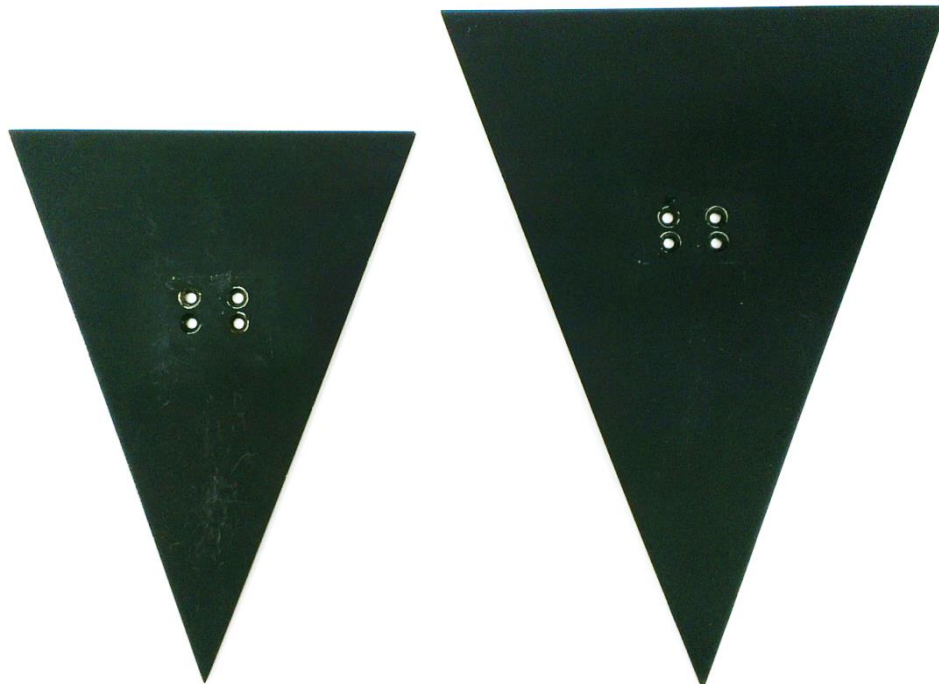


Figure 3.8: Image of the reverse delta type add-on devices.

The geometric size of the reverse delta type add-on devices was selected based on the lift and drag penalties associated with them. Aerodynamic performance tests were conducted on various add-on device geometric sizes and found that an add-on device smaller than S-rdw has a large lift penalty and an add-on device larger than the L-rdw has a large drag penalty, as shown in Figure 3.9. Therefore, S-rdw and L-rdw were selected because nominal lift and drag penalties were associated with them.

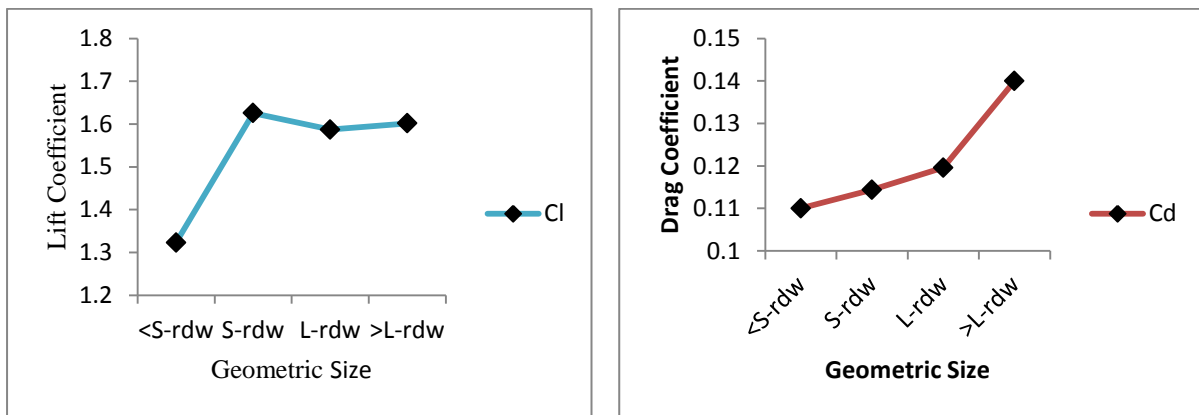


Figure 3.9: Plot of geometric size of reverse delta type add-on device versus lift and drag coefficient.

3.2.4 The complete model

The reverse delta type add-on devices are attached to the main wing model by a 35 mm long adjustable mounting which is used to make angle of attack and roll angle variations, as shown in Figures 3.10 and 3.11. The effect of the mounting height of the reverse delta type add-on device is to be studied thoroughly as a separate research work as it could have a significant impact on aerodynamics and flow characteristics.

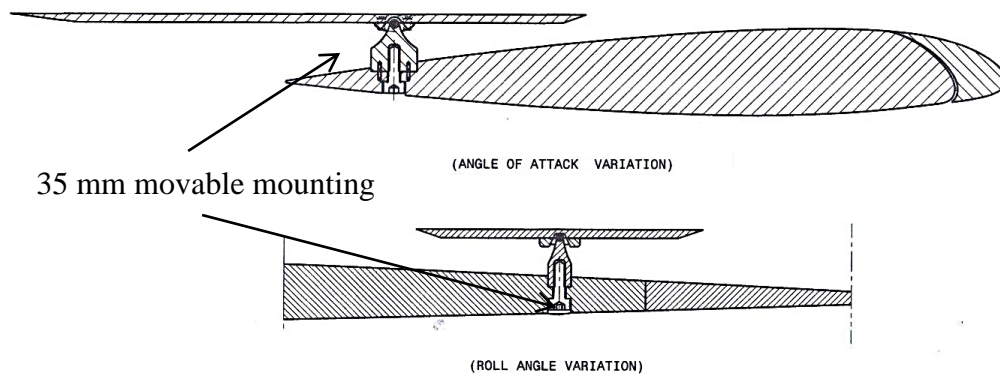


Figure 3.10: Schematic diagram showing the angle of attack and roll angle variation of the reverse delta type add-on device.

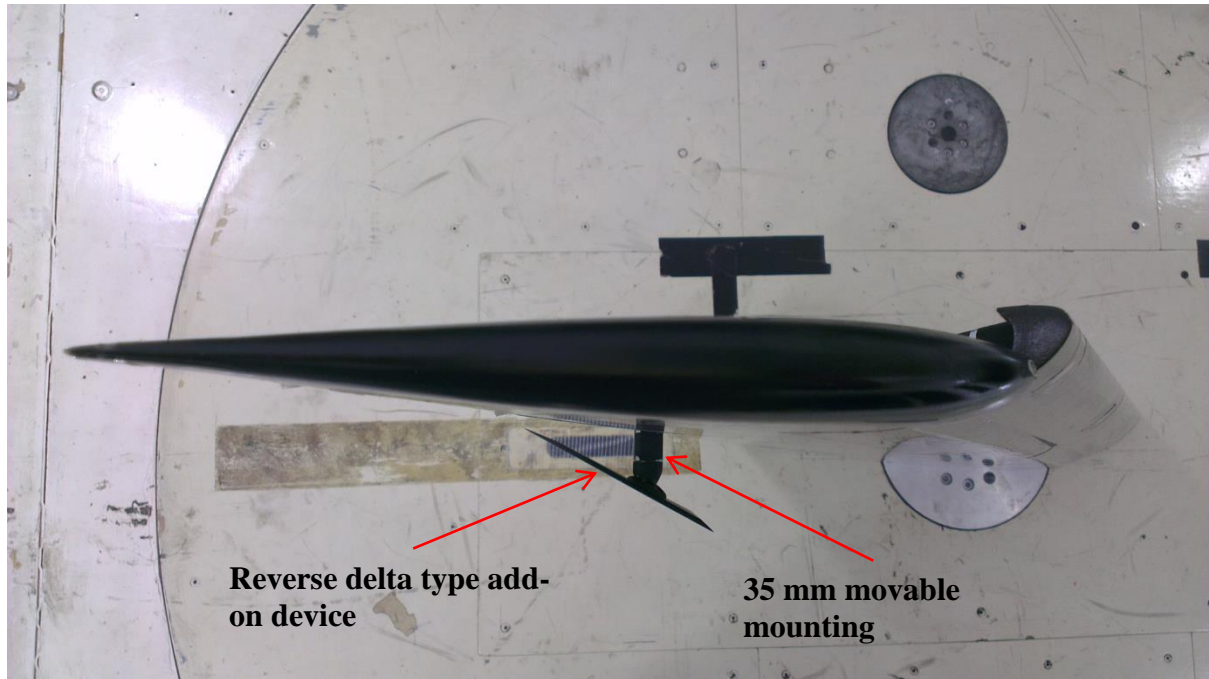


Figure 3.11: Image showing the movable mounting used for angle of attack and roll angle variation of the reverse delta type add-on device.

The selection of the location of the add-on device on the main wing was based on the idea that an instant instability within the wingtip vortex is required so that the roll-up process of the wingtip vortex may immediately be weakened, hence, allowing significant alleviation to be achieved. The results support this claim as the roll-up process of the wingtip vortex is seen to be significantly weakened (velocity vectors not strongly bonded).

Figures 3.12 and 3.13 show the half-span wing model with a reverse delta type add-on device attached in close proximity of the outboard flap-tip.

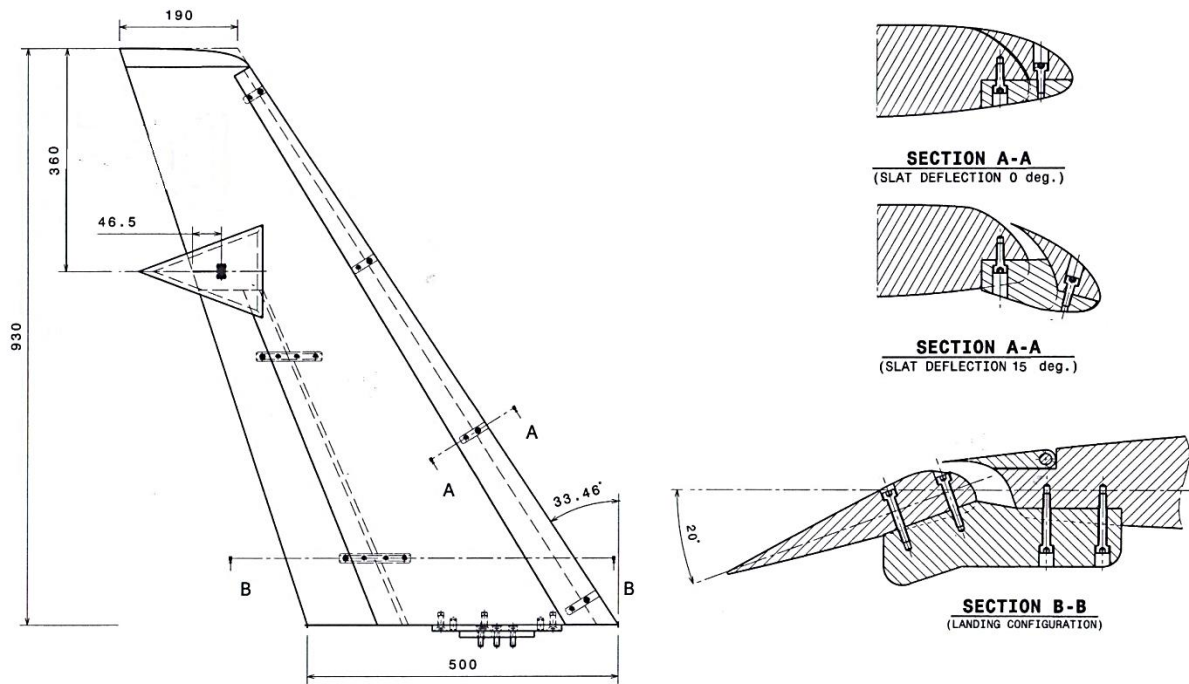


Figure 3.12: Schematic diagram of the half-span wing model with a reverse delta type add-on device attached.

The model is placed on the turn table attached to the tunnel floor and extends vertically with the wingtip pointing towards the ceiling of the wind tunnel.

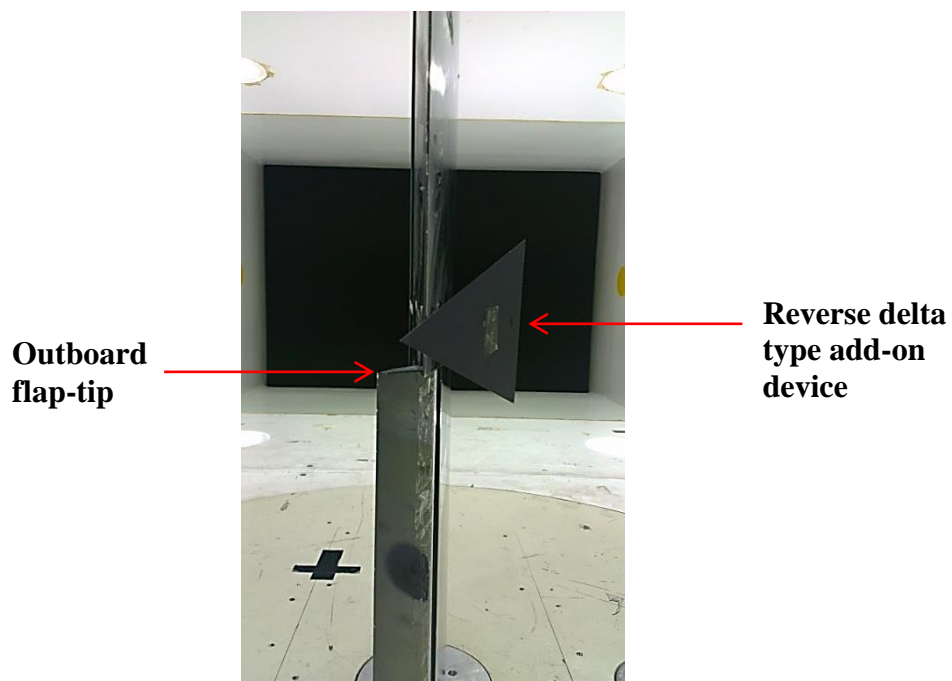


Figure 3.13: Image of the half-span wing model with a reverse delta type add-on device attached.

3.3 RESEARCH METHODOLOGY

Particle Image Velocimetry (PIV), a minimally intrusive method, is used in this work to study the characteristics of the vortex interactions of vortices created by a reverse delta type add-on device and the flap-tip/wingtip of a half-span wing model.

PIV is an optical method used to obtain instantaneous velocity measurements and related properties in fluids. PIV measures the velocities of micron-sized particles following the flow. The fluid is seeded with 1 micron diameter sized tracer particles which are usually assumed to faithfully follow the flow dynamics. Motion of the seeding particles is used to calculate velocity information of the flow being investigated. Figure 3.14 summarizes the principle layout of the PIV system used in this study.

The PIV image frames are split into a large number of interrogation areas or windows. The size of the interrogation window was chosen to have at least 6 particles per window on average. For accurate PIV analysis, it is ideal that the region of the flow that is of interest displays an average particle displacement of about 8 pixels. This is a compromise between a longer time spacing which would allow the particles to travel farther between frames, making it harder to identify which interrogation window travelled to which point, and a shorter time spacing, which could make it overly difficult to identify any displacement within the flow. For PIV to be effective, the seeding particle concentration should be good. Individual seeding particles should be visible and the image frame should be filled with seeding particles so that the motion of the seeding particles can be easily tracked.

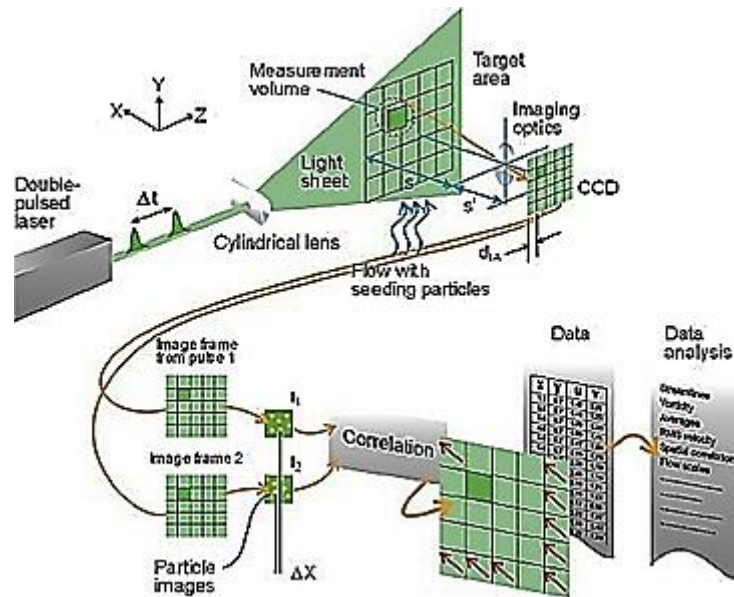


Figure 3.14: Principle layout of a PIV system [Dantec Dynamics, 2004].

The main advantages of PIV are that:

- It is non-intrusive/minimally intrusive whereas Hot-wire Anemometry is an intrusive method.
- It can determine fluid velocity at all locations within an entire two-dimensional cross-sectional plane simultaneously instead of having to make separate measurements at a series of different point locations. This is an important feature for analyzing some forms of unsteady flow.
- Large number of image pairs can be processed on a personal computer and analyzed in real time or at a later time, and a large amount of near continuous information can be gained.
- Sub-pixel displacement values permit a high degree of accuracy, since each vector is the statistical average of many particles within a particular interrogation tile. Accuracy can normally be down to 10% of one pixel on the image plane.

The working principle of PIV is best described in Raffel et al. (2007) and Flow-Manager Software and Introduction to PIV Instrumentation (2004). The PIV working principle has been summarized below:

1. Light reflecting tracer particles are added to the flow (usually fog is used in air and glass beads in water).

Seeding the flow with light reflecting tracer particles is necessary in order to image the flow field. The particle dimension should be small enough to follow the flow but large enough to reflect the required amount of laser light for the camera to be able to detect them. The particles should have approximately the same density as the fluid itself. The tracer particles whose motion is used to represent that of a flow field should be:

- Able to loyally follow the flow.
- Good light reflectors.
- Easy to generate.
- Inexpensive.
- Non-hazardous, non-corrosive, non-abrasive.
- Slow to evaporate.
- Chemically inactive.
- Clean.

2. A light sheet is used to illuminate the tracer particles in the measurement plane and a camera is used to take two exposures of the illuminated plane.

Lasers are extensively used in PIV because of their capability to emit monochromatic light with high energy density which can easily be bundled into thin light sheets for illuminating and recording the tracer particles without chromatic irregularities. Nd:YAG (Neodymium Yttrium Aluminium Garnet)

lasers emit light with a wavelength of 1064 nm (infrared range). It is unfavorable to not see the light sheet when positioning it in the measurement section. For this reason, the wavelength of the Nd:YAG laser is halved to 532 nm using a device called a harmonic generator. The specifications of the laser are:

Maximum Pulse Energy: 120 mJ

Maximum Pulse Rate: 15 Hz

Wavelength (output): 532 nm

3. The two exposures must be taken within a small time interval so that the same particles are caught in both exposures. The two exposures can be taken either as a double exposure of one image or as two different images. The method with two images and cross-correlation is more commonly used.

PIV applications require a special camera to be used, particularly if the flow velocity is high, the imaged area is small and the tracer particles are small. The CCD (Charge Coupled Device) camera is required to capture two images within a short period of time in order for the same individual particles to appear in both images.

4. The velocity vectors are derived from subsections of the target area of the particle seeded flow by measuring the movement of particles between two light pulses.

$$V = \frac{\Delta x}{\Delta t}$$

3.4 EXPERIMENTAL PROCEDURE

The velocity components in planes perpendicular to the stream-wise direction at four locations in the downstream direction are investigated. The experimental setup is shown in Figures 3.15 and 3.16. The results are obtained at four downstream planes; $x/(b/2) = 0.021, 0.548, 1.075$ and 2.387 , as shown in Figure 3.17. Multiple laser positions are chosen to

differentiate between the vortex flow characteristics in terms of roll up, vortex core size, tangential velocity, vorticity and circulation.

PIV measurements are taken only at the half-span wing model flap-tip/wingtip location with/without the reverse delta type add-on device attached at four downstream planes. The CCD camera is centered at the half-span wing model flap-tip/wingtip at all downstream planes to quantify the influence of the reverse delta type add-on device on the flap-tip/wingtip vortex characteristics.

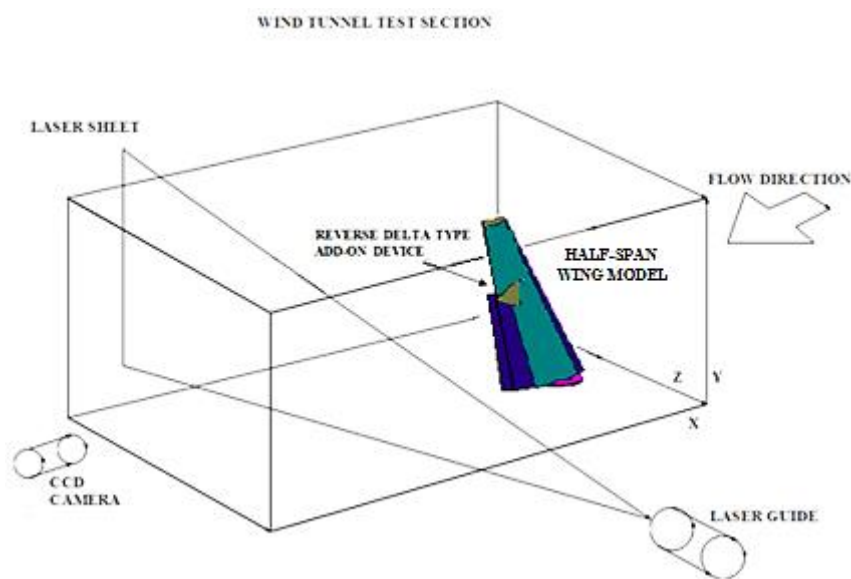


Figure 3.15: Schematic diagram of the experimental setup.

The free stream velocity was set to 12 m/s corresponding to a mean chord-based Reynolds Number, $Re_c = 2.74 \times 10^5$. The flow was seeded by particles of mean diameter of 1 μm . The seeding particles are generated by a Fog Generator (Safex Nebelgerat – F2010) and are injected into the wind tunnel using a duct (diameter: 6 cm, length: 1.50 m) placed approximately 3 metres downstream of the half-span wing model. The duct is fixed to the wind tunnel floor equidistant from the wind tunnel walls, as shown in Figure 3.16. This setup enables the seeding particles to be distributed equally throughout the test section. PIV measurements are taken approximately 2 minutes after the injection of the seeding particles. This is to ensure that the seeding particles are distributed throughout the wind tunnel test

section before PIV measurements are taken.

The vortices are produced at the flap-tip and wingtip of the half-span wing model, which are at a distance of 540 mm and 930 mm respectively from the wind tunnel floor. It can be said that the measurement area is away from the disturbance created by the duct.

Zhang et al. (2006) found that once the distance between the measurement plane and a blunt object placed in the wind tunnel exceeds 2 mean chords of the experimental model, the influence of the blunt object on the flow in the measurement plane was less than 5% on the scattering of vortex centers and less than 2% on maximum vorticity. Therefore, for this research work, it can be concluded that the effect of the duct on the flow is considered to be insignificant as it is more than 3 mean chords away from the measurement plane.

Important PIV data acquisition parameters such as time interval ($\Delta t = 60 \mu s$) and laser sheet thickness (2 mm) were fixed. A light sheet from a Nd:YAG laser system of wavelength 532 nm was used to illuminate the flow. A Flow Sense M2 8 bit CCD camera with a Micro-Nikkor 60 mm camera lens was placed perpendicular to the laser sheet; 3 to 10 mean chords downstream of the wing. The camera traversing system did not affect the flow in the measurement plane.

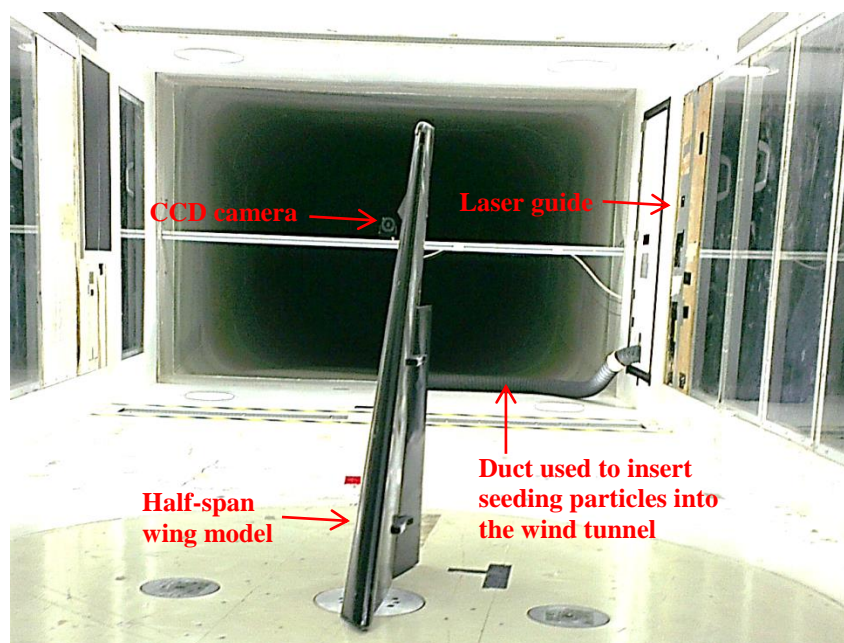


Figure 3.16: Image of the experimental setup in the wind tunnel.

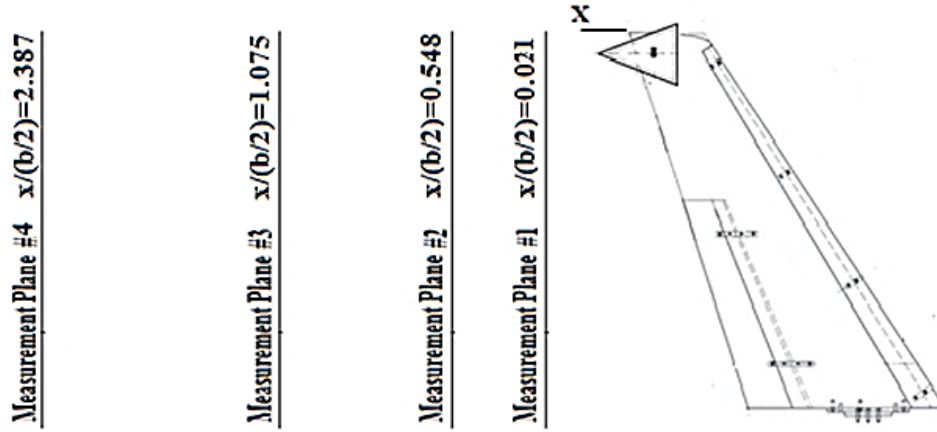


Figure 3.17: Schematic diagram of the downstream measurement planes.

PIV data was obtained for the High Lift Configuration (HLC) and HLC with reverse delta type add-on devices at $\alpha=9^\circ$. At 12 m/s, the HLC at an angle of attack 7° yields a target lift coefficient $C_L=1.06$. When an add-on device was attached to the half-span wing model at HLC, it was expected that by increasing the half-span wing model angle of attack by 1° - 2° would recover the target lift coefficient that was achieved at HLC without the add-on device. Hence, the half-span wing model with the add-on device is tested at $\alpha=9^\circ$.

The reverse delta type add-on device has angle of attack fixed at $\alpha_{rdw}=+30^\circ$. Tests were also performed for $\alpha_{rdw}= \pm 20^\circ$ but the most favorable case of $\alpha_{rdw}=+30^\circ$ was chosen. The angle of attack of the add-on device is measured relative to the flow direction. A total of 100 PIV images were recorded in each case and were post-processed using adaptive correlation with a 25% overlap. The measurement resolution is 1600×1186 pixels. An initial interrogation area size of 256×256 pixels is used, which is reduced to a final interrogation area size of 32×32 pixels by making 3 refinement passes that yield 66×49 vectors per image. For each PIV vector map, the center position of the vortex is precisely located (most likely a single vector with a velocity magnitude exists at the center of the vortex). Then the center positions of the 100 PIV vector maps are corrected ensuring that the center of all the 100 PIV vector maps have the same y and z co-ordinates. After correcting the center position of the

vortices, the 100 PIV vector maps are averaged to estimate the mean velocity in the region of focus. Figure 3.18 shows a PIV image map of the wingtip vortex.

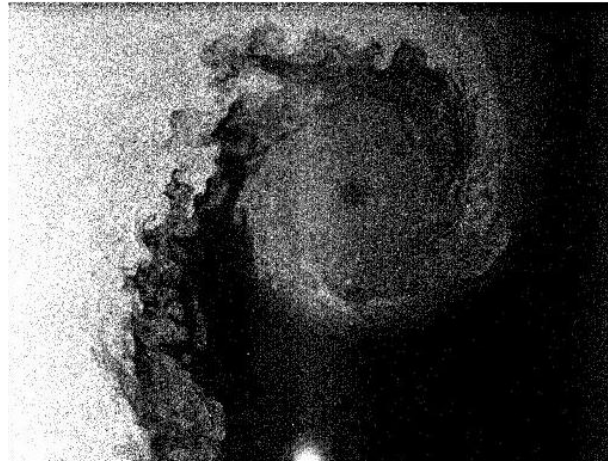


Figure 3.18: PIV image map of the wingtip vortex at $\alpha=7^\circ$ at $x/(b/2)=0.548$ (without the reverse delta type add-on device).

3.5 PIV UNCERTAINTY ANALYSIS

Various sources of errors exist in PIV velocity measurements. Uncertainty analysis techniques are described in Goldstein (1996) and Figliola and Beasley (1995). Two types of errors exist in all measurements, namely Bias/Systematic and Precision/Random errors. Bias/Systematic errors are those that happen to be the same whenever a measurement is made. Precision/Random errors are those that are different for successive measurements.

An approximation of uncertainty in velocity measurements is made by considering the statistical uncertainty, the uncertainty in the wing angle of attack and the uncertainty in the displacement Δx and Δy . All uncertainties are based on 95% confidence intervals. The emphasis of this research is to characterize vortex flow through velocity measurements. Hence, only sources of uncertainty that affect the findings of the various cases that have been studied are considered.

Bias errors that affect all datasets, such as geometric uncertainty in wing dimensions are not considered.

For the purpose of this thesis, only an uncertainty analysis of the High Lift Configuration (HLC) for $\alpha=7^\circ$ at a location of $x/(b/2)=0.548$ downstream has been provided since the bulk of the total uncertainty is derived from the uncertainty in displacement, which for all sets of data at a particular laser position is constant.

3.5.1 STATISTICAL UNCERTAINTY

Statistical uncertainty in the mean velocity measurements is estimated using average standard deviation in velocity. It is defined as the square root of the variance

$$\sigma V = \frac{N \sum_{i=1}^N V_i^2 - (\sum_{i=1}^N V_i)^2}{N(N-1)} \quad (3.1)$$

where N is the number of measurement samples taken per case and V_i is the mean velocity for each measurement. A total of 100 measurement samples were taken per case, hence, $N=100$. Each measurement will have its own average velocity magnitude. Thus, for each case, 100 values of average velocity will be recorded.

The variance is $\sigma V=0.00354$ and the square root of the variance yields the standard deviation in velocity, $\Delta V_i = \pm 0.0595$ m/s.

3.5.2 UNCERTAINTY IN THE WING ANGLE OF ATTACK

The uncertainty in the wing angle of attack contributes to the uncertainty in tangential velocity by affecting the vortex circulation and is given by

$$\frac{\partial V_\theta}{\partial \alpha} = \frac{1}{2\pi r} \frac{\partial \Gamma_0}{\partial \alpha} \quad (3.2)$$

The lift curve slope of the high lift configuration case was estimated from the six component force balance data obtained. It was estimated to be $\frac{\partial C_l}{\partial \alpha} = 0.0634$. The circulation sensitivity was obtained from

$$\frac{\partial \Gamma_0}{\partial \alpha} = \frac{1}{2} V_{\infty} C \frac{\partial C_l}{\partial \alpha} \quad (3.3)$$

which yields $\frac{\partial \Gamma_0}{\partial \alpha} = 0.1413$. The tangential velocity sensitivity was obtained from

$$\frac{\partial V_{\theta}}{\partial \alpha} = \frac{1}{2\pi r} \frac{\partial \Gamma_0}{\partial \alpha}, \text{ which yields } \frac{\partial V_{\theta}}{\partial \alpha} = 1.406 \left(\frac{m}{s}\right)/^{\circ}.$$

The value of r was taken to be 16 mm, which is equal to the vortex internal core radius based on maximum tangential velocity for the HLC at $\alpha=7^{\circ}$.

The uncertainty in the angle of attack is $\pm 0.05^{\circ}$. Hence, the uncertainty in the tangential velocity due to the uncertainty in the angle of attack is $\Delta V_{\theta} = \pm 0.0703$ m/s.

3.5.3 UNCERTAINTY IN DISPLACEMENT

The uncertainty in velocity due to the uncertainty in displacement is given by

$$V_{dis} = \frac{\Delta x}{\Delta t} \quad (3.4)$$

The relative uncertainty in velocity due to the uncertainty in the displacement can be expressed as $\frac{\delta \Delta x'}{\Delta x} = \left(\frac{0.5^2 \text{ pix}}{3^2}\right)^{\frac{1}{2}} = 0.1667 \text{ pix}$. The Scale factor is 15.888; hence, 0.1667 pixels will correspond to 0.0105 mm as shown below.

$$15.888 \text{ pix} = 1 \text{ mm}$$

$$0.1667 \text{ pix} = \frac{1 \text{ mm}}{15.888 \text{ pix}} \times 0.1667 \text{ pix}$$

$$0.1667 \text{ pix} = 0.0105 \text{ mm}$$

Thus, for $\Delta t = 60 \mu s$,

$$\Delta V_{dis} = \frac{\Delta x}{\Delta t} = \frac{0.0105 \times 10^{-3} \text{ m}}{60 \times 10^{-6} \text{ s}} = \pm 0.175 \frac{\text{m}}{\text{s}}$$

3.5.4 TOTAL UNCERTAINTY

The total uncertainty in velocity is;

$$\begin{aligned}\Delta V_T &= \pm(\Delta V_i^2 + \Delta V_\theta^2 + \Delta V_{dis}^2)^{\frac{1}{2}} \\ \Delta V_T &= \pm(0.0595^2 + 0.0703^2 + 0.175^2)^{\frac{1}{2}} \\ \Delta V_T &= \pm 0.198 \text{ m/s}\end{aligned}\tag{3.5}$$

Therefore, the total uncertainty based on 95% confidence level is;

$$\Delta V_T = \pm(0.95 \times 0.198) = \pm 0.188 \text{ m/s}$$

This corresponds to an uncertainty in vorticity, $\Delta \zeta = \pm 99.6 \text{ s}^{-1}$.

The uncertainty in velocity is less than 2% of the free stream velocity.

3.6 SUMMARY

A detailed explanation of the experimental apparatus used and the experimental procedure has been provided. This chapter also highlights the working principles, advantages of PIV and an elaborate PIV uncertainty analysis. Uncertainty analysis is performed to approximate the errors in measurements, thus, providing an overall idea of the accuracy of the measurements.

This chapter provides the uncertainty analysis in the velocity measurements of the PIV data. Results, from a sample case, point out that the velocity measurements are flawed by a value of $\pm 0.188 \text{ m/s}$, which leads to an uncertainty in vorticity of $\pm 99.6 \text{ s}^{-1}$, based on 95% confidence level. This means that the actual velocity and vorticity of the PIV measurements is either higher or lower than the stated value obtained from the PIV analysis by $\pm 0.188 \text{ m/s}$ and $\pm 99.6 \text{ s}^{-1}$, respectively.

CHAPTER FOUR

THREE DIMENSIONAL FLOW BOUNDARY CORRECTIONS

4.1 INTRODUCTION

In the case of aircrafts or ground vehicles, the flow conditions in a wind tunnel cannot recreate flow fields identical as in free-air. Wind tunnel flows are different to free-air due to several factors. These differences demand corrections to be applied to measurements obtained in wind tunnels. Relatively small deviations can have significant effects on resulting surface stress distributions and corresponding total forces.

There are numerous sources of inaccuracy for three dimensional experiments in the wind tunnel. The most important are: Buoyancy, Solid Blockage, Wake Blockage and Streamline Curvature.

The purpose of this chapter is to obtain true values of data by performing the boundary corrections. A sample calculation has been done for High Lift Configuration (HLC) at $\alpha=7^\circ$. Similarly, calculations have been performed for the reverse delta type add-on device cases ($\alpha=9^\circ$) and have been tabulated. The figures listed in this chapter are from chapter 10 of Barlow et al. (1999).

4.2 BUOYANCY

Buoyancy is initiated by the growth of the boundary layer on the walls of the test section. Boundary layer development is equivalent to the shrinkage of the test section area. Due to the thickening of the boundary layer and the reduction of the test section area, the flow is accelerated triggering a disparity in the static pressure along the axis of the test section.

Therefore, wind tunnel models with a large frontal area are pushed backwards. Some tunnels have slightly expanding test sections to diminish this effect.

Buoyancy correction is given by:

$$\Delta D_B = \frac{dp}{dl} (Volume) \quad (4.1)$$

where $\frac{dp}{dl}$ is the slope of the pressure coefficient distribution in a stream-wise direction at the center of the test section obtained from wind tunnel data.

$$\begin{aligned} \Delta D_B &= \frac{dp}{dl} (Volume) = \left(\frac{0.00545 \frac{N}{m^2}}{m} \right) \left(\frac{1}{2} (0.50 + 0.19)(0.93)(0.0555)m^3 \right) \\ &= 9.705 \times 10^{-5} N \end{aligned}$$

4.3 SOLID BLOCKAGE

The presence of a model and the tunnel walls in the test section reduce the area through which air can flow as compared to free-air conditions. By continuity and Bernoulli's equation, the air velocity is increased over the model. This increase of velocity, which is approximated as a constant over the model for regular model sizes, is called solid blockage. The effect of solid blockage can be corrected by increasing the effective wind tunnel air speed.

The solid blockage correction for a wing is given by:

$$\varepsilon_{sb,W} = \frac{\Delta V}{V_u} = \frac{K_1 \tau_1 (wing\ volume)}{C^{\frac{3}{2}}} \quad (4.2)$$

where K_I is the body shape factor, from Figure 4.1; τ_I is a factor depending on the tunnel test section shape and the model span to tunnel width ratio, from Figure 4.2; C is the tunnel test section area.

From Figure 4.1, $K_I=1.01$ for $\frac{t}{c} = 0.12$

$$\frac{2b}{B} = \frac{2(0.93) m}{2.30 m} = 0.81$$

$$\frac{B}{H} = \frac{2.30 m}{1.50 m} = 1.53$$

where b is the wing half-span; B is the tunnel width; H is the tunnel height.

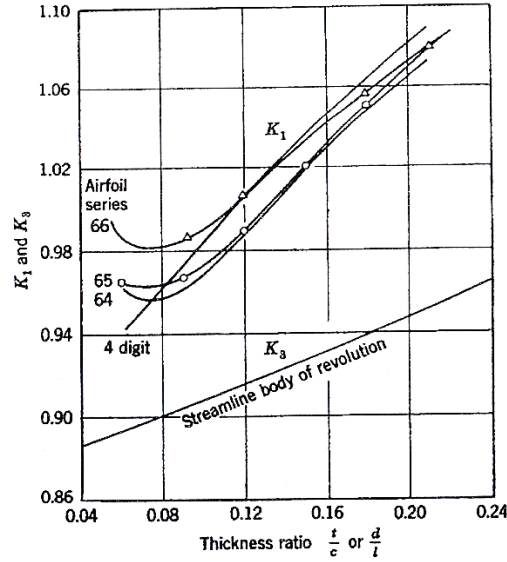


Figure 4.1: Body shape factor (K_1 and K_3) versus thickness ratio for a number of bodies [Barlow et al., 1999].

From Figure 4.2, $\tau_1=0.89$

$$\varepsilon_{sb,W} = \frac{\Delta V}{V_u} = \frac{K_1 \tau_1 (\text{wing volume})}{C^{\frac{3}{2}}} = \frac{(1.01)(0.89)(0.017807)}{(2.30 \times 1.50)^{\frac{3}{2}}} = 2.49 \times 10^{-3}$$

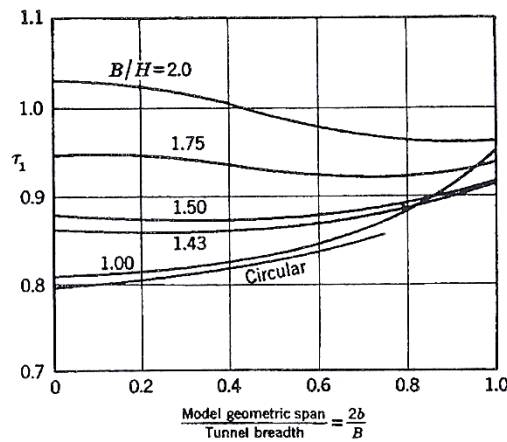


Figure 4.2: Ratio of tunnel test section shape versus (model span/tunnel width) for a number of tunnel types [Barlow et al., 1999].

4.4 WAKE BLOCKAGE

Wake blockage effects are produced by lateral-wall constraint on the wake and result in lower wake pressure and hence, lower model base pressures than would occur in free-air. The wake blockage effect can also be corrected by increasing the effective wind tunnel air speed.

The wake blockage is given as:

$$\varepsilon_{wb} = \frac{\Delta V}{V_u} = \frac{S}{4C} C_{Du} \quad (4.3)$$

where, S is the wing area, C is the test section area and C_{Du} is the uncorrected drag coefficient.

At $\alpha=7^\circ$, $C_{Du}=0.0985$; where C_{Du} is the measured drag coefficient from the six component force balance.

$$\varepsilon_{wb} = \frac{\Delta V}{V_u} = \frac{S}{4C} C_{Du} = \frac{0.32085}{4(2.30 \times 1.50)} (0.0985) = 2.29 \times 10^{-3}$$

Therefore, the total blockage is:

$$\varepsilon_T = \varepsilon_{sb} + \varepsilon_{wb} = (2.49 \times 10^{-3}) + (2.29 \times 10^{-3}) = 4.78 \times 10^{-3} \quad (4.4)$$

4.5 STREAMLINE CURVATURE

The curvature of the flow streamlines around the model is artificially straightened by the wind tunnel ceiling and floor. The model seems to have more camber than it really has, i.e. the model appears to have more lift than it really has. The streamline curvature effect requires corrections to angle of attack, lift coefficient and moment coefficient.

The streamline curvature effect on the angle is given as:

$$\Delta\alpha_{sc} = \frac{c}{4B} \frac{d\tau_2}{d\left(\frac{l_t}{B}\right)} \delta \frac{S}{C} C_{LW} (57.3) \quad (4.5)$$

where c is the chord length; B is tunnel width; $\frac{d\tau_2}{d\left(\frac{l_t}{B}\right)}$ is the gradient of the downwash

correction factor with respect to the ratio of tail length to the tunnel width; δ is the boundary

correction factor; S is the surface area of model; C is the test section area; C_{LW} is the wing lift coefficient.

$$l_t = \frac{1}{4}c = \frac{1}{4}(0.371) = 0.0928 \text{ m}$$

where l_t is the tail length. Note: Value of τ_2 is found from Figure 4.4 using $\frac{1}{4}c$ as the tail length to determine τ_2 .

$$\frac{l_t}{B} = \frac{0.0928 \text{ m}}{2.030 \text{ m}} = 0.0403$$

From Figure 4.3, for $K = \frac{b}{B} = \frac{0.93 \text{ m}}{2.30 \text{ m}} = 0.404$ and $\lambda = \frac{H}{B} = \frac{1.50 \text{ m}}{2.30 \text{ m}} = 0.652$, δ is 0.125

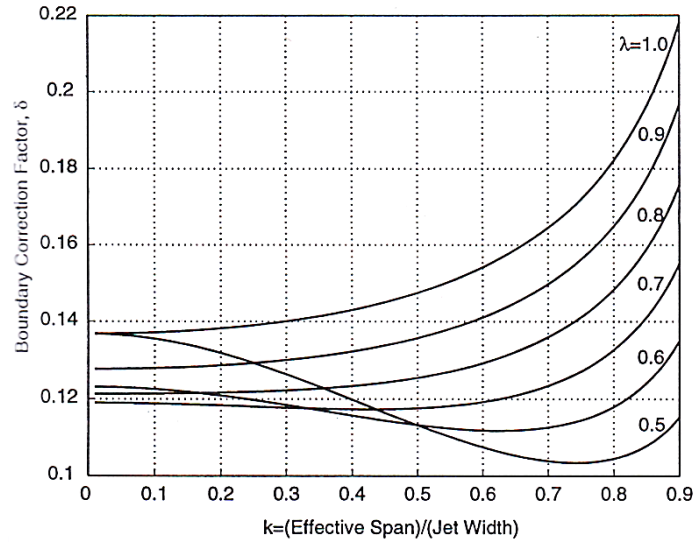


Figure 4.3: Boundary correction factor (δ) for a wing with uniform loading in a closed rectangular tunnel [Barlow et al., 1999].

From Figure 4.4, for a closed jet, the gradient $\frac{d\tau_2}{d\left(\frac{l_t}{B}\right)} = \frac{0.6}{0.2} = 3.0$

For High Lift Configuration at $\alpha=7^\circ$, $C_{LW}=1.06$

$$\begin{aligned} \Delta\alpha_{sc} &= \frac{c}{4B} \frac{d\tau_2}{d\left(\frac{l_t}{B}\right)} \delta \frac{S}{C} C_{LW}(57.3) = \frac{0.371}{(4 \times 2.30)} (3)(0.125) \frac{0.32085}{(2.30 \times 1.50)} (1.06)(57.3) \\ &= 0.085^\circ \end{aligned}$$

The additive lift correction is given as

$$\Delta C_{L,SC} = -\Delta \alpha_{sc} \cdot a \quad (4.6)$$

where, a = wing lift curve slope.

The wing lift curve slope for the HLC is

$$\frac{dc_l}{d\alpha} = 0.0703$$

$$\Delta C_{L,SC} = -\Delta \alpha_{sc} \cdot a = -0.085(0.0703) = -6.0 \times 10^{-3}$$

The additive correction to the moment coefficient is derived as

$$\Delta C_{m,SC} = -0.25 \Delta C_{L,SC} \quad (4.7)$$

$$\Delta C_{m,SC} = -0.25 \Delta C_{L,SC} = -0.25(-6.0 \times 10^{-3}) = 1.50 \times 10^{-3}$$

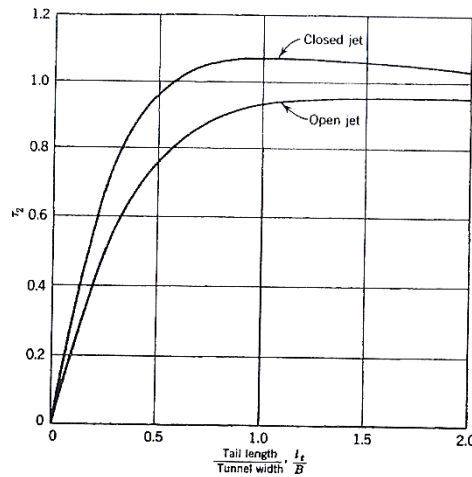


Figure 4.4: Downwash correction factor (τ_2) for open and closed jets [Barlow et al., 1999].

4.6 DATA CORRECTIONS

For HLC at $\alpha=7^\circ$, $C_L=1.06$

The induced angle due to the boundaries is

$$\Delta \alpha_i = \frac{\frac{S}{C}}{8} C_L \quad (4.8)$$

where, S is the wing area, C is the tunnel cross-sectional area and C_L is the wing lift.

$$\Delta\alpha_i = \frac{0.32085}{(2.30 \times 1.50)} (1.06) = 0.012^\circ$$

The induced drag increment due to the boundaries is

$$\Delta C_{Di} = \frac{\frac{s}{c}}{8} C_L^2 \quad (4.9)$$

$$\Delta C_{Di} = \frac{0.32085}{(2.30 \times 1.50)} (1.06)^2 = 0.013$$

The true values, at $\alpha=7^\circ$, become

$$\alpha = \alpha_u + \delta \frac{s}{c} C_{LW} (57.3) \quad (4.10)$$

where, α_u is the uncorrected angle of attack and $\delta = 0.125$ for a round closed test section when the wing is small and has uniform loading.

$$\alpha = 7 + (0.125) \frac{0.32085}{(2.30 \times 1.50)} (1.06)(57.3) = 7.71^\circ$$

At $\alpha=7^\circ$, $C_{Du}=0.0985$; where C_{Du} is the measured drag coefficient from the six component force balance.

$$C_D = C_{Du} + \delta \frac{s}{c} C_{LW}^2 \quad (4.11)$$

$$C_D = 0.099 + (0.125) \frac{0.32085}{(2.30 \times 1.50)} (1.06)^2 = 0.112$$

The total corrected free stream velocity is:

$$V = V_u(1 + \varepsilon_T) = (12)(1 + 0.00486) = 12.06 \text{ m/s} \quad (4.12)$$

The total corrected dynamic pressure is:

$$q = q_u(1 + 2\varepsilon_T) = (82.08)(1 + 0.00972) = 82.88 \text{ pa} \quad (4.13)$$

The total corrected Reynolds number is:

$$Re = Re_u(1 + \varepsilon_T) = (2.74 \times 10^5)(1 + 0.00486) = 2.75 \times 10^5 \quad (4.14)$$

Table 4.1
Corrected values of aerodynamic coefficients.

α_u	C_{Du}	C_{Lu}	C_{mu}	$\Delta\alpha_{sc}$	$\Delta C_{L,sc}$	$\Delta C_{m,sc}$	$\Delta\alpha_i$	ΔC_{Di}
7° (HLC)	0.099	1.06	0.073	0.085°	-6.01×10^{-3}	1.50×10^{-3}	0.012°	0.013
9° (S-rdw)	0.125	1.13	-0.038	0.091°	-6.09×10^{-3}	1.52×10^{-3}	0.013°	0.015
9° (L-rdw)	0.133	1.10	0.053	0.089°	-5.72×10^{-3}	1.43×10^{-3}	0.013°	0.014
Corrected values								
				α_{sc}	α	C_L	C_D	C_m
				7.08° (HLC)	7.7°	1.054	0.112	0.075
				9.09° (S-rdw)	9.7°	1.124	0.140	-0.037
				9.09° (L-rdw)	9.7°	1.094	0.147	0.054

Table 4.2
Percentage change in the corrected and uncorrected values.

Configuration	% error α	% error C_L	% error C_D	% error C_m
HLC	9.2	0.57	11.6	2.7
S-rdw	7.7	0.53	10.7	2.6
L-rdw	7.5	0.54	9.5	1.9

4.7 SUMMARY

Boundary corrections in the wind tunnel are performed to get an estimate of the errors associated with the angle of attack, lift, drag and moment coefficients of the model used. The error in angle of attack of the model propagates into the error in lift, drag and moment coefficients. As can be seen from the boundary corrections performed in this chapter, the error in angle of attack and drag coefficient is significant whereas the error in lift coefficient and moment coefficient is small. A small error in angle of attack of the model corresponds to a significant error in drag coefficient.

CHAPTER FIVE

RESULTS AND DISCUSSIONS

5.1 INTRODUCTION

The research work is divided into five cases and this chapter will discuss the findings of these five cases in detail. For each case, the velocity components in planes perpendicular to the stream-wise direction at four locations; $x/(b/2) = 0.021, 0.548, 1.075$ and 2.387 , (where b is the wing span) in the downstream direction are investigated. The same downstream planes are used in the entire study. The justification for choosing these locations is discussed in chapter 3. PIV data was analysed thoroughly. Important information such as tangential velocity, vorticity and circulation was retrieved and plotted in the form of distributions.

This chapter includes an elaborate account of the details of velocity vectors, tangential velocity contours, vorticity contours, tangential velocity distributions, circulation distributions and six component force balance results obtained for five cases.

For cases 1-4, only the angle of attack of the reverse delta type add-on device (α_{rdw}) is varied whereas the roll angle is fixed at $\phi_{rdw} = 0^\circ$. The selected angles of attack were $\alpha_{rdw} = \pm 20^\circ, +30^\circ$. Aim of cases 1-4 is to demonstrate an ideal attachment location and angle of attack of the reverse delta type add-on device for significant wake vortex alleviation. For case 5, only the roll angle of the reverse delta type add-on device is varied whereas the angle of attack is fixed at $\alpha_{rdw} = 0^\circ$. The selected roll angles were $\phi_{rdw} = \pm 20^\circ, \pm 30^\circ$. Case 5 aims to demonstrate if changes in roll angle cause significant wake vortex alleviation.

5.2 CASE 1

Half-span wing model landing configuration for case 1 is as below:

Location of add-on device: as shown in Figure 5.1

Deflection of add-on device: $\alpha_{rdw} = +30^\circ$, $\phi_{rdw} = 0^\circ$

Slat deflection: 15°

Flap deflection: 20°

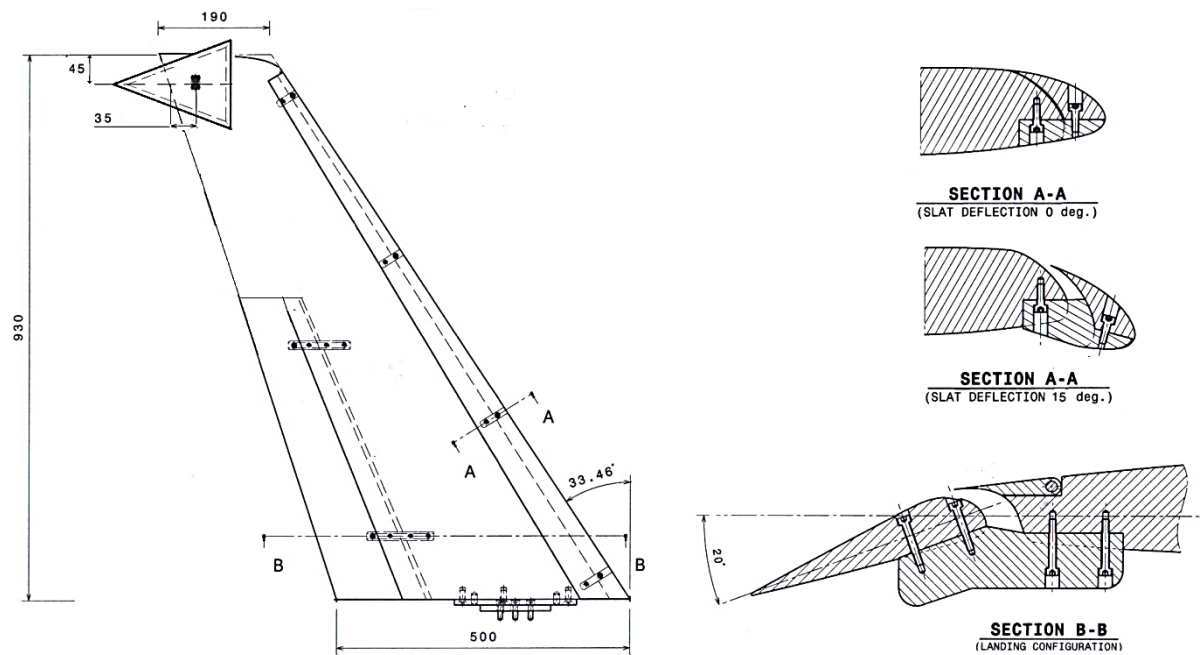


Figure 5.1: Schematic of the half-span wing model with a large reverse delta type add-on device attached. Linear dimensions are in millimetres (mm).

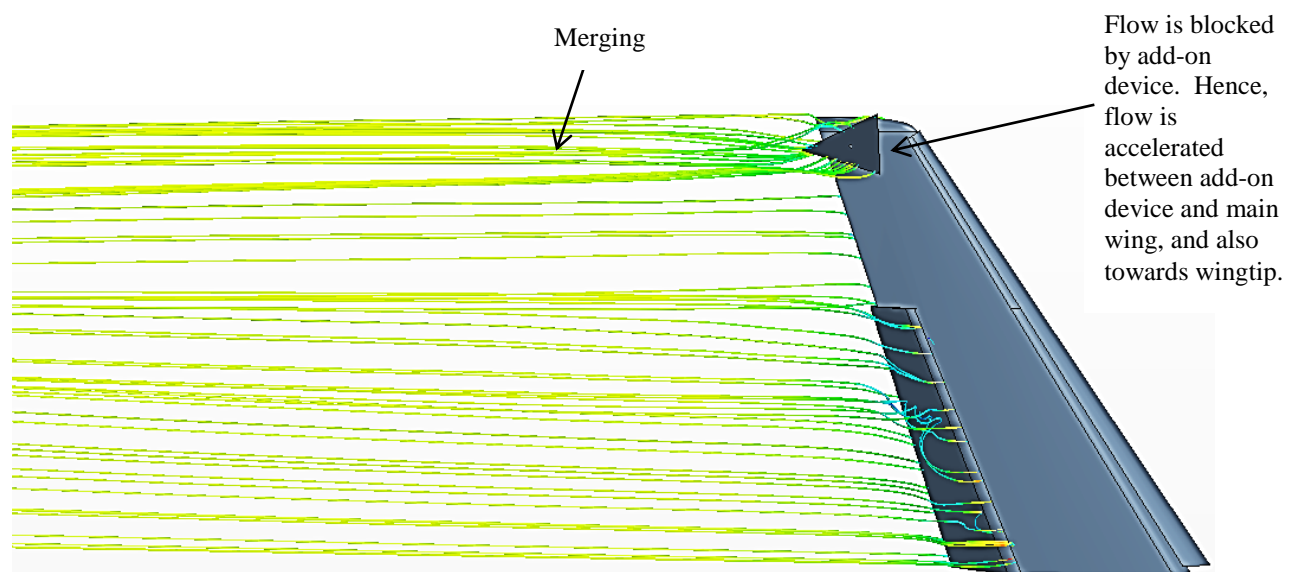


Figure 5.2: Streamlines showing the merging of the wingtip vortex, flap-tip vortex and reverse delta type add-on device vortices downstream. (Courtesy: Haziq Nasir)

5.2.1 Velocity Vectors and Vorticity Contours

The purpose of the above half-span wing model with reverse delta type add-on device configuration is to investigate if the vortices produced by the reverse delta type add-on device are able to implant a fast growing instability (counter-sign vorticity) into the wingtip vortex and alter the roll-up and decay process of the wingtip vortex. The add-on device vortices and the wingtip vortex are hypothesized to merge downstream and instigate significant wake vortex alleviation.

Figures 5.4 to 5.7 show the velocity vectors on downstream planes normal to the flow near the wingtip for a half-span wing model at HLC with/without a reverse delta type add-on device attached.

Figures 5.4a, 5.5a, 5.6a and 5.7a show the velocity vectors, tangential velocity magnitude and vorticity contours of the HLC wingtip vortex at the 4 downstream planes. Wingtip vortices are known to rollup exceedingly quickly within a few chords downstream of the wing (Prandtl, 1919). It is clearly noticeable that the wingtip vortex is well formed and the vortex rollup is better at a plane farther downstream. The tangential velocity is seen to decrease between downstream planes. Reynolds (1876) attributed the reduction in the tangential velocity to the growth of the vortex in order to conserve momentum. As the vortex propagates through the fluid its volume increases with time due to the entrainment of the surrounding fluid.

Figures 5.4b-c, 5.5b-c, 5.6b-c and 5.7b-c, show the velocity vectors, tangential velocity magnitude and vorticity contours of the vortices of the HLC with an add-on device in place. In this case the vortex size is seen to be increasing rapidly between the downstream planes.

It is important to state that the tangential velocity is much lower when a reverse delta type add-on device is used, as shown in figures 5.4b-c, 5.5b-c, 5.6b-c and 5.7b-c. The wingtip vortex of the HLC without the add-on device exhibits a better rollup (downstream location 2-

4) than the HLC with the add-on device. The tangential velocity reduction from downstream plane 2 to downstream plane 4 for the HLC is 7.6% only. Whereas, the tangential velocity reduction between HLC and HLC with add-on devices at downstream plane 2 for the Small reverse delta type add-on device (S-rdw) case and Large reverse delta type add-on device (L-rdw) case is 55.6% and 56.3%, respectively. At downstream plane 3, the tangential velocity reduction between HLC and HLC with add-on devices for S-rdw and L-rdw add-on devices is 58.5% and 65.0%, respectively. At downstream plane 4, the tangential velocity reduction between HLC and HLC with add-on devices for S-rdw and L-rdw add-on devices is 69.8% and 82.9%, respectively. The HLC wingtip vortex size (without the add-on device) does not vary rapidly between the downstream planes and thus, the tangential velocity reduction is minimal as there is minimal increase in the vortex core volume.

The reverse delta type add-on device is seen to modify the flow in numerous ways in all the cases investigated. Firstly, it accelerates the flow between the add-on device and the main wing, and also accelerates the flow in the span-wise direction. Secondly, the add-on device is seen to introduce secondary vorticity in the vicinity of the wingtip/flap-tip vortex. The secondary vorticity wraps around the wingtip/flap-tip vortex (primary vortex) and destabilizes/deforms it. These secondary vorticity structures (counter-rotating add-on device vortices) weaken the wingtip/flap-tip vortex. The vortices produced by the add-on device create a fast growing instability (counter-sign vorticity) into the wingtip/flap-tip vortex causing the modification of the rollup and decay processes.

The add-on device blocks the path of travel of air from the lower wing surface to the upper wing surface at the wingtip (similar to winglets). This yields a resultant vortex with a weaker rollup (more diffused vortex); comparing figure 5.5a with 5.5b-c, figure 5.6a with 5.6b-c and figure 5.7a with 5.7b-c; causing an increase in the vortex core size. The interaction of the wingtip vortex with the vortices produced by the add-on device also contributes to the

weakening of the resultant vortex and increase of the resultant vortex core size. The vortex system with co-rotating and counter-rotating vortices (add-on device vortices and wingtip/flap-tip vortex) experiences a lower tangential velocity due to instabilities created by the interaction of the co-rotating and counter-rotating vortices within the vortex system which lead to an enlarged and weaker resultant vortex (Coustols et. al., 2006), as shown in figures 5.4b-c.

Also, co-rotating vortices can create instability within the vortex system. At landing configuration, co-rotating wingtip and flap-tip vortices merge far downstream and form a significantly weaker resultant vortex (Fabre et. al., 2002). The merging of the wingtip and flap-tip vortices introduces instabilities, resulting in significant breakdown of the resultant vortex core (Fabre et. al., 2002). The unstable resultant vortex diffuses more rapidly.

Similarly, the co-rotating wingtip vortex and the reverse delta type add-on device vortex in close proximity of the wingtip, see figure 5.4b-c, merge downstream and form a weaker resultant vortex. These co-rotating vortices are not synchronized (i.e. are not formed at the same stream-wise location). These co-rotating vortices are very close to each other and at the point where the vortices meet; they have opposite velocity direction, as shown in figure 5.3. This creates small scale instabilities within the vortex system causing the resultant vortex to become distorted (weaker rollup). Modification of the rollup process is followed by rapid diffusion. It can be concluded that the introduction of a reverse delta type add-on device enhances the dissipation rate of the resultant vortex.

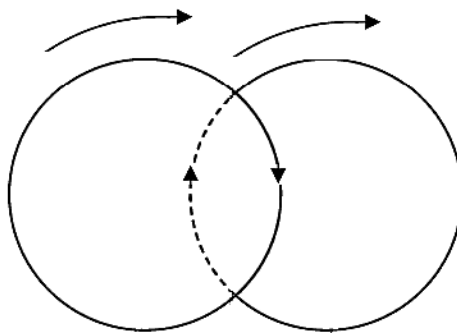


Figure 5.3: Interaction of co-rotating cylindrical vortices.

For all investigated cases, the vorticity decreased gradually from a maximum at the centre to nearly zero at the outer region of the vortices. For the HLC, closer vorticity contours at the centre of the vortex are recorded, as shown in figures 5.4a, 5.5a, 5.6a and 5.7a. It can be noticed that the vortices exhibit uniform spacing of vorticity contours nearly throughout the vortex core, implying a linear profile of vorticity with radial distance, but small patches of vorticity exist away from the vortex core. From figure 5.4a, it is seen that small patches of vorticity exist at the outer regions of the vortex, suggesting that the entire vorticity shed by the half-span wing model is not engulfed within the wingtip vortex core. From figure 5.6a, it can be seen that the number of small patches of vorticity have decreased, suggesting that more vorticity has been engulfed within the vortex core. The vorticity magnitude at the centre of the vortex in Figure 5.6a is slightly higher than in Figure 5.5a which supports the claim that more surrounding vorticity has diffused into the vortex core. In Figure 5.7a, the vorticity magnitude at the centre of the vortex core has reduced and the small patches of vorticity have increased in number. Tangential velocity gradients exist throughout the vortex due to small patches of vorticity that are distributed to regions outside the vortex core. The vortex does not exhibit constant tangential velocity as is assumed by the inviscid theory. This suggests that the vorticity from the vortex core may have been deposited in to regions outside the vortex core and hence, the vorticity magnitude at the core decreases, see figure 5.7a. The rejection of vorticity reduces the circulation of the vortex and its strength (Maxworthy, 1972).

For the HLC with the add-on devices the vorticity reduces rapidly, as shown in figures 5.5b-c, 5.6b-c and 5.7b-c. Secondary vorticity of the add-on device vortices can be seen from figures 5.4b-c. There are no distinguishable vortex contours within the vortex core and there are small patches of vorticity aplenty (more than the case of HLC without add-on devices) all over the outer regions of the vortex core because the resultant vortex core has been broken down by the counter-sign vorticity injected into the resultant vortex by the reverse delta type

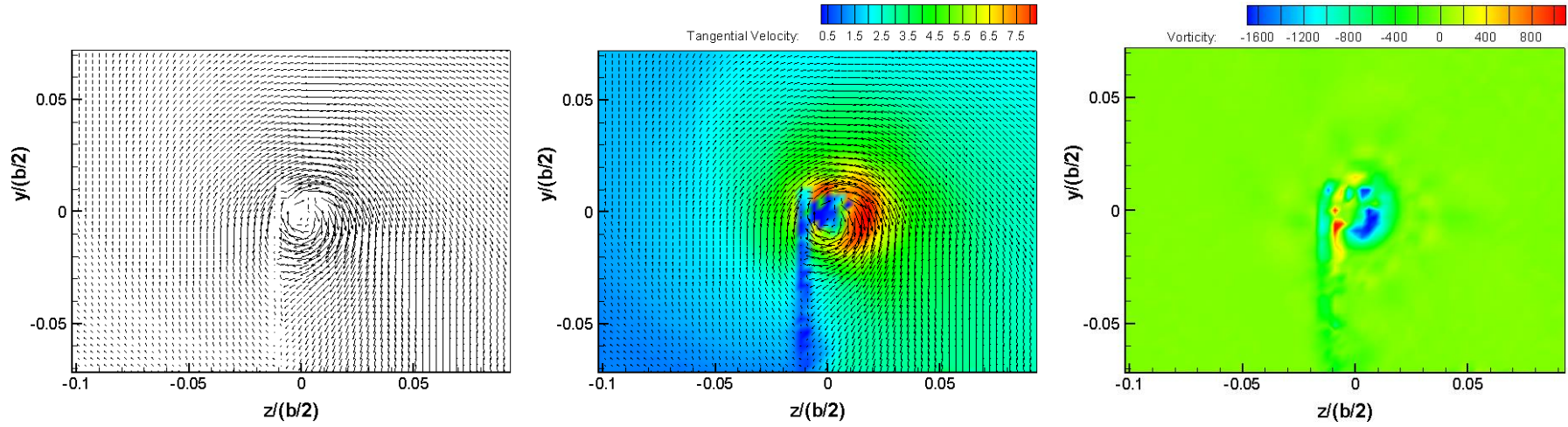
add-on device vortices. Due to this, the vortex core does not exhibit clear and distinct vorticity contours as the vortex has been greatly weakened and deformed. The L-rdw case vortex exhibits lower vorticity magnitudes than the S-rdw case vortex at all downstream planes. The larger the size of the add-on device, the more the air from the lower wing surface to the upper wing surface is blocked and the weaker the vortex rollup leading to lower vorticity magnitude of the resultant vortex. Also, the larger the size of the add-on device, the stronger the counter-sign vorticity injected into the vortex system and the weaker the resultant vortex. The weak rolled up resultant vortex causes the vortex core size to increase significantly and also rejects vorticity in to regions outside the resultant vortex core. The weakened resultant vortex is seen to diffuse rapidly. The vorticity reduction from downstream plane 2 to downstream plane 4 for the HLC is 16.6% only. The vorticity reduction between HLC and HLC with add-on devices at downstream plane 2 for the S-rdw case and L-rdw case is 84.3% and 85.5%, respectively. At downstream plane 3, the vorticity reduction for S-rdw case and L-rdw case is 89.3% and 91.4%, respectively. At downstream plane 4, the vorticity reduction for S-rdw case and L-rdw case is 89.5% and 92.6%, respectively.

The core radius of a vortex is defined as the radius where maximum tangential velocity occurs (Saffman, 1978). The HLC vortex core radius is much smaller compared to the HLC with the add-on device resultant vortex core radius. The resultant vortex core of the HLC with the add-on device is diffusing rapidly causing the resultant vortex core radius to increase. The difference in the sizes of the vortex cores is evident from figures 5.4 to 5.6. At $x/(b/2)=0.548$, the resultant vortex core radius compared to the HLC vortex core radius has diffused (enlarged) by a factor of 3.49 and 3.74 for the S-rdw and L-rdw, respectively. At $x/(b/2)=1.075$, the resultant vortex core radius compared to the HLC vortex core radius has increased by a factor of 4.08 and 4.81 for the S-rdw and L-rdw, respectively. At

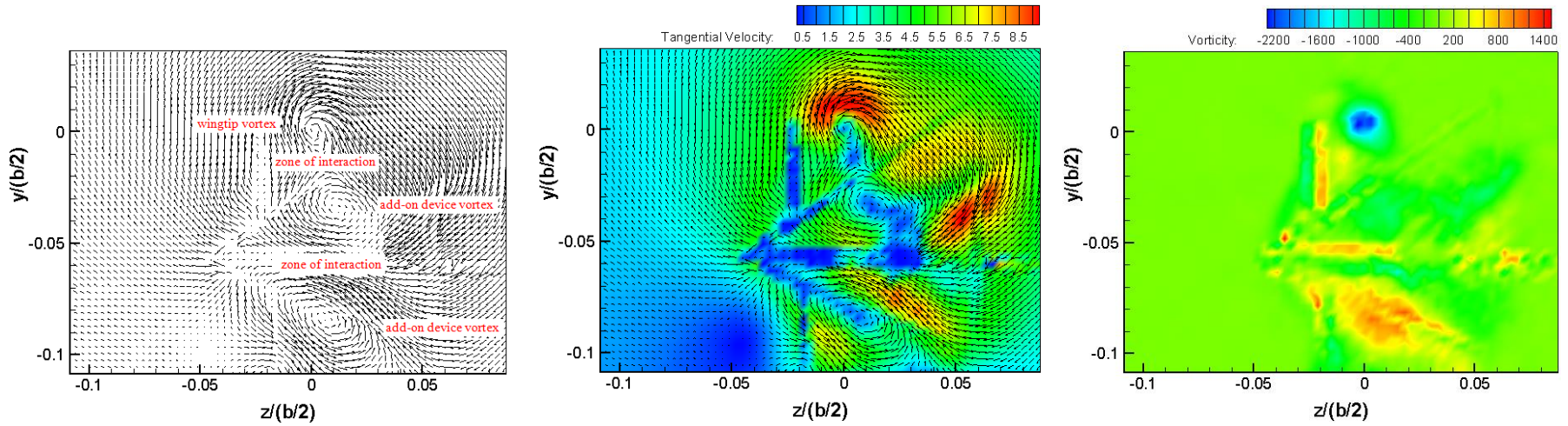
$x/(b/2)=2.387$, the resultant vortex core radius compared to the HLC vortex core radius has increased by a factor of 5.07 and 6.57 for the S-rdw and L-rdw, respectively. This implies that when the L-rdw is used, the resultant core radius size is 6.57 times more than the core radius of the HLC case vortex at the same downstream plane. This highlights that the resultant vortex is less coherent and there is significant diffusion of the resultant vortex caused when an add-on device is used. The enlarged resultant vortex is weaker in strength and is expected to dissipate more rapidly than the HLC wingtip vortex.

For HLC without the add-on device, the growth rate of the wingtip vortex from plane 1 to 2 is 2.84%, from plane 2 to 3 is 5.22% and from plane 3 to 4 is 5.62%. For HLC with S-rdw, the growth rate of the resultant vortex from plane 2 to 3 is 23.3% and from plane 3 to 4 is 31.2%. For HLC with L-rdw, the growth rate of the resultant vortex from plane 2 to 3 is 35.2% and from plane 3 to 4 is 44.3%.

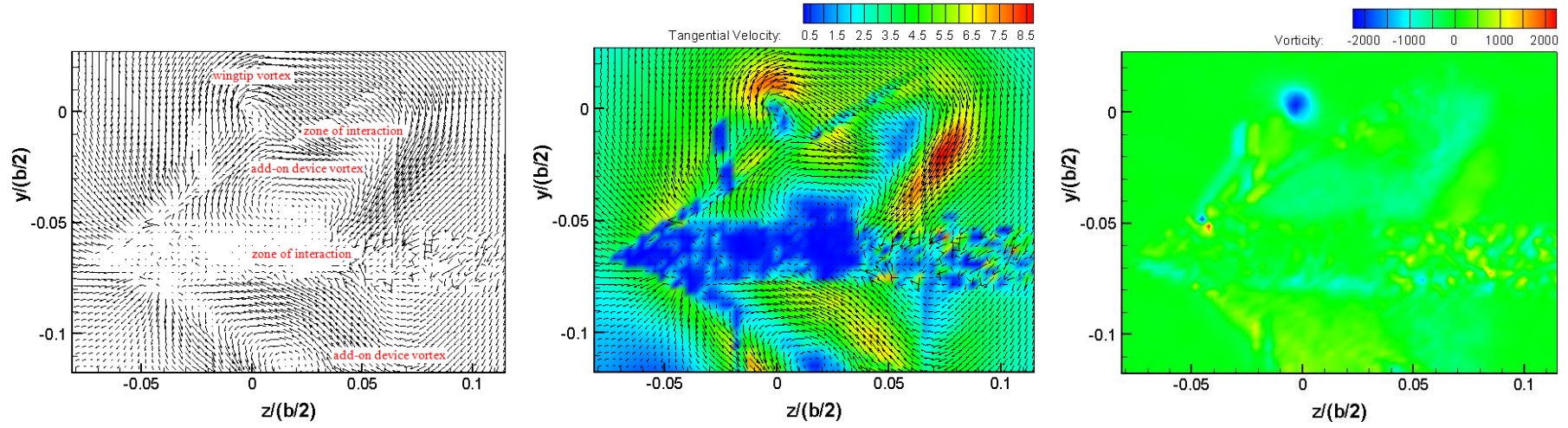
The weaker vortices generated downstream of a wing with a reverse delta type add-on device are a desirable consequence which will help to avoid trailing aircraft from being immersed in strong swirling vortical flows during consecutive landings and take-offs. Thus, allowing for reduced separation of aircraft during landing and take-off.



a) High Lift Configuration case, $\alpha=7.7^\circ$, $x/(b/2)=0.021$, $V_\infty=12$ m/s.

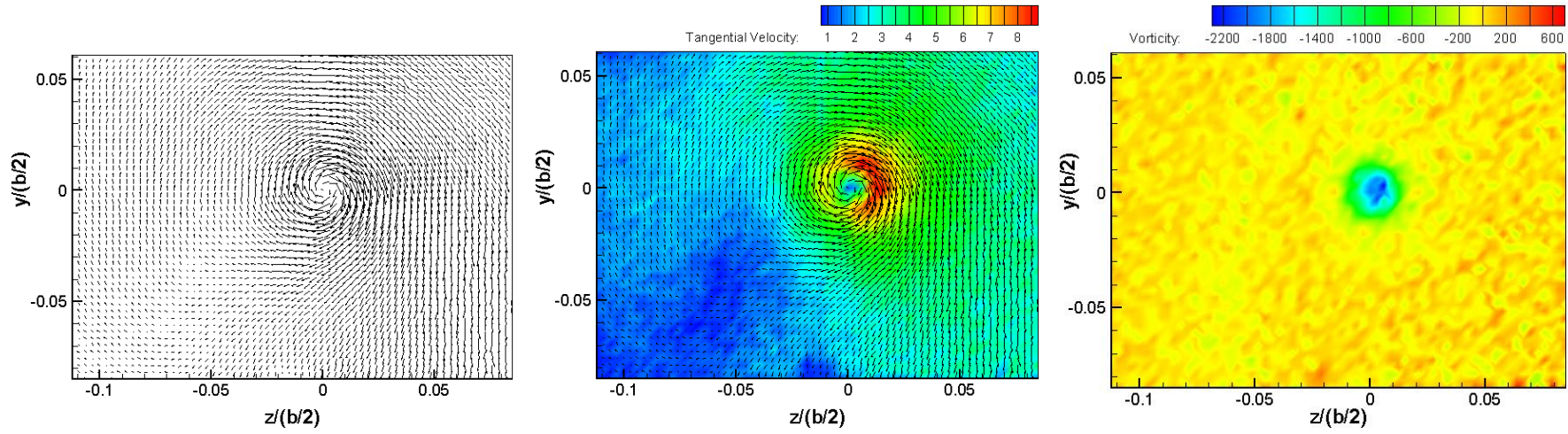


b) High Lift Configuration case, $\alpha=9.7^\circ$; with S-rdw add-on device, $\alpha_{S-rdw}=30^\circ$, $x/(b/2)=0.021$, $V_\infty=12$ m/s.

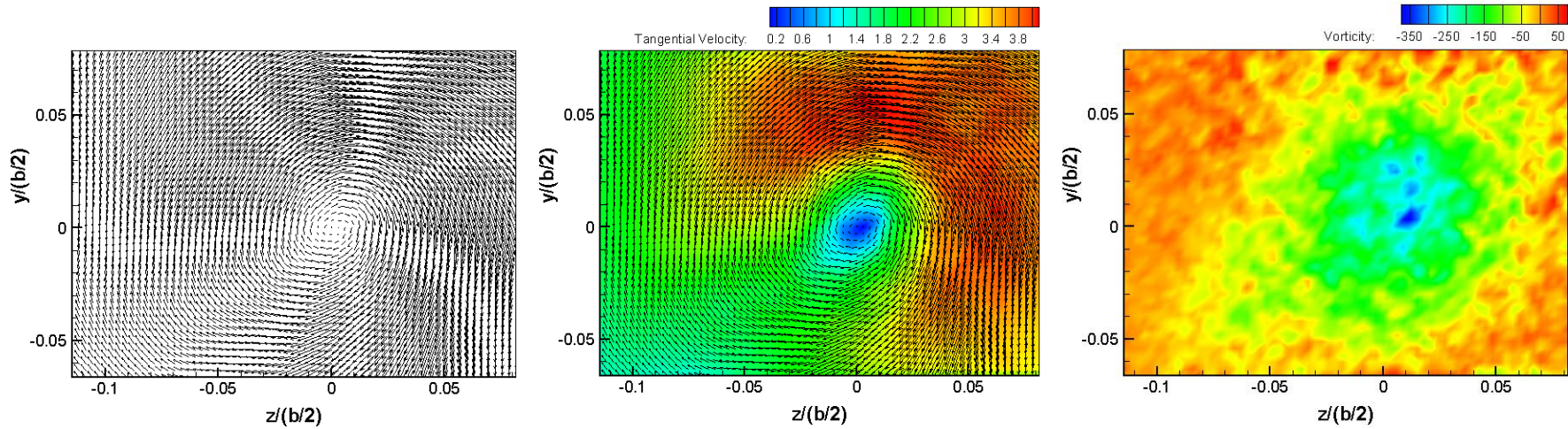


c) High Lift Configuration case, $\alpha=9.7^\circ$; with L-rdw add-on device, $\alpha_{L-rdw}=30^\circ$, $x/(b/2)=0.021$, $V_\infty=12$ m/s.

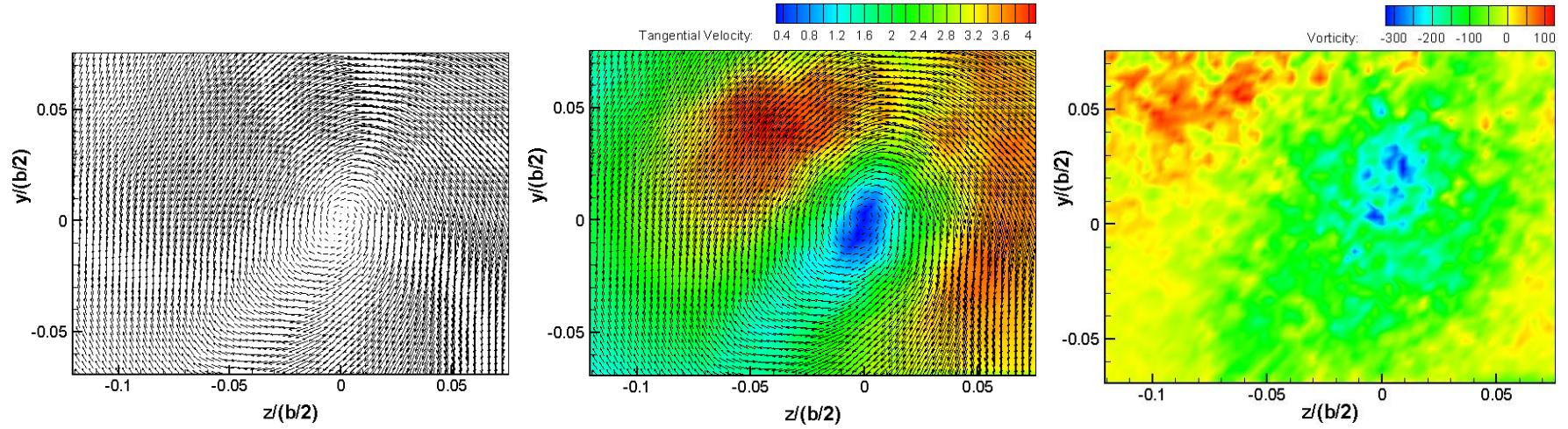
Figure 5.4: Velocity Vectors, Tangential Velocity Magnitude and Vorticity Contours at $x/(b/2)=0.021$ for (a) High Lift Configuration $\alpha=7.7^\circ$, (b) High Lift Configuration $\alpha=9.7^\circ$ with S-rdw add-on device ($\alpha_{S-rdw}=30^\circ$) and (c) High Lift Configuration $\alpha=9.7^\circ$ with L-rdw add-on device ($\alpha_{L-rdw}=30^\circ$).



a) High Lift Configuration case, $\alpha=7.7^\circ$, $x/(b/2)=0.548$, $V_\infty=12$ m/s.

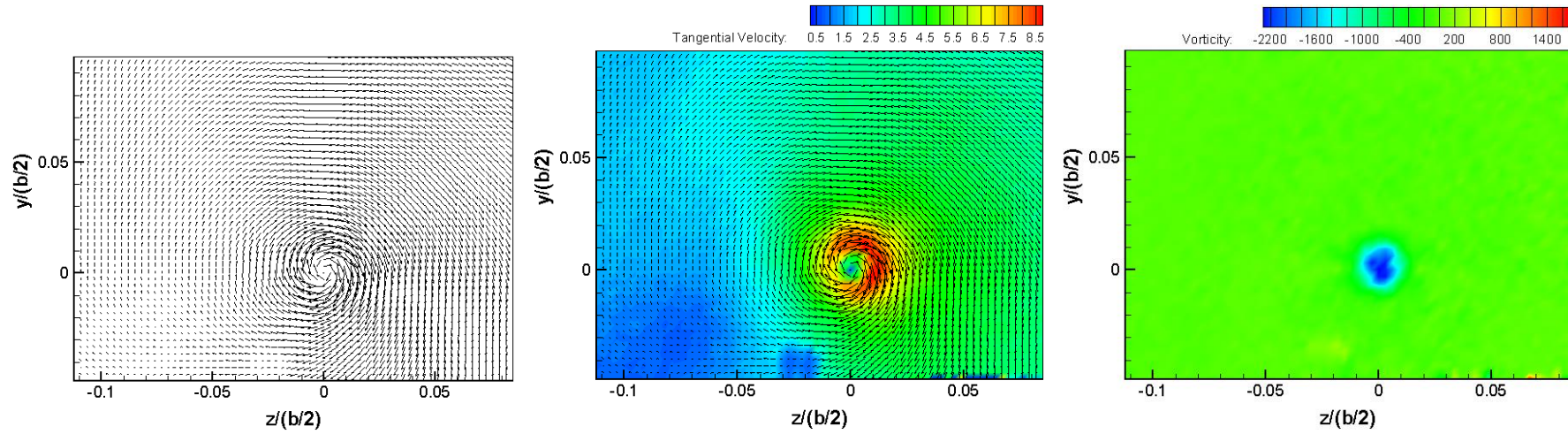


b) High Lift Configuration case, $\alpha=9.7^\circ$; with S-rdw add-on device, $\alpha_{S-rdw}=30^\circ$, $x/(b/2)=0.548$, $V_\infty=12$ m/s.

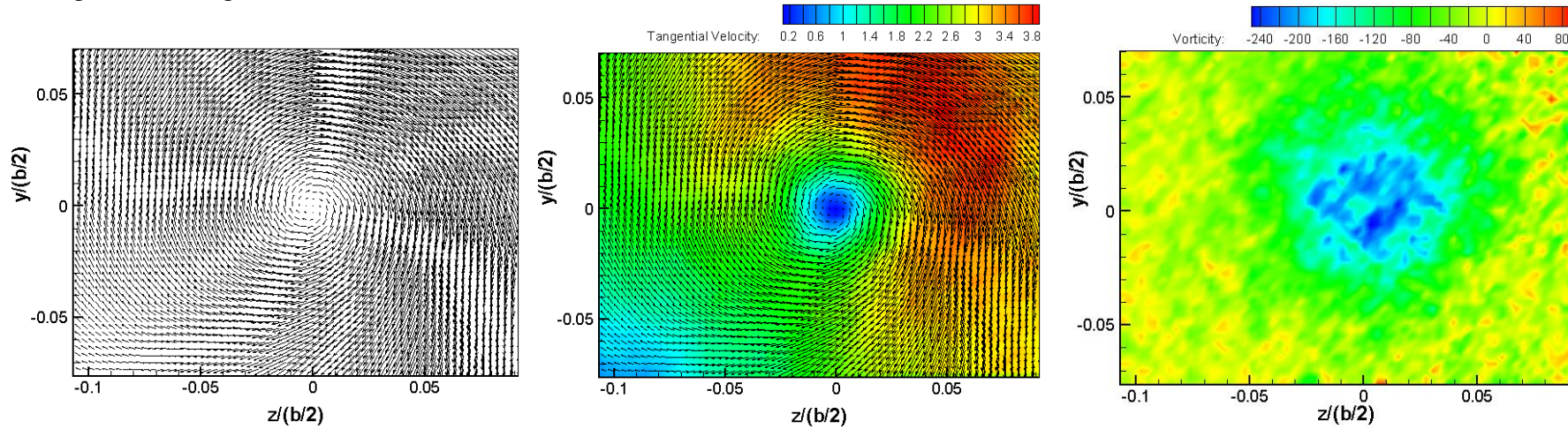


c) High Lift Configuration case, $\alpha=9.7^\circ$; with L-rdw add-on device, $\alpha_{Lrdw}=30^\circ$, $x/(b/2)=0.548$, $V_\infty=12$ m/s.

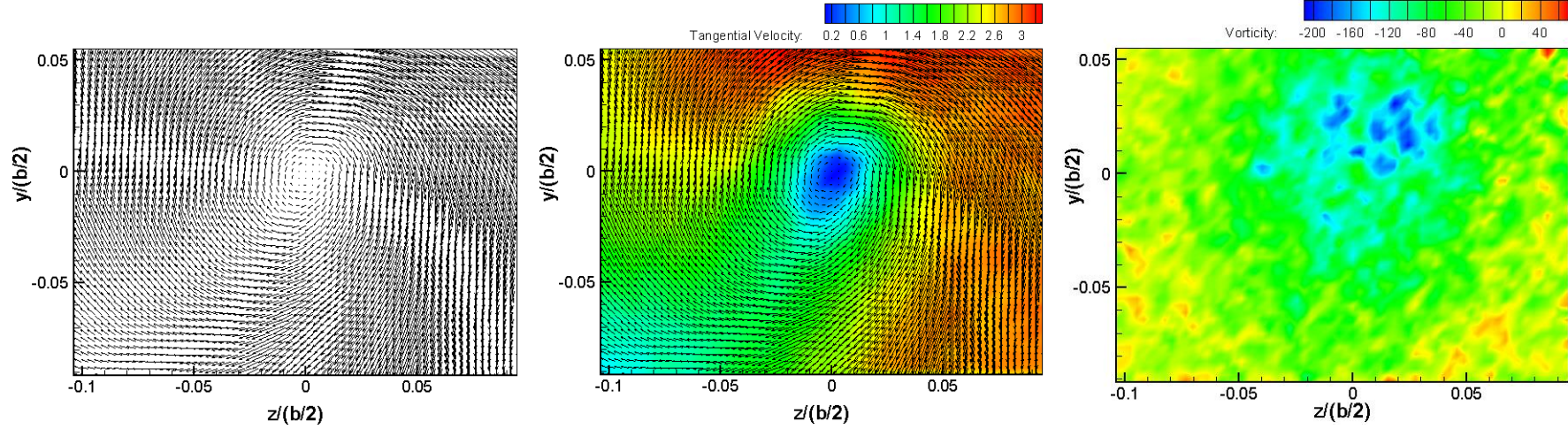
Figure 5.5: Velocity Vectors, Tangential Velocity Magnitude and Vorticity Contours at $x/(b/2)=0.548$ for (a) High Lift Configuration $\alpha=7.7^\circ$, (b) High Lift Configuration $\alpha=9.7^\circ$ with S-rdw add-on device ($\alpha_{S-rdw}=30^\circ$) and (c) High Lift Configuration $\alpha=9.7^\circ$ with L-rdw add-on device ($\alpha_{L-rdw}=30^\circ$).



a) High Lift Configuration case, $\alpha=7.7^\circ$, $x/(b/2)=1.075$, $V_\infty=12$ m/s.

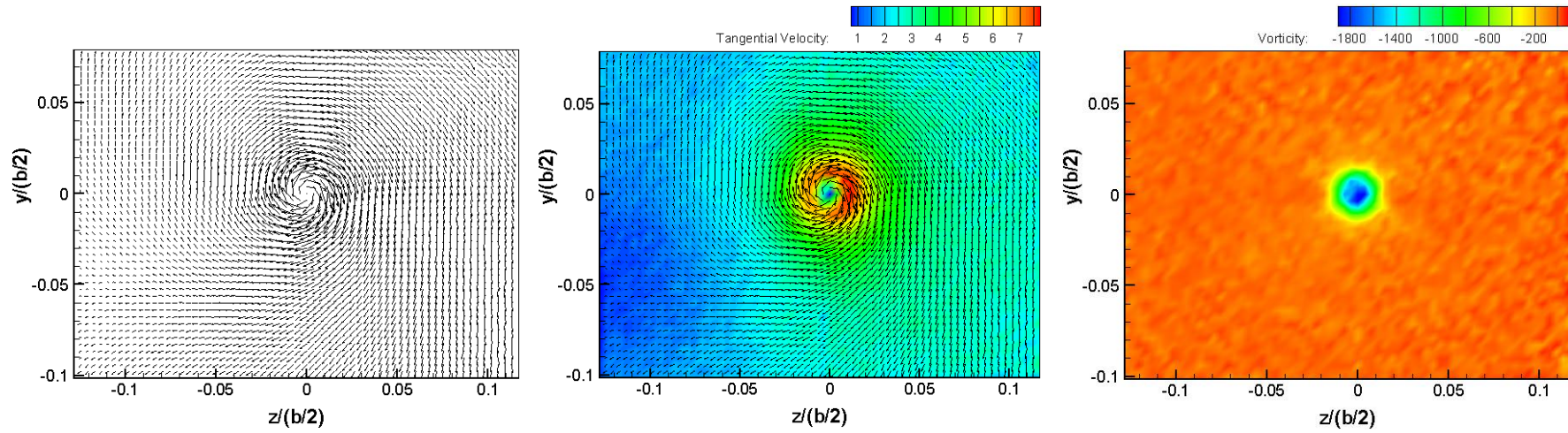


b) High Lift Configuration case, $\alpha=9.7^\circ$; with S-rdw add-on device, $\alpha_{S-rdw}=30^\circ$, $x/(b/2)=1.075$, $V_\infty=12$ m/s.

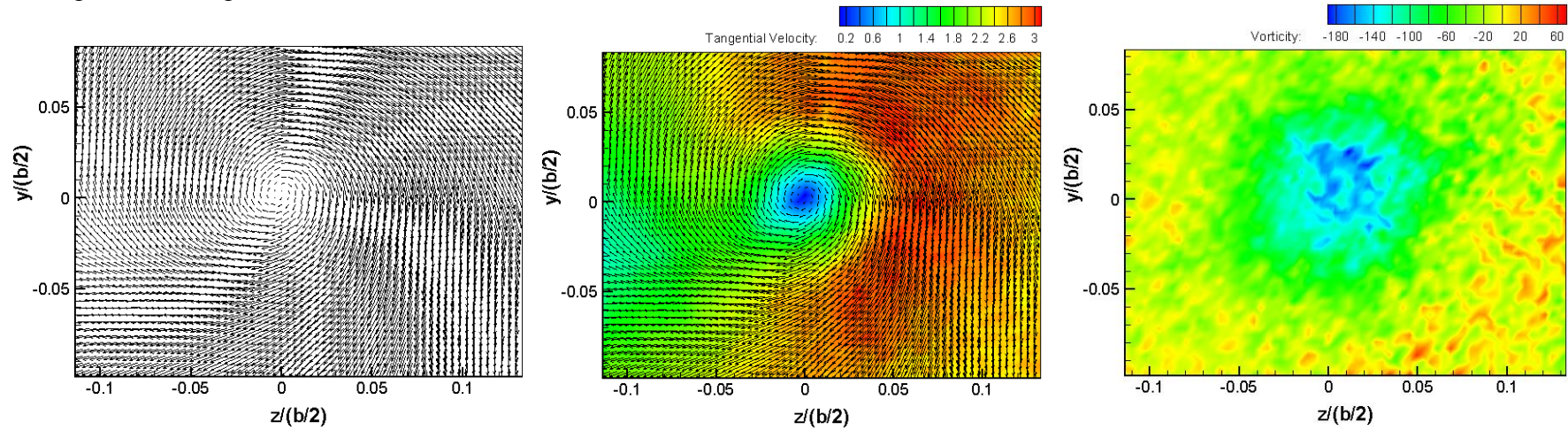


c) High Lift Configuration case, $\alpha=9.7^\circ$; with L-rdw add-on device, $\alpha_{L\text{-rdw}}=30^\circ$, $x/(b/2)=1.075$, $V_\infty=12$ m/s.

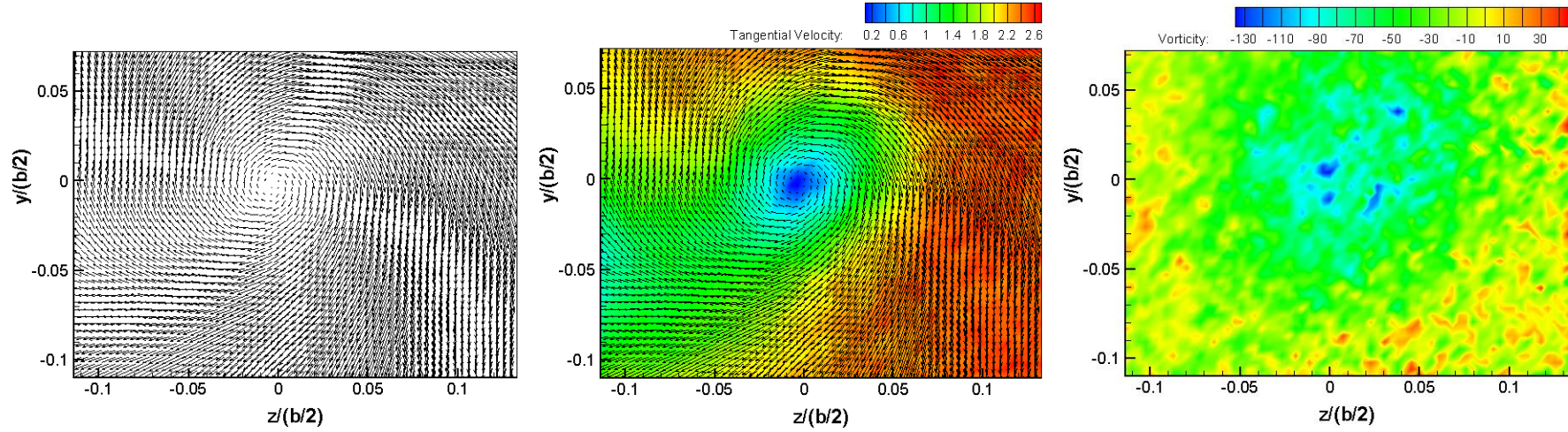
Figure 5.6: Velocity Vectors, Tangential Velocity Magnitude and Vorticity Contours at $x/(b/2)=1.075$ for (a) High Lift Configuration $\alpha=7.7^\circ$, (b) High Lift Configuration $\alpha=9.7^\circ$ with S-rdw add-on device ($\alpha_{S\text{-rdw}}=30^\circ$) and (c) High Lift Configuration $\alpha=9.7^\circ$ with L-rdw add-on device ($\alpha_{L\text{-rdw}}=30^\circ$).



a) High Lift Configuration case, $\alpha=7.7^\circ$, $x/(b/2)=2.387$, $V_\infty=12$ m/s.



b) High Lift Configuration case, $\alpha=9.7^\circ$; with S-rdw add-on device, $\alpha_{S-rdw}=30^\circ$, $x/(b/2)=2.387$, $V_\infty=12$ m/s.



c) High Lift Configuration case, $\alpha=9.7^\circ$; with L-rdw add-on device, $\alpha_{L\text{-rdw}}=30^\circ$, $x/(b/2)=2.387$, $V_\infty=12$ m/s.

Figure 5.7: Velocity Vectors, Tangential Velocity Magnitude and Vorticity Contours at $x/(b/2)=2.387$ for (a) High Lift Configuration $\alpha=7.7^\circ$, (b) High Lift Configuration $\alpha=9.7^\circ$ with S-rdw add-on device ($\alpha_{S\text{-rdw}}=30^\circ$) and (c) High Lift Configuration $\alpha=9.7^\circ$ with L-rdw add-on device ($\alpha_{L\text{-rdw}}=30^\circ$).

5.2.2 Tangential Velocity

The tangential velocity around the vortex centerline, V_θ , is calculated as

$$v_\theta(r) = \frac{1}{k} \sum_{i=1}^k v_{\theta,i}(y, z) \Big|_{r=\sqrt{y^2+z^2}} \text{ where } k \text{ is the number of points for each radius; } r = \sqrt{y^2 + z^2};$$

V_θ is normalized by the free stream velocity V_∞ and plotted versus the radial distance from the vortex centerline r , normalized by the half span ($b/2$); and r_c is defined as the core radius of the tip vortex, where maximum tangential velocity occurs (Saffman, 1978).

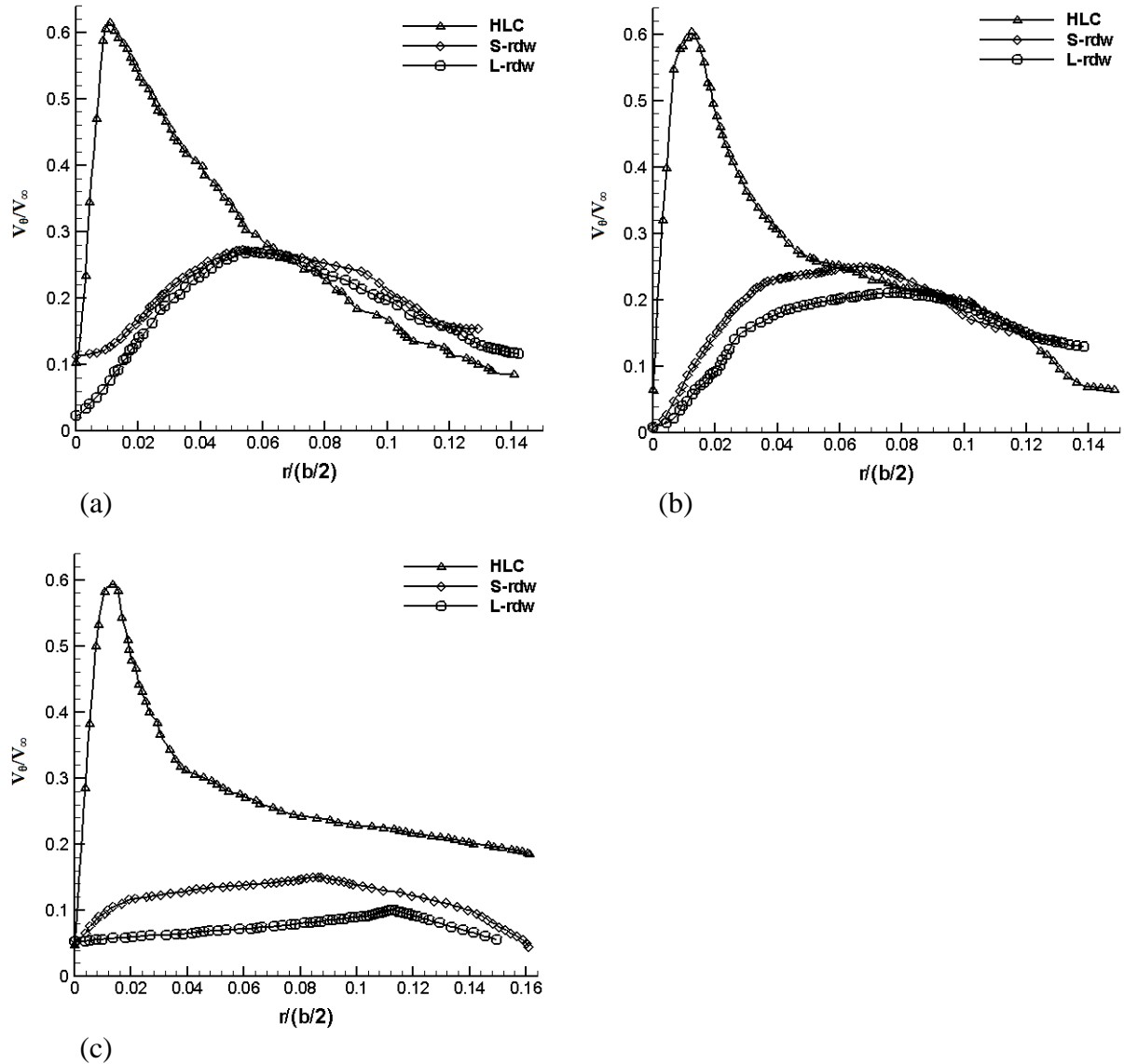


Figure 5.8: Non-dimensional tangential velocity distributions of HLC, HLC with S-rdw and HLC with L-rdw at (a) $x/(b/2)=0.548$, (b) $x/(b/2)=1.075$ and (c) $x/(b/2)=2.387$.

Figures 5.8a-c show the tangential velocity distributions of HLC, HLC with S-rdw and

HLC with L-rdw at downstream planes $x/(b/2) = 0.548, 1.075$ and 2.387 . At $x/(b/2)=0.021$, the resultant vortex is not fully formed. Therefore, it is not possible to determine its core radius and plot its tangential velocity distribution. The tangential velocity distributions increase rapidly to a maximum value at the core radius, and then decay inversely up till the edge of the analysis window. Wingtip vortices are known to be strong, exhibit higher tangential velocity magnitude and roll-up exceedingly quickly within a few chord lengths downstream (Prandtl, 1919). From Figures 5.8a-c, the HLC without the add-on devices exhibits more than twice the tangential velocity magnitude than the HLC with the add-on devices. This is consistent with a much stronger and quicker rollup for the HLC without the add-on devices. As the vortex moves downstream, the tangential velocity magnitude decreases slightly for all cases. This is expected as the vortex dissipates.

The difference in the sizes of the vortex cores is evident from the tangential velocity distributions. HLC with L-rdw exhibits a more diffused vortex core.

5.2.3 Circulation

The circular contours are centered about coordinates of maximum vorticity and plotted to estimate circulation. In Anderson (2001) and Dobrev et. al. (2008), circulation is estimated by

$$\Gamma = \int_A \zeta dA, \text{ which in turn yields } \Gamma = 2\pi r v_\theta \text{ for an axisymmetric vortex that is treated as a}$$

cylinder. The circulation is normalized by $V_\infty(b/2)$.

Figures 5.9a-c shows the circulation distributions for the HLC, HLC with S-rdw and HLC with L-rdw. Circulation is dependent on two variables; core radius, $r/(b/2)$ and tangential velocity, V_θ . Between $x/(b/2)=0.548$ and $x/(b/2)=1.075$, the circulation magnitude of the HLC case has increased. The strength of the wingtip vortex will continue to increase until a maximum and then gradually decrease as the vortex starts to decay. The HLC with the reverse delta type add-on devices shows that the circulation of the resultant vortex decreases.

The diffusion of the resultant vortex causes rapid increase in its core radius and rapid decrease in its tangential velocity. The counter-sign vorticity introduced in to the wingtip vortex by the add-on device vortices weakens the resultant vortex and breaks down the resultant vortex core (vorticity core is broken down). Small individual vorticity patches are formed which have lower vorticity magnitudes. The decrease of vorticity magnitude in the resultant vortex core causes a decrease in its circulation (strength). Between $x/(b/2)=1.075$ and $x/(b/2)=2.387$, the circulation magnitude of the HLC is nearly identical, as shown in figures 5.9b and 5.9c. This shows that the wingtip vortex strength has not decreased. The wingtip vortex core is still very compact at downstream plane 4 (concentrated vorticity core) and has not started to diffuse significantly yet, as shown in figure 5.7a. The HLC with the reverse delta type add-on devices shows that the circulation magnitude has reduced, indicating that the strength of the resultant vortex core has decreased. The resultant vortex core will decay rapidly farther downstream. The L-rdw records a greater reduction in circulation.

For the S-rdw and L-rdw cases, the circulation magnitude decreases significantly as the resultant vortex core has broken down. At $x/(b/2)= 2.387$, the circulation magnitude for S-rdw case and L-rdw case compared to the HLC case has decreased by 26.1% and 42.8%, respectively. Since, there is a significant decrease in the circulation magnitude from downstream plane 2 to downstream plane 4 for the S-rdw and L-rdw cases, it can be said that for these cases significant vortex decay has taken place as the resultant vortex core (vorticity core) is broken into many small patches. It is expected that farther downstream, the circulation magnitude will continue to decrease and eventually become insignificant. From the trend of circulation distributions, the L-rdw case resultant vortex is likely to decay more rapidly, followed by the S-rdw case and HLC case, respectively.

It can be concluded that the reverse delta type add-on device, attached at the wingtip on

the upper surface of the wing, is capable of alleviating wake vortex significantly.

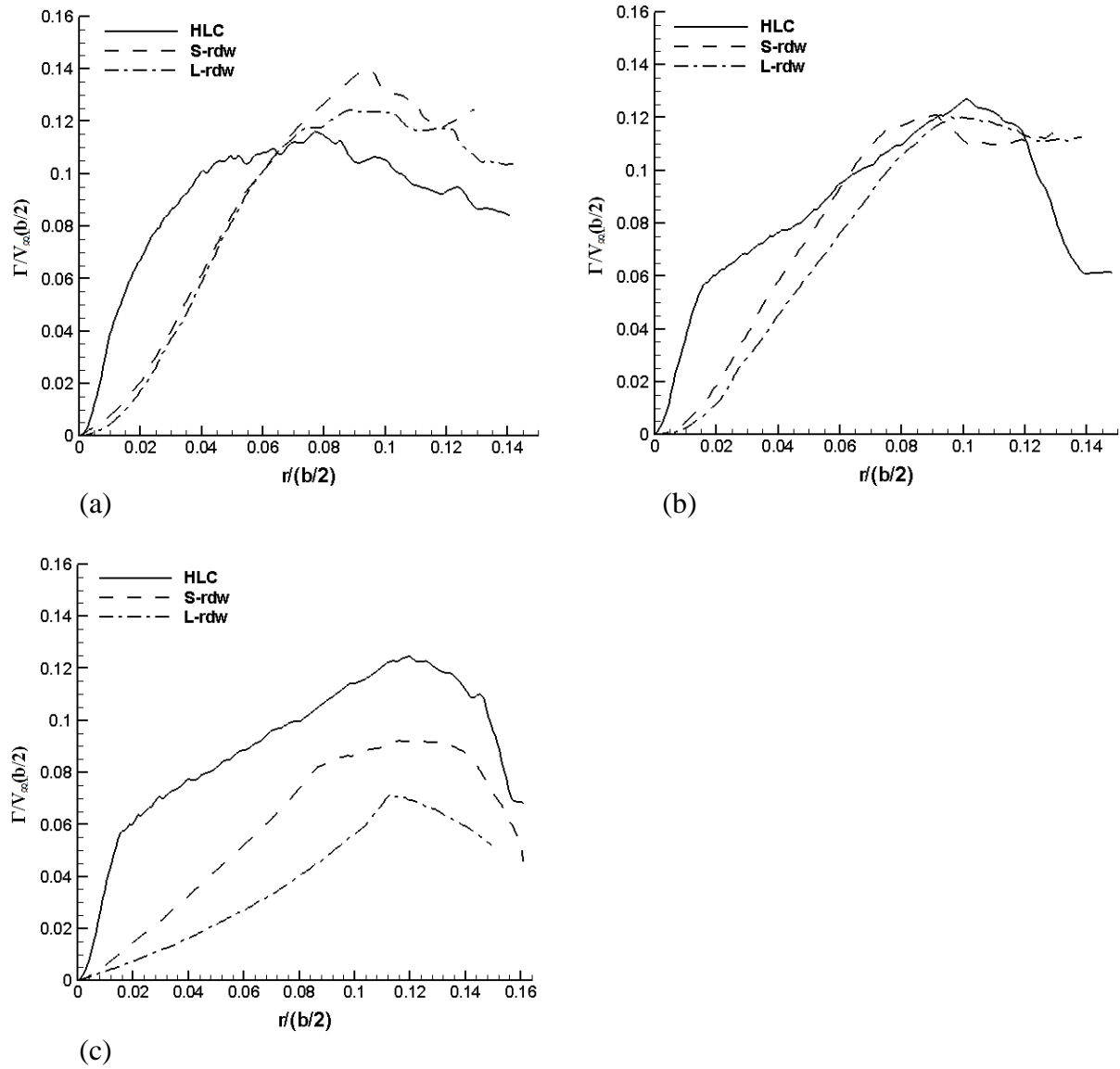


Figure 5.9: Vortex strength $\Gamma/V_\infty(b/2)$ versus radius $r/(b/2)$ of wingtip vortex of HLC, HLC with S-rdw and HLC with L-rdw at (a) $x/(b/2)=0.548$, (b) $x/(b/2)=1.075$ and (c) $x/(b/2)=2.387$.

From Figures 5.10 and 5.11, it can be concluded that the greatest tangential velocity and vorticity reduction for the S-rdw and L-rdw occurs when the add-on device is at $+30^\circ$ angle of attack. PIV results for only $+30^\circ$ angle of attack are plotted as the other two angles of attack yield slightly stronger vortex structures (less wake vortex alleviation). Angle of attack $+30^\circ$ yields the best results in terms of wake vortex alleviation. This is because at a higher angle of attack of the add-on device, stronger add-on device vortices are produced;

which are able to introduce a stronger instability (counter-sign vorticity) into the wingtip/flap-tip vortex, enabling significant wake vortex alleviation to take place.

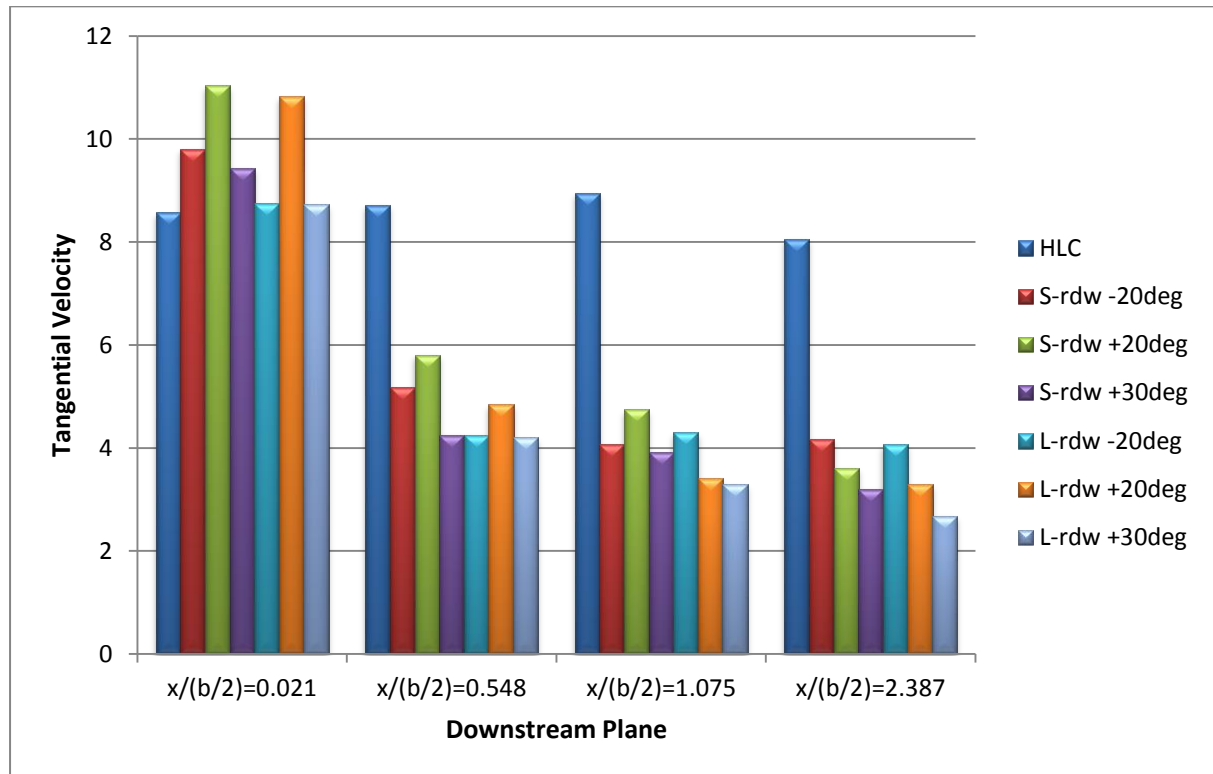


Figure 5.10: Peak tangential velocity magnitude of all investigated configurations at four downstream planes for Case 1.

The performance penalty (lift and drag penalties) is nearly similar for all angles of attack of the add-on device studied. The lift and drag penalties of the S-rdw and L-rdw are different for all cases. The greatest performance penalty is obtained when L-rdw is used.

It can be seen that at a particular downstream plane (other than $x/(b/2)=0.021$), the difference between the HLC case and the add-on device cases is large. The difference increases with an increase in downstream position. Hence, it can be concluded that a reverse delta type add-on device is capable of significant wake vortex alleviation.

The results show the same trend for all the cases studied. Hence, it is not deemed necessary to plot column charts for all cases studied in this chapter.

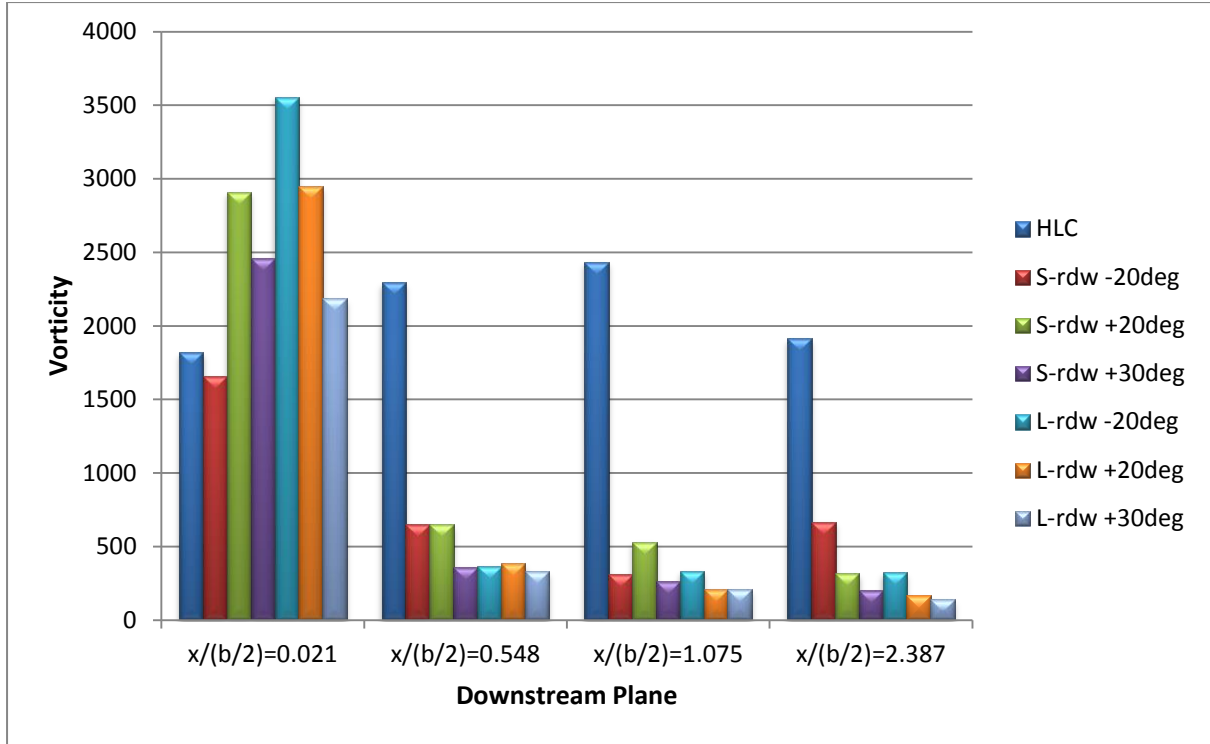


Figure 5.11: Vorticity magnitude of all investigated configurations at four downstream planes for Case 1.

5.2.4 Aerodynamic Performance

The six-component force balance in the IIUM closed loop low-speed wind tunnel was used to obtain the aerodynamic performance of the half-span wing model with/without the reverse delta type add-on device. Also, the aerodynamic performance of the plain wing configuration (slat extension 0° and flap extension 0°) was obtained. The add-on device angle of attack is fixed to $\alpha_{rdw} = +30^\circ$ for all cases studied. The add-on device angle of attack variation has minimal influence on the aerodynamic performance of the half-span wing model.

Figure 5.12a shows the lift coefficient and the moment coefficient curves of all the cases studied. HLC exhibits the highest lift coefficient at $\alpha = 18^\circ$ and it stalls between $\alpha = 18^\circ$ and $\alpha = 19^\circ$. The S-rdw and L-rdw configurations stall between $\alpha = 19^\circ$ and $\alpha = 20^\circ$. This is an advantageous phenomenon, which allows the stall of the wing to be delayed by 1° by using an add-on device. This happens because the air between the add-on device and the main wing is accelerated and delays the separation of the flow over the main wing. The lift coefficient

curves are nearly identical until $\alpha=0^\circ$ and then diverge slowly beyond that. The maximum reduction in the lift coefficient values between the HLC, S-rdw and L-rdw cases is 4.9%. The moment coefficient curves show that the stability of the wing is maintained for all investigated cases.

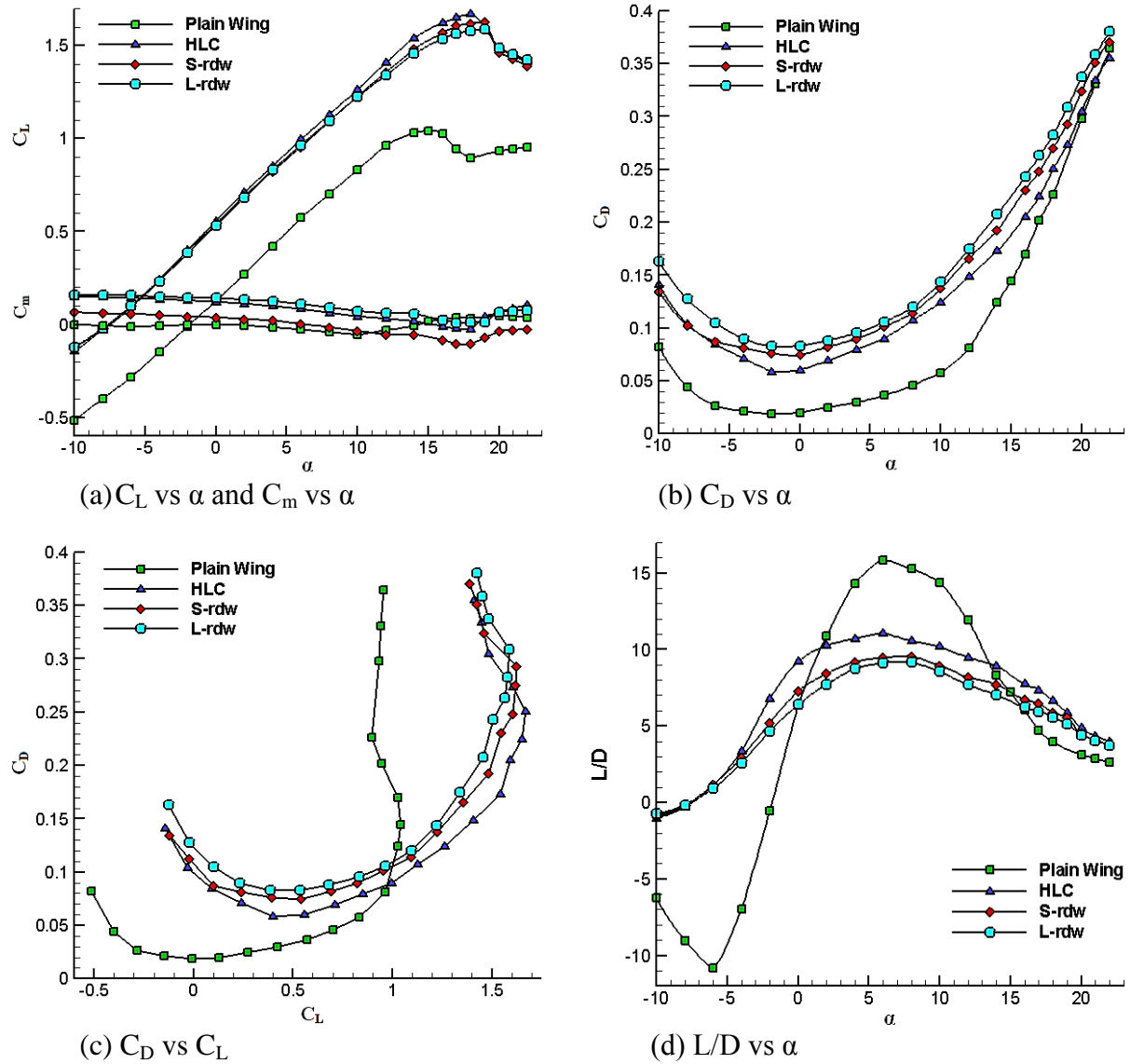


Figure 5.12: Aerodynamic performance of the Plain Wing, HLC, HLC with S-rdw and HLC with L-rdw.

Lift reduction is not normally important since it is possible to increase the lift by increasing the geometric angle of attack of the wing slightly to offset the effective angle of attack reduction caused by the wing downwash. However, induced drag on wings is a very

significant problem. Approximately 35% of the drag on a typical transport aircraft is lift induced drag (Thomas, 1985; Webber and Dansby, 1983).

Figure 5.12b shows the drag coefficient curves for all cases studied. The drag increment (compared with the HLC drag as the base value at target lift coefficient) for S-rdw case is 11.3% and for L-rdw case is 15.2%. To maintain the target lift coefficient, it was found that an increase of 0.5° in the angle of attack of the wing is required to compensate for the reduction of lift when the add-on device is used.

During the landing phase, the rate of increase in drag is higher than the rate of increase in lift due to the extension of slats and the trailing edge flaps to give the aircraft a lower stall speed so the landing approach can be made at lower speed, which also allows the aircraft to land in a shorter distance. A lower rate of increase in lift compared to drag at landing phase means a lower L/D ratio, as shown in figure 5.12d. It can be said that the add-on devices provide favourable conditions for the landing phase.

Table 5.1
Overall findings of Case 1

Vortex Core Size	Tangential Velocity	Vorticity	Circulation	Lift Coefficient	Drag Coefficient
+557% (factor of 6.57)	-82.9%	-92.6%	-42.8%	-4.9%	+15.2%

‘+’ indicates increase

‘-’ indicates decrease

5.3 CASE 2

Half-span wing model landing configuration for case 2 is as below:

Location of add-on device: as shown in Figure 5.13

Deflection of add-on device: $\alpha_{rdw} = +30^\circ$, $\phi_{rdw} = 0^\circ$

Slat deflection: 15°

Flap deflection: 20°

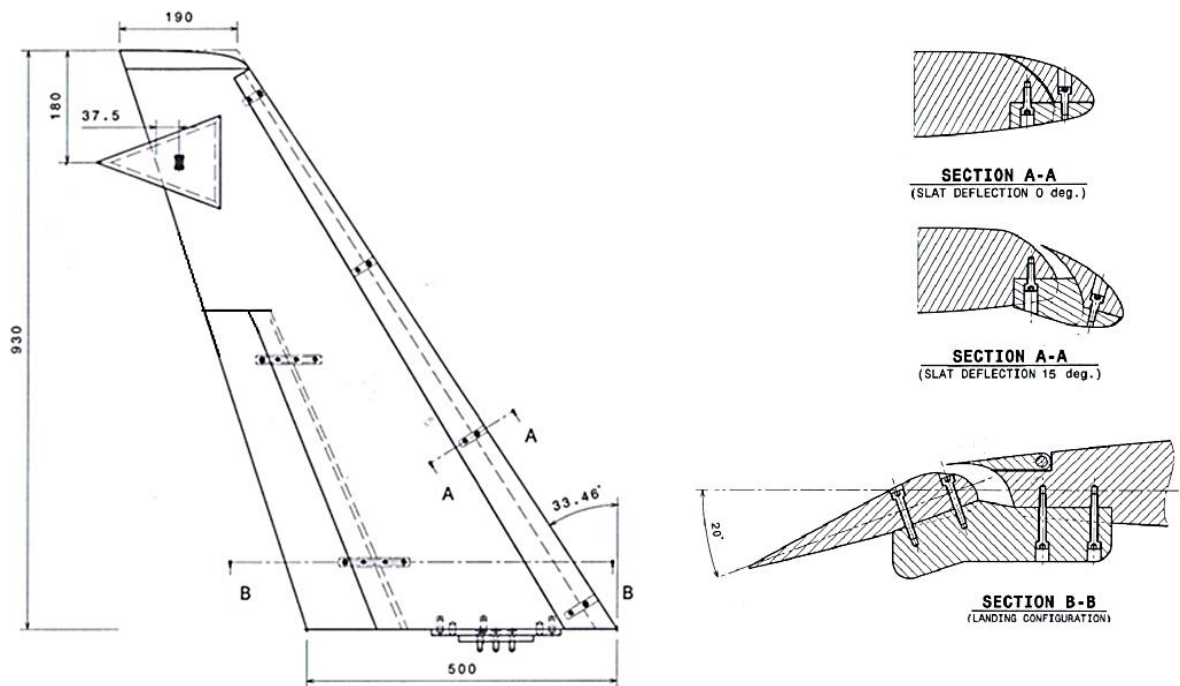


Figure 5.13: Schematic of the half-span wing model with a large reverse delta type add-on device attached. Linear dimensions are in millimetres (mm).

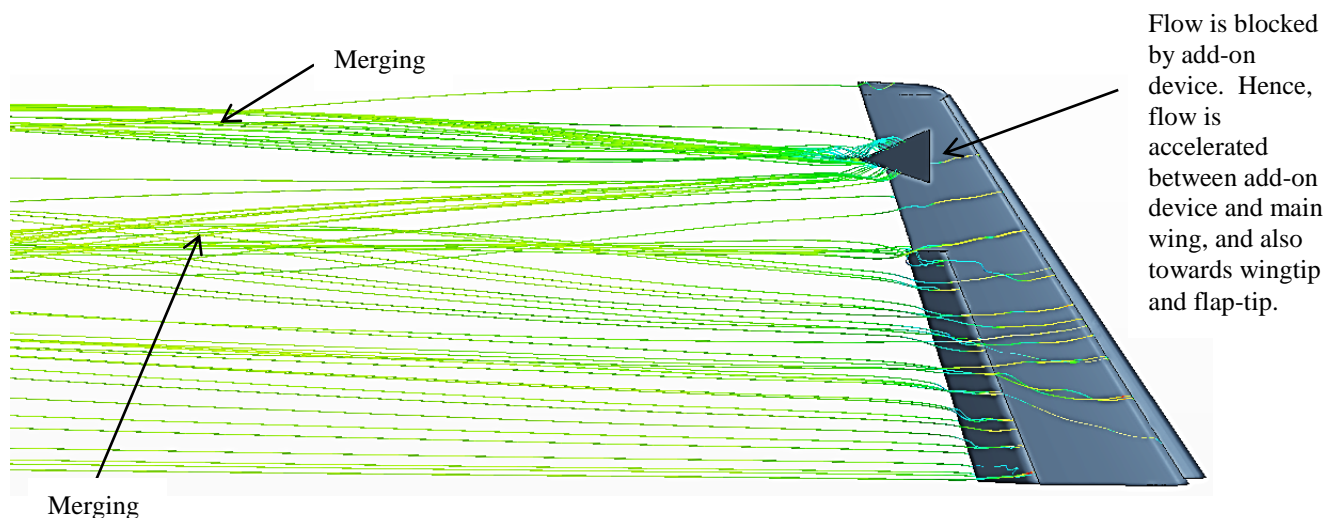


Figure 5.14: Streamlines showing the merging of the wingtip vortex, flap-tip vortex and reverse delta type add-on device vortices downstream. (Courtesy: Haziq Nasir)

5.3.1 Velocity Vectors and Vorticity Contours

The purpose of the above half-span wing model with reverse delta type add-on device configuration is to investigate if the vortices shed by the reverse delta type add-on device will instill a fast growing instability (counter-sign vorticity) into the wingtip vortex and alter the roll-up process of the wingtip vortex. To determine the optimal location of the add-on device on the main wing, the location of the add-on device is varied from case 1. Optimal location of the add-on device is determined by the amount of wake vortex alleviation achieved. The add-on device vortices and the wingtip vortex are hypothesized to merge downstream and instigate significant wake vortex alleviation. Interaction and merging with the flap-tip vortex is also expected, however this case does not study the impact on the flap-tip vortex.

Figures 5.15 to 5.18 show the velocity vectors of a half-span wing model at HLC with/without a reverse delta type add-on device attached at a location midway from the wingtip and flap-tip. The results for HLC without the add-on device at the wingtip are discussed in case 1, however, the results have been reproduced in this section for easier comparison.

Figures 5.15b-c, 5.16b-c, 5.17b-c and 5.18b-c, show the velocity vectors, tangential velocity magnitude and vorticity contours of the vortices of the HLC with an add-on device in place. The resultant vortex core size is seen to be increasing significantly between the downstream planes. This indicates a rapid increase in vortex volume which reduces the tangential velocity rapidly.

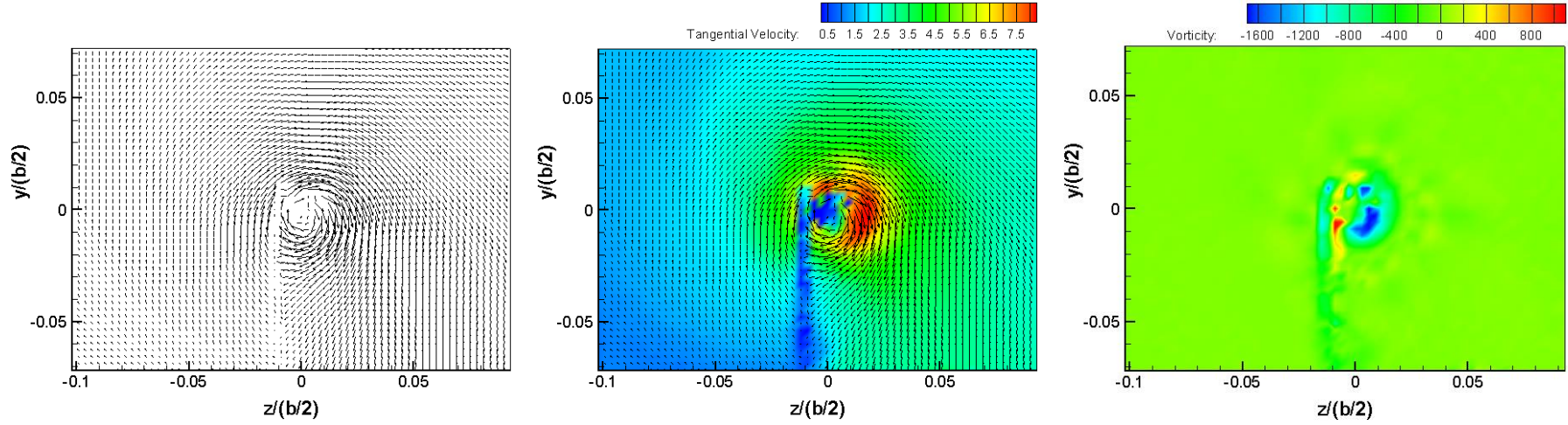
At downstream plane 1, the add-on device cases exhibit higher tangential velocity magnitudes than the HLC case. This happens because the reverse delta type add-on device blocks the flow in its vicinity and the flow is forced to move around the reverse delta type add-on device. The flow moves along the span of the wing towards the wingtip and flap-tip. This accelerates the flow towards the wingtip and flap-tip, causing the existing flow at the

wingtip and flap-tip to also accelerate. Hence, the tangential velocity magnitude at downstream plane 1 is higher for the add-on device cases. At farther downstream planes, the fluid physics are different as co-rotating and counter-rotating vortices (counter-sign vorticity exists), shed by the half-span model wingtip and the reverse delta type add-on device, exist and merge to form a weaker diffused resultant vortex. The tangential velocity reduction between HLC and HLC with the add-on device at downstream plane 2 for the S-rdw case and L-rdw case is 7.7% and 20.6%, respectively. At downstream plane 3, the tangential velocity reduction between HLC and HLC with the add-on device for S-rdw and L-rdw cases is 30.9% and 57.0%, respectively. At downstream plane 4, the tangential velocity reduction between HLC and HLC with the add-on device for S-rdw and L-rdw add-on devices is 54.3% and 79.6%, respectively.

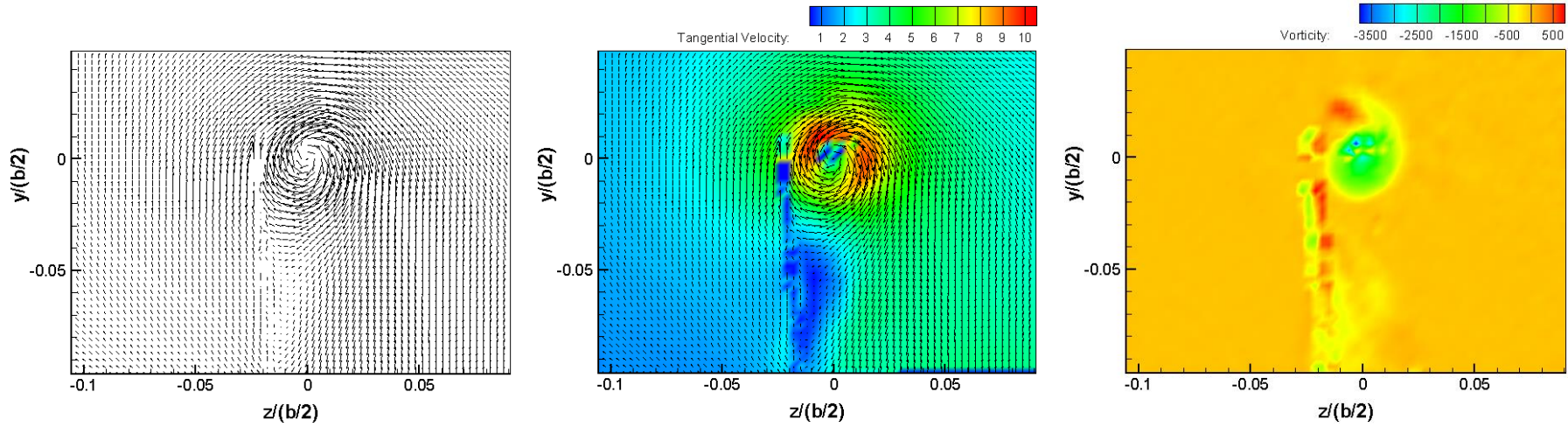
For the HLC with the add-on device, the vorticity is higher than the HLC case at downstream planes 1 and 2. The vorticity reduces rapidly, as shown in figures 5.15b-c, 5.16b-c, 5.17b-c and 5.18b-c. Distinguishable vortex contours within the vortex core can be seen. At downstream planes 1 to 3, it can be noticed that the vortices exhibit uniform spacing of vorticity contours nearly throughout the vortex core. The vortex core size is significantly larger than the HLC case. At downstream plane 4, the resultant vortex core (vorticity core) is mostly broken down and diffused, as shown in figure 5.18c. The vorticity magnitude recorded is much lower than the HLC case. This highlights that there is rapid diffusion of vorticity from the vortex core in to regions outside the vortex core. The resultant vortex core has been significantly weakened and its strength has been reduced. The L-rdw case vortex exhibits lower vorticity magnitudes than the S-rdw case vortex at all four downstream planes. The vorticity reduction from downstream plane 1 to downstream plane 4 for the HLC is 16.6% only. Since, the vorticity magnitudes at downstream planes 1 and 2 exhibited by the resultant vortex are higher than the HLC case, the reduction in vorticity can only be

compared at downstream planes 3 and 4. The vorticity reduction between HLC and HLC with an add-on device at downstream plane 3 for the S-rdw case and L-rdw case is 42.3% and 74.9%, respectively. At downstream plane 4, the vorticity reduction between HLC and HLC with an add-on device for S-rdw case and L-rdw case is 59.0% and 85.6%, respectively.

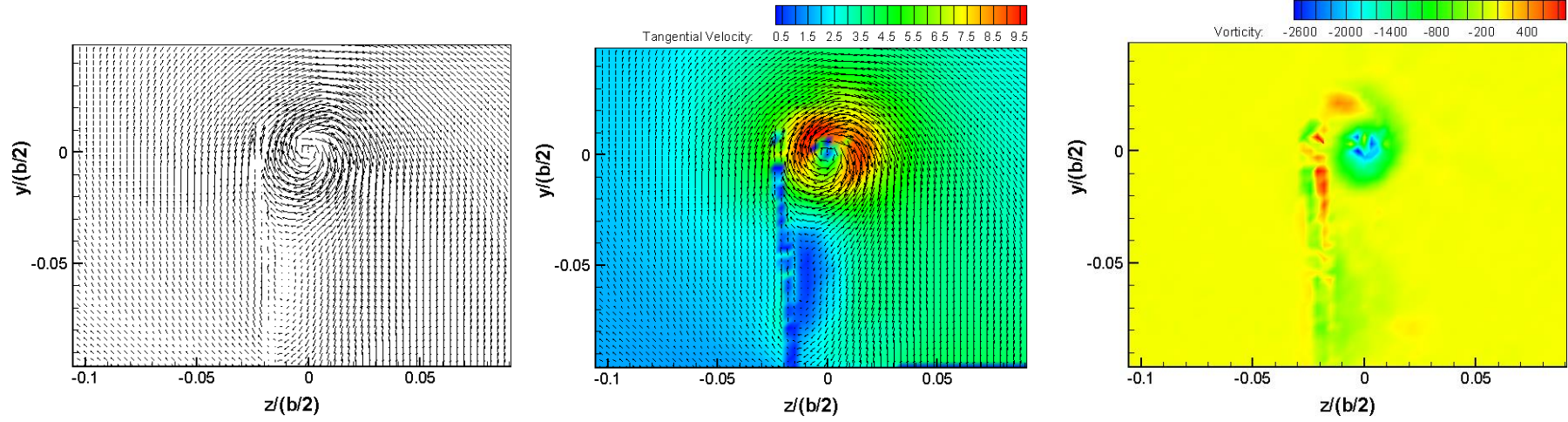
From the above observations, it can be concluded that the diffused resultant vortex is expected to dissipate more rapidly than the HLC wingtip vortex.



a) High Lift Configuration case, $\alpha=7.7^\circ$, $x/(b/2)=0.021$, $V_\infty=12$ m/s.

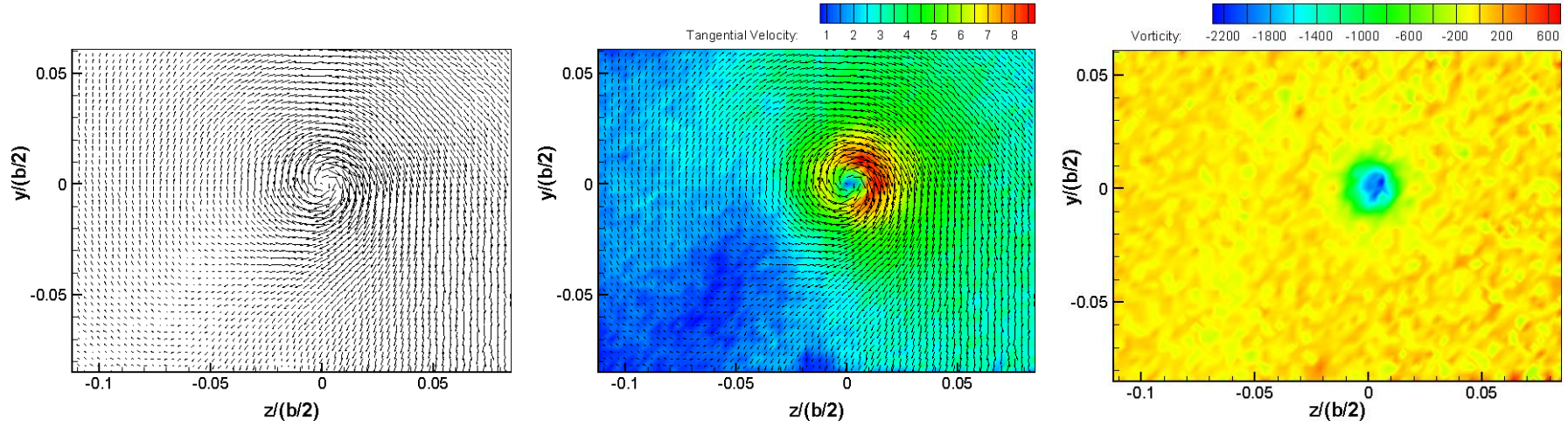


b) High Lift Configuration case, $\alpha=9.7^\circ$; with S-rdw add-on device, $\alpha_{S-rdw}=30^\circ$, $x/(b/2)=0.021$, $V_\infty=12$ m/s.

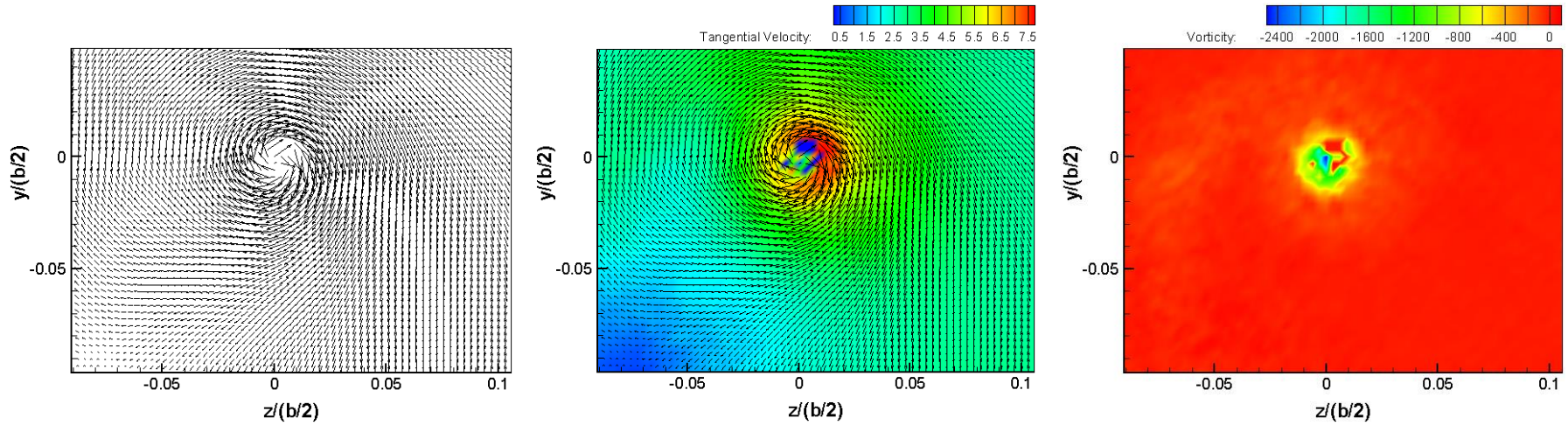


c) High Lift Configuration case, $\alpha=9.7^\circ$; with L-rdw add-on device, $\alpha_{L\text{-rdw}}=30^\circ$, $x/(b/2)=0.021$, $V_\infty=12$ m/s.

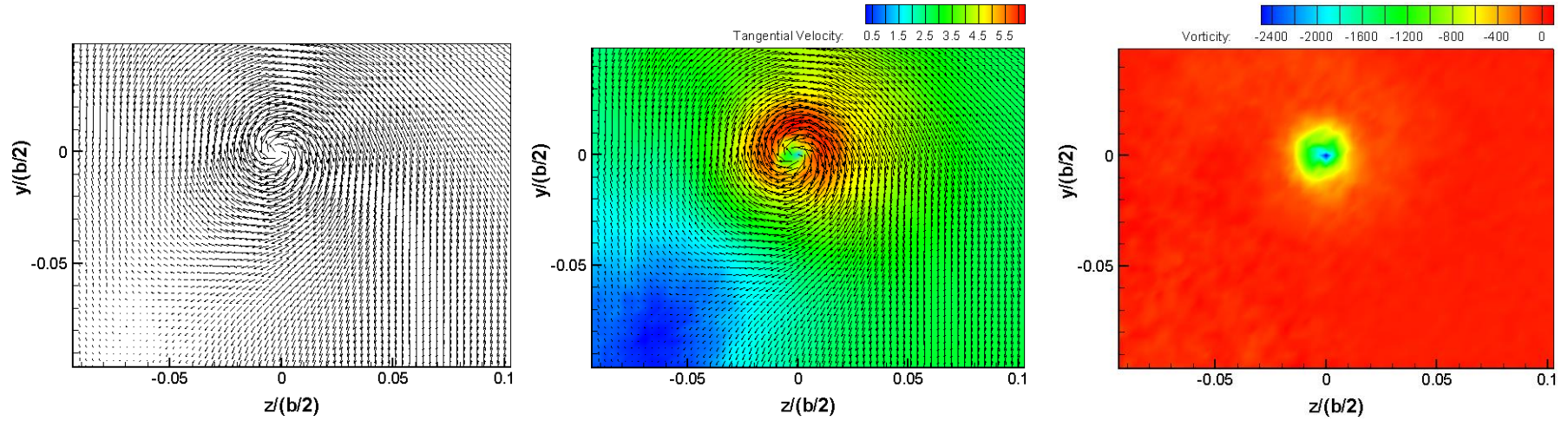
Figure 5.15: Velocity Vectors, Tangential Velocity Magnitude and Vorticity Contours at $x/(b/2)=0.021$ for (a) High Lift Configuration $\alpha=7.7^\circ$, (b) High Lift Configuration $\alpha=9.7^\circ$ with S-rdw add-on device ($\alpha_{S\text{-rdw}}=30^\circ$) and (c) High Lift Configuration $\alpha=9.7^\circ$ with L-rdw add-on device ($\alpha_{L\text{-rdw}}=30^\circ$).



a) High Lift Configuration case, $\alpha=7.7^\circ$, $x/(b/2)=0.548$, $V_\infty=12$ m/s.

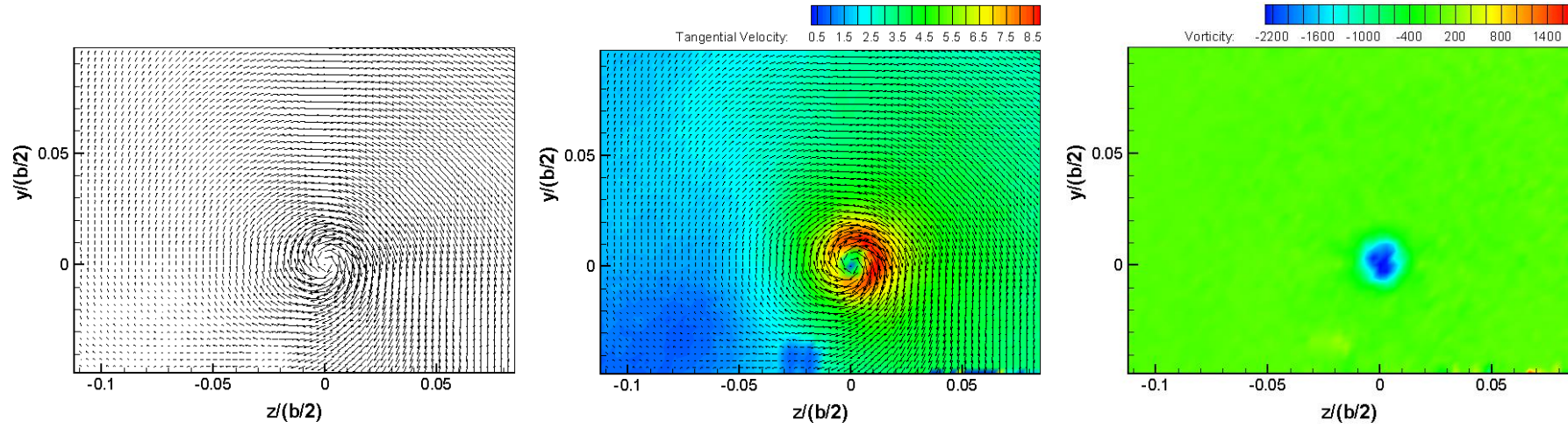


b) High Lift Configuration case, $\alpha=9.7^\circ$; with S-rdw add-on device, $\alpha_{S\text{-rdw}}=30^\circ$, $x/(b/2)=0.548$, $V_\infty=12$ m/s.

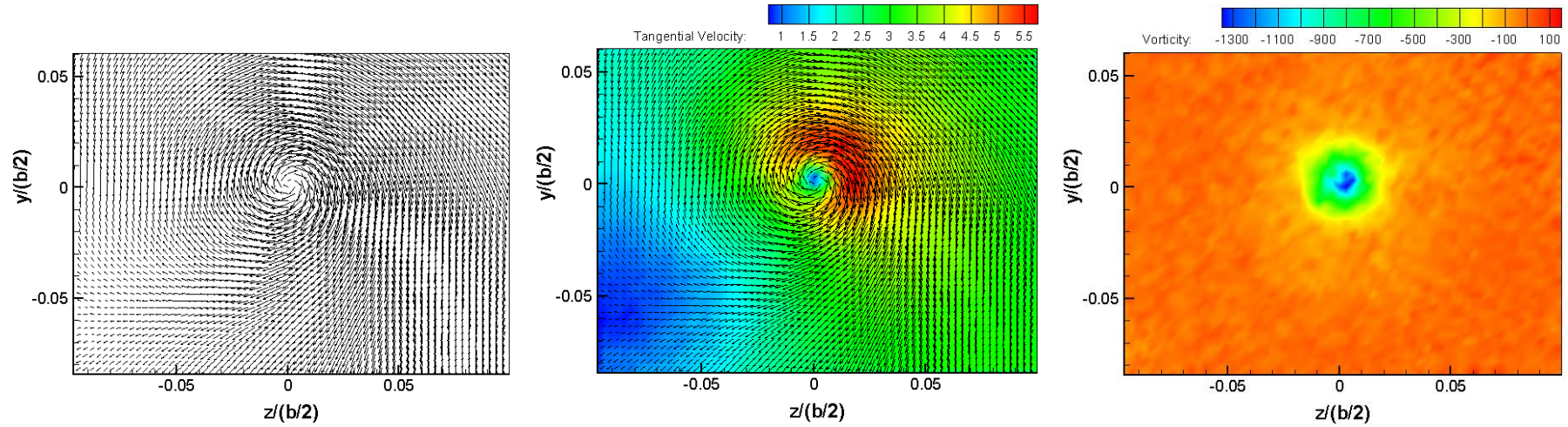


c) High Lift Configuration case, $\alpha=9.7^\circ$; with L-rdw add-on device, $\alpha_{Lrdw}=30^\circ$, $x/(b/2)=0.548$, $V_\infty=12$ m/s.

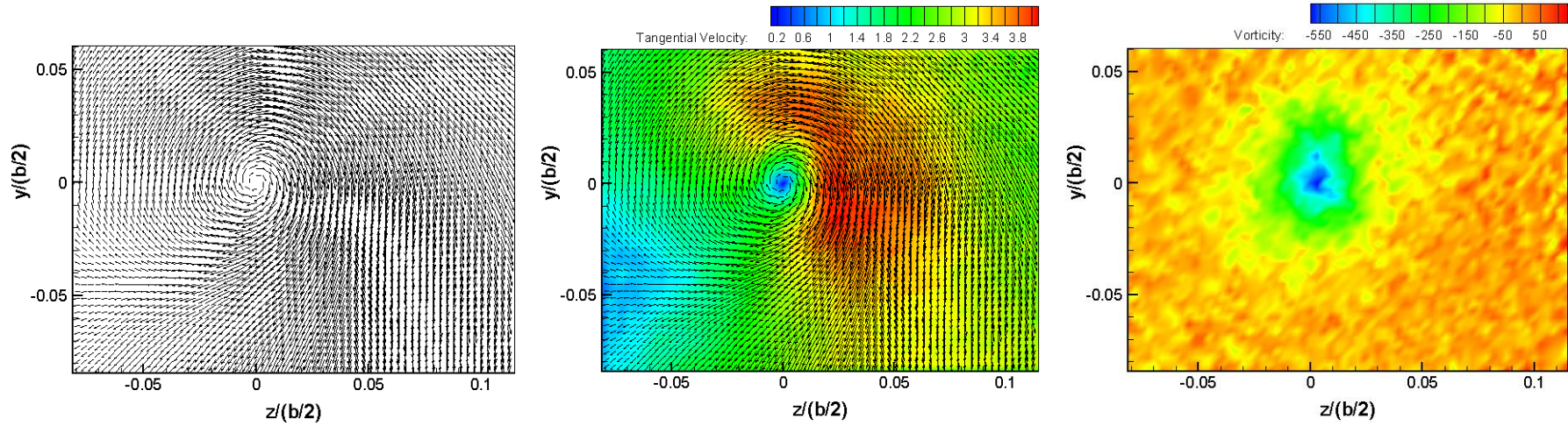
Figure 5.16: Velocity Vectors, Tangential Velocity Magnitude and Vorticity Contours at $x/(b/2)=0.548$ for (a) High Lift Configuration $\alpha=7.7^\circ$, (b) High Lift Configuration $\alpha=9.7^\circ$ with S-rdw add-on device ($\alpha_{S-rdw}=30^\circ$) and (c) High Lift Configuration $\alpha=9.7^\circ$ with L-rdw add-on device ($\alpha_{L-rdw}=30^\circ$).



a) High Lift Configuration case, $\alpha=7.7^\circ$, $x/(b/2)=1.075$, $V_\infty=12$ m/s.

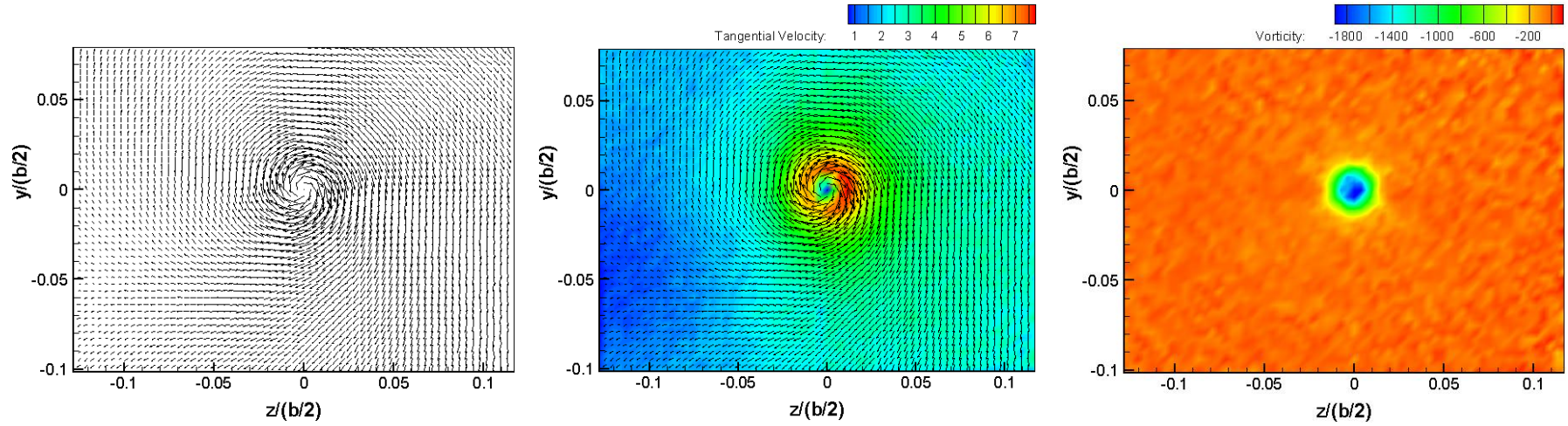


b) High Lift Configuration case, $\alpha=9.7^\circ$; with S-rdw add-on device, $\alpha_{S\text{-rdw}}=30^\circ$, $x/(b/2)=1.075$, $V_\infty=12$ m/s.

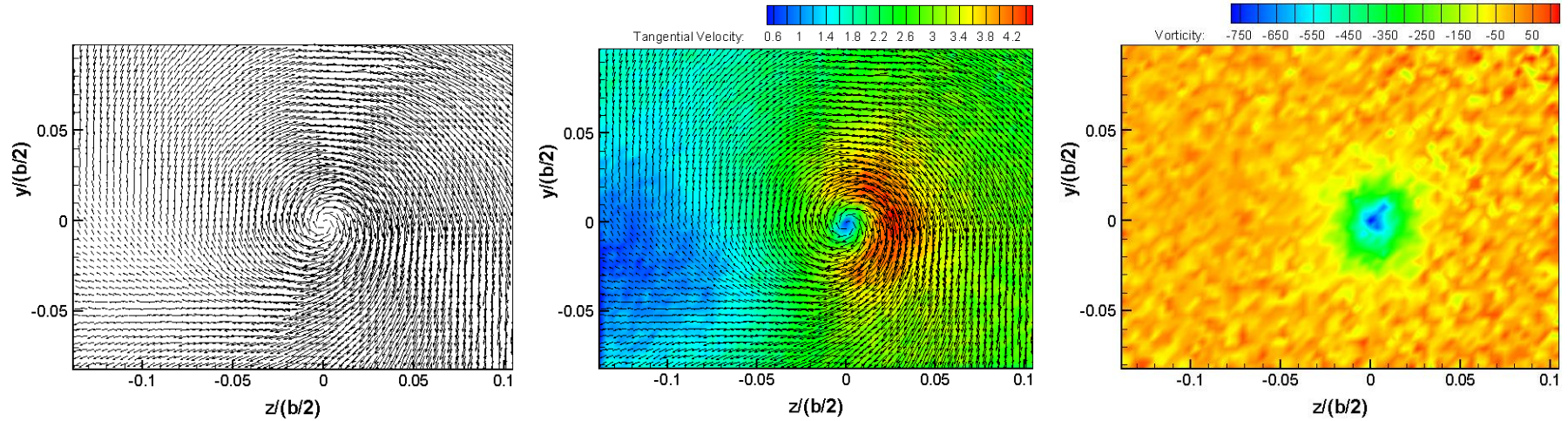


c) High Lift Configuration case, $\alpha=9.7^\circ$; with L-rdw add-on device, $\alpha_{L-rdw}=30^\circ$, $x/(b/2)=1.075$, $V_\infty=12$ m/s.

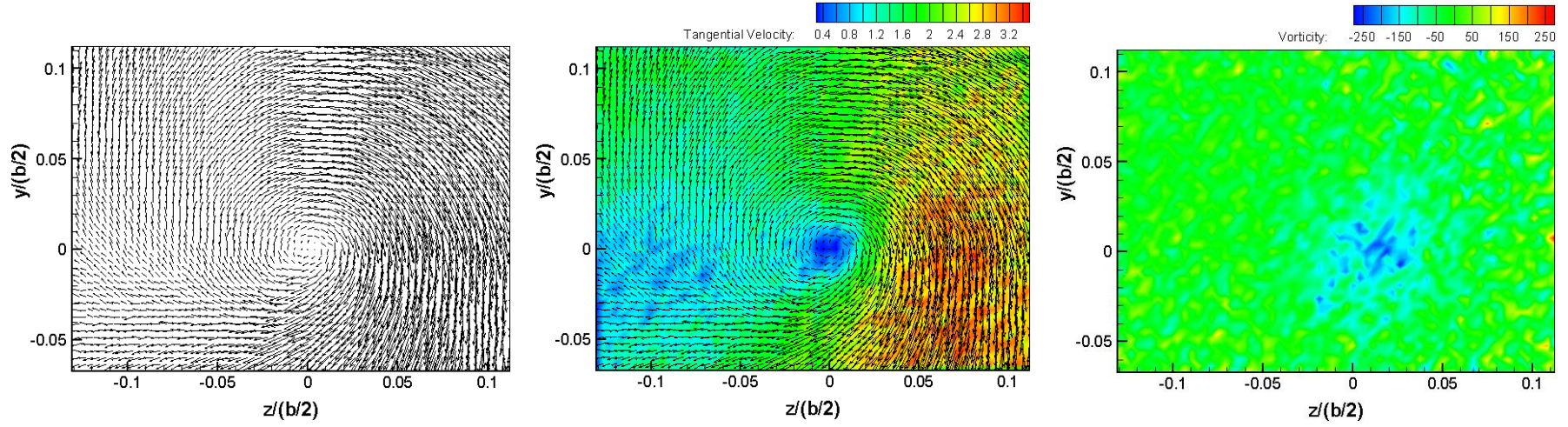
Figure 5.17: Velocity Vectors, Tangential Velocity Magnitude and Vorticity Contours at $x/(b/2)=1.075$ for (a) High Lift Configuration $\alpha=7.7^\circ$, (b) High Lift Configuration $\alpha=9.7^\circ$ with S-rdw add-on device ($\alpha_{S-rdw}=30^\circ$) and (c) High Lift Configuration $\alpha=9.7^\circ$ with L-rdw add-on device ($\alpha_{L-rdw}=30^\circ$).



a) High Lift Configuration case, $\alpha=7.7^\circ$, $x/(b/2)=2.387$, $V_\infty=12$ m/s.



b) High Lift Configuration case, $\alpha=9.7^\circ$; with S-rdw add-on device, $\alpha_{S-rdw}=30^\circ$, $x/(b/2)=2.387$, $V_\infty=12$ m/s.



c) High Lift Configuration case, $\alpha=9.7^\circ$; with L-rdw add-on device, $\alpha_{L\text{-rdw}}=30^\circ$, $x/(b/2)=2.387$, $V_\infty=12$ m/s.

Figure 5.18: Velocity Vectors, Tangential Velocity Magnitude and Vorticity Contours at $x/(b/2)=2.387$ for (a) High Lift Configuration $\alpha=7.7^\circ$, (b) High Lift Configuration $\alpha=9.7^\circ$ with S-rdw add-on device ($\alpha_{S\text{-rdw}}=30^\circ$) and (c) High Lift Configuration $\alpha=9.7^\circ$ with L-rdw add-on device ($\alpha_{L\text{-rdw}}=30^\circ$).

5.3.2 Tangential Velocity

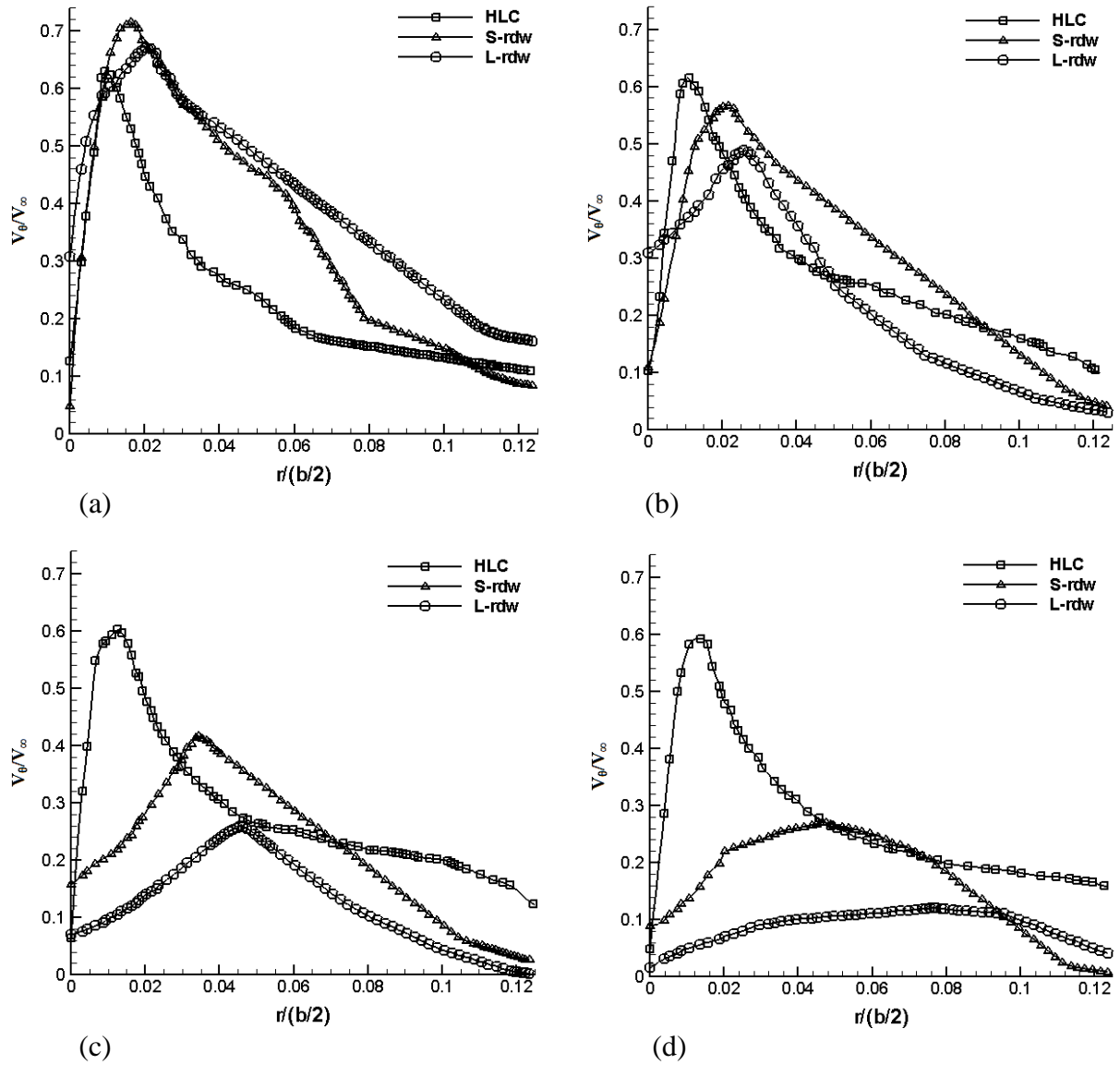


Figure 5.19: Non-dimensional tangential velocity distributions of HLC, HLC with S-rdw and HLC with L-rdw at (a) $x/(b/2)=0.021$, (b) $x/(b/2)=0.548$, (c) $x/(b/2)=1.075$ and (d) $x/(b/2)=2.387$.

Figures 5.19a-d show the tangential velocity distributions of HLC, HLC with S-rdw and HLC with L-rdw at downstream planes $x/(b/2) = 0.021, 0.548, 1.075$ and 2.387 . Figure 5.19a shows that the tangential velocity magnitude for the HLC case is lower than the tangential velocity magnitude for the add-on device cases. This is in agreement with figures 5.15a-c. From figures 5.19b-d, the HLC case exhibits higher tangential velocity magnitude than the S-rdw and L-rdw cases. The tangential velocity magnitude for the HLC with the add-

on device cases decreases rapidly from $x/(b/2)=0.548$ to $x/(b/2)=2.387$.

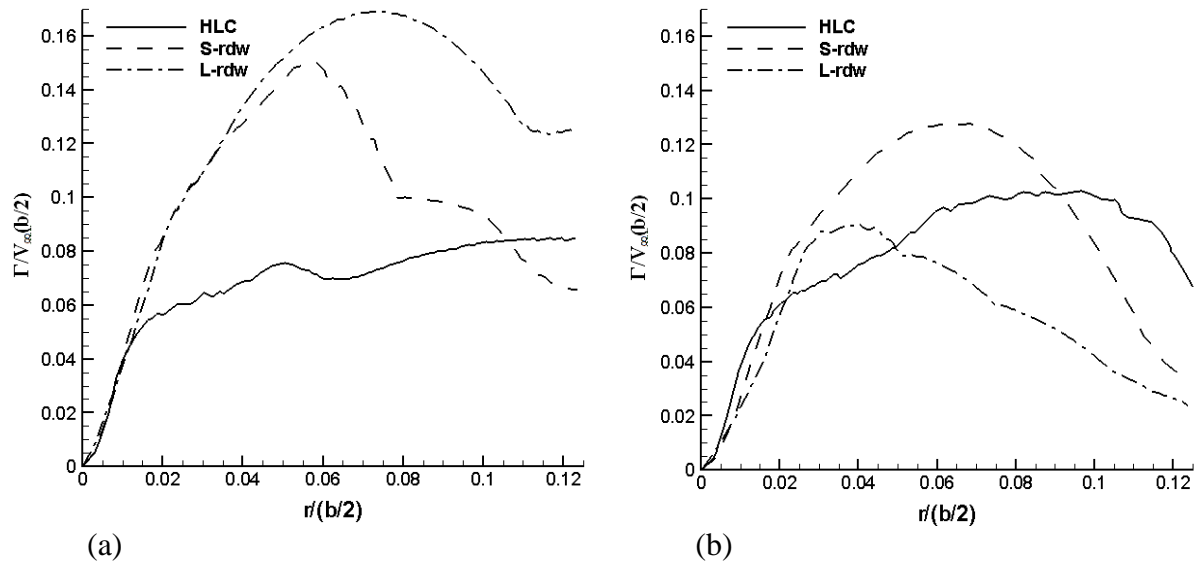
The HLC vortex core radius is much smaller compared to the HLC with the add-on device resultant vortex core radius at all four downstream locations. The difference in the sizes of the vortex cores is evident from the tangential velocity distributions. At $x/(b/2)=0.021$, the resultant vortex core radius (when add-on device is used) compared to the HLC vortex core radius has diffused (enlarged) by a factor of 1.72 and 2.23 for the S-rdw and L-rdw, respectively. At $x/(b/2)=0.548$, the resultant vortex core radius has increased by a factor of 1.93 and 2.31 for the S-rdw and L-rdw, respectively. At $x/(b/2)=1.075$, the resultant vortex core radius has increased by a factor of 2.72 and 3.62 for the S-rdw and L-rdw, respectively. At $x/(b/2)=2.387$, the resultant vortex core radius has increased by a factor of 3.39 and 5.63 for the S-rdw and L-rdw, respectively. This implies that when the L-rdw is used, the resultant core radius size is 5.63 times more than the core radius of the HLC case. For HLC with S-rdw, the growth rate of the resultant vortex from plane 1 to 2 is 31.3%, from plane 2 to 3 is 61.9% and from plane 3 to 4 is 35.3%. For HLC with L-rdw, the growth rate of the resultant vortex from plane 1 to 2 is 21.7%, from plane 2 to 3 is 79.4% and from plane 3 to 4 is 69.2%. This indicates that the growth rate of the resultant vortex is larger than that of the wingtip vortex.

5.3.3 Circulation

Figures 5.20a-d shows the circulation distributions for the HLC, HLC with S-rdw and HLC with L-rdw. The HLC with the reverse delta type add-on device shows that the circulation of the resultant vortex decreases steadily from downstream plane 1 to 4. At downstream planes 1 and 2, the circulation magnitude of the resultant vortex is higher than the HLC vortex because the tangential velocity and vorticity magnitudes are higher, as shown in figures 5.20a and 5.20b. For the S-rdw and L-rdw cases, the circulation magnitude decreases significantly

as counter-sign vorticity is injected in to the wingtip vortex by the add-on device. At $x/(b/2)=1.075$, the circulation magnitude for S-rdw case and L-rdw case has decreased by 14.4% and 39.6%, respectively. At $x/(b/2)=2.387$, the circulation magnitude of the S-rdw case and L-rdw case has further decreased by 20.6% and 48.7%, respectively. There is significant decrease in the circulation magnitude from downstream plane 1 to downstream plane 4 for the S-rdw and L-rdw cases and thus, it can be said that for these cases significant vortex decay has taken place as the resultant vortex core (vorticity core) has started to deform (figure 5.18b) and broken into many small vorticity patches (figure 5.18c). It is expected that farther downstream, the circulation magnitude will continue to decrease and eventually become insignificant. From the circulation distributions trend, the L-rdw case resultant vortex is likely to decay more rapidly, followed by the S-rdw and HLC cases, respectively.

It can be concluded that the reverse delta type add-on device is capable of alleviating wake vortex significantly. From figures 5.20a-d, it can be concluded that the enlarged resultant vortex is weaker in strength and is expected to dissipate more rapidly than the HLC wingtip vortex.



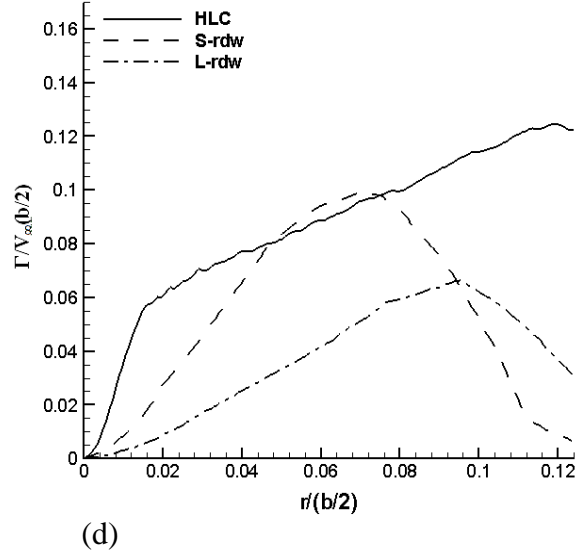
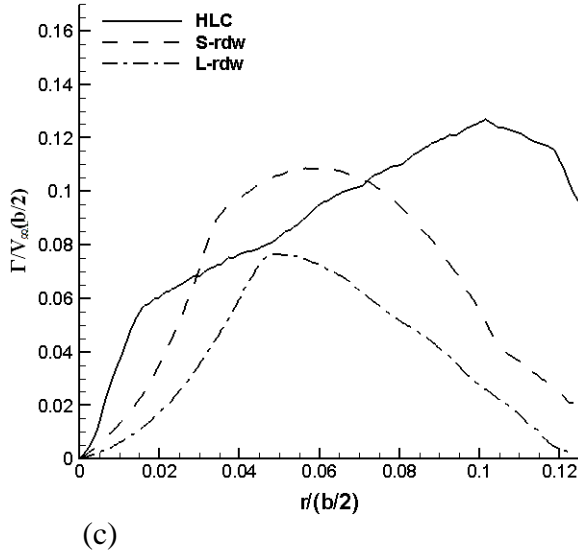
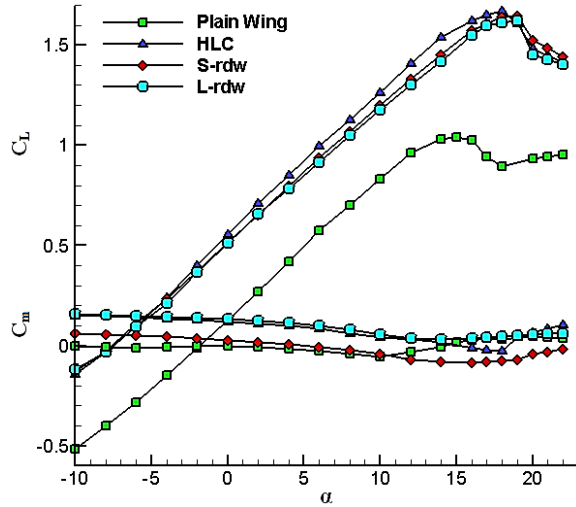
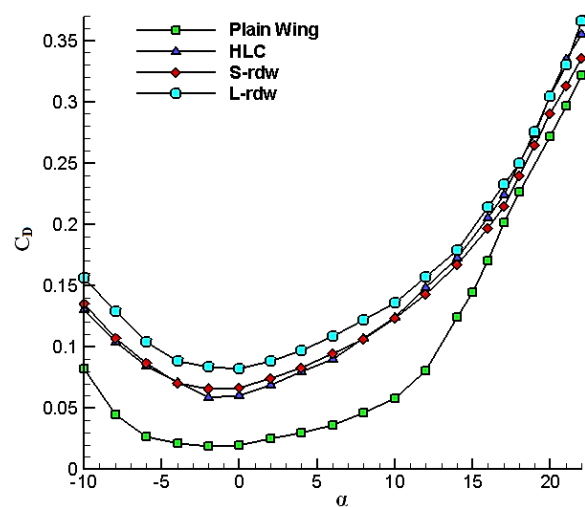


Figure 5.20: Vortex strength $\Gamma/V_\infty(b/2)$ versus radius $r/(b/2)$ of wingtip vortex of HLC, HLC with S-rdw and HLC with L-rdw at (a) $x/(b/2)=0.021$, (b) $x/(b/2)=0.548$, (c) $x/(b/2)=1.075$ and (d) $x/(b/2)=2.387$.

5.3.4 Aerodynamic Performance



(a) C_L vs α and C_m vs α



(b) C_D vs α

The trend of figure 5.21 is similar to figure 5.12 (case 1) and case 2 configuration stalls at the same angle of attack as in case 1. The reduction in the lift coefficient values between the HLC, S-rdw and L-rdw cases is 2.9%. The drag increment (compared with the HLC drag as the base value at target lift coefficient) for S-rdw case is 6.9% and for L-rdw case is 14.5%. To maintain the target lift coefficient, it was found that an increase of 1.0° in the

angle of attack of the wing is required to compensate for the reduction of lift when the add-on device is used.

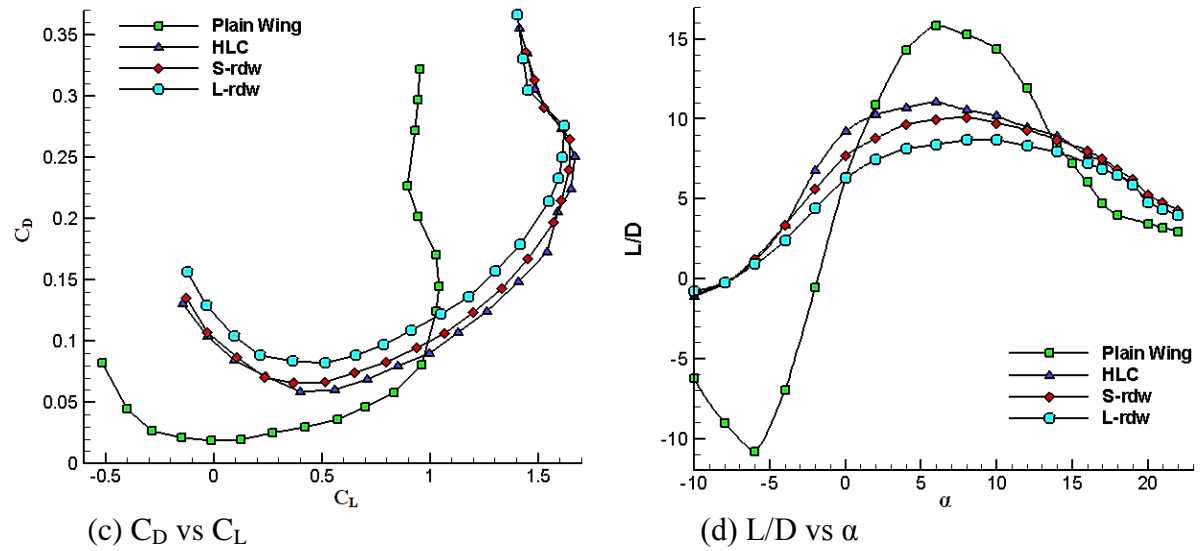


Figure 5.21: Aerodynamic performance of the Plain Wing, HLC, HLC with S-rdw and HLC with L-rdw.

Table 5.2
Overall findings of Case 2

Vortex Core Size	Tangential Velocity	Vorticity	Circulation	Lift Coefficient	Drag Coefficient
+463% (factor of 5.63)	-79.6%	-85.6%	-48.7%	-2.9%	+14.5%

‘+’ indicates increase

‘-’ indicates decrease

5.4 CASE 3

Half-span wing model landing configuration for case 3 is as below:

Location of add-on device: as shown in Figure 5.22

Deflection of add-on device: $\alpha_{rdw} = +30^\circ$, $\phi_{rdw} = 0^\circ$

Slat deflection: 15°

Flap deflection: 20°

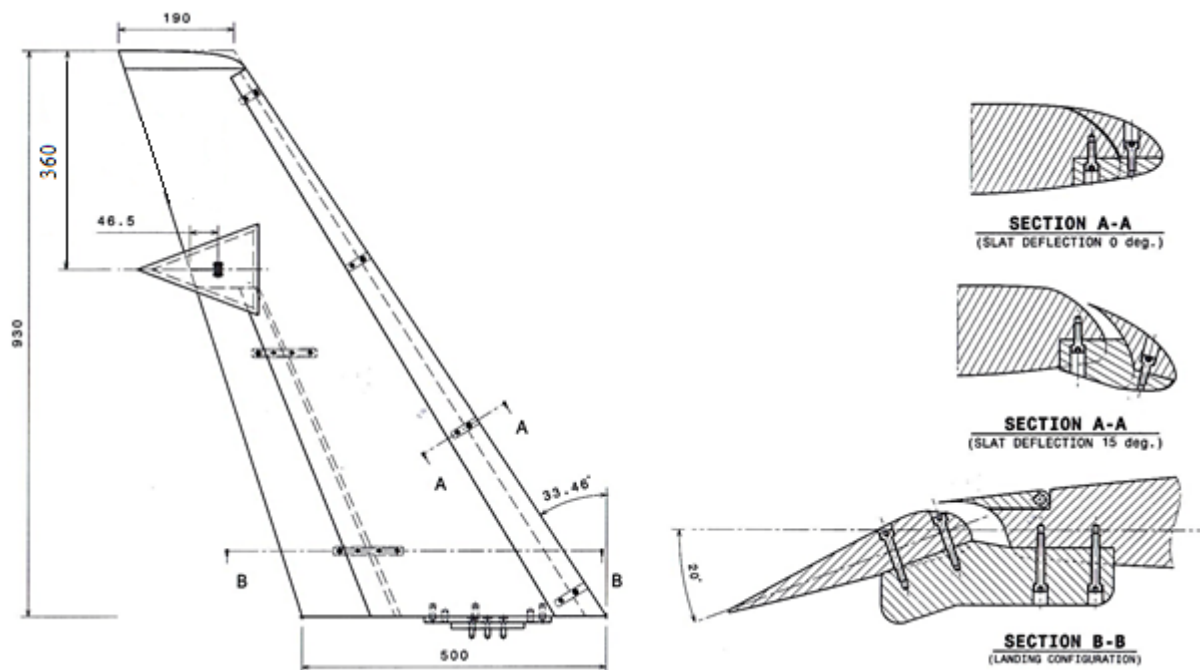


Figure 5.22: Schematic of the half-span wing model with a large reverse delta type add-on device attached. Linear dimensions are in millimetres (mm).

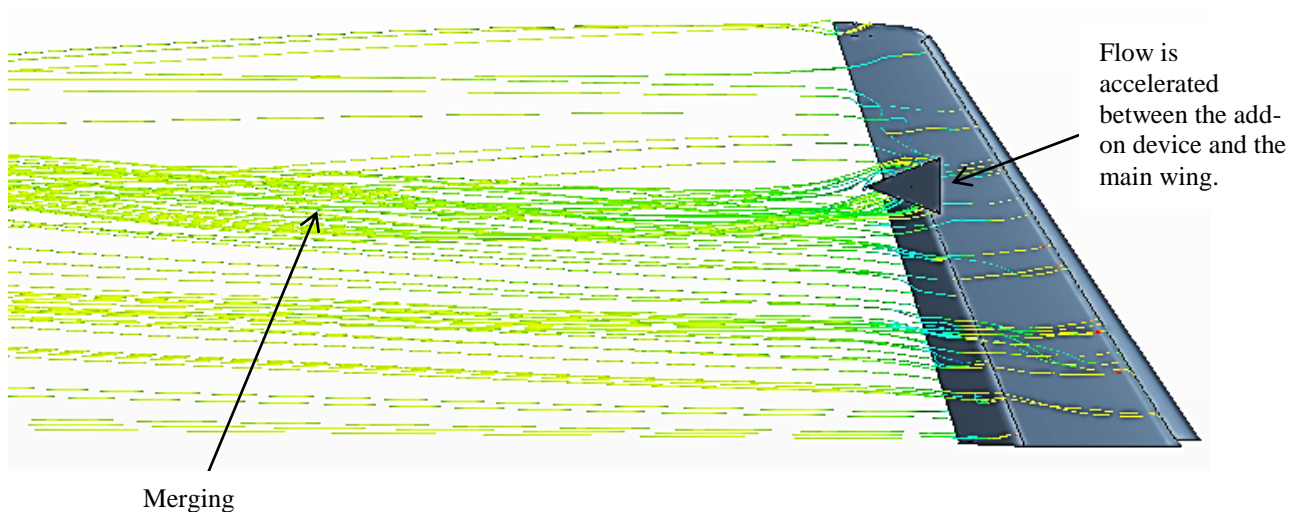


Figure 5.23: Streamlines showing the merging of the flap-tip vortex and the reverse delta type add-on device vortices. (Courtesy: Haziq Nasir)

5.4.1 Velocity Vectors and Vorticity Contours

The purpose of the above half-span wing model with reverse delta type add-on device configuration is to investigate if the vortices shed by the reverse delta type add-on device will introduce a fast growing instability (counter-sign vorticity) into the flap-tip vortex and alter the roll-up process of the flap-tip vortex. The add-on device vortices and the flap-tip vortex are hypothesized to merge downstream and instigate significant wake vortex alleviation.

Figures 5.24 to 5.27 show the velocity vectors of a half-span wing model at HLC with/without a reverse delta type add-on device attached at a location near the half-span model outboard flap-tip.

Figures 5.24a, 5.25a, 5.26a and 5.27a show the velocity vectors, tangential velocity magnitude and vorticity contours of the HLC flap-tip vortex. It is observable that the flap-tip vortex is not very strong. The flap being used is a small single element flap and flap deflection is set to $\delta=20^\circ$. A flap deflection of $\delta=20^\circ$ will yield a weaker vortex than a flap deflection of $\delta=40^\circ$ as less pressure differential exists. The half-span wing model was fabricated with only one flap and slat setting; identical to the landing configuration of airplanes. Therefore, it was not possible to expand the research study by varying flap and slat deflections. It is clearly noticeable that the flap-tip vortex is well rolled up at downstream plane $x/(b/2)=0.548$ but the vortex rollup is weaker (less coherent vortex) at farther downstream planes.

The flap-tip vortex of the HLC without the add-on device exhibits a better rollup than the HLC with the add-on device, as shown in figures 5.25a, 5.26a and 5.27a. The flap-tip vortex of the HLC has diffused (enlarged) from $x/(b/2)=0.548$ to $x/(b/2)=1.075$ by 12.1% and from $x/(b/2)=1.075$ to $x/(b/2)=2.387$ by 20.8%. Whereas, the growth rate of the wingtip from $x/(b/2)=0.548$ to $x/(b/2)=1.075$ is 5.22% and from $x/(b/2)=1.075$ to $x/(b/2)=2.387$ is 5.62%. The increase in flap-tip vortex core radius within 2 half-span lengths is significantly high.

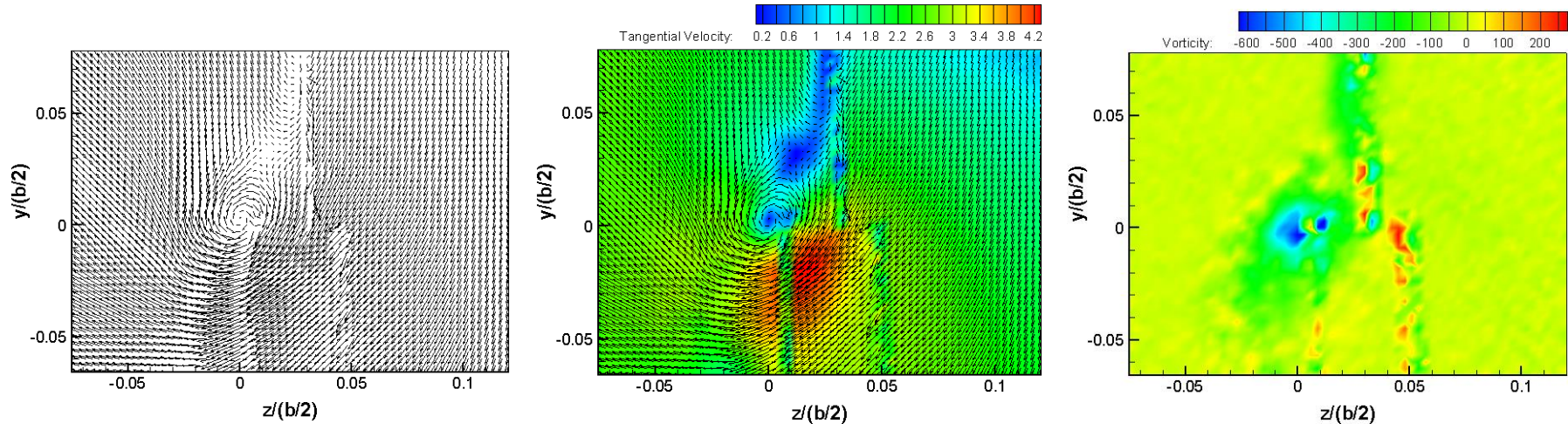
This indicates that the flap-tip vortex of the HLC is not as strong as the wingtip vortex. The flap-tip has significantly diffused with respect to the wingtip vortex without any instabilities being introduced.

When the reverse delta type add-on device is used, as shown in figures 5.25b-c, 5.26b-c and 5.27b-c, the vortex core radius is found to have diffused more than the HLC case. At $x/(b/2)=0.548$, the resultant vortex core radius compared to the flap-tip vortex core radius of the HLC has increased by a factor of 1.25 and 1.32 for the S-rdw case and L-rdw case, respectively. At $x/(b/2)=1.075$, the resultant vortex core radius compared to the flap-tip vortex core radius of the HLC has increased by a factor of 1.23 and 1.37 for the S-rdw case and L-rdw case, respectively. At $x/(b/2)=2.387$, the resultant vortex core radius compared to the flap-tip vortex core radius of the HLC has increased by 1.20 and 1.33 for the S-rdw case and L-rdw case, respectively. The above results suggest that the weak flap-tip vortex of the HLC is diffusing significantly. When an add-on device is used, the resultant vortex core size increases significantly more than the HLC flap-tip vortex. The significant increase in resultant vortex core radius indicates that it will diffuse rapidly farther downstream.

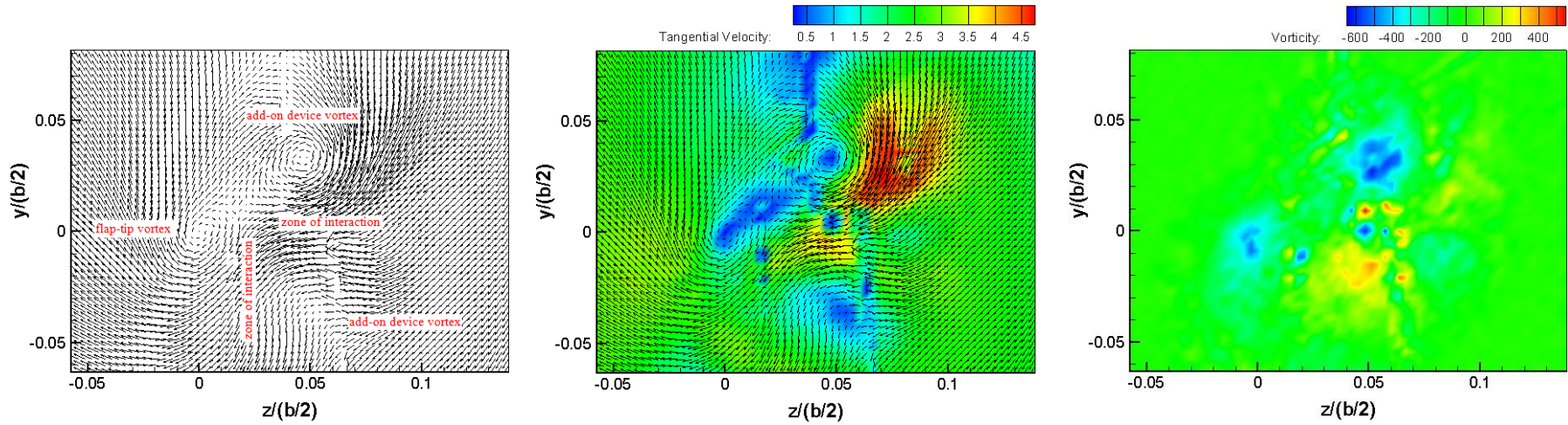
When a reverse delta type add-on device is used, as shown in figures 5.25b-c, 5.26b-c and 5.27b-c, the tangential velocity magnitude of the resultant vortex is seen to decrease slightly with respect to the HLC flap-tip vortex. It can be said that the add-on device introduces secondary vorticity (counter-sign vorticity) into the flap-tip vortex causing the resultant vortex to become less coherent (weaker). The weaker resultant vortex is expected to diffuse more rapidly farther downstream.

For all investigated cases, the vorticity decreased gradually from a maximum at the centre to nearly zero at the outer region of the vortices. At $x/(b/2)=0.021$, closer vorticity contours at the centre of the vortex are recorded, as shown in figures 5.24a-c. It can be noticed that the vortex cores are distinguishable. At $x/(b/2)=0.548$, the vortex core for the

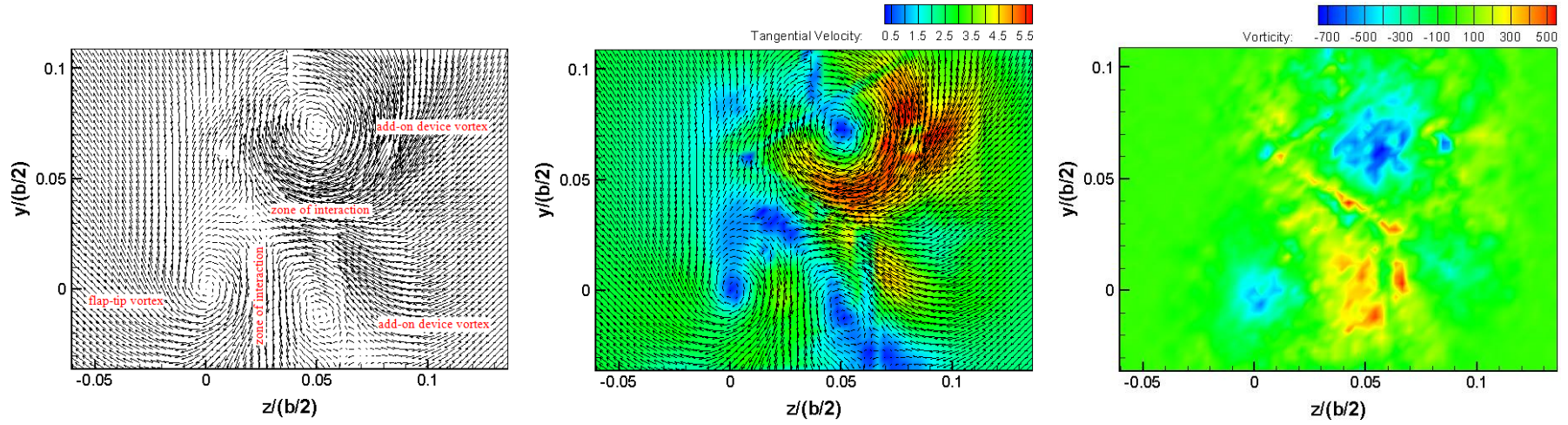
HLC only is distinguishable (figure 5.25a), whereas the vorticity contours for the add-on device cases (figures 5.25b-c) are broken into small vorticity patches. These small patches of vorticity have high individual vorticity magnitudes but they do not pose a hazard as they are too tiny to cause any significant circulation of the entire vortex core. At farther downstream locations, the tiny vorticity patches increase in number for the add-on device cases. This suggests that the resultant vortex core has mostly broken down. The breakdown of the resultant vortex core creates a weaker and more diffused/scattered/distributed vortex. Hazard from such vortices is minimal. For the HLC, the vortex core is only largely diffused at $x/(b/2) = 2.387$. Thus, it can be said that when the add-on device is used, the resultant vortex formed breaks down rapidly due to secondary vorticity introduced into the vortex. The weak resultant vortex diffuses significantly more than the HLC case.



a) High Lift Configuration case, $\alpha=7.7^\circ$, $x/(b/2)=0.021$, $V_\infty=12$ m/s.

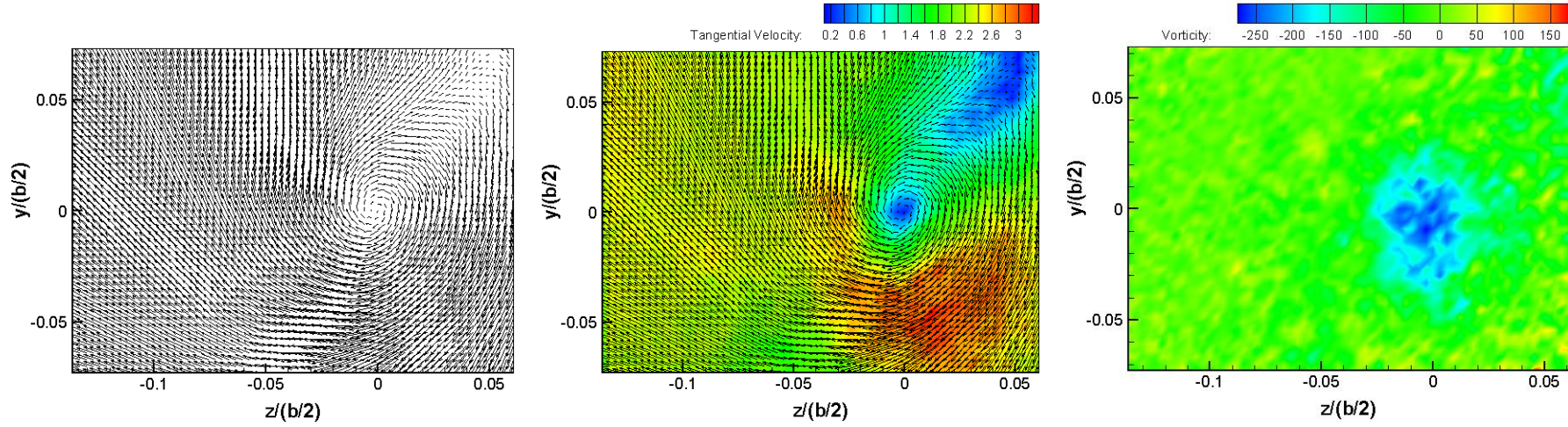


b) High Lift Configuration case, $\alpha=9.7^\circ$; with S-rdw add-on device, $\alpha_{S-rdw}=30^\circ$, $x/(b/2)=0.021$, $V_\infty=12$ m/s.

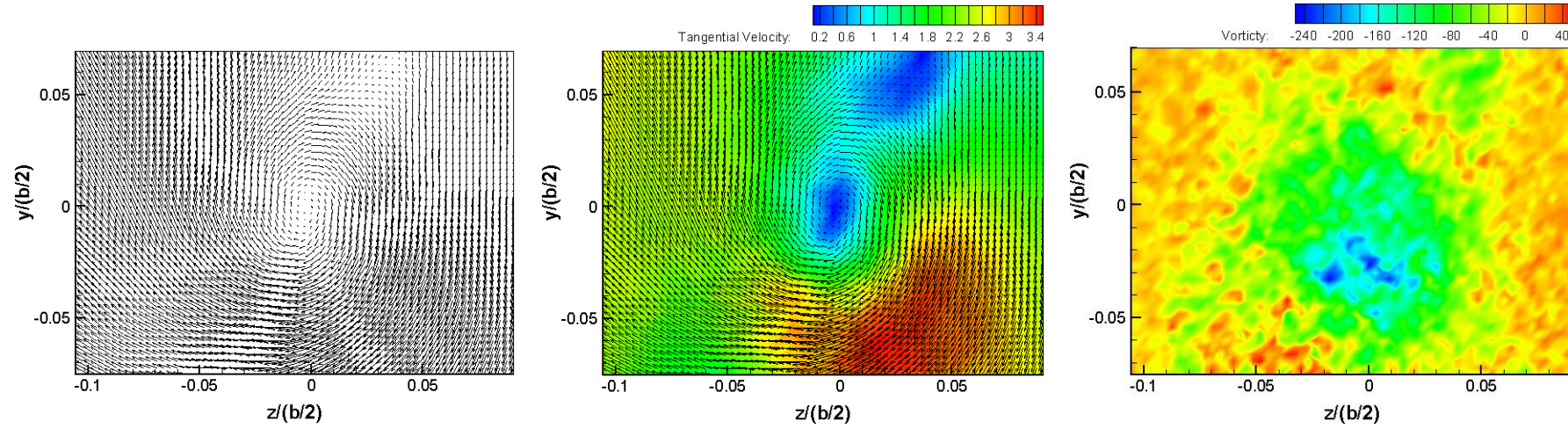


c) High Lift Configuration case, $\alpha=9.7^\circ$; with L-rdw add-on device, $\alpha_{L-rdw}=30^\circ$, $x/(b/2)=0.021$, $V_\infty=12$ m/s.

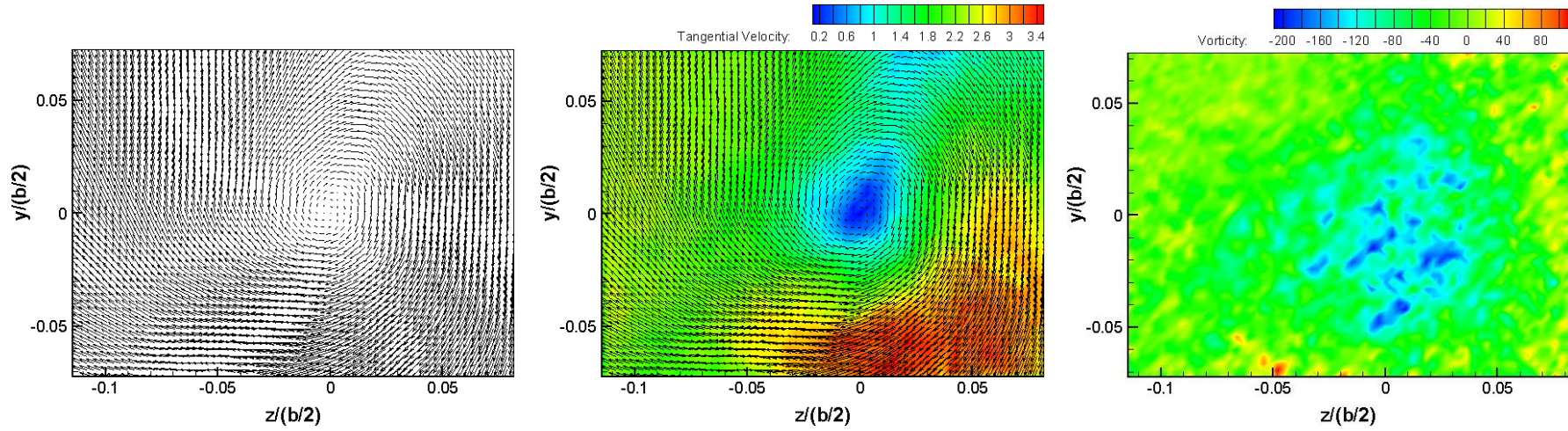
Figure 5.24: Velocity Vectors, Tangential Velocity Magnitude and Vorticity Contours at $x/(b/2)=0.021$ for (a) High Lift Configuration $\alpha=7.7^\circ$, (b) High Lift Configuration $\alpha=9.7^\circ$ with S-rdw add-on device ($\alpha_{S-rdw}=30^\circ$) and (c) High Lift Configuration $\alpha=9.7^\circ$ with L-rdw add-on device ($\alpha_{L-rdw}=30^\circ$).



a) High Lift Configuration case, $\alpha=7.7^\circ$, $x/(b/2)=0.548$, $V_\infty=12$ m/s.

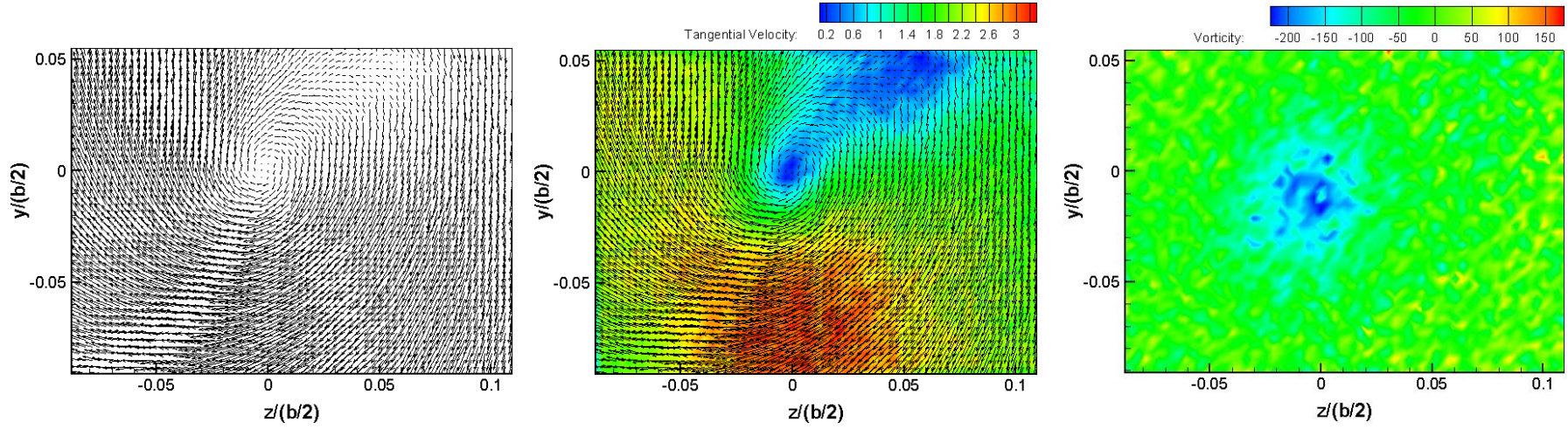


b) High Lift Configuration case, $\alpha=9.7^\circ$; with S-rdw add-on device, $\alpha_{S-rdw}=30^\circ$, $x/(b/2)=0.548$, $V_\infty=12$ m/s.

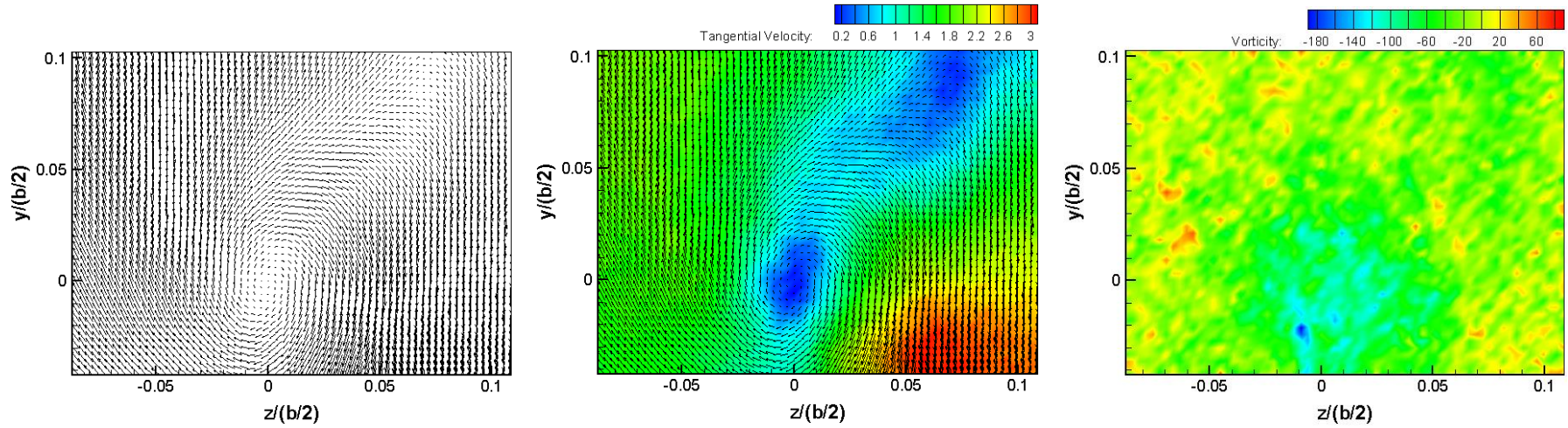


c) High Lift Configuration case, $\alpha=9.7^\circ$; with L-rdw add-on device, $\alpha_{Lrdw}=30^\circ$, $x/(b/2)=0.548$, $V_\infty=12$ m/s.

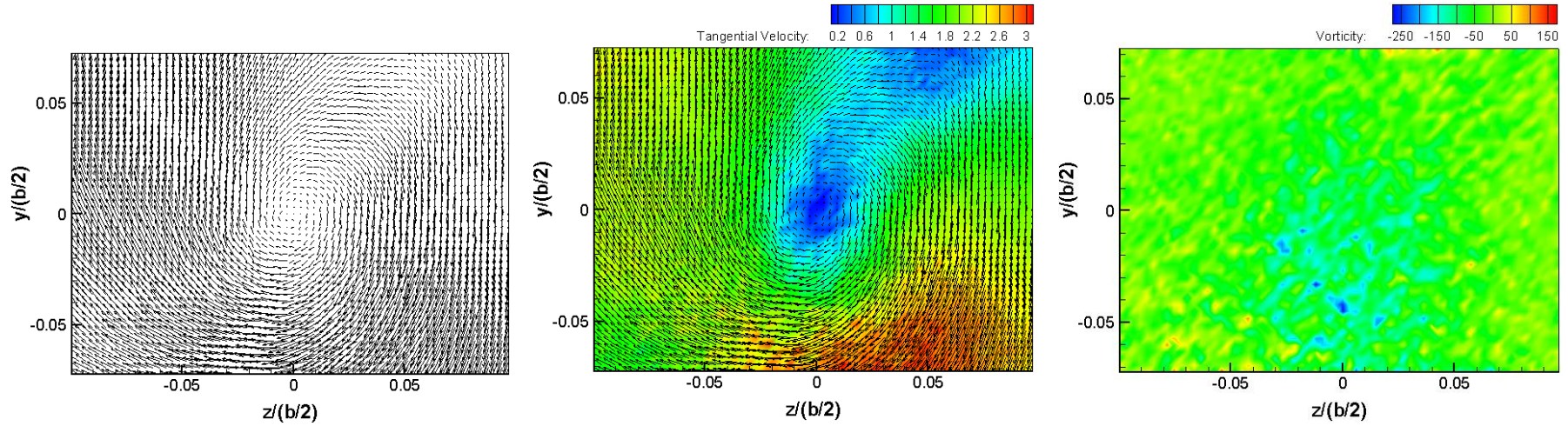
Figure 5.25: Velocity Vectors, Tangential Velocity Magnitude and Vorticity Contours at $x/(b/2)=0.548$ for (a) High Lift Configuration $\alpha=7.7^\circ$, (b) High Lift Configuration $\alpha=9.7^\circ$ with S-rdw add-on device ($\alpha_{S-rdw}=30^\circ$) and (c) High Lift Configuration $\alpha=9.7^\circ$ with L-rdw add-on device ($\alpha_{L-rdw}=30^\circ$).



a) High Lift Configuration case, $\alpha=7.7^\circ$, $x/(b/2)=1.075$, $V_\infty=12$ m/s.

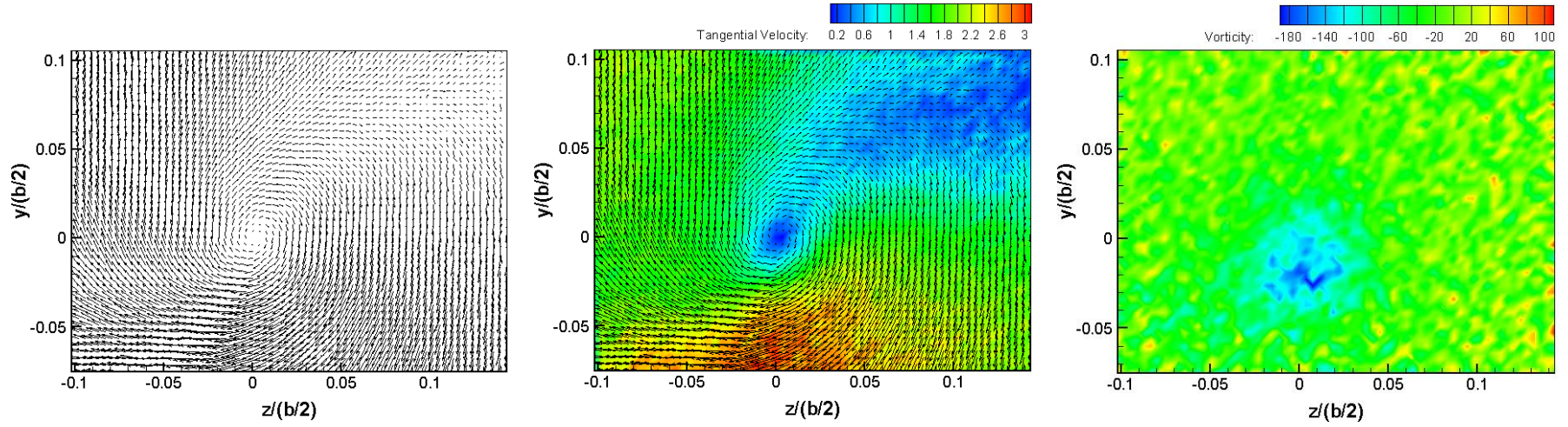


b) High Lift Configuration case, $\alpha=9.7^\circ$; with S-rdw add-on device, $\alpha_{S\text{-rdw}}=30^\circ$, $x/(b/2)=1.075$, $V_\infty=12$ m/s.

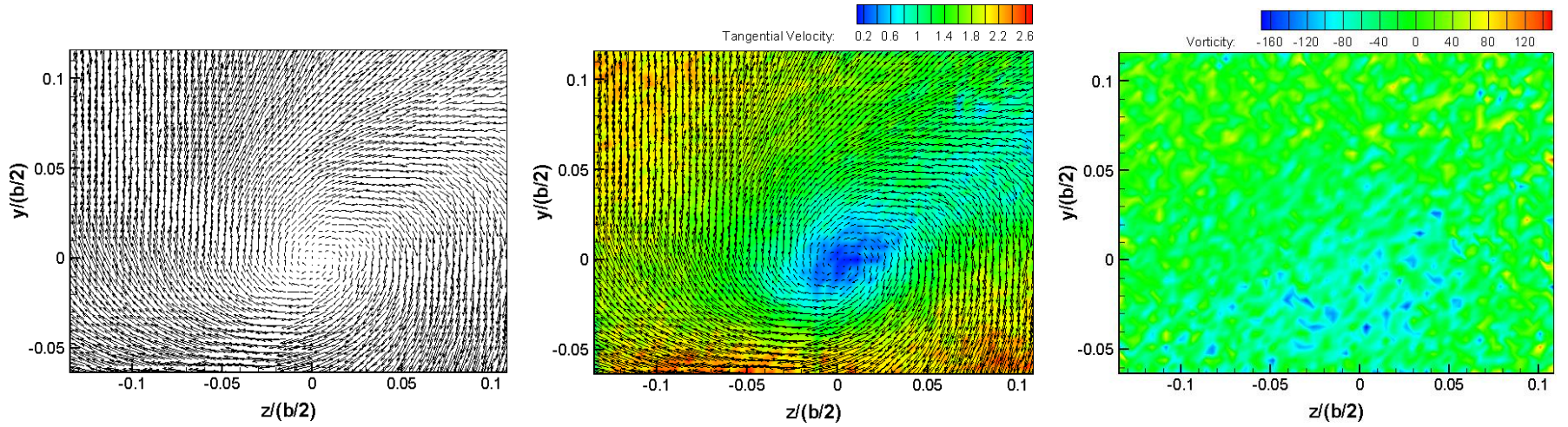


c) High Lift Configuration case, $\alpha=9.7^\circ$; with L-rdw add-on device, $\alpha_{Lrdw}=30^\circ$, $x/(b/2)=1.075$, $V_\infty=12$ m/s.

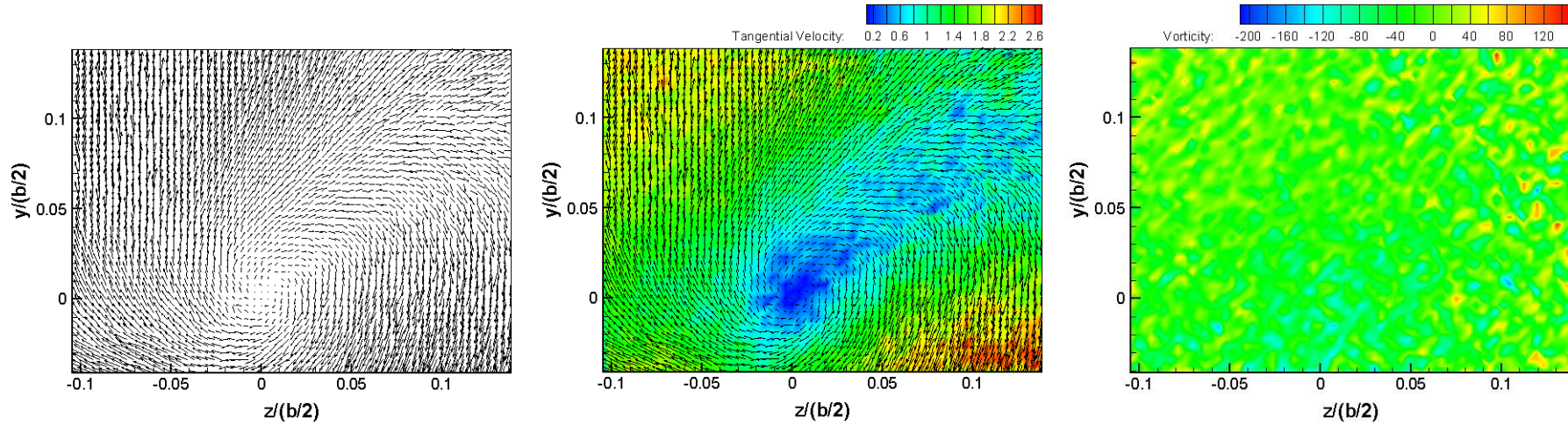
Figure 5.26: Velocity Vectors, Tangential Velocity Magnitude and Vorticity Contours at $x/(b/2)=1.075$ for (a) High Lift Configuration $\alpha=7.7^\circ$, (b) High Lift Configuration $\alpha=9.7^\circ$ with S-rdw add-on device ($\alpha_{S-rdw}=30^\circ$) and (c) High Lift Configuration $\alpha=9.7^\circ$ with L-rdw add-on device ($\alpha_{L-rdw}=30^\circ$).



a) High Lift Configuration case, $\alpha=7.7^\circ$, $x/(b/2)=2.387$, $V_\infty=12$ m/s.



b) High Lift Configuration case, $\alpha=9.7^\circ$; with S-rdw add-on device, $\alpha_{S-rdw}=30^\circ$, $x/(b/2)=2.387$, $V_\infty=12$ m/s.



c) High Lift Configuration case, $\alpha=9.7^\circ$; with L-rdw add-on device, $\alpha_{Lrdw}=30^\circ$, $x/(b/2)=2.387$, $V_\infty=12$ m/s.

Figure 5.27: Velocity Vectors, Tangential Velocity Magnitude and Vorticity Contours at $x/(b/2)=2.387$ for (a) High Lift Configuration $\alpha=7.7^\circ$, (b) High Lift Configuration $\alpha=9.7^\circ$ with S-rdw add-on device ($\alpha_{S-rdw}=30^\circ$) and (c) High Lift Configuration $\alpha=9.7^\circ$ with L-rdw add-on device ($\alpha_{L-rdw}=30^\circ$).

5.4.2 Tangential Velocity

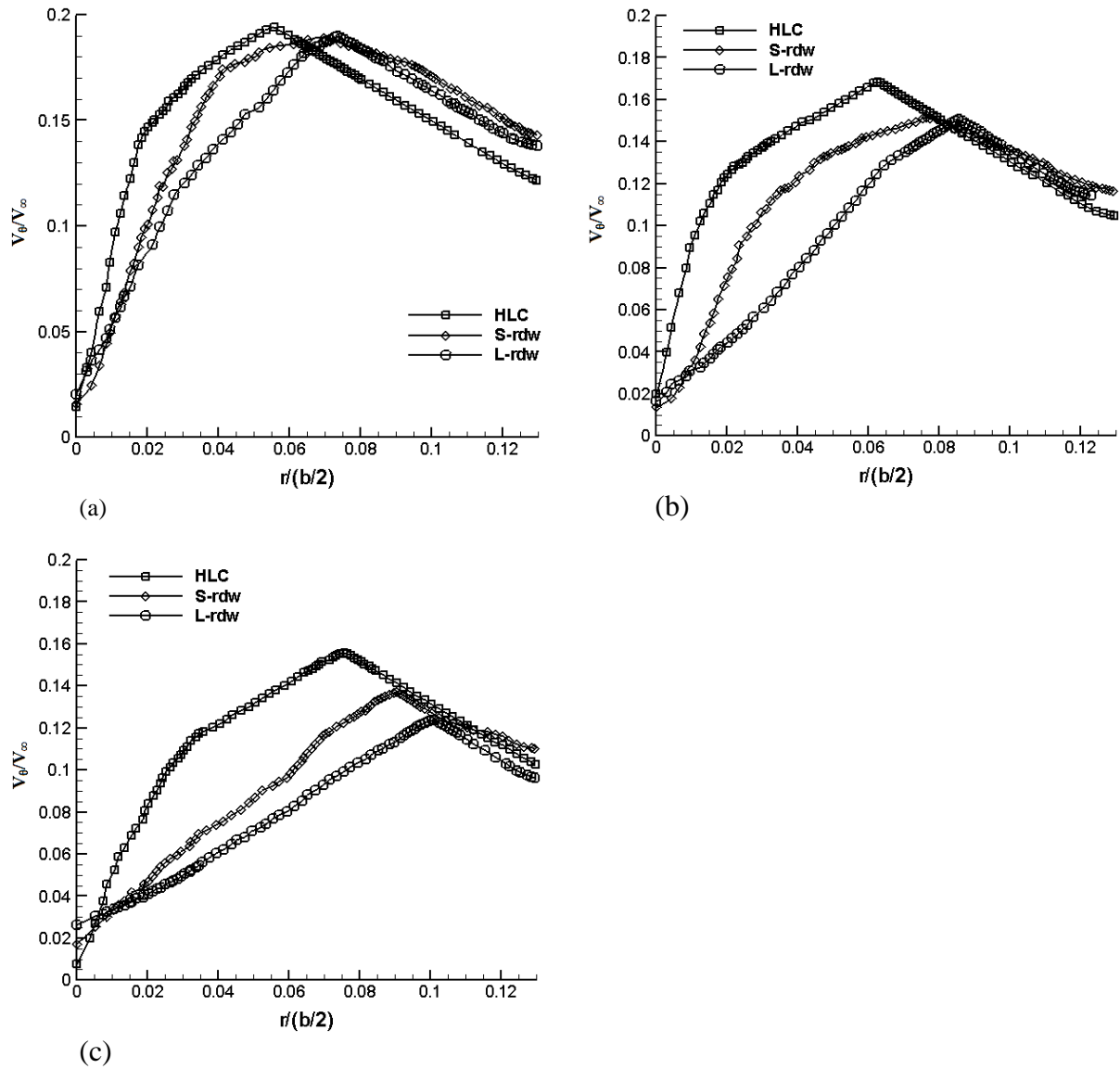


Figure 5.28: Non-dimensional tangential velocity distributions of HLC, HLC with S-rdw and HLC with L-rdw at (a) $x/(b/2)=0.548$, (b) $x/(b/2)=1.075$ and (c) $x/(b/2)=2.387$.

From figures 5.28a-c, the reduction of tangential velocity at the vortex core for the HLC from $x/(b/2)=0.548$ to $x/(b/2)=2.387$ is 19.6%. Whereas, the tangential velocity reduction of the resultant vortex core from $x/(b/2)=0.548$ to $x/(b/2)=2.387$ for the S-rdw case is 29.3% and for the L-rdw case is 36.1%. There is a 16.5% more reduction in tangential velocity magnitude when a large reverse delta type add-on device is used.

From figures 5.28a-c, it is clearly evident that the resultant vortex core radius has increased significantly when the reverse delta type add-on devices are used.

5.4.3 Aerodynamic Performance

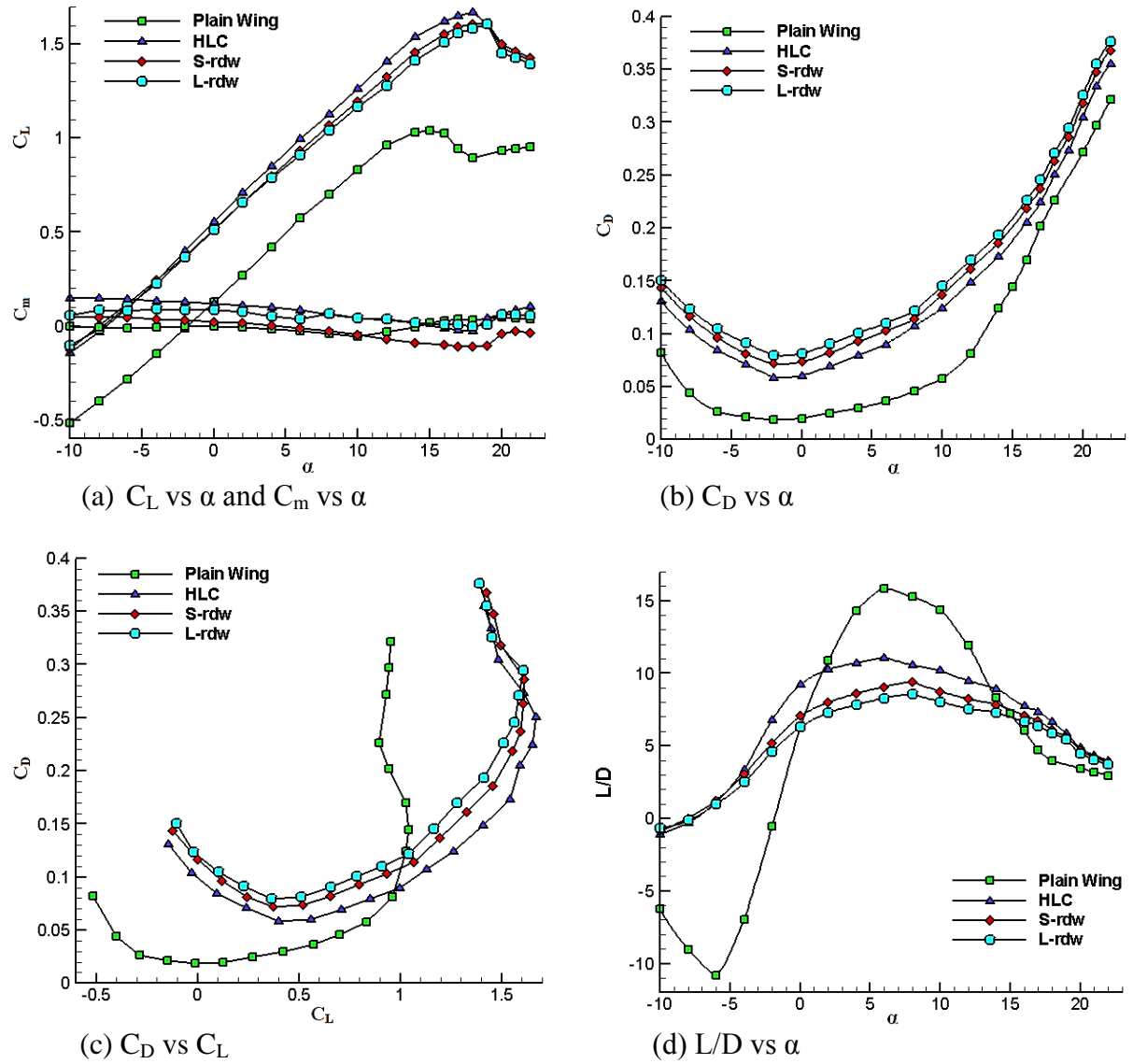


Figure 5.29: Aerodynamic performance of the Plain Wing, HLC, HLC with S-rdw and HLC with L-rdw.

The trend of figure 5.29 is similar to figures 5.12 (case 1) and 5.21 (case 2). Case 3 configuration stalls at the same angle of attack as in case 1 and 2. The reduction in the lift coefficient values between the HLC, S-rdw and L-rdw cases is 3.8%. The drag increment (compared with the HLC drag as the base value at target lift coefficient) for S-rdw case is 7.7% and for L-rdw case is 14.9%. To maintain the target lift coefficient, it was found that an

increase of 1.0° in the angle of attack of the wing is required to compensate for the reduction of lift when the add-on device is used.

Table 5.3
Overall findings of Case 3

Vortex Core Size	Tangential Velocity	Lift Coefficient	Drag Coefficient
+37% (factor of 1.37)	-36.1%	-3.8%	+14.9%

‘+’ indicates increase

‘-’ indicates decrease

5.5 CASE 4

Half-span wing model landing configuration for case 4 is as below:

Location of add-on devices: as shown in Figure 5.30

Deflection of add-on devices: $\alpha_{rdw} = +30^\circ$, $\phi_{rdw} = 0^\circ$

Slat deflection: 15°

Flap deflection: 20°

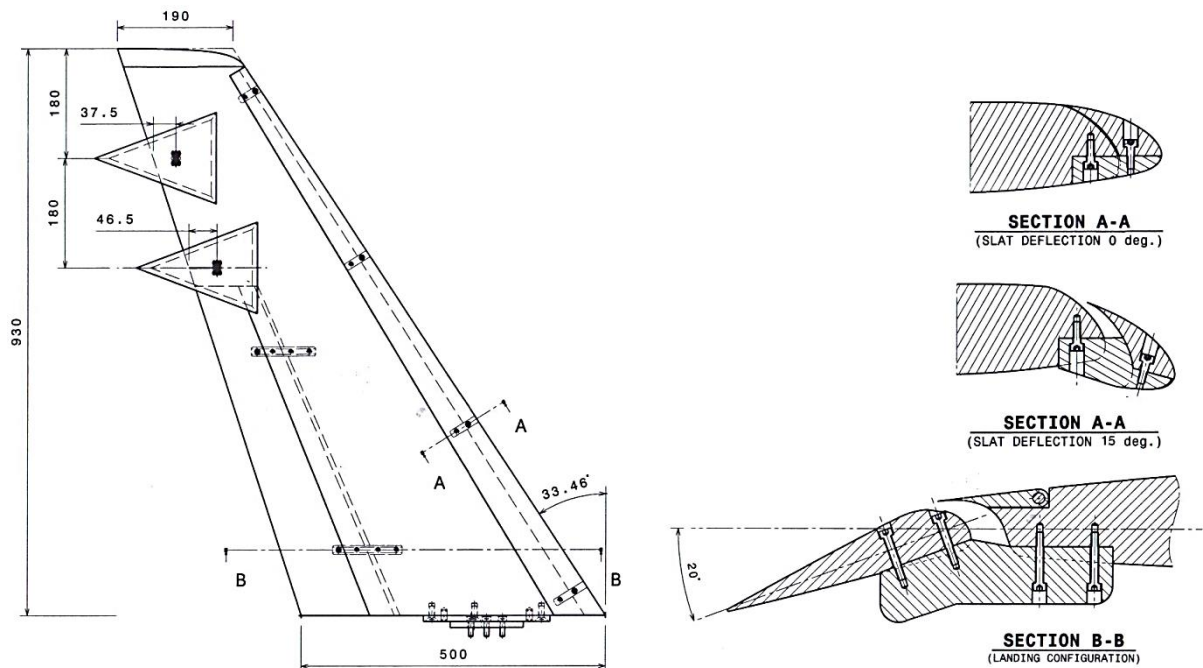


Figure 5.30: Schematic of the half-span wing model with a large reverse delta type add-on device attached. Linear dimensions are in millimetres (mm).

The purpose of the above half-span wing model with reverse delta type add-on device configuration is to investigate if the vortices shed by the reverse delta type add-on devices will introduce a fast growing instability (counter-sign vorticity) into the wingtip and flap-tip vortices and alter their roll-up process. The vortices of the add-on devices and the wingtip/flap-tip vortex are expected to merge downstream and instigate significant wake vortex alleviation. One add-on device configurations (case 1, 2 & 3) have shown promise in alleviating wake vortex significantly and it was thought-provoking to discover what a two add-on device configuration would yield. Hence, the researcher was motivated to conduct a two add-on device study.

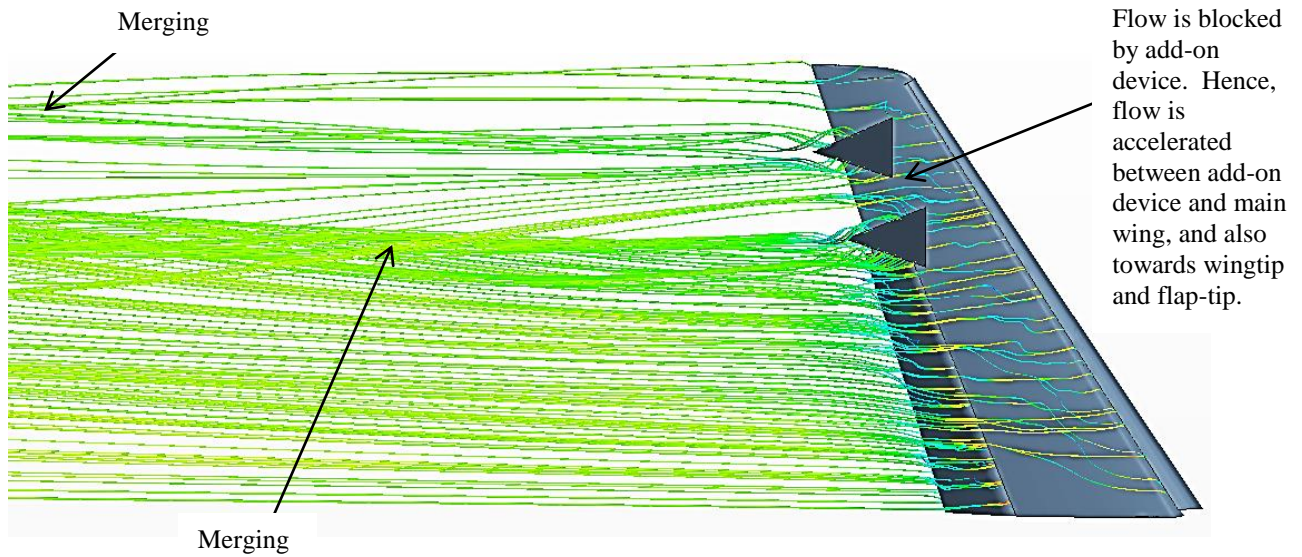


Figure 5.31: Streamlines showing the merging of the flap-tip vortex and the reverse delta type add-on device vortices. (Courtesy: Haziq Nasir)

5.5.1 Velocity Vectors and Vorticity Contours (wingtip location)

Figures 5.32 to 5.35 show the velocity vectors of a half-span wing model at HLC with/without a reverse delta type add-on device attached at a location midway from the wingtip and flap-tip.

Figures 5.32 - 5.35 show the velocity vectors, tangential velocity magnitude and vorticity contours of the HLC with/without the reverse delta type add-on device. The results for HLC without the add-on device at the wingtip are discussed in case 1, however, the results have been reproduced in this section for easier comparison.

The tangential velocity reduction between HLC and HLC with the add-on device at downstream plane 2 for the S-rdw case and L-rdw case is 6.3% and 33.6%, respectively. At downstream plane 3, the tangential velocity reduction between HLC and HLC with the add-on device for S-rdw and L-rdw cases is 40.7% and 51.8%, respectively. At downstream plane 4, the tangential velocity reduction between HLC and HLC with the add-on device for S-rdw and L-rdw add-on devices is 42.5% and 55.3%, respectively.

For the HLC with the add-on device, the vorticity is higher than the HLC case at

downstream planes 1 and 2. This is because the tangential velocity magnitude of the resultant vortex at downstream plane 1 is higher due to the acceleration of the flow towards the wingtip due to the presence of the add-on device. The L-rdw case vortex exhibits lower vorticity magnitudes than the S-rdw case vortex at all four downstream planes. Since, the vorticity magnitudes at downstream planes 1 and 2 exhibited by the resultant vortex are higher than the HLC case, the reduction in vorticity can only be compared at downstream planes 3 and 4. The vorticity reduction between HLC and HLC with an add-on device at downstream plane 3 for the S-rdw case and L-rdw case is 46.7% and 81.2%, respectively. At downstream plane 4, the vorticity reduction between HLC and HLC with an add-on device for S-rdw case and L-rdw case is 59.6% and 87.5%, respectively.

The resultant vortex core size is seen to be increasing significantly between the downstream planes. This indicates a rapid increase in vortex volume which reduces the tangential velocity rapidly. The HLC vortex core radius is much smaller compared to the HLC with the add-on device resultant vortex core radius. At $x/(b/2)=0.021$, the resultant vortex core radius (when add-on device is used) compared to the HLC vortex core radius has diffused (enlarged) by a factor of 1.11 and 1.16 for the S-rdw and L-rdw, respectively. At $x/(b/2)=0.548$, the resultant vortex core radius has increased by a factor of 1.15 and 1.40 for the S-rdw and L-rdw, respectively. At $x/(b/2)=1.075$, the resultant vortex core radius has increased by a factor of 1.82 and 3.29 for the S-rdw and L-rdw, respectively. At $x/(b/2)=2.387$, the resultant vortex core radius has increased by a factor of 2.36 and 4.40 for the S-rdw and L-rdw, respectively. This implies that when the L-rdw is used, the resultant core radius size is 4.40 times more than the core radius of the HLC case shed vortex.

The reduction in tangential velocity magnitude, reduction in vorticity magnitude and increase in the resultant vortex core dimension is significantly less than that of case 1. The reason is that the two reverse delta type add-on device configuration accelerates the flow

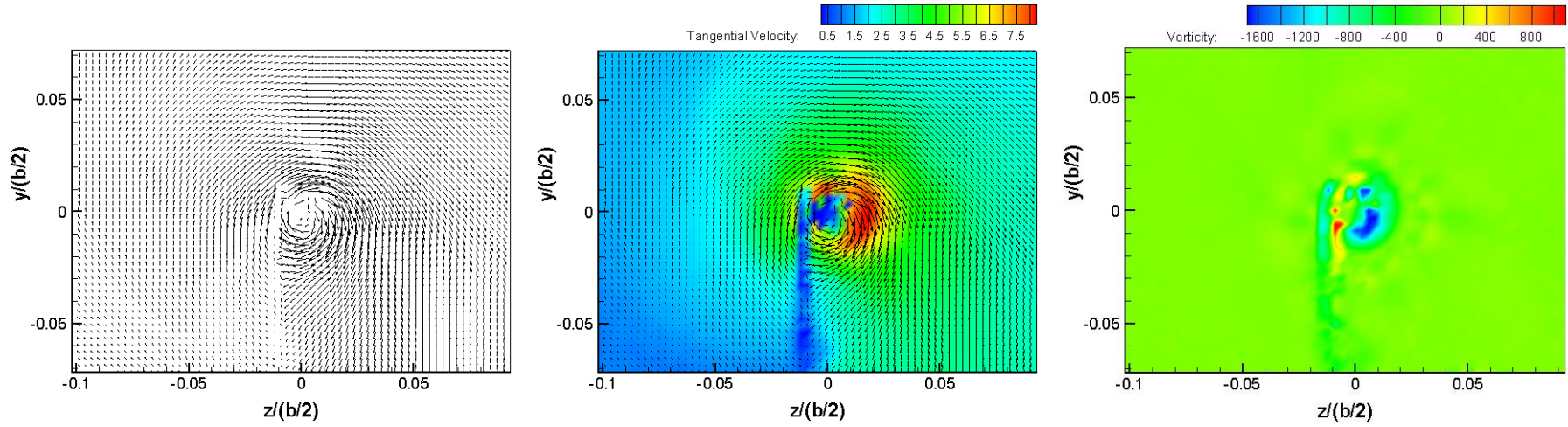
towards the wingtip causing an increase in the tangential velocity and hence, creates a more coherent resultant vortex. Hence, wake vortex alleviation is not as high as in case 1. The findings of case 1 and case 4 are tabulated in table 5.8 for comparison purposes.

Table 5.4
Overall findings of Case 4 (wingtip)

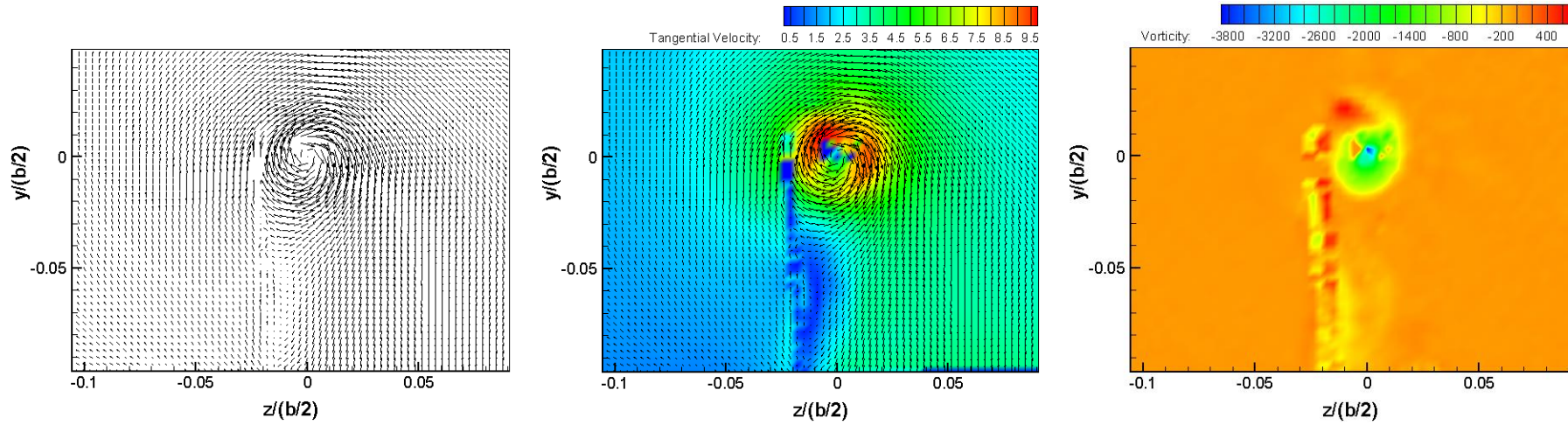
Vortex Core Size	Tangential Velocity	Vorticity
+340% (factor of 4.40)	-55.3%	-87.5%

‘+’ indicates increase

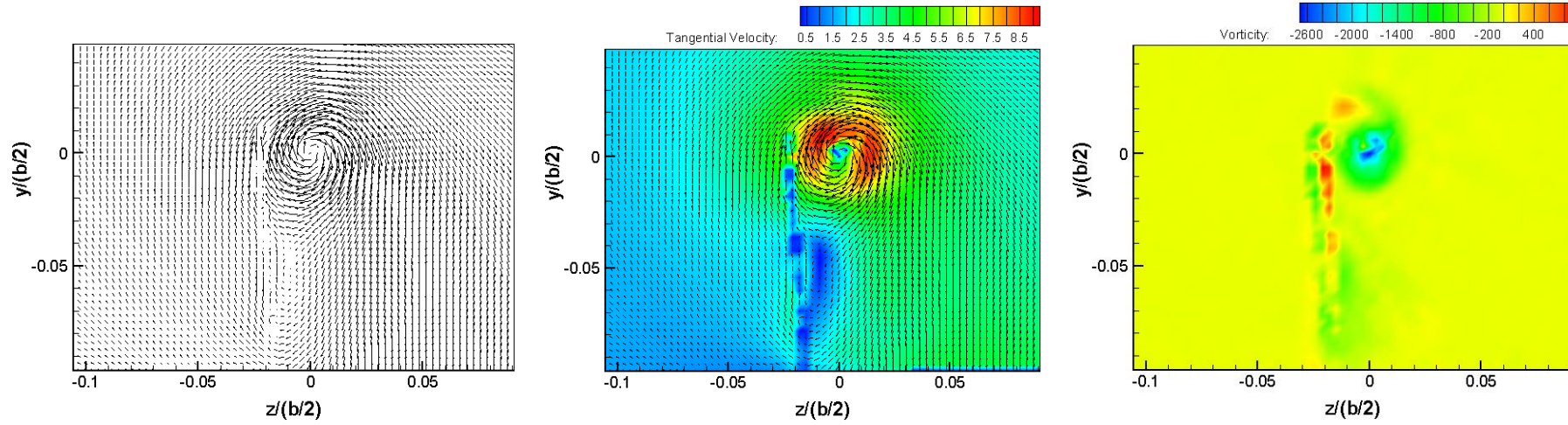
‘-’ indicates decrease



a) High Lift Configuration case, $\alpha=7.7^\circ$, $x/(b/2)=0.021$, $V_\infty=12$ m/s.

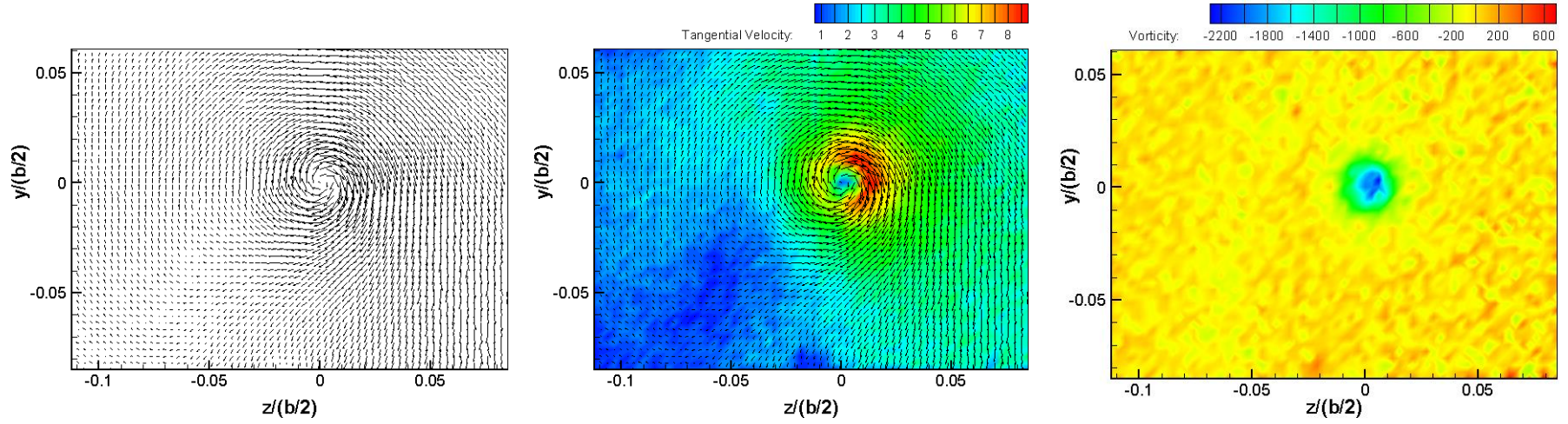


b) High Lift Configuration case, $\alpha=9.7^\circ$; with S-rdw add-on device, $\alpha_{S\text{-rdw}}=30^\circ$, $x/(b/2)=0.021$, $V_\infty=12$ m/s.

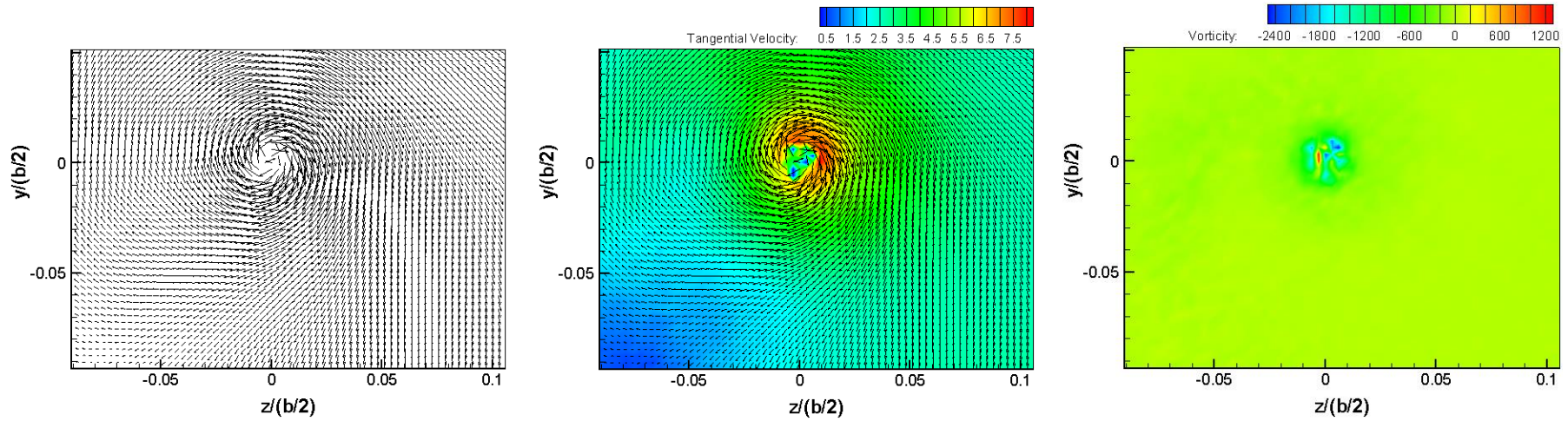


c) High Lift Configuration case, $\alpha=9.7^\circ$; with L-rdw add-on device, $\alpha_{Lrdw}=30^\circ$, $x/(b/2)=0.021$, $V_\infty=12$ m/s.

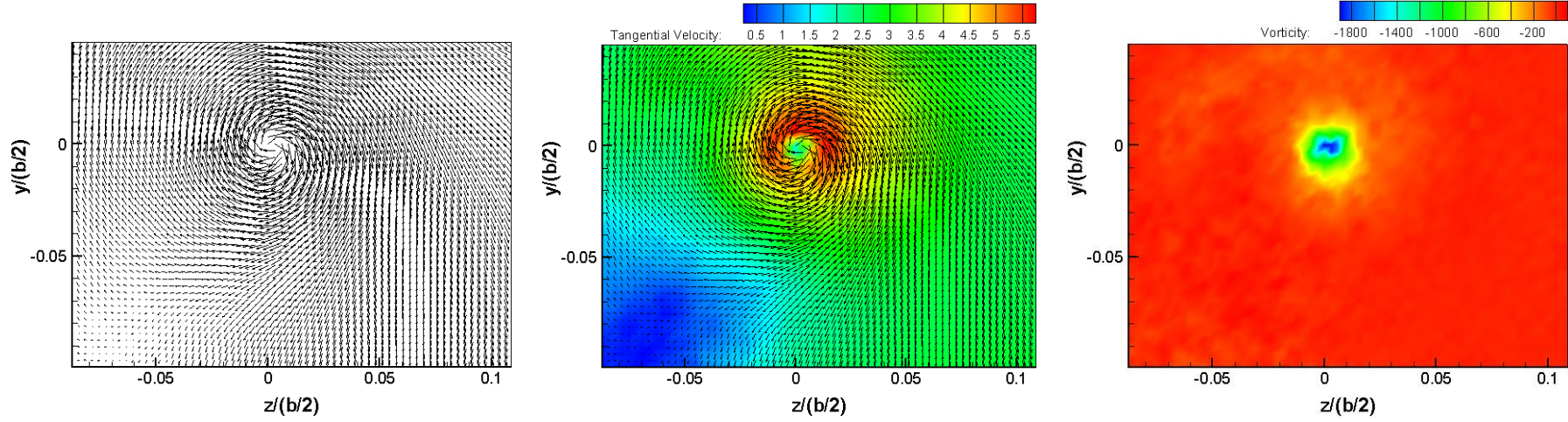
Figure 5.32: Velocity Vectors, Tangential Velocity Magnitude and Vorticity Contours at $x/(b/2)=0.021$ for (a) High Lift Configuration $\alpha=7.7^\circ$, (b) High Lift Configuration $\alpha=9.7^\circ$ with S-rdw add-on device ($\alpha_{S-rdw}=30^\circ$) and (c) High Lift Configuration $\alpha=9.7^\circ$ with L-rdw add-on device ($\alpha_{L-rdw}=30^\circ$).



a) High Lift Configuration case, $\alpha=7.7^\circ$, $x/(b/2)=0.548$, $V_\infty=12$ m/s.

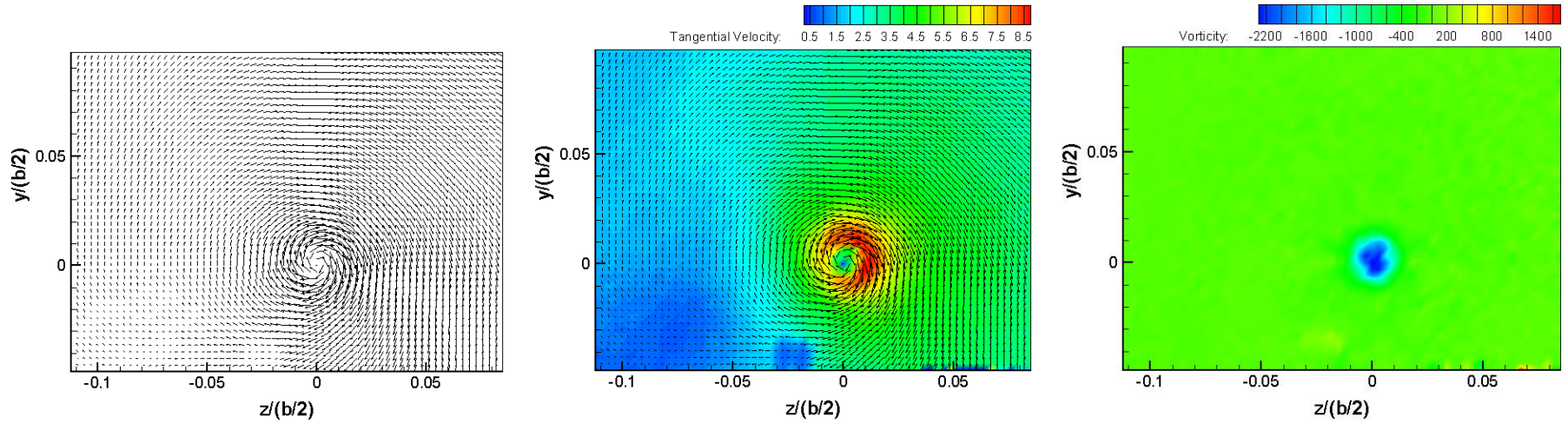


b) High Lift Configuration case, $\alpha=9.7^\circ$; with S-rdw add-on device, $\alpha_{S\text{-rdw}}=30^\circ$, $x/(b/2)=0.548$, $V_\infty=12$ m/s.

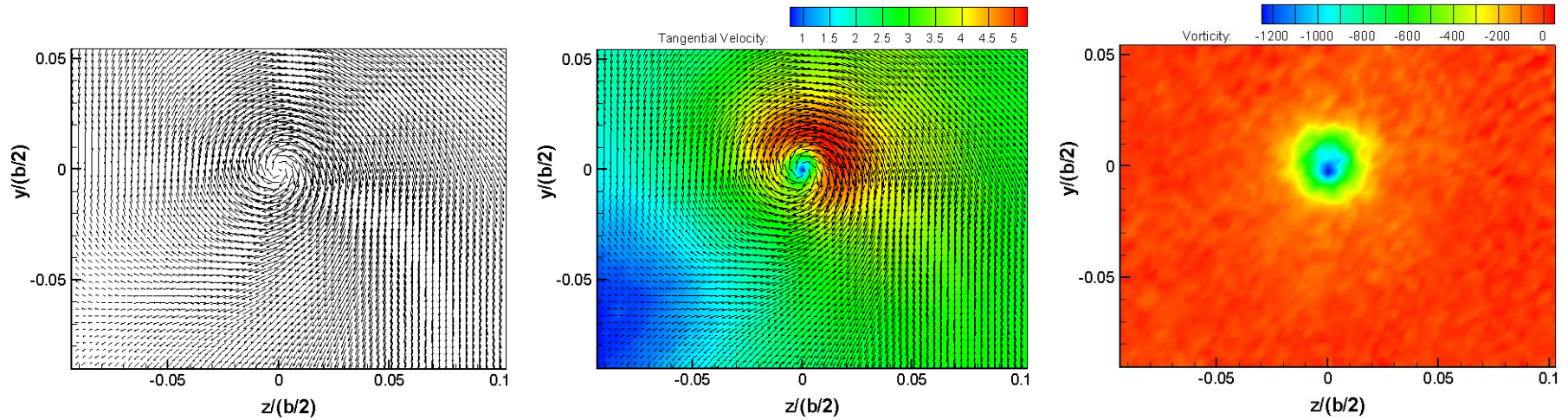


c) High Lift Configuration case, $\alpha=9.7^\circ$; with L-rdw add-on device, $\alpha_{L-rdw}=30^\circ$, $x/(b/2)=0.548$, $V_\infty=12$ m/s.

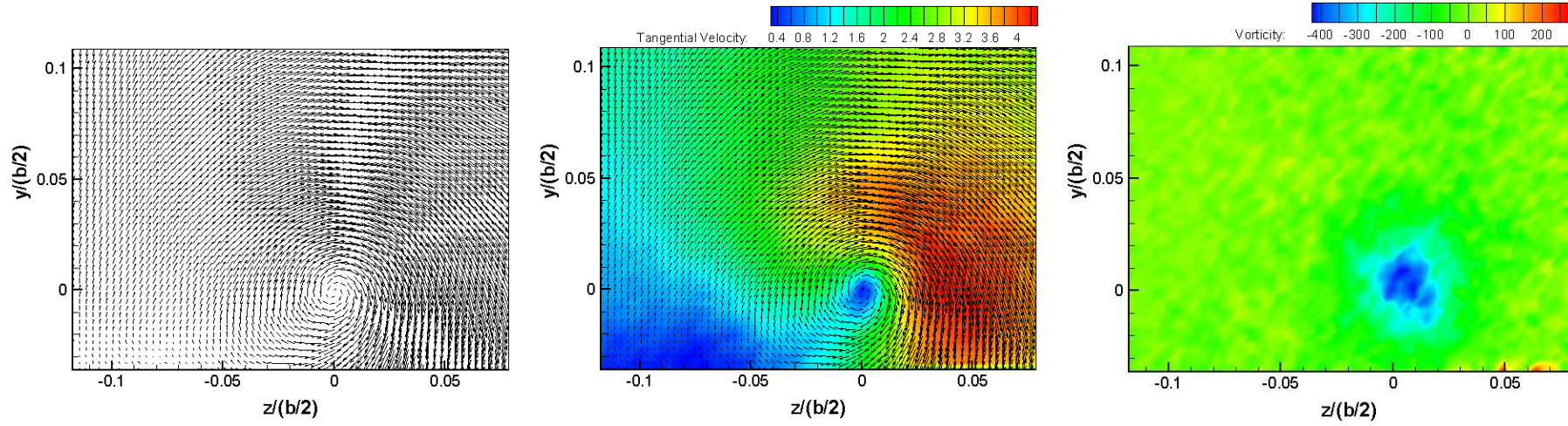
Figure 5.33: Velocity Vectors, Tangential Velocity Magnitude and Vorticity Contours at $x/(b/2)=0.548$ for (a) High Lift Configuration $\alpha=7.7^\circ$, (b) High Lift Configuration $\alpha=9.7^\circ$ with S-rdw add-on device ($\alpha_{S-rdw}=30^\circ$) and (c) High Lift Configuration $\alpha=9.7^\circ$ with L-rdw add-on device ($\alpha_{L-rdw}=30^\circ$).



a) High Lift Configuration case, $\alpha=7.7^\circ$, $x/(b/2)=1.075$, $V_\infty=12$ m/s.

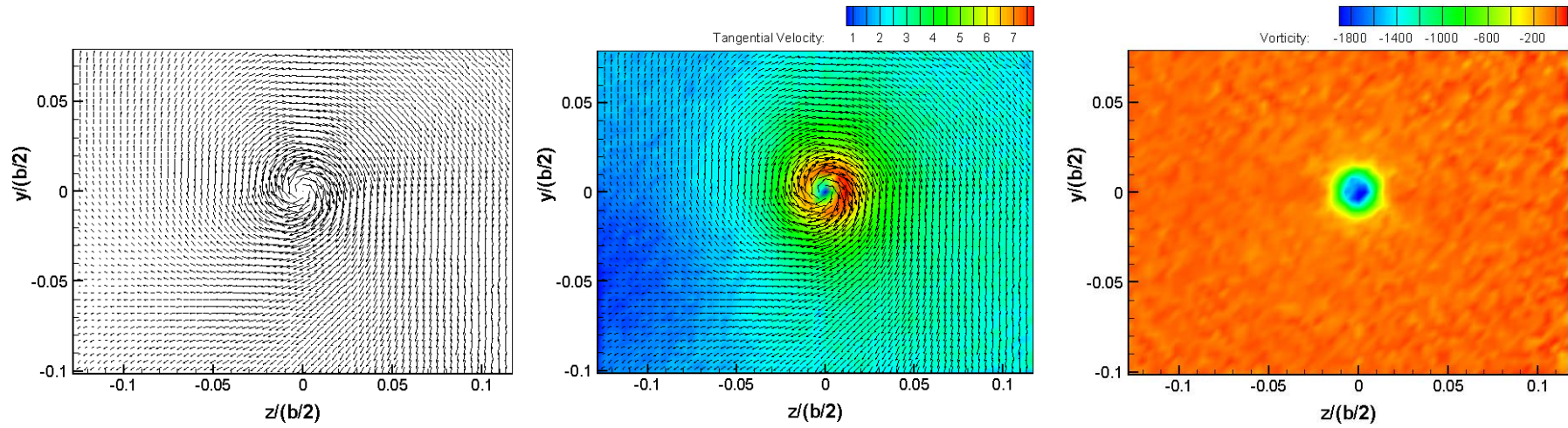


b) High Lift Configuration case, $\alpha=9.7^\circ$; with S-rdw add-on device, $\alpha_{S-rdw}=30^\circ$, $x/(b/2)=1.075$, $V_\infty=12$ m/s.

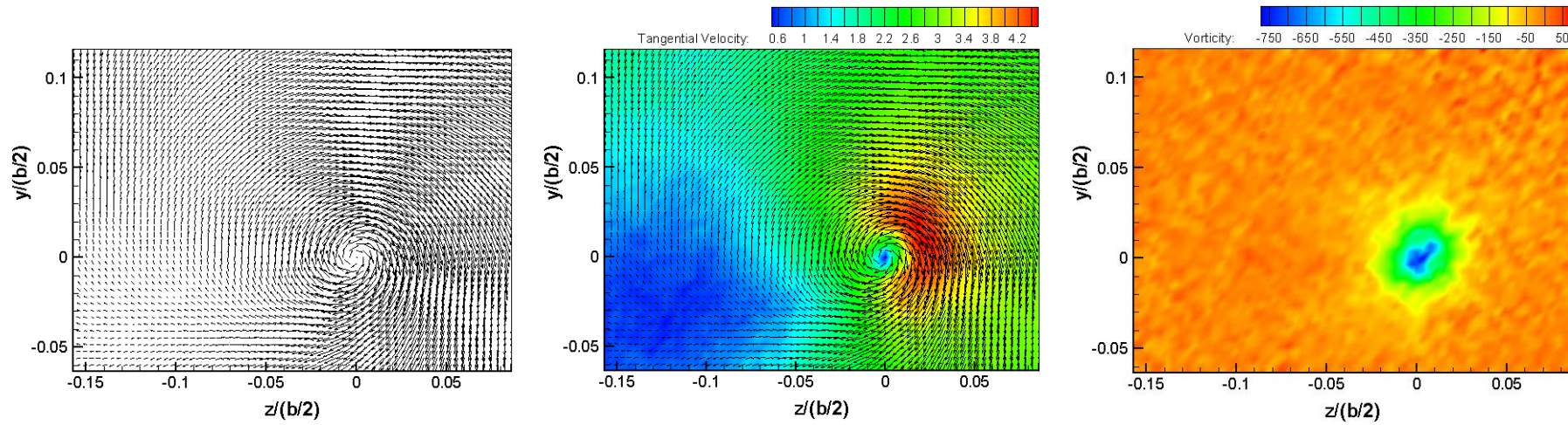


c) High Lift Configuration case, $\alpha=9.7^\circ$; with L-rdw add-on device, $\alpha_{Lrdw}=30^\circ$, $x/(b/2)=1.075$, $V_\infty=12$ m/s.

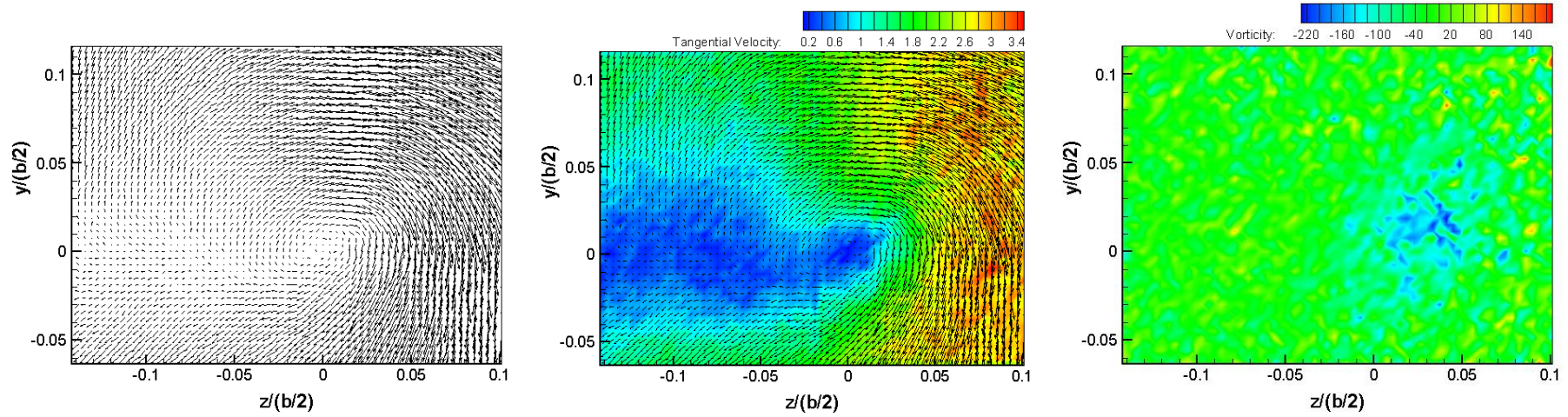
Figure 5.34: Velocity Vectors, Tangential Velocity Magnitude and Vorticity Contours at $x/(b/2)=1.075$ for (a) High Lift Configuration $\alpha=7.7^\circ$, (b) High Lift Configuration $\alpha=9.7^\circ$ with S-rdw add-on device ($\alpha_{S-rdw}=30^\circ$) and (c) High Lift Configuration $\alpha=9.7^\circ$ with L-rdw add-on device ($\alpha_{L-rdw}=30^\circ$).



a) High Lift Configuration case, $\alpha=7.7^\circ$, $x/(b/2)=2.387$, $V_\infty=12$ m/s.



b) High Lift Configuration case, $\alpha=9.7^\circ$; with S-rdw add-on device, $\alpha_{S-rdw}=30^\circ$, $x/(b/2)=2.387$, $V_\infty=12$ m/s.



c) High Lift Configuration case, $\alpha=9.7^\circ$; with L-rdw add-on device, $\alpha_{Lrdw}=30^\circ$, $x/(b/2)=2.387$, $V_\infty=12$ m/s.

Figure 5.35: Velocity Vectors, Tangential Velocity Magnitude and Vorticity Contours at $x/(b/2)=2.387$ for (a) High Lift Configuration $\alpha=7.7^\circ$, (b) High Lift Configuration $\alpha=9.7^\circ$ with S-rdw add-on device ($\alpha_{S-rdw}=30^\circ$) and (c) High Lift Configuration $\alpha=9.7^\circ$ with L-rdw add-on device ($\alpha_{L-rdw}=30^\circ$).

5.5.2 Velocity Vectors and Vorticity Contours (flap-tip location)

Figures 5.36 to 5.39 show the velocity vectors of a half-span wing model at HLC with/without a reverse delta type add-on device attached at a location near the half-span model outboard flap-tip.

Figures 5.36 - 5.39 show the velocity vectors, tangential velocity magnitude and vorticity contours of the HLC with/without the reverse delta type add-on device. The results for HLC without the add-on device at the flap-tip are discussed in case 3, however, the results have been reproduced in this section for easier comparison.

When the reverse delta type add-on device is used, as shown in figures 5.37b-c, 5.38b-c and 5.39b-c, the vortex core radius is found to have diffused more than the HLC case. At $x/(b/2)=0.548$, the resultant vortex core radius compared to the flap-tip vortex core radius of the HLC has increased by a factor of 1.13 and 1.29 for the S-rdw case and L-rdw case, respectively. At $x/(b/2)=1.075$, the resultant vortex core radius compared to the flap-tip vortex core radius of the HLC has increased by a factor of 1.20 and 1.33 for the S-rdw case and L-rdw case, respectively. At $x/(b/2)=2.387$, the resultant vortex core is not distinguishable (core has broken down into small vorticity patches). Hence, it can be said that significant wake vortex alleviation has taken place at downstream plane 4. The above results suggest that the weak flap-tip vortex of the HLC is diffusing significantly. When an add-on device is used, the resultant vortex core size increases significantly more than the HLC flap-tip vortex. The significant increase in resultant vortex core radius indicates that the resultant vortex is expected to diffuse rapidly farther downstream and decay earlier than it would actually decay if an add-on device is not used.

When a reverse delta type add-on device is used, the flow is accelerated towards the wingtip and flap-tip causing an increase in tangential velocity magnitude, as can be seen in figure 5.36b-c. Farther downstream, as shown in figures 5.37b-c, 5.38b-c and 5.39b-c, the

tangential velocity magnitude of the resultant vortex is seen to decrease slightly with respect to the HLC flap-tip vortex. At $x/(b/2)=2.387$, the reduction in tangential velocity magnitude between the HLC case and the add-on device cases is 16.1%.

For all investigated cases, the vorticity decreased gradually from a maximum at the centre to nearly zero at the outer region of the vortices. At $x/(b/2)= 0.021$, it can be noticed that the vortex cores are distinguishable. At $x/(b/2)= 0.548$, the vortex core for the HLC and add-on device cases have broken into small vorticity pathes, but the vortex core of the HLC (figure 5.37a), is more coherent than the vortex core of the add-on device cases (figures 5.37b-c). At $x/(b/2)=1.075$, the vortex core of the add-on device cases are broken into small vorticity patches, whereas the vortex core of the HLC case is still intact. These small patches of vorticity have high individual vorticity magnitudes but they do not pose a hazard as they are too small to cause any significant circulation of the entire vortex core. At farther downstream locations, the small vorticity patches increase in number for the add-on device cases. This suggests that the vortex core is mostly broken down. The breakdown of the resultant vortex creates a weaker and more diffused/scattered/distributed vortex. Hazard from such vortices is minimal. Thus, it can be said that when the add-on device is used, the resultant vortex formed diffuses rapidly due to small scale instabilities (counter-sign vorticity) created into the vortex.

It can be said that the add-on device creates small scale instabilities into the flap-tip vortex causing the resultant vortex core to breakdown significantly.

The reduction in tangential velocity magnitude and increase in the resultant vortex core dimension is significantly less than that of case 3. The reason is that the two reverse delta type add-on device configuration accelerates the flow towards the flap-tip causing an increase in the tangential velocity and creating a more compact resultant vortex. Hence, wake vortex

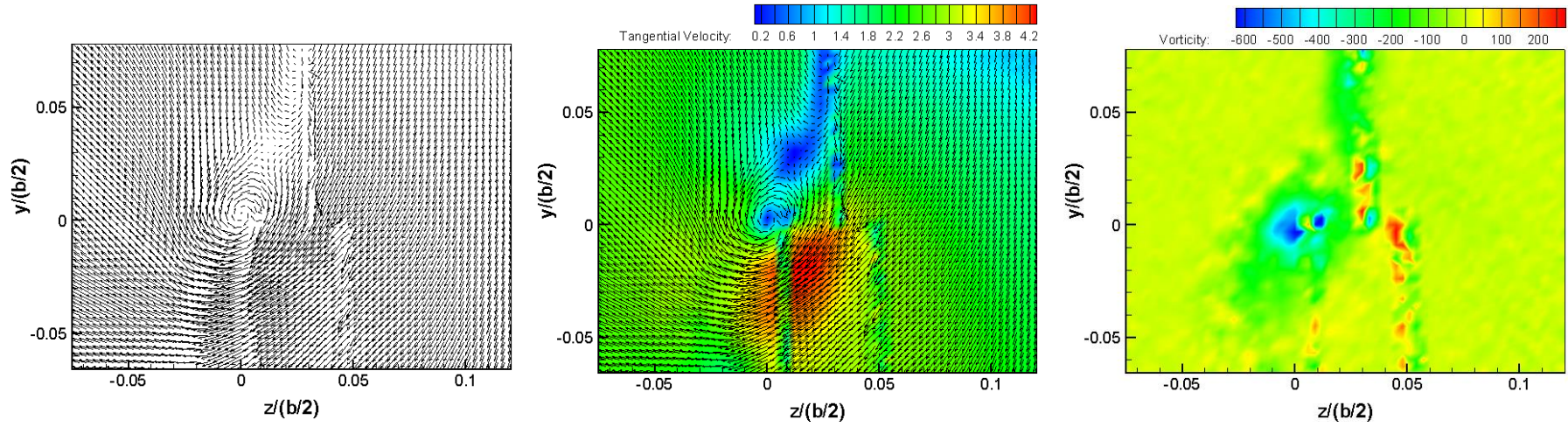
alleviation is not as high as in case 3. The findings of case 3 and case 4 are tabulated in table 5.8 for comparison purposes.

Table 5.5
Overall findings of Case 4 (flap-tip)

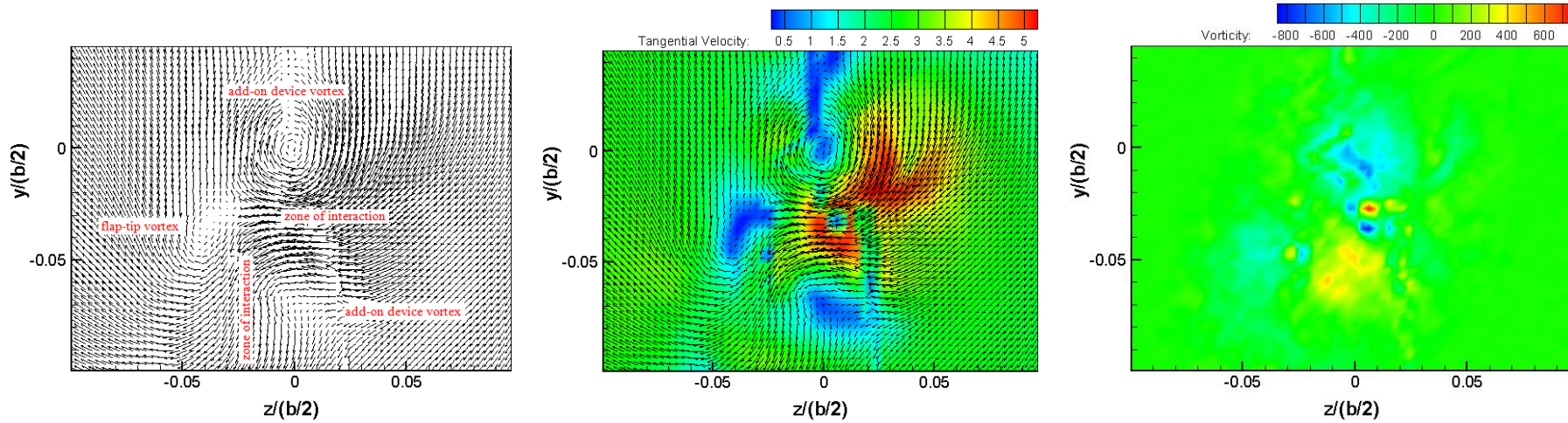
Vortex Core Size	Tangential Velocity
+33% (factor of 1.33)	-16.1%

‘+’ indicates increase

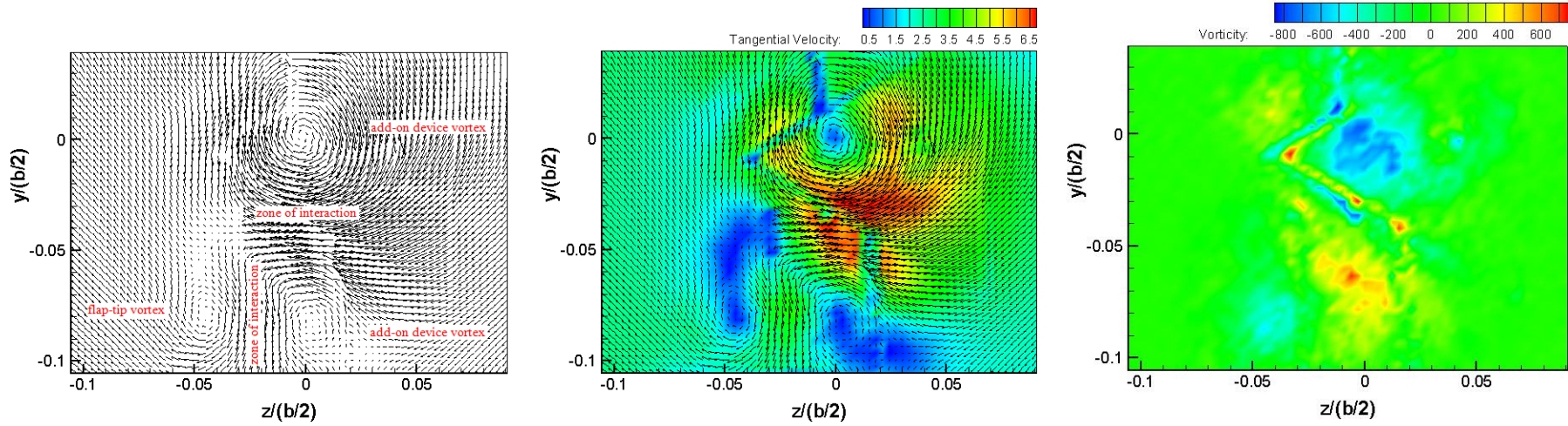
‘-’ indicates decrease



a) High Lift Configuration case, $\alpha=7.7^\circ$, $x/(b/2)=0.021$, $V_\infty=12$ m/s.

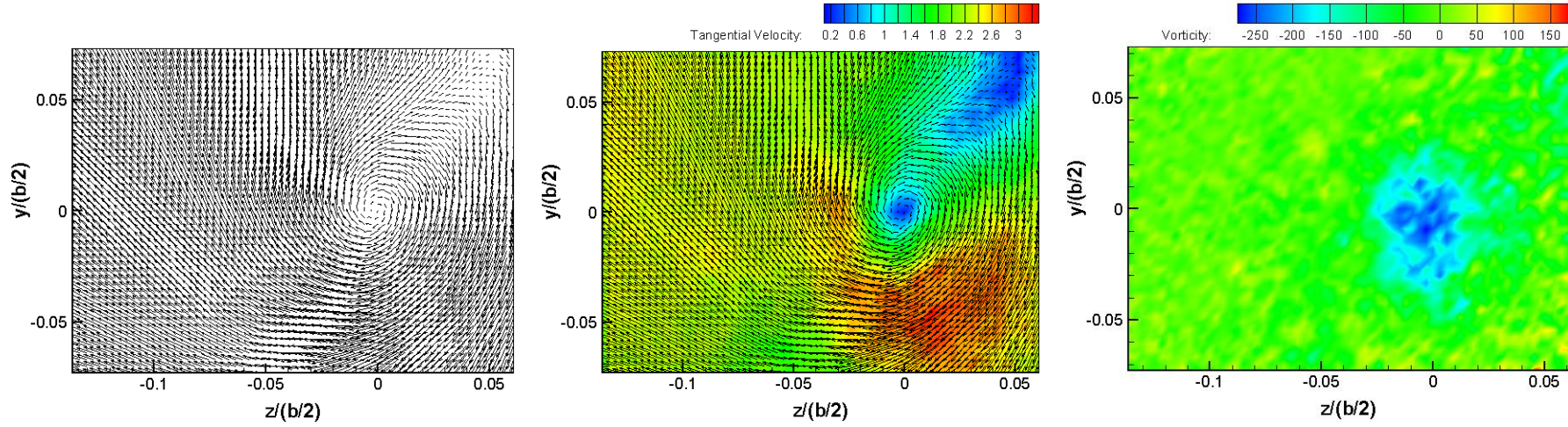


b) High Lift Configuration case, $\alpha=9.7^\circ$; with S-rdw add-on device, $\alpha_{S-rdw}=30^\circ$, $x/(b/2)=0.021$, $V_\infty=12$ m/s.

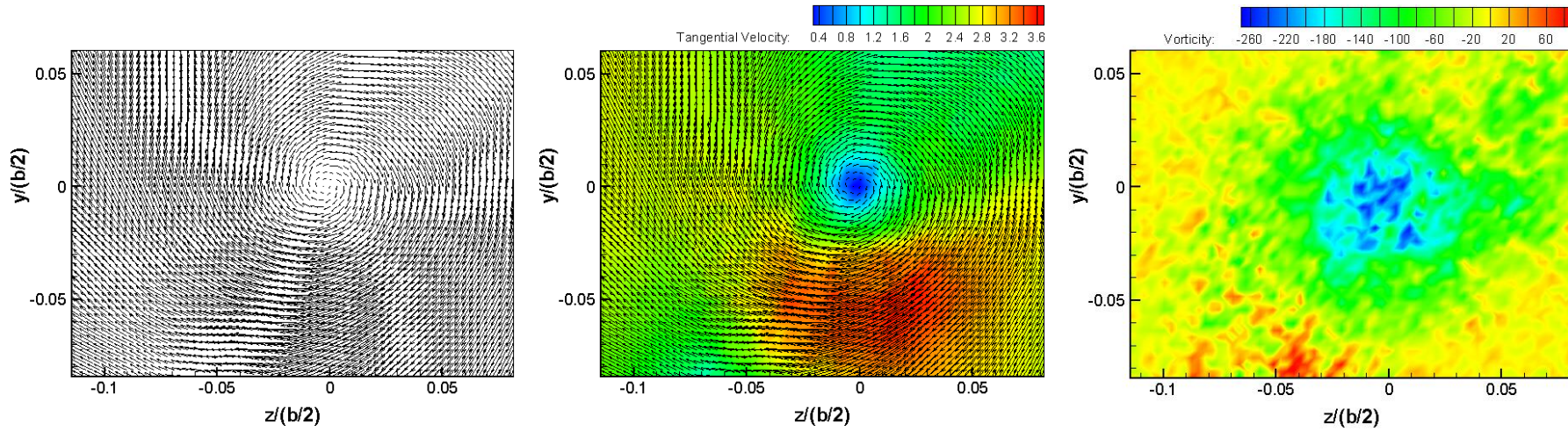


c) High Lift Configuration case, $\alpha=9.7^\circ$; with L-rdw add-on device, $\alpha_{L-rdw}=30^\circ$, $x/(b/2)=0.021$, $V_\infty=12$ m/s.

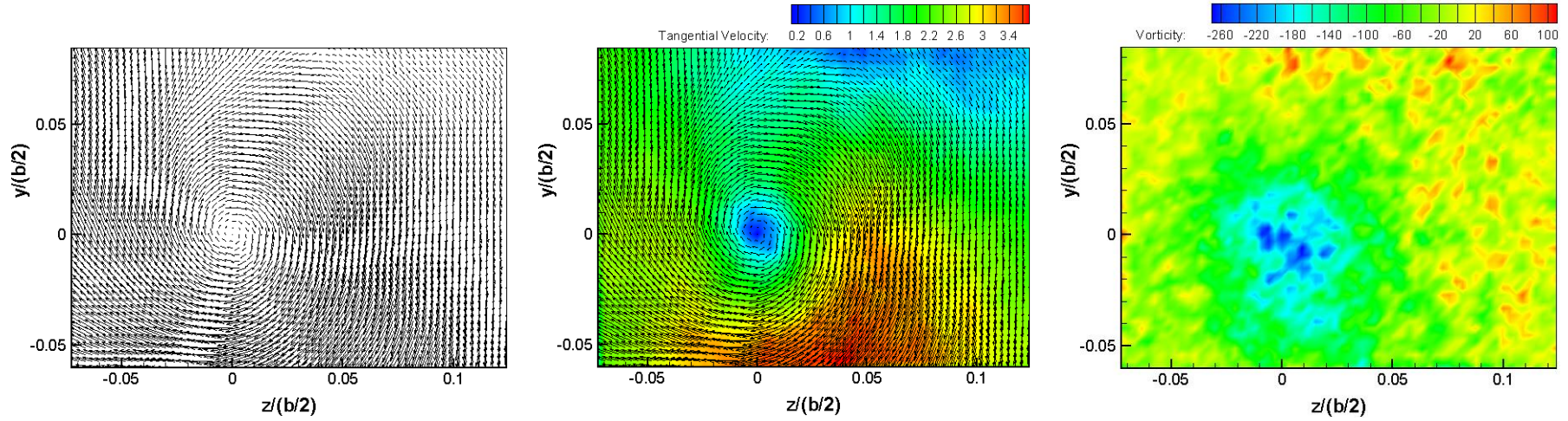
Figure 5.36: Velocity Vectors, Tangential Velocity Magnitude and Vorticity Contours at $x/(b/2)=0.021$ for (a) High Lift Configuration $\alpha=7.7^\circ$, (b) High Lift Configuration $\alpha=9.7^\circ$ with S-rdw add-on device ($\alpha_{S-rdw}=30^\circ$) and (c) High Lift Configuration $\alpha=9.7^\circ$ with L-rdw add-on device ($\alpha_{L-rdw}=30^\circ$).



a) High Lift Configuration case, $\alpha=7.7^\circ$, $x/(b/2)=0.548$, $V_\infty=12$ m/s.

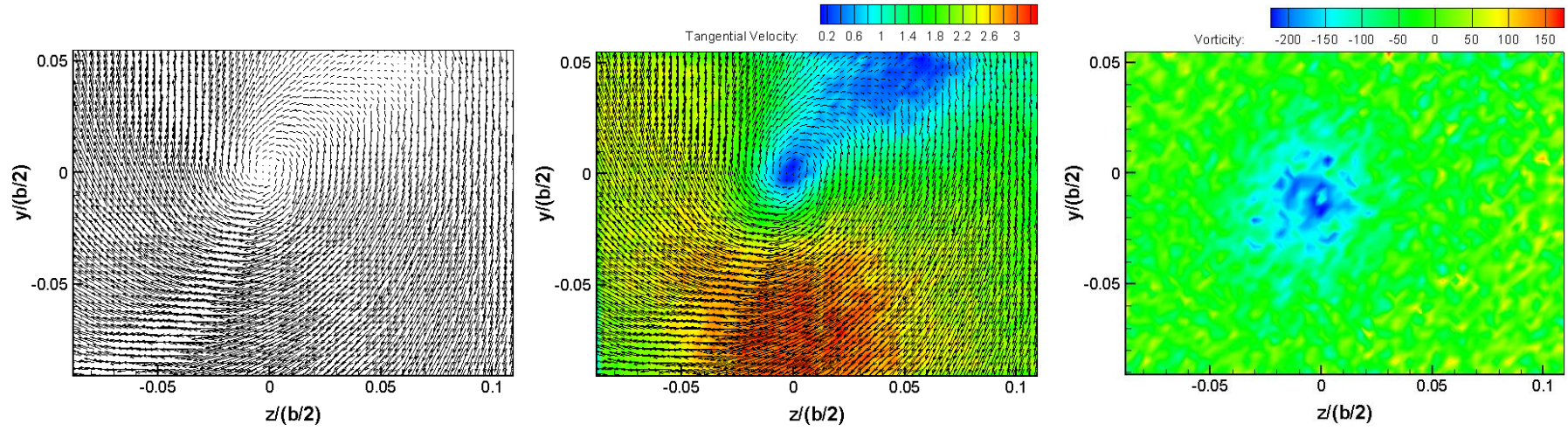


b) High Lift Configuration case, $\alpha=9.7^\circ$; with S-rdw add-on device, $\alpha_{S-rdw}=30^\circ$, $x/(b/2)=0.548$, $V_\infty=12$ m/s.

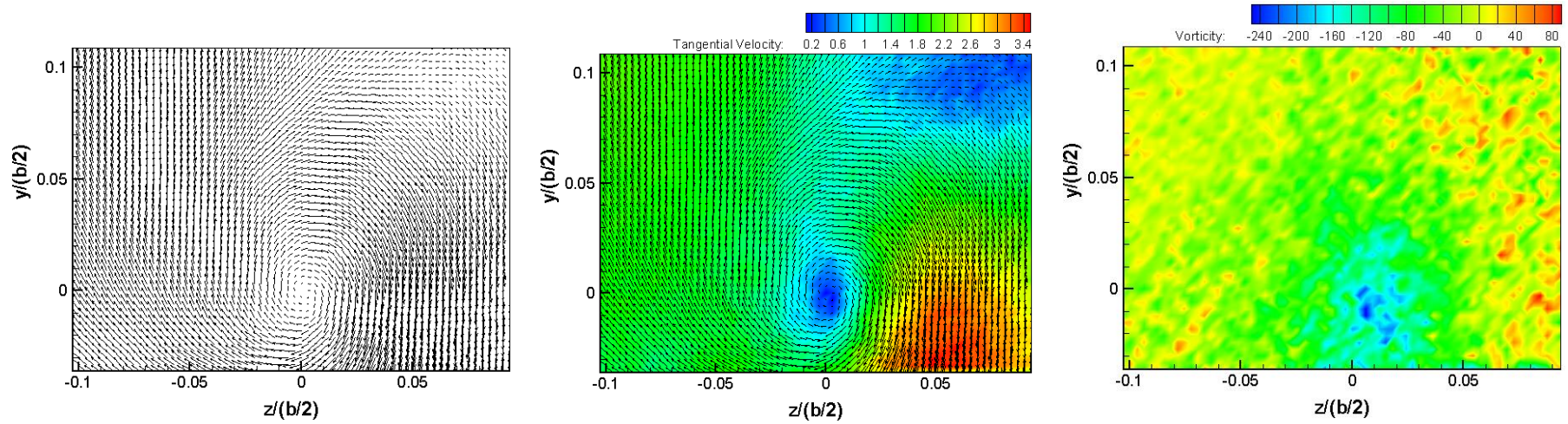


c) High Lift Configuration case, $\alpha=9.7^\circ$; with L-rdw add-on device, $\alpha_{Lrdw}=30^\circ$, $x/(b/2)=0.548$, $V_\infty=12$ m/s.

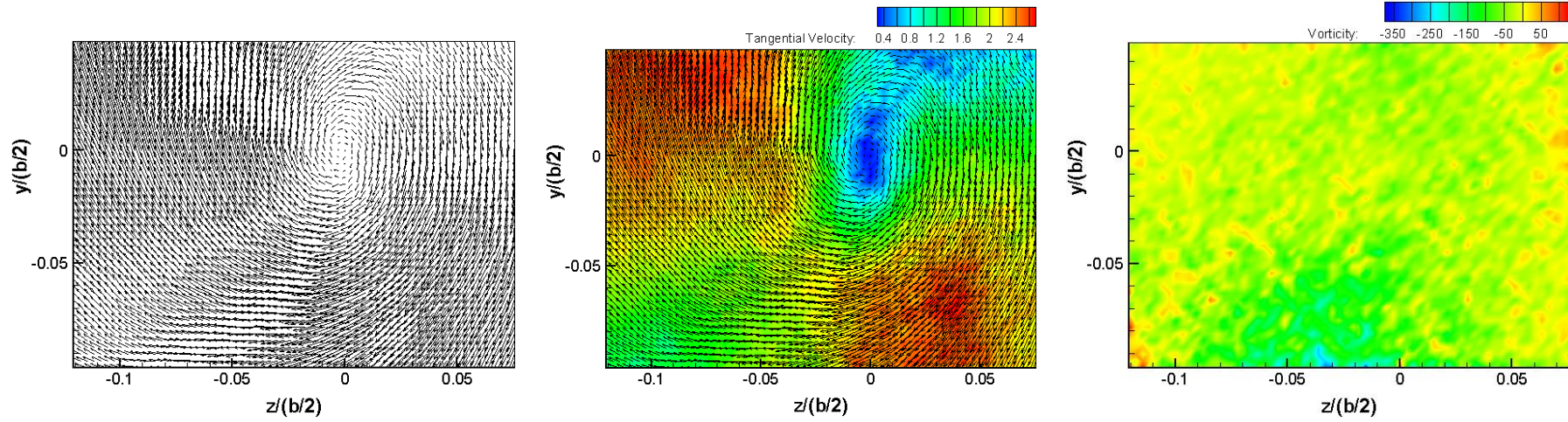
Figure 5.37: Velocity Vectors, Tangential Velocity Magnitude and Vorticity Contours at $x/(b/2)=0.548$ for (a) High Lift Configuration $\alpha=7.7^\circ$, (b) High Lift Configuration $\alpha=9.7^\circ$ with S-rdw add-on device ($\alpha_{S-rdw}=30^\circ$) and (c) High Lift Configuration $\alpha=9.7^\circ$ with L-rdw add-on device ($\alpha_{L-rdw}=30^\circ$).



a) High Lift Configuration case, $\alpha=7.7^\circ$, $x/(b/2)=1.075$, $V_\infty=12$ m/s.

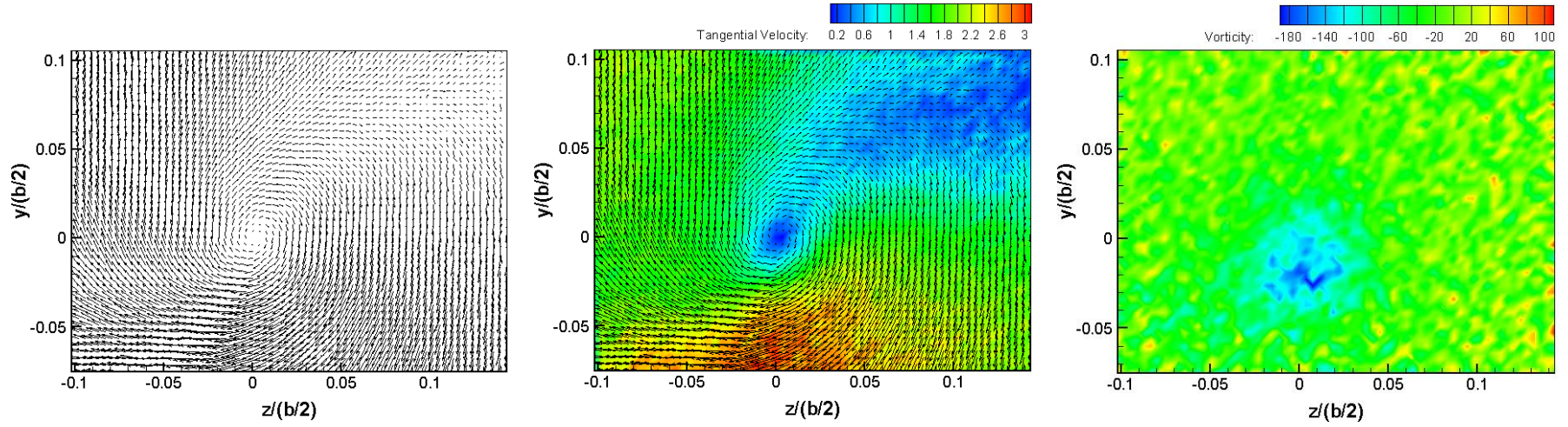


b) High Lift Configuration case, $\alpha=9.7^\circ$; with S-rdw add-on device, $\alpha_{S-rdw}=30^\circ$, $x/(b/2)=1.075$, $V_\infty=12$ m/s.

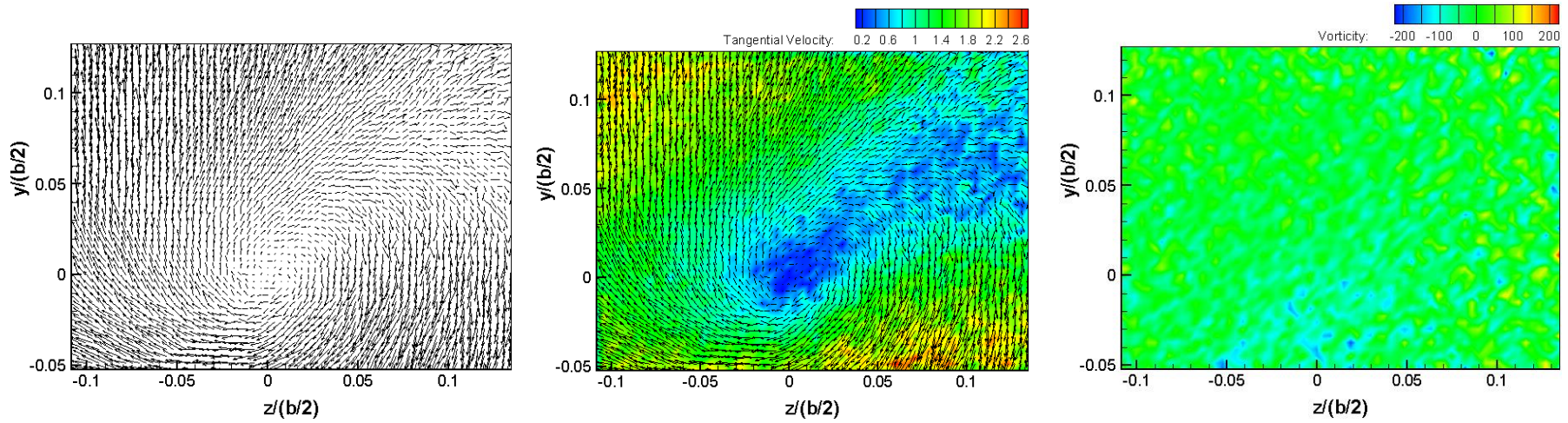


c) High Lift Configuration case, $\alpha=9.7^\circ$; with L-rdw add-on device, $\alpha_{Lrdw}=30^\circ$, $x/(b/2)=1.075$, $V_\infty=12$ m/s.

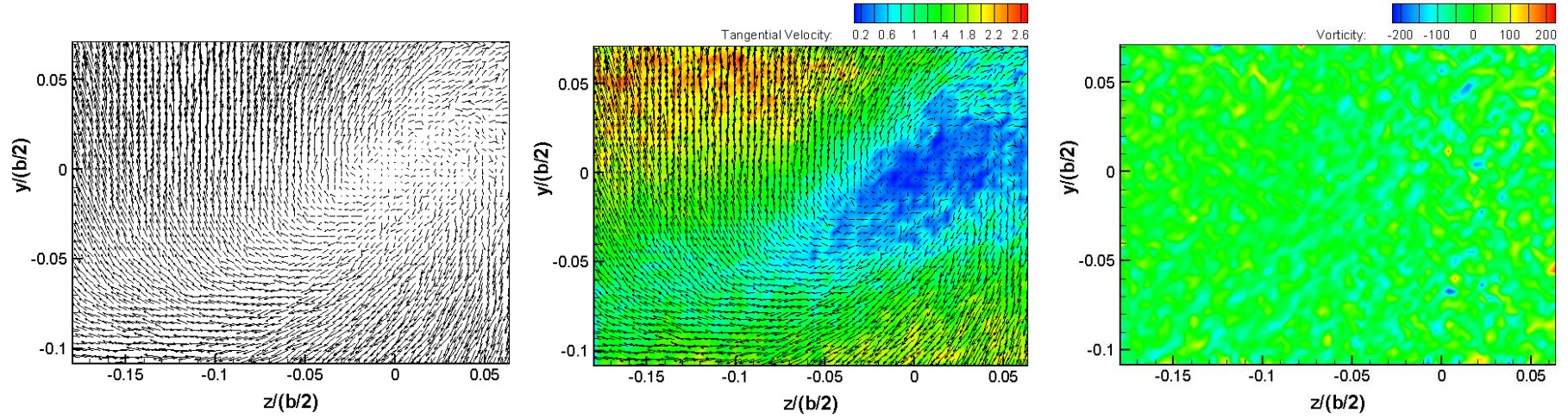
Figure 5.38: Velocity Vectors, Tangential Velocity Magnitude and Vorticity Contours at $x/(b/2)=1.075$ for (a) High Lift Configuration $\alpha=7.7^\circ$, (b) High Lift Configuration $\alpha=9.7^\circ$ with S-rdw add-on device ($\alpha_{S-rdw}=30^\circ$) and (c) High Lift Configuration $\alpha=9.7^\circ$ with L-rdw add-on device ($\alpha_{L-rdw}=30^\circ$).



a) High Lift Configuration case, $\alpha=7.7^\circ$, $x/(b/2)=2.387$, $V_\infty=12$ m/s.



b) High Lift Configuration case, $\alpha=9.7^\circ$; with S-rdw add-on device, $\alpha_{S-rdw}=30^\circ$, $x/(b/2)=2.387$, $V_\infty=12$ m/s.



c) High Lift Configuration case, $\alpha=9.7^\circ$; with L-rdw add-on device, $\alpha_{Lrdw}=30^\circ$, $x/(b/2)=2.387$, $V_\infty=12$ m/s.

Figure 5.39: Velocity Vectors, Tangential Velocity Magnitude and Vorticity Contours at $x/(b/2)=2.387$ for (a) High Lift Configuration $\alpha=7.7^\circ$, (b) High Lift Configuration $\alpha=9.7^\circ$ with S-rdw add-on device ($\alpha_{S-rdw}=30^\circ$) and (c) High Lift Configuration $\alpha=9.7^\circ$ with L-rdw add-on device ($\alpha_{L-rdw}=30^\circ$).

5.5.3 Aerodynamic Performance

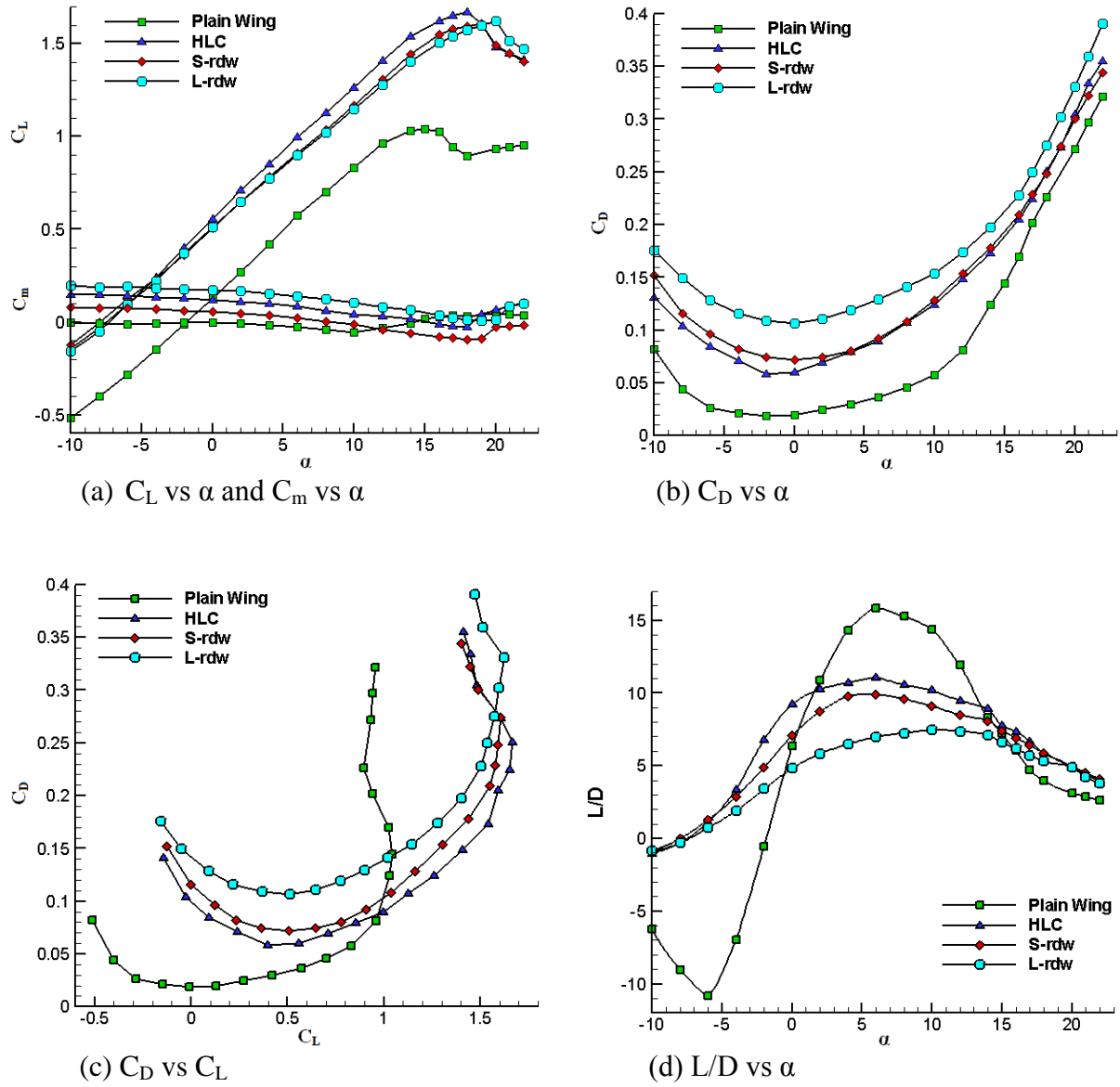


Figure 5.40: Aerodynamic performance of the Plain Wing, HLC, HLC with S-rdw and HLC with L-rdw.

The trend of figure 5.40 is similar to the other cases discussed earlier. Figure 5.40a shows that the stall of the wing is delayed by 2° when the L-rdw is used. The reduction in the lift coefficient values between the HLC, S-rdw and L-rdw cases is 3.6%.

The drag increment (compared with the HLC drag as the base value at target lift coefficient) for S-rdw case is 8.9% and for L-rdw case is 23.6%. To maintain the target lift

coefficient, it was found that an increase of 1.0° in the angle of attack of the wing is required to compensate for the reduction of lift when the add-on device is used.

Table 5.6
Overall findings of Case 4

Vortex Core Size	Tangential Velocity	Vorticity	Lift Coefficient	Drag Coefficient
+340% (factor of 4.40)	-55.3%	-87.5%	-3.6%	+23.6%

‘+’ indicates increase

‘-’ indicates decrease

It can be concluded that Case 4 is not a practical solution to wake vortex alleviation because the drag penalty associated with it is high.

5.6 CASE 5

Half-span wing model landing configuration for case 5 is as below:

Location of add-on device: as shown in Figure 5.41

Deflection of add-on device: $\alpha_{rdw} = 0^\circ$, $\phi_{rdw} = -30^\circ$

Slat deflection: 15°

Flap deflection: 20°

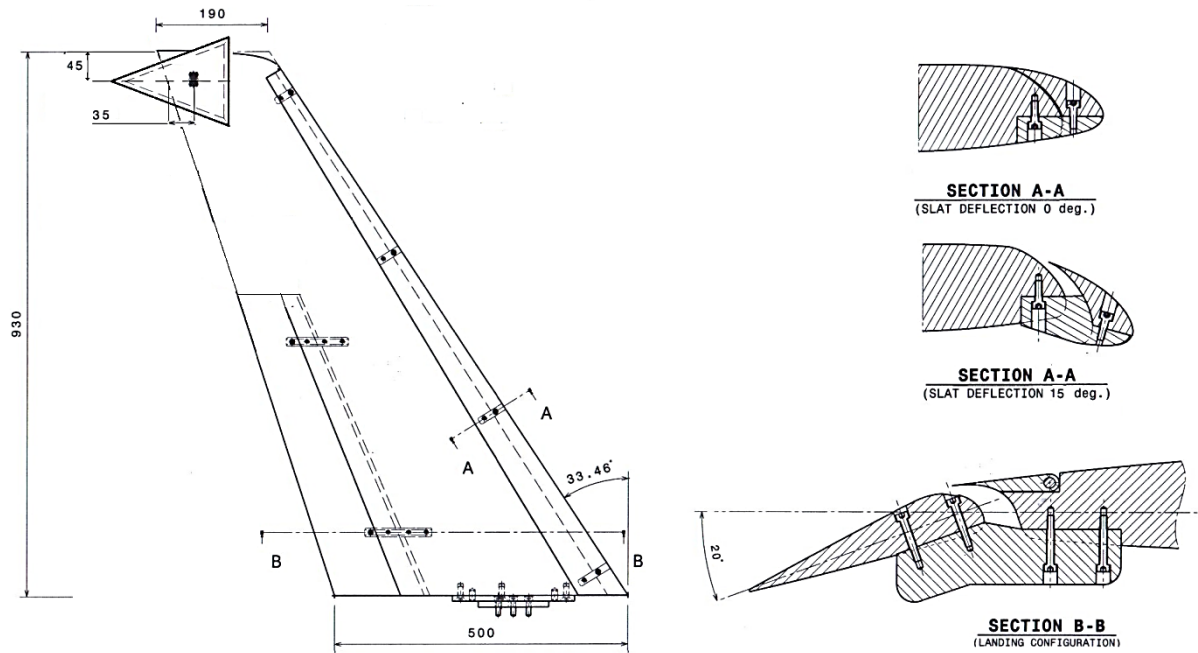


Figure 5.41: Schematic of the half-span wing model with a large reverse delta type add-on device attached. Linear dimensions are in millimetres (mm).

The configuration in Figure 5.41 was used to investigate the effect of roll angle of the reverse delta type add-on device on the resultant vortex structure behind the half-span wing at the wingtip location. The camera is focused at the half-span model wingtip. Only roll angle of the add-on device is changed whereas the angle of attack of the add-on device is fixed at $\alpha_{rdw}=0^\circ$ (not same as earlier cases). The add-on device roll angles selected were $\phi_{rdw}=\pm 20^\circ$, $\pm 30^\circ$. Positive roll angle indicates that the add-on device is rotated clockwise, whereas negative roll angle indicates that the add-on device is rotated counter-clockwise (as seen by the camera which is placed downstream of the half-span wing model). Both S-rdw and L-rdw

cases were studied. It was found that roll angle $\phi = -30^\circ$ yields the best results in terms of tangential velocity and vorticity reduction (see Figures 5.42 and 5.43).

From Figures 5.42 and 5.43, it can be concluded that the largest tangential velocity and vorticity reduction for the S-rdw and L-rdw occurs when the add-on device is at roll angle $\phi = -30^\circ$. This is the reason the researcher has only plotted the PIV results for roll angle $\phi = -30^\circ$ as the other three roll angles yield slightly stronger vortex structures (less wake vortex alleviation).

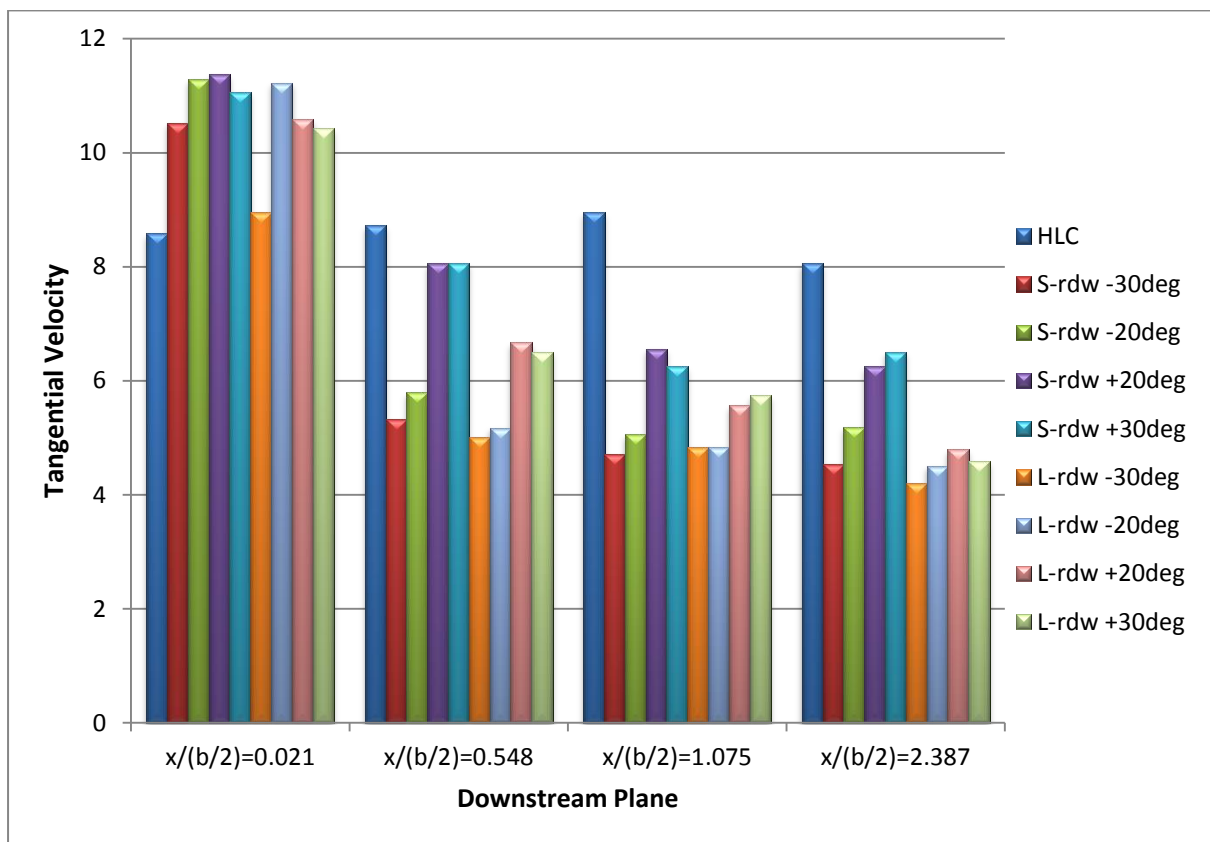


Figure 5.42: Peak tangential Velocity magnitude of all investigated configurations at four downstream planes for Case 5.

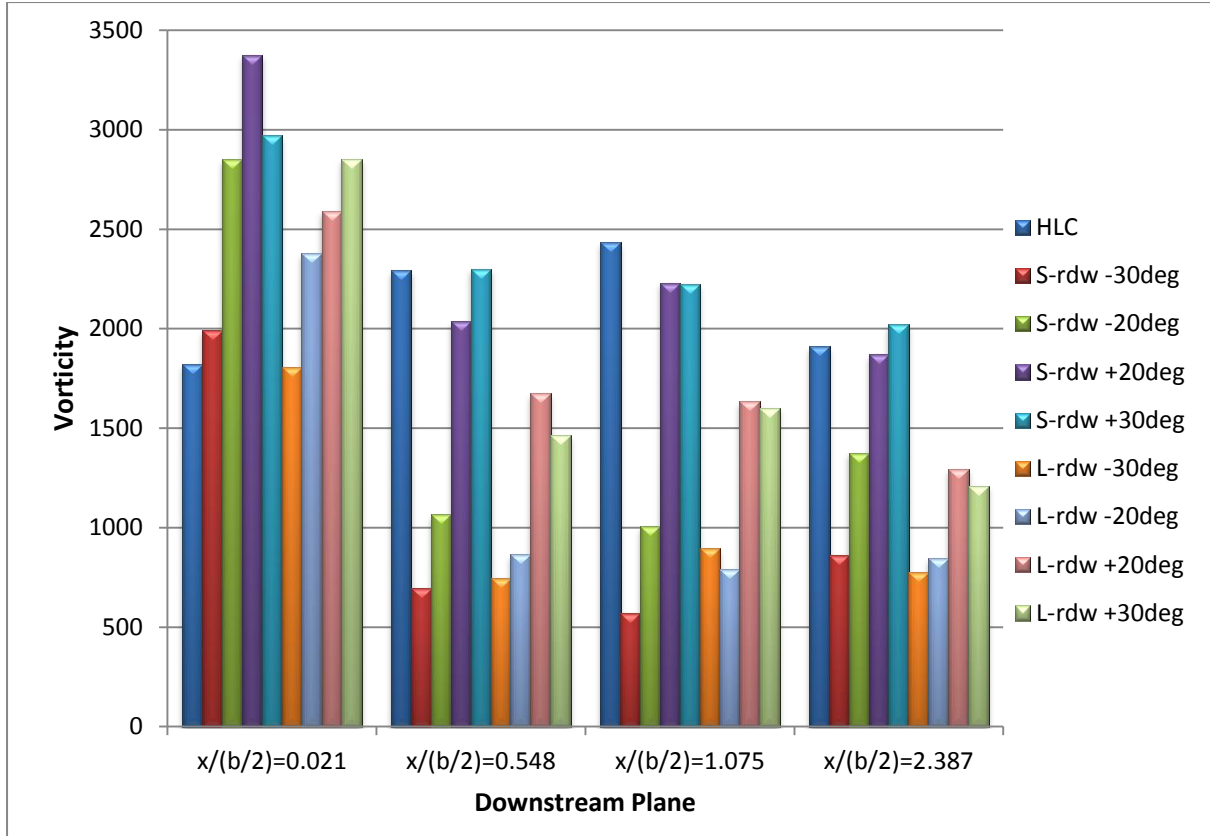


Figure 5.43: Vorticity magnitude of all investigated configurations at four downstream planes for Case 5.

5.6.1 Velocity Vectors and Vorticity

The purpose of the above half-span wing model with reverse delta type add-on device configuration is to investigate if the vortices shed by the reverse delta type add-on device at roll angle $\phi = -30^\circ$ are able to implant an instability that grows rapidly into the wingtip vortex and alters the roll-up process of the wingtip vortex. The add-on device vortices and the wingtip vortex are expected to merge downstream and instigate significant wake vortex alleviation.

Figures 5.44 to 5.47 show the velocity vectors of a half-span wing model at HLC with/without a reverse delta type add-on device attached at a location near the half-span model wingtip. The results are obtained at four downstream planes; $x/(b/2) = 0.021, 0.548, 1.075$ and 2.387 .

Figures 5.44b and 5.44c show that the add-on device vortices merge with the wingtip vortex of the half-span model. Two vortex cores are clearly visible in figure 5.44c. The tangential velocity and vorticity magnitudes are higher than the HLC because the inclusion of the add-on device accelerates the flow in the vicinity of the add-on device.

From Figures 5.45-5.47, the add-on device cases show that the vortex core dimension has increased significantly. Also, the tangential velocity and vorticity magnitudes have decreased significantly between downstream planes 1 to 4. The resultant vortex has a better roll up at downstream plane 4.

The vorticity contours in Figures 5.44b-c to 5.47b-c show that the resultant vortex is intact. In fact, the resultant vortex core is compact and strong. There is plenty of shed vorticity (small patches of vorticity) from the vortex core, but the vortex core itself has not broken down yet. This indicates that the resultant vortex will not diffuse as rapidly as the earlier studied cases.

The tangential velocity reduction for the HLC from downstream plane 2 to plane 4 is 7.6% only, whereas, the maximum tangential velocity reduction between HLC and HLC with add-on devices from downstream plane 2 to plane 4 is 43.6% for the S-rdw and 44.1% for the L-rdw.

The vorticity reduction for the HLC from downstream plane 2 to plane 4 is 16.6% only, whereas, the maximum vorticity reduction between the HLC and HLC with add-on device from downstream plane 2 to plane 4 is 54.9% for the S-rdw and 59.4% for the L-rdw.

The difference in the sizes of the vortex cores is evident from figures 5.44 to 5.47. At $x/(b/2)=0.548$, the resultant vortex core radius compared to the HLC vortex core radius has diffused (enlarged) by a factor of 2.81 and 3.21 for the S-rdw and L-rdw, respectively. At $x/(b/2)=1.075$, the resultant vortex core radius compared to the HLC vortex core radius has increased by a factor of 3.47 and 4.02 for the S-rdw and L-rdw, respectively. At

$x/(b/2)=2.387$, the resultant vortex core radius compared to the HLC vortex core radius has increased by a factor of 3.50 and 4.05 for the S-rdw and L-rdw, respectively.

Table 5.7
Overall findings of Case 5

Vortex Core Size	Tangential Velocity	Vorticity
+305% (factor of 4.05)	-44.1%	-59.4%

‘+’ indicates increase

‘-’ indicates decrease

It can be concluded that inducing instability into the wingtip vortex by a reverse delta type add-on device at roll angles (at zero angle of attack) does not alleviate the wake vortex as significantly as is done by a reverse delta type add-on device at angles of attack (at zero roll angle), as shown in case 1. It should be noted that the aerodynamic performance for case 5 is identical to case 1.

For ease of comparison, the findings of all investigated cases are summarized in Table 5.8 below.

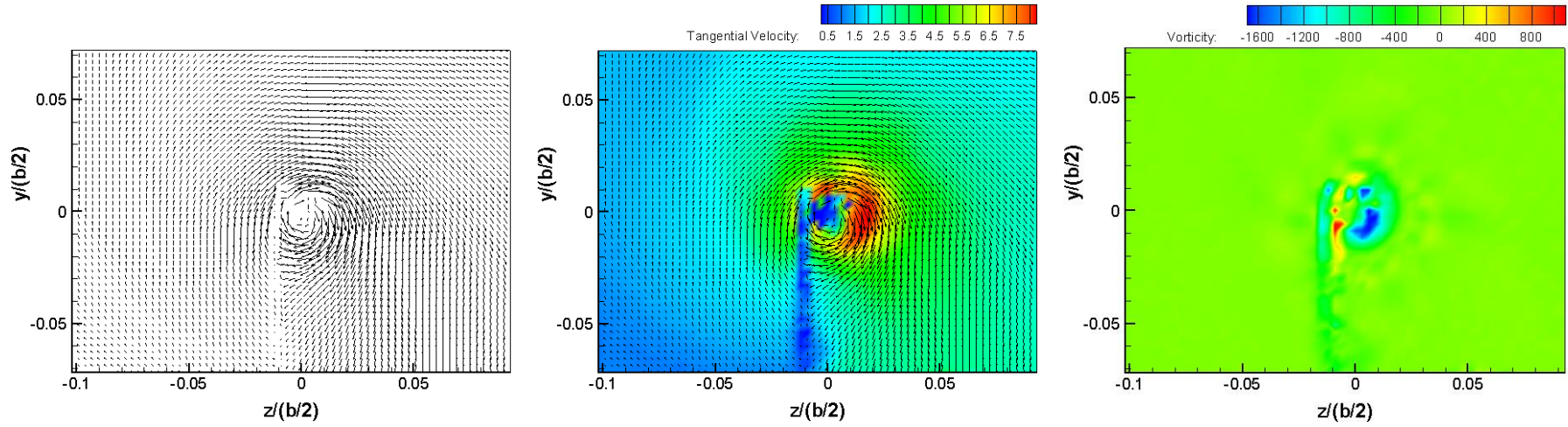
Table 5.8
Findings of all cases studied

Case	Vortex Core Size	Tangential Velocity	Vorticity	Lift Coefficient	Drag Coefficient
1	+557% (factor of 6.57)	-82.9%	-92.6%	-4.9%	+15.2%
2	+463% (factor of 5.63)	-79.6%	-85.6%	-2.9%	+14.5%
3	+37% (factor of 1.37)	-36.1%	N/A	-3.8%	+14.9%

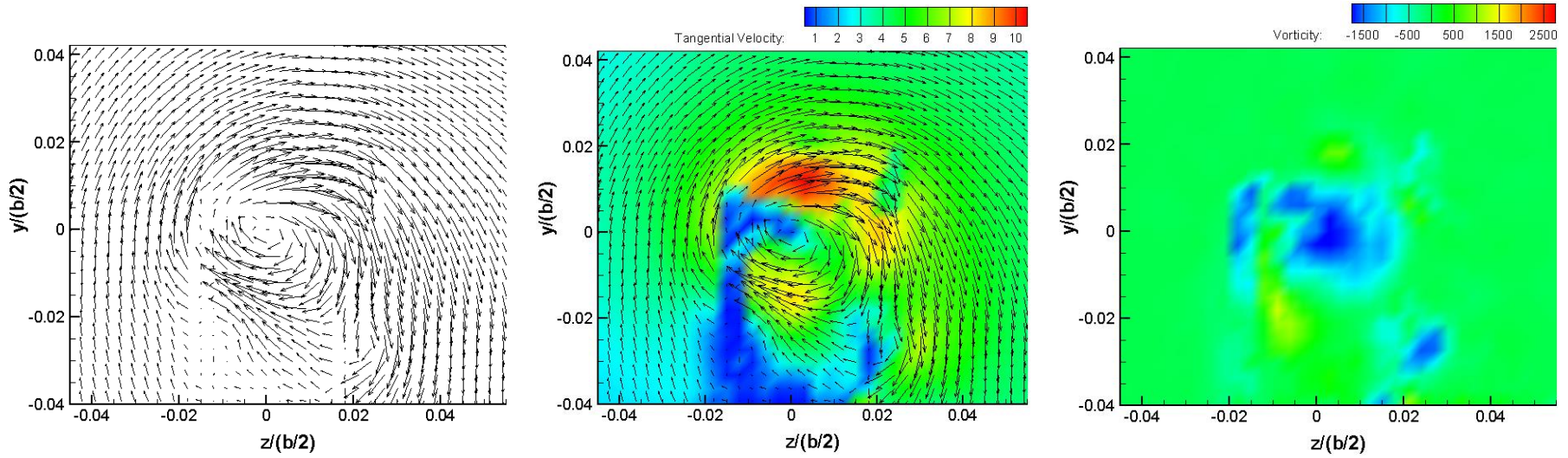
4 (wingtip)	+340% (factor of 4.40)	-55.3%	-87.5%	-3.6%	+23.6%
4 (flap-tip)	+33% (factor of 1.33)	-16.1%	N/A		
5	+305% (factor of 4.05)	-44.1%	-59.4%	-4.9%	+15.2%

‘+’ indicates increase

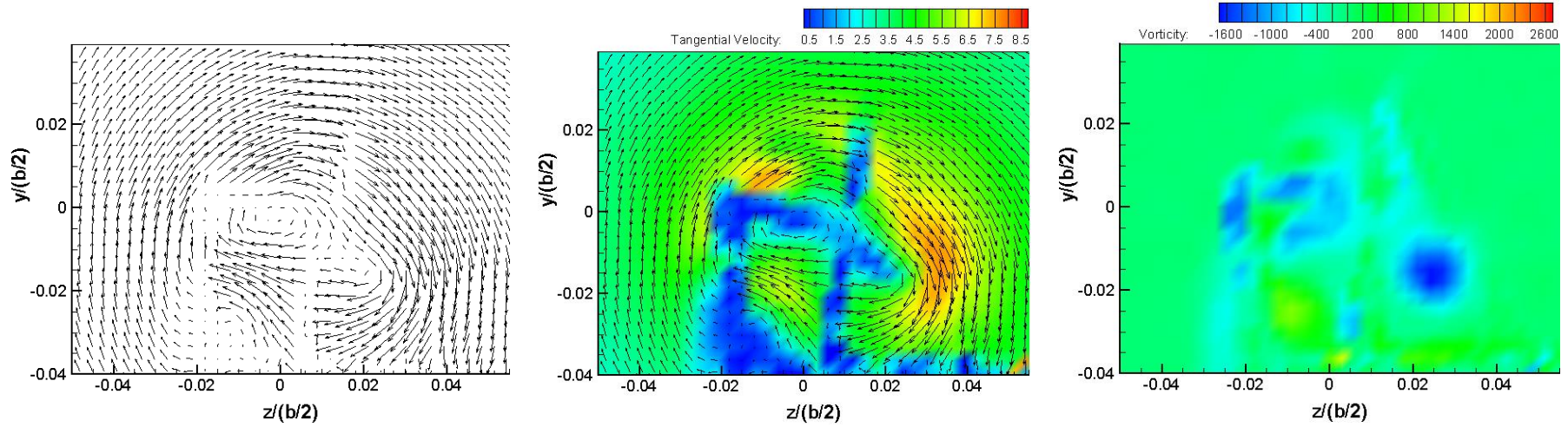
‘-’ indicates decrease



a) High Lift Configuration case, $\alpha=7.7^\circ$, $x/(b/2)=0.021$, $V_\infty=12$ m/s.

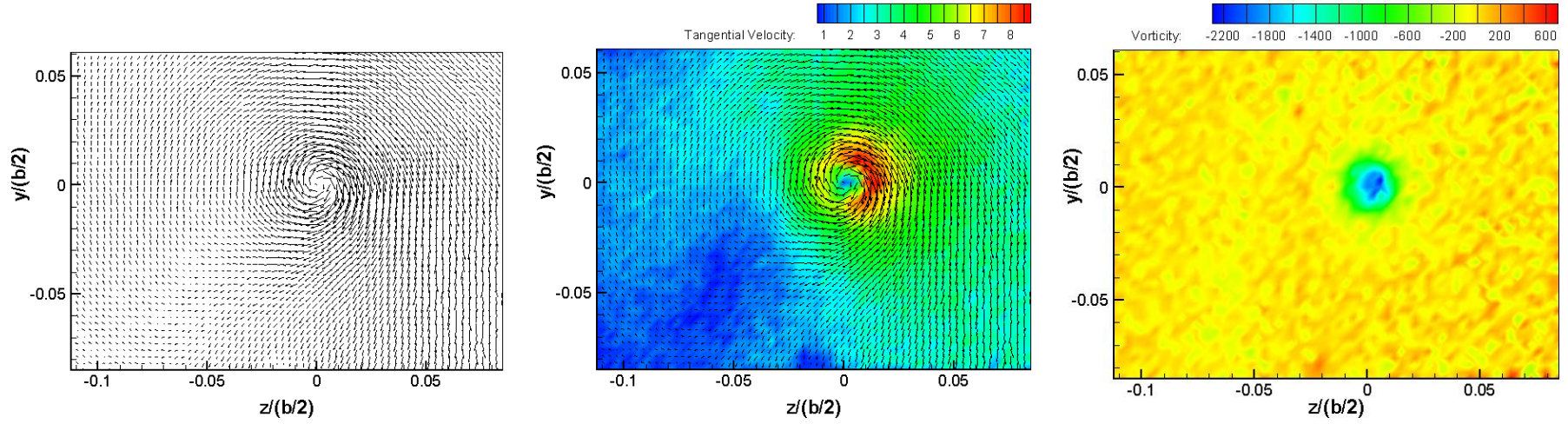


b) High Lift Configuration case, $\alpha=9.7^\circ$; with S-rdw add-on device, $\phi_{S-rdw} = -30^\circ$, $x/(b/2)=0.021$, $V_\infty=12$ m/s.

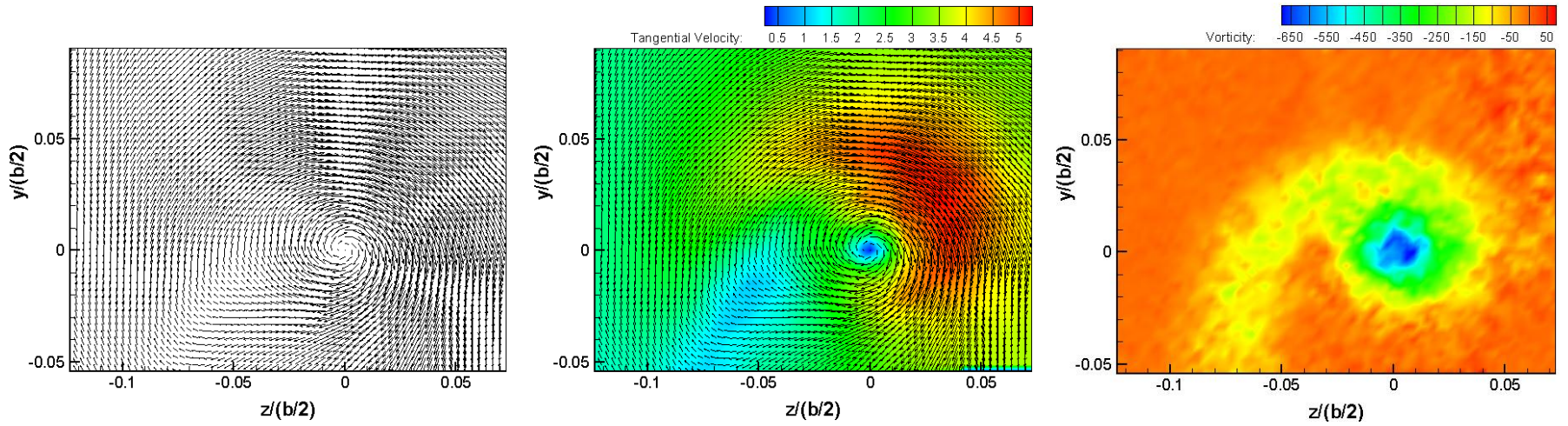


c) High Lift Configuration case, $\alpha=9.7^\circ$; with L-rdw add-on device, $\phi_{L-rdw} = -30^\circ$, $x/(b/2)=0.021$, $V_\infty=12$ m/s.

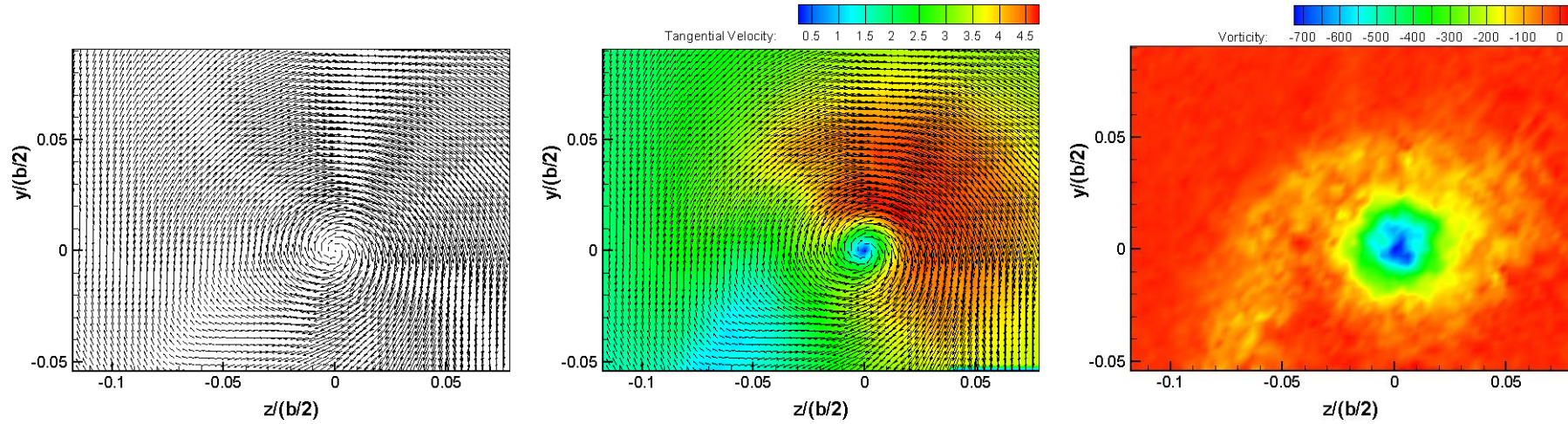
Figure 5.44: Velocity Vectors, Tangential Velocity Magnitude and Vorticity Contours at $x/(b/2)=0.021$ for (a) High Lift Configuration $\alpha=7.7^\circ$, (b) High Lift Configuration $\alpha=9.7^\circ$ with S-rdw add-on device ($\phi_{S-rdw} = -30^\circ$) and (c) High Lift Configuration $\alpha=9.7^\circ$ with L-rdw add-on device ($\phi_{L-rdw} = -30^\circ$).



a) High Lift Configuration case, $\alpha=7.7^\circ$, $x/(b/2)=0.548$, $V_\infty=12$ m/s.

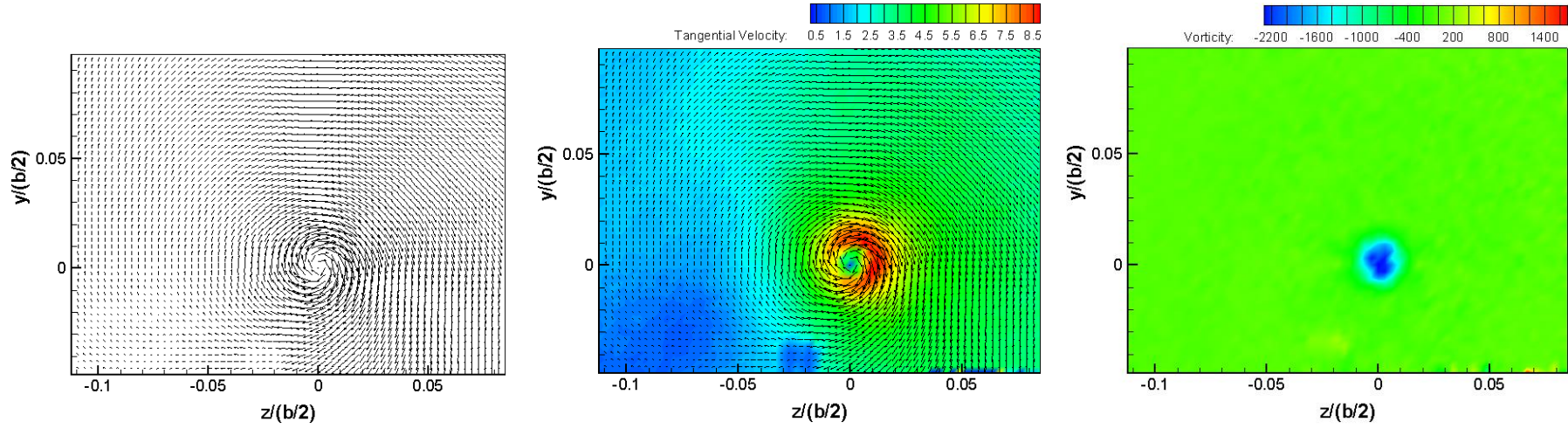


b) High Lift Configuration case, $\alpha=9.7^\circ$; with S-rdw add-on device, $\phi_{S-rdw}=-30^\circ$, $x/(b/2)=0.548$, $V_\infty=12$ m/s.

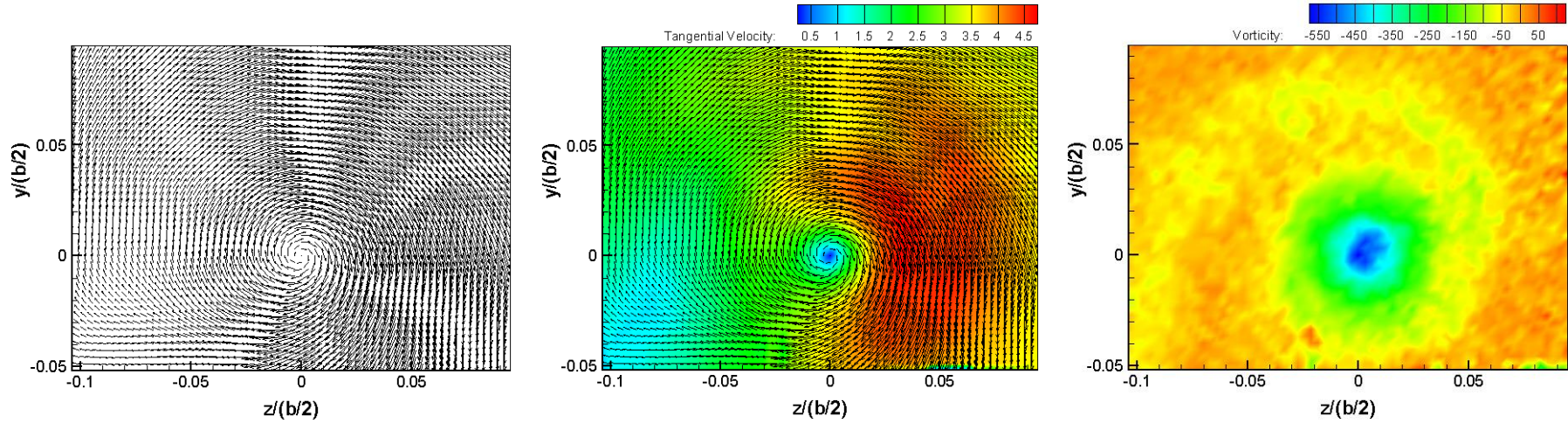


c) High Lift Configuration case, $\alpha=9.7^\circ$; with L-rdw add-on device, $\phi_{L-rdw} = -30^\circ$, $x/(b/2)=0.548$, $V_\infty=12$ m/s.

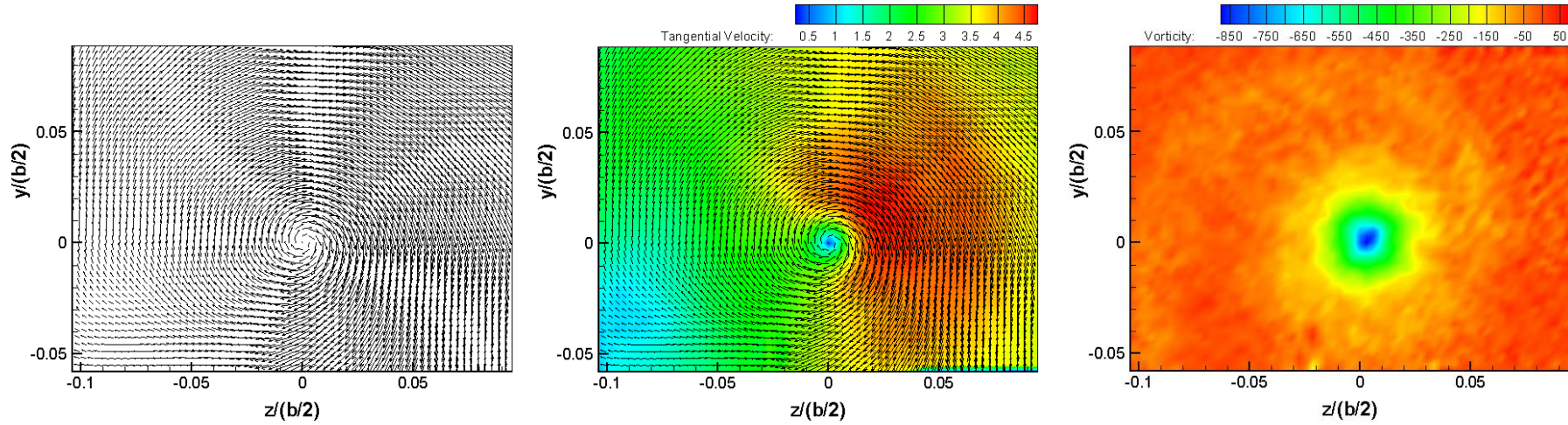
Figure 5.45: Velocity Vectors, Tangential Velocity Magnitude and Vorticity Contours at $x/(b/2)=0.548$ for (a) High Lift Configuration $\alpha=7.7^\circ$, (b) High Lift Configuration $\alpha=9.7^\circ$ with S-rdw add-on device ($\phi_{S-rdw} = -30^\circ$) and (c) High Lift Configuration $\alpha=9.7^\circ$ with L-rdw add-on device ($\phi_{L-rdw} = -30^\circ$).



a) High Lift Configuration case, $\alpha=7.7^\circ$, $x/(b/2)=1.075$, $V_\infty=12$ m/s.

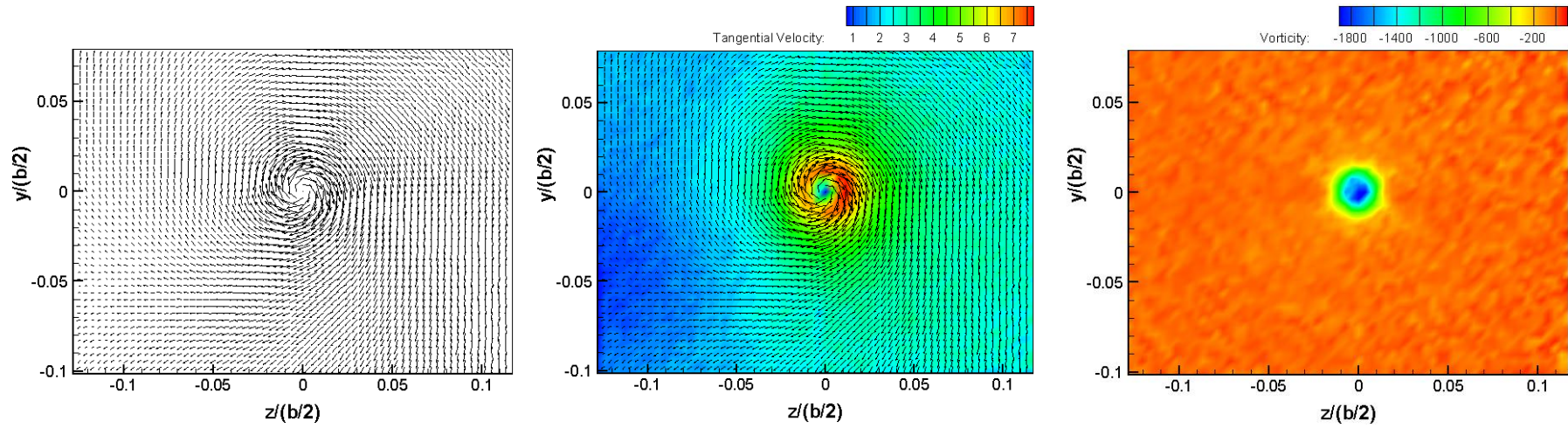


b) High Lift Configuration case, $\alpha=9.7^\circ$; with S-rdw add-on device, $\phi_{S-rdw}=-30^\circ$, $x/(b/2)=1.075$, $V_\infty=12$ m/s.

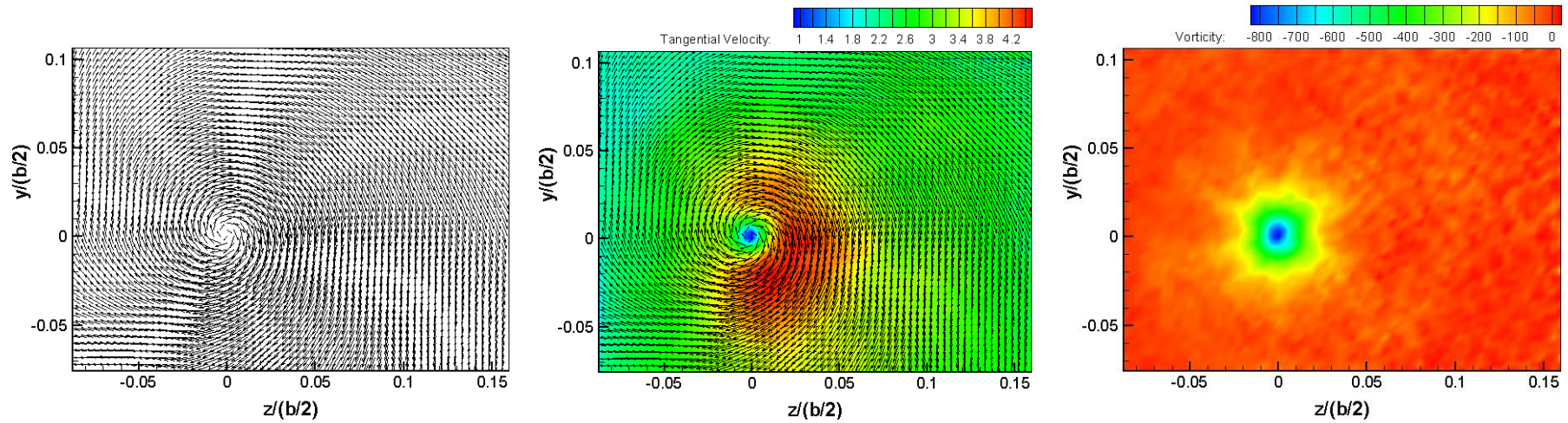


c) High Lift Configuration case, $\alpha=9.7^\circ$; with L-rdw add-on device, $\phi_{L-rdw} = -30^\circ$, $x/(b/2)=1.075$, $V_\infty=12$ m/s.

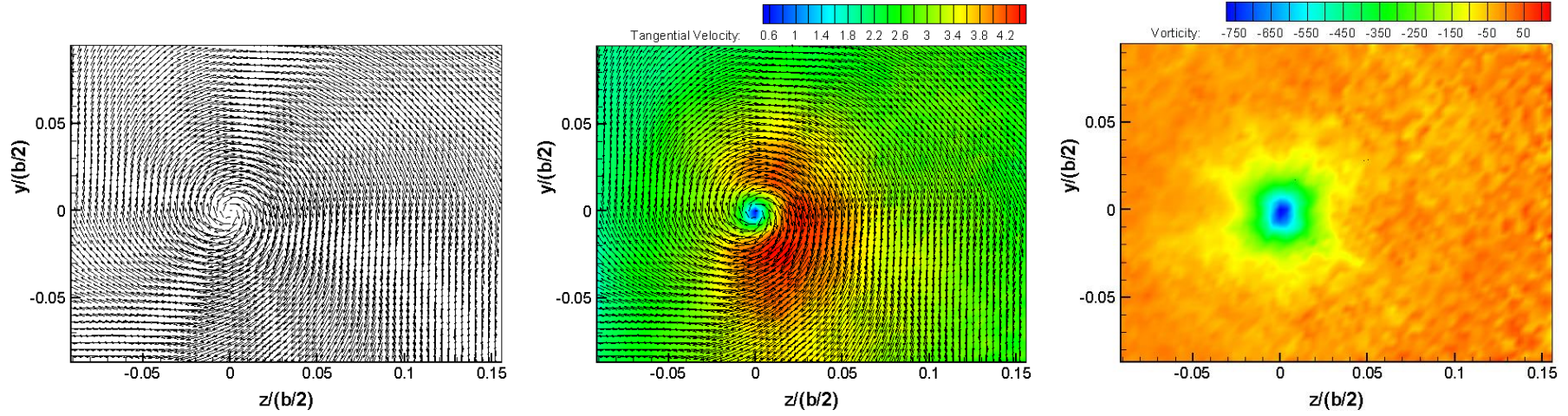
Figure 5.46: Velocity Vectors, Tangential Velocity Magnitude and Vorticity Contours at $x/(b/2)=1.075$ for (a) High Lift Configuration $\alpha=7.7^\circ$, (b) High Lift Configuration $\alpha=9.7^\circ$ with S-rdw add-on device ($\phi_{S-rdw} = -30^\circ$) and (c) High Lift Configuration $\alpha=9.7^\circ$ with L-rdw add-on device ($\phi_{L-rdw} = -30^\circ$).



a) High Lift Configuration case, $\alpha=7.7^\circ$, $x/(b/2)=2.387$, $V_\infty=12$ m/s.



b) High Lift Configuration case, $\alpha=9.7^\circ$; with S-rdw add-on device, $\phi_{S-rdw}=-30^\circ$, $x/(b/2)=2.387$, $V_\infty=12$ m/s.



c) High Lift Configuration case, $\alpha=9.7^\circ$; with L-rdw add-on device, $\phi_{L-rdw} = -30^\circ$, $x/(b/2)=2.387$, $V_\infty=12$ m/s.

Figure 5.47: Velocity Vectors, Tangential Velocity Magnitude and Vorticity Contours at $x/(b/2)=2.387$ for (a) High Lift Configuration $\alpha=7.7^\circ$, (b) High Lift Configuration $\alpha=9.7^\circ$ with S-rdw add-on device ($\phi_{S-rdw} = -30^\circ$) and (c) High Lift Configuration $\alpha=9.7^\circ$ with L-rdw add-on device ($\phi_{L-rdw} = -30^\circ$).

5.7 Lift and Drag Penalties of Wake Vortex Alleviation Methods

Some of the investigators listed in the table below have used more than one configuration for wake vortex alleviation. The configuration which yielded the largest reduction in lift and largest increment in drag has been selected and presented in Table 5.9. The percentage changes are computed with reference to the baseline configuration. Lift and drag changes, as shown in Table 5.9, were in some cases obtained from the lift and drag curves from the investigators' work as some had not directly stated the lift reduction and drag increment. Below are brief descriptions of the model and device configurations used by the investigators mentioned in Table 5.9.

Table 5.9
Comparison of lift and drag penalties with other wake vortex alleviation techniques

Authors	Device	Lift Reduction	Drag Increment
D. R. Croom, 1976	Spoilers	7.5%	15%
D. R. Croom, R. D. Vogler & J. A. Thelander, 1976	Spoilers	10.8%	21.1%
D. R. Croom, R. D. Vogler & G. M. Williams, 1976	Spoilers	6.5%	21.1%
V. J. Rossow, 1978	Fins	No lift penalty	10%
D. R. Croom & G. T. Holbrook, 1979	Fins	13.3%	28.6%
D. R. Croom, 1979	Spoilers	9.2%	28.6%
J. D. Crouch, G. D. Miller & P. R. Spalart, 2001	Wing control surfaces	6.0%	Unavailable
E. Ozger, I. Schell & D. Jacob, 2001	Wing control surfaces and fins	7.0%	Unavailable
O. A. Elsayed, 2010	Spoilers	9.1%	Unavailable
Breitsamter, 2011	Double delta spoiler	2.9%	Unavailable
Present Study	Reverse delta type add-on device	4.9%	15.2%

In Croom (1976) all data was obtained with a transport aircraft model at a trimmed lift coefficient of 1.2, ($C_{L,trim}=1.2$). All tests were conducted with leading edge devices extended. Flight spoiler segments 1 and 2 were deflected by 45°.

The data in Croom et al. (1976) was obtained using a transport aircraft model at a trimmed lift coefficient of 1.2, ($C_{L,trim}=1.2$). Flight spoiler segments 1 and 2 were deflected by 60° at landing flap configuration and landing gear down.

Croom et al. (1976) obtained data with a transport aircraft model at a trimmed lift coefficient of 1.2, ($C_{L,trim}=1.2$). All tests were performed with leading edge devices and landing gear extended. Flight spoiler segments 2 and 3 were deflected by 60° at landing flap configuration.

Rossow (1978) used a rectangular planform fin (fin chord=10.5cm, fin height=5.25cm). All tests were conducted with leading edge devices extended, landing gear down and landing flaps deflected to 30° . Most of the tests were performed with $\alpha_{fin}=18^\circ$.

In Croom et al. (1979) the data was obtained with a transport aircraft model at a trimmed lift coefficient of 1.2, ($C_{L,trim}=1.2$). All tests were conducted with leading edge devices extended, landing gear down and landing flaps deflected to 30° . Two fin configuration was used at a fin incidence angle of 36° .

Croom (1979) gives results obtained with a transport aircraft model at a trimmed lift coefficient of 1.2, ($C_{L,trim}=1.2$). All tests were performed with leading edge devices extended, landing gear down and landing flaps deflected to 30° . Flight spoilers 1, 2, 3 and 4 were deflected by 45° .

In Crouch et al. (2001) tests were performed at flaps down configuration to trigger the breakup of trailing vortices.

Ozger et al. (2001) conducted tests with wing control surfaces at a slat deflection angle of 25° , flap deflections 0° , 10° and 20° . Tests with fins were carried out at slat deflection 25° , flap deflection 20° and fin incidence angles -20° and 20° .

Elsayed et al. (2010) obtained data using a half aircraft model at a target lift coefficient of 0.797. All tests were performed with the leading edge devices extended by 15° and landing flaps deflected by 20° . Flight spoilers 5 and 6 were deflected by 40° .

Breitsamter (2011) conducted tests with a double swept leading edge spoiler. Spoiler incidence angle is 25° .

For the present study, the data was obtained with half-span wing model at a target lift coefficient of 1.06. All tests were made with leading edge devices extended by 15° and landing flaps deflected by 20° . Reverse delta type add-on device incidence angle is set to 30° .

It can be seen from Table 5.9 that the reverse delta type add-on device minimally affects the aerodynamic performance of the half-span wing model compared to other wake vortex alleviation techniques. The present study yields significantly lower drag increment compared to most of the other studies summarized in Table 5.9. The reduction in lift caused by the use of the reverse delta type add-on device is minimum compared to most of the wake vortex alleviation devices that are listed in Table 5.9.

Therefore, it can be concluded that the use of a reverse delta type add-on device has minimal detrimental effect on the aerodynamic performance of the half-span wing model.

5.8 SUMMARY

This chapter provides an elaborate account of the findings of five cases that have been studied. The findings point out that among the five cases, case 1 (where add-on device is attached near the wingtip) yields the best wake vortex alleviation results. Case 1 yields the greatest reduction in tangential velocity (82.9%), vorticity (92.6%) and circulation (42.8%) magnitudes when L-rdw is used. Case 1 also yields the greatest increase in the resultant vortex core dimension (factor of 6.57) when L-rdw is used. Hence, it can be claimed that significant wake vortex alleviation is possible by the use of a reverse delta type add-on

device. The six component force balance results indicate that the aerodynamic performance of the half-span wing model is only marginally adversely affected by the use of a reverse delta type add-on device, except case 4 in which the drag penalty is very large.

CHAPTER SIX

CONCLUSIONS AND RECOMMENDATIONS

6.1 CONCLUSIONS

The objectives of the research work have been achieved and analysis of the data collected has led to several new findings. The following conclusions can be drawn from the research work:

1. As the angle of attack of the reverse delta type add-on device increases (within the range that was studied), the tangential velocity magnitude, vorticity magnitude and circulation magnitude decreases for the resultant vortex for all cases studied.
2. The resultant vortex structure of the half-span wing model with a reverse delta type add-on device attached near the wingtip/flap-tip exhibits weaker roll-up than the resultant vortex structure of the half-span wing model alone, indicative of a weak vortex.
3. The resultant vortex structure downstream of the half-span wing model with a reverse delta type add-on device is more enlarged and diffused than the vortex structure of the half-span wing model alone.
4. From case 1 configuration, the maximum reduction recorded in the tangential velocity, vorticity and circulation magnitude is 82.9%, 92.6% and 42.8%, respectively, for L-rdw for case 1 when the add-on device is attached near the wingtip at an angle of attack $\alpha_{rdw} = +30^\circ$ and roll angle $\phi_{rdw} = 0^\circ$. At a distance of 2.387 wing half-spans ($b/2$), the resultant vortex core radius has increased by a maximum factor of 6.57 when L-rdw is used. Reduction in lift coefficient is 4.9% and increment in drag coefficient is 15.2% when L-rdw is used.

The add-on device blocks the path of travel of air from the lower wing surface to the upper wing surface at the wingtip. This yields a resultant vortex with a weaker rollup (more diffused vortex) causing an increase in the vortex core size, and reduction in tangential velocity and vorticity magnitudes. Also, interaction of the wingtip vortex with the vortices generated by the add-on device creates a vortex system with co-rotating and counter-rotating vortices (counter-sign vorticity) which experiences lower tangential velocity and vorticity magnitudes.

5. From case 2 configuration, the maximum reduction recorded in tangential velocity, vorticity and circulation magnitudes is 79.6%, 85.6% and 48.7%, respectively, for L-rdw add-on device attached mid-way from the wingtip and flap-tip at an angle of attack $\alpha_{rdw} = +30^\circ$ and roll angle $\phi_{rdw} = 0^\circ$. At a distance of 2.387 wing half-spans ($b/2$), the resultant vortex core radius has increased by a maximum factor of 5.63 when L-rdw is used. Reduction in lift coefficient is 2.9% and increment in drag coefficient is 14.5% when L-rdw is used.
6. From case 3 configuration, the maximum reduction recorded in tangential velocity magnitude is 36.1% for L-rdw add-on device attached near the flap-tip at an angle of attack $\alpha_{rdw} = +30^\circ$ and roll angle $\phi_{rdw} = 0^\circ$. At a distance of 2.387 wing half-spans ($b/2$), the resultant vortex core radius has increased by a maximum factor of 1.37 when L-rdw is used. Reduction in lift coefficient is 3.8% and increment in drag coefficient is 14.9% when L-rdw is used.
7. From case 4 (two add-on device) configuration, the maximum reduction in tangential velocity and vorticity magnitudes recorded for the resultant wingtip vortex is 55.3% and 87.5%, respectively, and the maximum reduction in tangential velocity for the resultant flap-tip vortex is 16.1%, when L-rdw is used at an angle of attack $\alpha_{rdw} = +30^\circ$ and roll angle $\phi_{rdw} = 0^\circ$. At a distance of 2.387 wing half-spans ($b/2$), the

resultant wingtip and flap-tip vortex core radius has increased by a maximum factor of 4.40 and 1.33, respectively, when L-rdw is used. Reduction in lift coefficient is 3.6% and increment in drag coefficient is 23.6% when L-rdw is used.

8. From case 5, it can be concluded that roll angle configurations are not as effective as angle of attack configurations in alleviating the wake vortex. The maximum reduction recorded in the tangential velocity and vorticity magnitude is 44.1% and 59.4%, respectively, for L-rdw attached near the wingtip at roll angle $\phi_{rdw} = -30^\circ$ and angle of attack $\alpha_{rdw} = 0^\circ$. At a distance of 2.387 wing half-spans ($b/2$), the resultant vortex core radius has increased by a maximum factor of 4.05 when L-rdw is used.

Roll angle variation is not as effective as angle of attack variation in alleviating wake vortex because at roll angle configuration (angle of attack fixed at zero degree), add-on device vortices shed are weaker than when the add-on device is at an angle of attack configuration due to a lower pressure differential which exists between the upper and lower surfaces of the add-on device.

Weaker add-on device vortices mean that a weaker instability (counter-sign vorticity) is implanted into the wingtip vortex, resulting in less wake vortex alleviation.

9. It was found that the aerodynamic performance of the half-span wing model was only slightly adversely affected by the use of a reverse delta type add-on device. It was found that the maximum reduction in lift is 4.9% (case 1 when L-rdw is used) and the maximum increment in drag is 15.2% (case 1 when L-rdw is used). Case 4 (two L-rdw configuration) has been classified as impractical due to the large drag increment of 23.6% associated with it, which happens to be a major problem with passive control techniques.
10. The uncertainty in velocity measurements due to statistical uncertainty, uncertainty in the half-span wing angle of attack and uncertainty in displacement yields a

satisfactory and acceptable result of $\Delta V = \pm 0.188$ m/s, which corresponds to an uncertainty in vorticity, $\Delta \zeta = \pm 99.6$ s⁻¹.

11. Case 1 and case 2 configurations are most effective in wake vortex alleviation for both S-rdw and L-rdw at an angle of attack $\alpha_{rdw} = +30^\circ$ and roll angle $\phi_{rdw} = 0^\circ$ because largest reductions in tangential velocity, vorticity and circulation magnitudes are attained.

6.2 RECOMMENDATIONS FOR FURTHER STUDIES

More research is required to bring out the full potential of a reverse delta type add-on device has and it's capability to successfully alleviate the wake vortex hazard. Practical considerations will also need to be considered when implementing on actual aircraft. Issues that need to be addressed are listed as follows:

1. Optimization study to determine the best design for the reverse delta type add-on device has to be performed and would be crucial in minimizing any negative impact on aerodynamic performance of the wing. The study should determine the best size and location of the reverse delta type add-on device to maximize its effectiveness as a wake vortex alleviation device. Design improvements of the study could result in increased resultant vortex decay with minimal lift and drag penalties. The study should be performed on a multi-element wing more representative of an actual aircraft wing. Present study indicates that a large reverse delta type add-on device (L-rdw) attached near the wingtip at high angles of attack ($\alpha_{rdw} \geq 30^\circ$) alleviates wake vortex significantly.
2. The reverse delta type add-on device would be deployed only during take-off and landing and would be embedded within the wing when not in use. A study of the extension of the add-on device (using actuators) in flight or in the wind tunnel with

wind on condition should be studied to note the immediate effect on the change in aerodynamic performance of the wing.

3. High accuracy experimental and computational investigations of the far wakes of aircraft with a reverse delta type add-on device are necessary to determine exactly how much spacing rules can be modified with no compromise in the level of safety. These studies will need to account for realistic airport conditions and variable atmospheric effects. Issues such as ground effect, wind, atmospheric turbulence, and thermal currents will need to be addressed.
4. The effect of the mounting height of the reverse delta type add-on device is to be studied extensively as it could have a great impact on the half-span wing model aerodynamics and flow characteristics. The present study is conducted with a mount height of 35 mm. Present study highlights that a small mount height is able to accelerate the flow between the main wing and the add-on device allowing the stall angle of the main wing to be increased by 1° . However, a large mount height may have its benefits too. Mount heights in the range of 20 mm to 60 mm are suggested for future studies.
5. A reverse delta type add-on device at a combination of roll and pitch angles should be tested on a multi-element wing model in the wind tunnel. In chapter 5, the add-on device was only either in roll or in pitch motion. It is suspected that if the add-on device is positioned in a combination of roll and pitch angles (e.g. $\alpha_{rdw} = +30^\circ$, $\phi_{rdw} = -30^\circ$), it may further alleviate the wake vortex generated by the half-span wing model.

6.3 SUMMARY

This chapter summarizes the findings of the research work and also provides recommendations for further studies of the reverse delta type add-on device as a wake vortex

alleviation technique. A reverse delta type add-on device attached near the wingtip at an angle of attack $\alpha_{rdw} = +30^\circ$ and roll angle $\phi_{rdw} = 0^\circ$ is observed to be the best case study in terms of maximum reductions in tangential velocity, vorticity and circulation magnitudes. This case study also indicates an increase in the resultant vortex core radius compared with the wingtip vortex core radius by a factor of 6.57 (557%). Aerodynamic performance of the half-span wing for all configurations is only slightly adversely affected by the use of a reverse delta type add-on device, except case 4 configuration in which the associated drag increment is very large.

References

- Altaf, A., Omar, A. A., Asrar, W. & Ludin, H. B. (2011). "*A study of the reverse delta wing*", Journal of Aircraft 48(1), pp. 277-286.
- Altaf, A., Thong, T. B., Omar, A. A. & Asrar, W. (2015). "*Influence of a reverse delta type add-on device on wake vortex alleviation*", AIAA Journal, doi: 10.2514/1.J054436.
- "*American Airlines Flight 587*", 12 November 2001. Retrieved from https://en.wikipedia.org/wiki/American_Airlines_Flight_587.
- Anderson, J. D. (2001). "*Fundamentals of aerodynamics*", 3rd ed., McGraw Hill, Singapore, pp. 215.
- Andrews, W. H. (1970). "*Flight evaluation of the wing vortex wake generated by large jet transports*", Symposium on Aircraft Wake Turbulence, Seattle, September, 1970.
- Arndt, R.E.A., Arakeri, V.H. & Higuchi, H. (1991). "*Some observations of tip vortex cavitation*", Journal of Fluid Mechanics, Vol. 229, pp. 269-289.
- Babie, B. M. & Nelson, R. C. (2004). "*Flow visualization study of far field wake vortex interactions*", 11th International Symposium on Flow Visualization, University of Notre Dame, Notre Dame, IN.
- Barber, M. R. & Tymczyszyn, J. J. (1980). "*Wake vortex attenuation flight tests: A Status Report*", NASA CP-2170.
- Barlow, J. B., Rae, W. H., & Pope, A. (1999). "*Low-speed wind tunnel testing*", 3rd edition, New York: John Wiley & Sons, pp. 367-427.
- Bearman, P., A. Heyes, C. Lear, & D. Smith (2006). "*Natural and forced evolution of a counter rotating vortex pair*", Experiments in Fluids 40(1), pp. 98–105.
- Bellastrada, C. & Breitsamter, C. (2006). "*Effect of differential flap settings on the wake vortex evolution of large transport aircraft*", Notes on Numerical Fluid Mechanics and Multidisciplinary Design, NNFM, vol. 92, Springer Verlag; pp. 25–32.
- Bilanin, A. J. & Widnall, S. E. (1973). "*Aircraft wake dissipation by sinusoidal instability and vortex breakdown*", AIAA Paper, pp. 73–107.
- Breitsamter, C. (2011). "*Wake vortex characteristics of transport aircraft*", Progress in Aerospace Sciences, 47(10), pp. 89-134.
- Butler, K. M. (1993). "*Estimation of wake vortex advection and decay using meteorological sensors and aircraft data*", DOT/FAA/RD-93/16, 28 September, pp. 1-36.
- Chevalier, H. (1973). "*Flight test studies of the formation and dissipation of trailing vortices*", Journal of Aircraft 10(1), 14–18.

- Combe, H., Kopp, F. & Keane, M. (2000). *“On-board wake vortex detection: Definition, ground experimentation and results in the MFLAME E.C. programme”*, Presentation at the third Wake-Net workshop, 22-23 May.
- Corsiglia V. R. , Jacobsen R.A. & Chigier N. (1971). *“An experimental investigation of trailing vortices behind a wing with a vortex dissipater”*, Aircraft Wake turbulence and its detection, Plenum Press, pp. 229-242.
- Coustols, E., Jacquin, L. & Schrauf, G. (2006). *“Status of wake vortex alleviation in the framework of european collaboration: validation attempts using tests and CFD results”*, European Conference on Computational Fluid Dynamics ECCOMAS CFD, TU Delft, The Netherlands, pp. 1-20.
- Coustols, E. (2006). *“An overview of European projects on wake vortices”*, Proceedings of the Workshop on "Principles of Wake Vortex Alleviation Devices, ONERA Toulouse.
- Coustols, E., Stumpf, E., Jacquin, L., Moens, F., Vollmers, H. & Gerz, T. (2003). *“Minimised wake: A collaborative research programme on aircraft wake vortices”*, AIAA Paper, pp. 2003-938.
- Croom, D. R. & Holbrook, G. T. (1979). *“Low speed wind tunnel investigation of wing fins as trailing vortex alleviation devices on a transport airplane model”*, NASA Technical Paper 1453, NASA, Washington, DC 20546.
- Croom, D. R. (1976). *“Low speed wind tunnel investigation of various segments of flight spoilers as trailing vortex alleviation devices on a transport aircraft model”*, NASA technical note 8162, NASA, Washington, DC 20546.
- Croom, D. R. (1977). *“Evaluation of flight spoilers for vortex alleviation”*, Journal of Aircraft 14 (8), pp. 823–825.
- Croom, D. R. (1979). *“Low speed wind tunnel parametric investigation of flight spoilers as trailing vortex alleviation devices on a transport aircraft model”*, NASA technical paper 1419, NASA, Washington, DC 20546.
- Croom, D. R., Vogler, R. D. & Thelander, J. A. (1976). *“Low speed wind tunnel investigation of flight spoilers as trailing vortex alleviation devices on an extended range wide body tri-jet airplane model”*, NASA technical note 8373, NASA, Washington, DC 20546.
- Croom, D. R., Vogler, R. D. & Williams, G. M. (1976). *“Low speed wind tunnel investigation of flight spoilers as trailing vortex alleviation devices on a medium range wide body tri-jet airplane model”*, NASA technical note 8360, NASA, Washington, DC 20546.
- Crouch, J. D., Miller, G. D. & Spalart, P. R. (2001). *“Active-control system for breakup of airplane trailing vortices”*, AIAA Journal 39(12), pp. 2374–2381.
- Crow S.C. (1970). *“Stability theory for a pair of trailing vortices”*, AIAA Journal, Vol. 8, No.12, pp. 2172-2179.

- Crow, S. C. & Bate, E. R. (1976). "*Lifespan of trailing vortices in a turbulent atmosphere*", Journal of Aircraft 13(7), pp. 476–482.
- Dantec Dynamics (2004). "*FlowManager software and introduction to PIV instrumentation, a software user's guide*", Malaysia.
- Dobrev, I., Maalouf, B., Troldborg, N. & Massouh, F. (2008), "*Investigation of the wind turbine vortex structure*", 14th International Symposium on Applications of Laser Techniques to Fluid Mechanics, Lisbon, Portugal.
- Durston, D. A., Walker, S. M., Driver, D. M. & Smith, S. C. (2005). "*Wake-vortex alleviation flowfield studies*", Journal of Aircraft 42(4), pp. 894–907.
- Elsayed, O. A., Asrar, W., Omar, A. A., & Kwon, K. (2010). "*Influence of differential spoiler settings on the wake vortex characterization and alleviation*", Journal of Aircraft, 47(5), pp. 1728-1738.
- Elsayed, O. A., Asrar, W., Omar, A. A., & Kwon, K. (2011). "*Effect of differential spoiler settings (DSS) on the wake vortices of a wing at high-lift-configuration (HLC)*", Journal of Aerospace Science and Technology, 15(7), pp. 555-566.
- Elsenaar, B. (2006). "*Improved wake vortex separation ruling and reduced wake signatures*", WakeNet2-Europe in collaboration with WakeNet-USA, Part 1, pp. 1-51.
- FAA. (2002). "*Air traffic control*", Order 7110.65N.
- Fabre, D., Jacquin, L. & Loof, A. (2002). "*Optimal perturbations in a four-vortex aircraft wake in counter-rotating configuration*", Journal of Fluid Mechanics 451, pp. 319–328.
- Figliola, R. S., & Beasley, D. E. (1995). "*Theory and design for mechanical measurements*", 2nd edition, Singapore: John Wiley & Sons Inc.
- Goldstein, R. J. (1996). "*Fluid mechanics measurements*", 2nd edition, Washington DC: Taylor & Francis.
- Hannon, S. M. & Thomson, J. A. L. (1994). "*Aircraft wake vortex detection and measurement with pulsed solid-state coherent laser radar*", Journal of Modern Optics.41 (11), pp. 2175–2196.
- Harris, M., Young, R. I., Kopp, F., Dolfi, A. & Cariou, J. P. (2002). "*Wake vortex detection and monitoring*", Aerospace Science and Technology 6, pp. 325–331.
- Haverkamp, S., Neuwerth, G. & Jacob, D. (2003). "*Studies on the influence of outboard flaps on the vortex wake of a rectangular wing*", Aerospace Science and Technology 7, pp. 331–339.
- Heyes, A. L. & Smith, D. A. R. (2004). "*Spatial perturbations of a wing-tip vortex using pulsed span-wise jets*", Experiments in Fluids 37 (1), pp. 120–127.

- Heyes, A. L. & Smith, D. A. R. (2005). "*Modification of a wing tip vortex by vortex generators*", Aerospace Science and Technology 9, pp. 469–475.
- Hinton, D. A. (1996). "*An aircraft vortex spacing system (AVOSS) for dynamical wake vortex spacing criteria*", In The Characterisation and Modification of Wakes from Lifting Vehicles in Fluid AGARD CP-584.
- Hinton, D. A., Charnock, J. K., Bagwell, D. R., & Grigsby, D. (1999). "*NASA aircraft vortex spacing system development status*", Presented at Proc 37th Aerospace sciences meeting and exhibit: Reno, Nevada. AIAA 1999-0753.
- Huffaker, R. M., Jelalian, A. V. & Thomson, J. A. L. (1970). "*Laser-doppler system for detection of aircraft trailing vortices*", Proceedings of the IEEE 58 (3), pp. 322–326.
- Jordan, F. L. J. (1983). "*Flow visualization of the wake of a transport aircraft model with lateral-control oscillations*", NASA TM-84623.
- Lee, T. & Pereira, J. (2013). "*Modification of Static-wing tip vortex via a slender half-delta wing*", Journal of Fluids and Structures.
- Lee, T. & Su, Y. Y. (2012). "*Wingtip vortex control via the use of a reverse half-delta wing*", Experiments in Fluids, 2012, doi: 10.1007/s00348-012-1274-8.
- Lezius, D. (1975). "*Unstable wing vortex rollup induced by lift tailoring in the wing-tip region*", In Proceedings of the Aircraft Wake Vortices Conference - Vol. 1 DOT/FAA/SD-92/1.1.
- Ludin, H. B., Omar, A. A. & Asrar, W. (2013). "*Numerical study of the effect of spoiler configuration on wake vortex alleviation*", Journal of Aerospace Engineering, [http://dx.doi.org/10.1061/\(ASCE\)AS.1943-5525.0000406](http://dx.doi.org/10.1061/(ASCE)AS.1943-5525.0000406), ASCE publication.
- Ludin, H. B., Omar, A. A. & Asrar, W. (2015). "*Engineering applications of computational fluid dynamics, advanced structured materials*", Chapter No. 7, "*Numerical investigation of the flow over delta wing and reverse delta wing*". Editor, Ku Zilati Ku Shaari and Mokhtar Awang, Springer International Publishing, pp85-101. ISBN: 978-3-319-02835-4.
- Margaris, P., Marles, D. & Gursul, I. (2008). "*Experiments on jet/vortex interaction*", Experiments in Fluids 44, pp. 261–278.
- Matalanis, C. G. & Eaton, J. K. (2007). "*Wake vortex alleviation using rapidly actuated segmented gurney flaps*", The Stanford Thermal and Fluid Sciences Affiliates and the Office of Naval Research, Stanford University, Stanford, Report No. 102.
- Maxworthy, T. (1972). "*The structure and stability of vortex rings*", Journal of Fluid Mechanics, Vol. 51, pp. 15-32.
- McGowen, W. A. (1968). "*Trailing vortex hazard*", Society of Automotive Engineers Business Aircraft Meeting, Wichita, Kansas.

- Ortega, J., Bristol, R. L. & Savas, O. (2002). “*Wake alleviation properties of triangular-flapped wings*”, AIAA Journal 40(4), pp. 709–721.
- Ortega, J., Bristol, R. L. & Savas, O. (2003). “*Experimental study of the instability of unequal-strength counter-rotating vortex pairs*”, Journal of Fluid Mechanics 474, pp. 35–84.
- Ozger, E., Schell, I. & Jacob, D. (2001). “*On the structure and attenuation of an aircraft wake*”, Journal of Aircraft 38(5), pp. 878–887.
- Page, R. D., Clawson, K. L., Garodz, L. J., & Rudis, R. P. (1991). “*Report on tower fly-by testing*”, Proceedings of the FAA Wake Vortices Conference, Washington, D.C.
- Patterson, J. C. (1975). “*Vortex attenuation obtained in the langley vortex research Facility*”, Journal of Aircraft 12(9), pp. 745–749.
- Prandtl, L. (1919), “*Tragflugeltheorie*”, Gottingen Nachrichten, II Mitteilung, Nachrichten von der koniglichen Gesellschaft der Wissenschaften zu Gottingen, Mathematisch-pysikalische Klasse, pp. 107-137.
- Raffel, M., Willert, C., Wereley, S., & Kompenhans, J. (2007). “*Particle image velocimetry: A practical guide*”, 2nd edition, New york: Springer. pp. 3-5.
- Ralf, H., Christoph, R., Sebastian, K., Gunther, N. & Rolf, H. (2007). “*Active manipulation of a rectangular wing vortex wake with oscillating ailerons and winglet-integrated rudders*”, New Res. in Numerical and Experimental Fluid Mechanics. VI, NNFM 96, pp. 44– 51.
- Reynolds, O. (1876). “*On the resistance encountered by vortex rings and relation between the vortex rings and the streamlines of a disk*”, Nature, Vol. 14, pp. 477-479.
- Robinson, J. J. (1996). “*A simulation-based study of the impact of aircraft wake turbulence weight categories on airport capacity*”, AGARD CP-584:1–15.
- Roeland, D. K. (2007). “*Vortex decay behind a generic wing-flap-jet aircraft model*”, Master of Science thesis, TU Delft, The Netherlands.
- Rossow, V. J. (1978). “*Effect of wing fins on lift-generated wakes*”, Journal of Aircraft, 15(3), pp. 160–167.
- Rossow, V. J. (1986). “*Wake hazard alleviation associated with roll oscillations of wake-generating aircraft*”, Journal of Aircraft 23(6), pp. 484–491.
- Rossow, V. J. (1991). “*Prospects for alleviation of hazard posed by lift-generated wakes*”, Proceedings of the Aircraft Wake Vortices Conference, DOT/FAA/SD-92/1.1, November 1991, pp. 22-40.
- Rubin, W. L., Burnham, D. C., Spitzer, E. A. & Rudis, R. P. (2000). “*Robust low cost airport wake vortex sensor*”, Journal of Aircraft 37(3), pp. 377–382.

- Saffman, P. G. (1978). *"The number of waves on unstable vortex rings"*, Journal of Fluid Mechanics, Vol. 84, pp. 625-639.
- Savas, O. (2005). *"Experimental investigations on wake vortices and their alleviation"*, Comptes Rendus Physique, Academie des Sciences, Paris, 6(4-5), pp. 415-429.
- Schell, I., Ozger, E. & Jacob, D. (2000). *"Influence of different flap settings on the wake-vortex structure of a rectangular wing with flaps and means of alleviation with wing fins"*, Aerospace Science and Technology 4, pp. 79-90.
- Scholl, R. H., C. Buxel, & G. Neuwerth (2006). *"Influence of spanwise loading and fins on extended near-field vortex wake"*, AIAA Paper 2006-62.
- Schwarz, C. (2010). *"The green wake project: UV LIDAR for wake vortex detection"*, DLR Institute of Flight Systems, Germany.
- Shaw, J. & Cole, R. (2002). *"Potential benefits of reducing wake vortex related aircraft spacing at the Dallas/Fort Worth International Airport"*, Lincoln Laboratory, Massachusetts Institute of Technology, project report ATC-304.
- Spalart, P. R. & Wray, A. A. (1996). *"Initiation of the crow instability by atmospheric turbulence"*, In the Characterisation and Modification of Wakes from Lifting Vehicles in Fluid AGARD CP-584.
- Spalart, P. R. (1998). *"Airplane trailing vortices"*, Annual Review of Fluid Mechanics 30, pp. 107-138.
- Stumpf, E. (2004). *"Numerical study of four-vortex aircraft wakes and layout of corresponding high-lift configurations"*, AIAA Paper 2004-1067.
- The Star Newspaper, *"Pilot's quick action saves lives"*, 18 December 2013. Retrieved from www.thestar.com.my/News/Nation/2013/12/18/Pilots-quick-action-saves-lives-Aircraft-was-caught-in-747s-slipstream/
- Thomas, A. S. W. (1985). *"Aircraft viscous drag reduction technology"*, Lockheed Horizons, Vol. 19, pp. 22-32.
- Thomson, J. A. L. & Meng, J. C. S. (1976). *"Scanning laser doppler velocimeter system simulation for sensing aircraft wake vortices"*, Journal of Aircraft 13(8), pp. 605-613.
- Traub, L. W., Mani, S., Galls, S. F. & Rediniotis, O. K. (1998). *"Application of the vortex breakdown phenomenon in the attenuation of trailing vortices"*, The Aeronautical Journal 102, pp. 439-444.
- Veillette, P. R. (2002). *"Data show that U.S. wake-turbulence accidents are most frequent at low altitude and during approach and landing"*, Flight Safety Foundation, Flight Safety Digest, March – April 2002, pp. 1-56.
- Webber, G. W., & Dansby, T. (1983). *"Wing tip devices for energy conservation and other purposes"*, Canada, Aerospace Space Journal, Vol. 29, pp. 105-120.

Zhang H. J., Zhou, Y. & Whitelaw, J. H. (2006). "*Near-Field wing-tip vortices and exponential vortex solution*", Journal of Aircraft Vol. 43, No. 2, 445-449.

Publications

Altaf, A., Thong, T. B., Omar, A. A. & Asrar, W. (2015). *“Influence of a reverse delta type add-on device on wake vortex alleviation”*, AIAA Journal, doi: 10.2514/1.J054436.

Altaf, A., Thong, T. B., Omar, A. A., & Asrar, W. (2015). *“Aerodynamic performance of a NACA 23012 half wing model with a reverse delta type add-on device”*. Presented at 8th Ankara International Aerospace Conference, 10-12 September 2015, METU, Ankara, Turkey.